Design, construction and characterisation of a low-level radioactivity counting system based on gamma-ray spectrometry with $LaBr_3$:Ce scintillator detectors

by

Munirat Bashir

Dissertation presented for the degree of Doctor of Philosophy (Physics) in the Faculty of Science at Stellenbosch University

Supervisor: Prof. R. T. Newman
Co-supervisor: Dr. P. Jones

March 2020

Declaration

By submitting this dissertation electronically, I declare that the entirety of the work contained therein is my own, original work, that I am the sole author thereof (save to the extent explicitly otherwise stated), that reproduction and publication thereof by Stellenbosch University will not infringe any third party rights and that I have not previously in its entirety or in part submitted it for obtaining any qualification.

Date: March 2020

Abstract

Design, construction and characterisation of a low-level radioactivity counting system based on gamma-ray spectrometry with $LaBr_3$:Ce scintillator detectors

M. Bashir

Department of Physics,
Stellenbosch University,
South Africa

Dissertation: PhD (Physics)

March 2020

The activity concentrations in naturally occurring radioactive material (NORM) samples are conventionally measured using a gamma-ray spectrometer with a single detector (mostly HPGe or NaI:Tl) enclosed in a lead shield. In this work, the GEANT4 Monte Carlo toolkit was used to design a passive water shielding to reduce background radiation from the measurement environment reaching the detectors which was then constructed. Volume soil samples placed in Marinelli beakers were measured in singles and coincidence modes using four $LaBr_3$:Ce detectors without shielding; two $LaBr_3$:Ce detectors without shielding and the same two $LaBr_3$:Ce detectors inside the constructed water shield. The samples were also measured using a NaI:Tl detector inside the water shield and a standard HPGe detector shielded with lead to compare and validate the results from measurements with the $LaBr_3$:Ce detectors. A novel method of background reduction was employed by using photon time-of-flight in addition to measurement of the two photon energies in coincidence. Both the simulated and measured results show that the water shield attenuates 2614.5 keV (^{208}Tl/^{232}Th series) gamma rays by 90 %. This energy is the maximum full-energy peak centroid in the gamma-ray spectrometry spectrum of NORMs. The activity concentrations of ^{238}U and ^{232}Th series and ^{40}K radionuclides in IAEA-375 soil were determined using the NaI:Tl detector inside the water

shield. The presence of ^{138}La and ^{227}Ac in the $LaBr_3$:Ce detector's crystal increases the minimum detectable activity (MDA) at 1460.8 keV (^{40}K) and 2614.5 keV gamma-ray energies. The measured internal activity of ^{138}La in the $LaBr_3$:Ce detector crystal is 263.8 $\pm$ 26.8 Bq kg^{-1} which is comparable to the calculated activity of 293.3 Bq kg^{-1}. The activity concentration of ^{40}K in IAEA-375 soil and beach sand measured using the $LaBr_3$:Ce detector geometries is below the MDA. The activity concentrations of ^{238}U and ^{232}Th series radionuclides in IAEA-375 soil were determined in coincidence mode using the four $LaBr_3$:Ce detector without shielding. The measured activity concentrations of ^{238}U and ^{232}Th series and ^{40}K radionuclides in IAEA-375 soil were comparable to certified values to within measurement uncertainty. The activity concentrations of ^{238}U and ^{232}Th series radionuclides inside beach sand were determined in both singles and coincidence modes. The results of the measured activity concentrations of ^{238}U and ^{232}Th series radionuclides in beach sand using $LaBr_3$:Ce and NaI:Tl detectors agree with those measured using the HPGe detector system to within 1σ to 2σ level. The water shield (50 cm thickness) performed well in shielding 2614.5 keV background gamma-ray energy by 90 % and energies less than 2614.5 keV by more than 90 % during low-level radioactivity measurements. The internal activity of the $LaBr_3$:Ce detector increases the MDA at 1460.8 keV and 2614.5 keV, which limits the measurement of ^{40}K radionuclide with low activity concentration in singles mode. The use of a coincidence method plus photon time-of-flight significantly suppresses the scattered/background radiation.

Uittreksel

Ontwerp, konstruksie en karakterisering van 'n lae-vlak radioaktiwiteit telsisteem gebaseer op gammastraal spektrometrie met $LaBr_3$:Ce sintillasie detektors

M. Bashir

Fisika Departement,
Universiteit van Stellenbosch,
Privaatsak X1, Matieland 7602,
Suid Afrika.

Proefskrif: PhD (Fisika)

Maart 2020

Die aktiwiteitskonsentrasies in monsters van radioaktiewe materiaal wat natuurlik voorkom (NORM) word normaalweg gemeet met 'n gammastraal spektrometer wat uit 'n enkele detektor (meestal HPGe of NaI:Tl) bestaan en omhul is in 'n loodskerm. In hierdie werk is 'n passiewe waterskerm, bedoel om die agtergrondstraling wat die detektors kan bereik te verminder, ontwerp met behulp van GEANT4 Monte Carlo simulasies en dan gebou. Volume grondmonsters wat in Marinelli bekers geplaas is, is gemeet in enkel- en gelyktydige-modus met behulp van vier $LaBr_3$:Ce detektors sonder afskerming; twee $LaBr_3$:Ce detektors sonder afskerming en dieselfde twee $LaBr_3$:Ce detektors binne die geboude waterskerm. Die monsters is ook gemeet met behulp van 'n NaI:Tl detektor binne die waterskerm en 'n standaard HPGe detektor, wat met lood afgeskerm is, om die resultate van metings met die $LaBr_3$:Ce detektors te vergelyk en te bekragtig. 'n Nuwe metode vir die vermindering van agtergrond, deur gebruik te maak van foton-vlugtyd, is aangewend saam met die gelyktydige meting van die twee fotonenergiee. Beide die gesimuleerde en gemete resultate toon dat die waterskerm gammastrale van energie 2614.5 keV (^{208}Tl / ^{232}Th-reeks) met 90 % verminder. Hierdie energie is die maksimum vol-energie piek in die gammastraalspektra van NORMs.

Die aktiwiteitskonsentrasies van ^{238}U en ^{232}Th-reeks en ^{40}K radionukliede in IAEA-375 grond is bepaal deur middel van die NaI:Tl detektor binne die waterskerm. Die teenwoordigheid van ^{138}La en ^{227}Ac in die kristal van die $LaBr_3$:Ce detektor verminder die minimum waarneembare aktiwiteit (MDA) by gammastraal energiee van 1460.8 keV (^{40}K) en 2614.5 keV. Die gemete interne aktiwiteit van ^{138}La in die $LaBr_3$:Ce detektorkristal is 263.8 $\pm$ 26.8 Bq kg^{-1}, wat vergelykbaar is met die berekende aktiwiteit van 293.3 Bq kg^{-1}. Die aktiwiteitskonsentrasie van ^{40}K in IAEA-375 grond en strandsand is laer as die MDA, soos gemeet met die $LaBr_3$:Ce detektor geometrie. Die aktiwiteitskonsentrasies van ^{238}U en die ^{232}Th-reeks radionukliede in IAEA-375 grond is in gelyktydige-modus bepaal met behulp van die vier $LaBr_3$:Ce detektors sonder afskering. Die resultate van die gemete aktiwiteitskonsentrasies van ^{238}U en ^{232}Th-reeks en ^{40}K radionukliede in IAEA-375 grond het binne eksperimentele onsekerheid met gesertifiseerde waardes ooreengestem. Die aktiwiteitskonsentrasies van ^{238}U en die ^{232}Th-reeks radionukliede in strandsand is in beide enkel- en gelyktydige-modus bepaal. Die resultate van die gemete aktiwiteitskonsentrasies van ^{238}U en ^{232}Th-reeks radionukliede in strandsand, soos gemeet met $LaBr_3$:Ce en NaI:Tl detektors, het binne die 1σ tot 2σ vlak ooreengestem met die gemeet met die HPGe detektorstelsel. Die waterskerm (50 cm dikte) het goed gevaar om agtergrond gammastrale van 2614.5 keV met 90 % af te skerm, en gammastraal energiee minder as 2614.5 keV met meer as 90 % af te skerm tydens lae-vlak radioaktiwiteitsmetings. Die interne aktiwiteit van die $LaBr_3$:Ce detektor verhoog die MDA by 1460.8 keV en 2614.5 keV, en dit beperk die meting van ^{40}K radionukliede met 'n lae aktiwiteitskonsentrasie in enkel-modus. Die gebruik van die gelyktydige-modus saam met foton vlugtyd onderdruk die verstrooide- / agtergrondstraling beduidend.

Acknowledgements

I thank my supervisors; Prof. R.T. Newman for his patient, guidance, advice and believing in my ability to independently manage my research and at the same time having interest in my work, wellbeing and success; and Dr. Pete Jones for his guidance, constructive criticism and for making me realise my abilities and strength. They were just the right combination of supervisors needed for me to succeed.

I am also grateful to Ibrahim Badamasi Babangida University/TETFund for the opportunity to do my PhD and the funding. I am also thankfull to the National Research Foundation of South Africa (grant number: 99037) for providing the equipment and iThemba LABS for the top-up funding and opportunity to attend numerous conferences and workshops. I also thank the Department of Physics and Faculty of Science, Stellenbosch University for the top-up funding received.

I am grateful to Dr. J.J. Van Zyl for translating my English abstract to Afrikaans. I also appreciate the support of the iThemba LABS INIT Department especially Prof. Paul Papka and Basil Martin for making the construction of the water shield possible.

I am thankful to my siblings; Abdullah, Hafsat, Amina and Suwaiba for all their love and support. And my friends; Amina, Joseph and Chinenye for their word of encouragement, emotional support and for always being ready to listen to me.

I thank Christian Brits for making my movement to iThemba LABS easy and my colleagues Lumkile Msebi, Abraham Avaa, Maluba Vernon Chisapi and Doris Kenfack for always being willing to help with moving detectors and electronics for my experimental setups. I also thank the staff members of Physics Department, Stellenbosch University and the Department of Subatomic Physics, iThemba LABS for their help; especially Stanley February, Avuyile Bulala, Dr. Peane P. Maleka and Hombakazi Wanana.

Munirat Bashir

Dedications

I dedicate this work to my mother, for her love, encouragement, moral and financial support towards achieving my goals and my late father for his guidance.

Contents

List of Figures

List of Tables

Chapter 1

Introduction

1.1 Background

Humans are continuously exposed to ionizing radiation from natural radioactive sources present in the Earth's crust, from cosmic radiation, and anthropogenic sources [1]. The measurements and understanding of radionuclides present in the environment, along with their pathways to humans, begins with the global concern about human radiation exposure due to atmospheric nuclear weapons testing [1]. Radionuclides present in environmental materials are often measured using a variety of spectrometry techniques, of which gamma-ray spectrometry is a tool for non-destructive radionuclide identification [2–4]. Peer-reviewed literature shows that a single scintillator (NaI:Tl) or semiconductor (HPGe) detector is often used in laboratory measurement of low-level radioactivity content of a sample gamma-ray emitting. The detector (or detection system) is shielded with lead to reduce the natural background radiation contribution as shown in Fig. 1.1 [5–12]. Since lead shielding generates X-rays, the inner part of the shielding is usually lined with one or combination of the

following materials; copper (Cu), cadmium (Cd), tin (Sn) to absorb the X-rays [5–9]. Occasionally, the spectrometer is situated in an underground laboratory for cosmic radiation suppression [6–8; 12]. It is noteworthy that ^{210}Pb from the ^{238}U series cannot be removed from Pb by the chemical-refining processes and the amount of ^{210}Pb in Pb depends on its origin and age [12; 13]. The progeny of ^{210}Pb; ^{210}Bi with a half-life of 5.0 days will lead to bremsstrahlung continuum stretching to low energy as it emits beta particles with maximum energy of 1161 keV [12]. Also, a study carried out by Keillor *et al.* [14] shows that commercial Pb in the U.S. contains roughly an order of magnitude higher ^{210}Pb levels except for stockpiled Doe Run Pb. This could be the reason for the use of 10 - 14.5 cm thick ordinary lead combined with 3.5 - 5 cm low-level lead, instead of 10 cm thickness of low-level radioactivity lead previously used [5–11]. Lead is expensive and requires the use of other materials in combination with it, thereby increasing the cost of shielding.

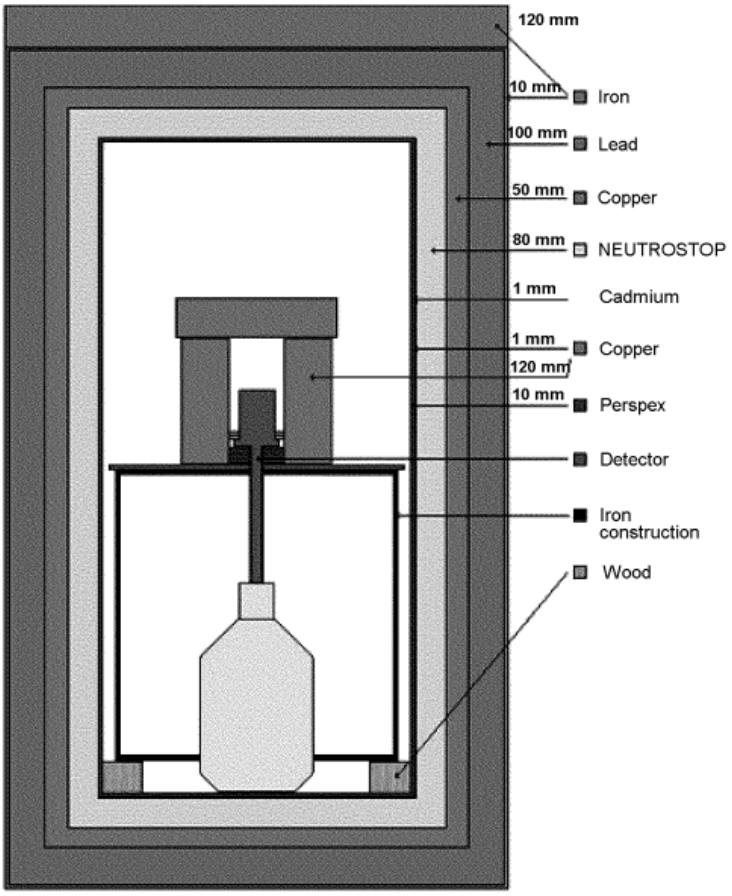

Figure 1.1: Low-level shielding for low background gamma-ray spectrometry (NEUTROSTOP material is polyethylene with boric acid). Image from reference [5].

Recently, the gamma-gamma coincidence method has been applied in the measurement of cascade-emitting radionuclides in environmental samples. This method has the advantage of minimising continuum background, eliminating interference, and reducing spectrum background, thereby reducing the minimum detectable activity (MDA) [15–18].

In 2009, Antovic and Svrkota [19, 20] measured the activity of ^{232}Th and ^{226}Ra progenies in soil with a 4π gamma-ray coincidence spectrometer called PRIYAT-2M. The spectrometer consists of six NaI:Tl crystals each with a di-

ameter of 15 cm and height of 10 cm. The spectrometer was shielded with Fe and Pb and has an outer dimension of 250 × 145 × 186 cm^3. Counting was done in integral mode and coincidence mode (2-, 3-, 4-, 5- and 6-fold) with PRIP software using buffer memory. The optimal activity concentration results were obtained with double coincidence mode of counting for ^{232}Th (583 keV and 2615 keV) and ^{226}Ra (609.3 keV). However, the overlapping gamma-ray peaks centred at 1120.3 and 1238.1 keV were not resolved because of the detector's limited energy resolution which is 10.5 % for 662 keV gamma-line of ^{137}Cs.

In 2015, Britton *et al.* [21, 22] developed a method to measure cascade gamma rays. This method uses a software package which in turn uses Evaluated Nuclear Structure Data File (ENSDF) records as input and calculates the efficiency as well as cascade summing corrected branching ratios. Calibration sources (^{54}Mn, ^{57,60}Co, ^{65}Zn, ^{88}Y, ^{109}Cd, ^{113}Sn, ^{137}Cs, ^{139}Ce, ^{241}Am) were measured using a gamma-gamma coincidence spectrometer to test the software. This spectrometer comprised two planar HPGe detectors (model BE6530) enclosed in a lead cave. The detector signals were linked to a LYNX^{TM} digital signal processor and data were acquired in list-mode. The gamma-gamma detection system produces singles spectra and coincidence matrices. Correction for time-walk associated with low energy events and removal of accidental coincidences were accomplished using the two gamma ray energies of ^{60}Co and their lifetime, which improved the width and shape of the peak. The results for the investigated nuclides were found to be accurate.

In 2017, Paradis *et al.* [23] and Markovic *et al.* [24] measured the radioactivity in environmental samples using a gamma-gamma coincidence spectrometer. Paradis *et al.* [23] uses a spectrometer called "Leda" to measure ^{40}K, ^{60}Co,

^{134,137}Cs, ^{108m,110m}Ag in the samples. Leda consists of two HPGe detectors and one NaI:Tl detector shielded with a 5 cm thick lead. This spectrometer was placed in a room shielded with 10 cm layer of lead and 5 mm oxygen-free high thermal conductivity (OFHC) copper which reduces the natural background radioactivity by two orders of magnitude. Data were acquired in list mode and sorted into singles, anti-coincidence and coincidence analysis channels using Python. The detection limits were improved for all the gamma-ray emitters using the coincidence method despite its low efficiency.

Markovic *et al.* [24] uses the Nutech Coincidence Low Energy Germanium Sandwich (NUCLeGeS) spectrometer to measure ^{134}Cs and ^{210}Pb in the NBL 103 certified reference material and a standardized set of filters. The NUCLeGeS comprises of two HPGe (Canberra LEGe GL3825R) detectors encased in 20 cm Pb with 0.5 cm Sn and 0.3 cm Cu inner lining. List-mode data were collected every 10 ns timestamp and post-processed using MATLAB based software to create two energy spectra. Coincidence spectra within the time window of 1,200,000 ps were generated and the total coincidence spectrum was subtracted from the total spectrum to obtain the anti-coincidence spectrum. The MDA for all the cascade emitting isotopes were improved based on coincidence measurement.

In 2018, Tillet *et al.* [25] measured the activity concentration of thorium and uranium daughters in Brazil nuts, potting mix and magazine paper using gamma-gamma coincidence spectrometry. The spectrometer comprises of two NaI:Tl detectors (each with a crystal length of 10.16 cm and diameter of 15.24 cm) inside a combination of lead, copper, aluminium and steel passive shielding. A lead plate was placed between the two detector faces to lessen the Compton scattered coincidence events. The thorium and uranium daughter's

activity concentrations were determined and the coincidence detection efficiencies for both ^{208}Tl and ^{214}Bi were < 1 %. The coincidence background count rates were lower by three orders of magnitude compared to the singles count rates.

1.1.1 $LaBr_3$:Ce Scintillator Detector

$LaBr_3$:Ce is an inorganic scintillator detector with high atomic number, density, intrinsic gamma-ray detection efficiency and light yield [12; 13; 26–30]. It also has good energy resolution and fast decay time [12; 13; 26–30]. These properties are the basic requirements for effective gamma-ray measurements [12; 13]. The energy resolution of $LaBr_3$:Ce detectors is superior to that of NaI:Tl detectors e.g. 3.0 % at 662 keV gamma ray of ^{137}Cs compared to 7 % for NaI:Tl detector [31]. The $LaBr_3$:Ce detectors are also more efficient at detecting gamma rays than NaI:Tl detectors (a factor of 1.5) at 662 keV [26; 31; 32]. In addition, $LaBr_3$:Ce compared to HPGe has the operational advantage of lack of need for liquid nitrogen cooling and sub-nanosecond intrinsic timing resolution [33].

$LaBr_3$:Ce detectors have been used in efficiency calibrations [27; 34], mobile and high energy gamma-ray spectroscopy [31; 35–38], gamma-gamma coincidence measurements [17; 39], luminescence and electron spin resonance dating applications [40]. It has also been applied in timing resolution measurements [41; 42], lifetime measurements [43; 44], positron-emission tomography (PET) time-of-flight [45; 46] and neutron measurements [47]. Finland's Radiation and Nuclear Safety Authority (STUK) is adopting $LaBr_3$:Ce detector as part of its environmental monitoring detection capability [48].

However, there is an issue with internal radioactivity in the $LaBr_3$:Ce detec-

tor due to natural lanthanum containing the radionuclides ^{138}La and ^{227}Ac [31; 32; 49]. The natural lanthanum contains 0.09 % of the ^{138}La which produces: a 788.7 keV gamma ray and 4.3 keV to 40.3 keV X-rays from beta decay to ^{138}Ce, and a 1435.8 keV gamma ray and 4.0 keV to 37.3 keV X-rays from electron capture to ^{138}Ba. Also, ^{227}Ac emits several alphas in decaying to stable ^{207}Pb, which appears in gamma-ray spectra between 1800 keV and 2700 keV [49]. For a 2" $\times$ 2" $LaBr_3$:Ce detector with a density of 5.08 g cm^{-3} and mass of 523.10 g, the expected activity concentration of ^{138}La is 293.3 Bq kg^{-1}. Before this study, it was not clear whether this internal radioactivity acts as a fundamental limitation for ex-situ (sample) low-level activity measurements of gamma rays from NORM.

This work investigated the use of $LaBr_3$:Ce scintillator detectors for measurement of primordial radionuclide activity concentrations in environmental samples (ex-situ) using singles and coincidence methods. Furthermore, it studies the extent to which $LaBr_3$:Ce internal radioactivity affects low-level activity measurements in the laboratory. It investigates an alternative shielding material (water) with little or no radioactive content which could serve the purpose with less cost.

1.2 Aim and Objectives

The aim of this research is to design, construct and characterise a low-level radioactivity counting system based on gamma-ray spectrometry with $LaBr_3$:Ce scintillator detectors.

To accomplish this aim, the objectives are:

- to measure reference gamma ray sources, a reference standard soil sample

and a soil sample using $LaBr_3$:Ce detectors, without shielding in singles and coincidence modes of gamma-ray counting;

- to simulate and design a water shield to minimise the background radiation reaching the detectors based on simulations with the GEANT4 Monte Carlo toolkit and to then construct the water shield;
- to measure reference sources and soil samples using $LaBr_3$:Ce detectors inside the constructed water shielding in singles and coincidence modes of gamma-ray counting; and
- to characterise the $LaBr_3$:Ce detector system in terms of energy resolution, full-energy peak gamma-ray detection efficiency, Peak-to-Total ratio and minimum detectable activity (MDAs), and to measure the same samples using a NaI:Tl detector inside the water shield and a standard HPGe detector shielded with Pb to compare and validate the $LaBr_3$:Ce detectors results.

1.3 Dissertation Overview

The dissertation structure is as follows; theory relevant to this study are reviewed in Chapter 2. The type of environmental radioactivity; primordial, cosmic and anthropogenic radiation and the radionuclides present in these sources are discussed. This is followed by a discussion on gamma-ray interaction mechanism such as photoelectric absorption, Compton scattering and pair production dominant in gamma-ray spectroscopy together with attenuation and mean-free path. Then, the band structure in solids, and the radiation detection processes with inorganic scintillator and semiconductor material are described. Furthermore, energy resolution, true coincidence summing, detec-

tion efficiency, activity concentration, Peak-to-total area ratio and MDA, dead time and gamma-ray energies emitted by NORM radionuclides are reviewed. Literature on low-level gamma-ray spectrometry setups and $LaBr_3$:Ce-based spectrometry systems are reviewed and summarised in Chapter 3. Chapter 4 describes the GEANT4 Monte Carlo simulations which include; introduction to Monte Carlo methods, GEANT4 implementation classes and the simulations performed by this work. Chapter 5 provides details of the experimental method. This include sample/reference material selection, measurement using four $LaBr_3$:Ce detectors without shielding, the associated electronics and data acquisition system, measurement using HPGe detector with lead shielding and measurement using $LaBr_3$:Ce and NaI:Tl detectors inside the constructed water shielding. Background/scattered gamma ray reduction using time-of-flight and measurement of two photons, and dead time measurement is also described. Chapter 6 includes a discussion of the data processing and analysis after data acquisition. This chapter includes a discussion on spectrum energy calibration, time spectra, time gated gamma-gamma spectra, gamma-ray energy spectra, evaluation of the gamma-ray spectra and calculations. Chapter 7 presents and discusses energy resolution, detection efficiency, attenuation of gamma rays with the water shield, Peak-to-Total area ratio and MDA, and activity concentration results. Lastly, Chapter 8 gives a summary of the results and conclusion. Publications stemming from this work are incorporated in Appendix C.

Chapter 2

Theory

In this chapter, theories relevant to this work will be reviewed. Since this research focuses on measuring the radionuclide in environmental samples, it is pertinent to understand the type of environmental radiation. Gamma-ray spectrometry techniques are used in measuring the radionuclides in the sample, therefore it is important to know what a gamma ray is, its mechanism of interaction with material and the type of material used in measuring it (detectors). Understanding the properties of the radiation detectors such as energy resolution, detection efficiency, Peak-to-Total area ratio and dead time allow for correct use of the detectors for measurement. Knowing the gamma-ray energies emitted by the NORM nuclides and their characteristics will help in choice of gamma-ray energies to use in quantifying the activity concentration of the radionuclides in the samples.

2.1 Environmental Radioactivity

Our environment contains various amounts of radioactive material [2; 50–52]. The sources of these radioactive material depend on the surrounding environ-

ment and location [51]. The types of environmental radiation are primordial radiation, cosmic radiation and anthropogenic radiation.

2.1.1 Primordial Radiation

Primordial radiation comes from long-lived radionuclides present on Earth since its creation ($\approx$ 4.5 billion years ago) [52; 53]. These radionuclides could occur either singly or in radioactive decay series [52]. There are at least 23 singly occurring radionuclides but only ^{40}K and ^{87}Rb are of biological importance [52]. The most abundant naturally occurring radioactive material is ^{40}K with a half-life of 1.28×10^9 yrs and β^- decays to stable ^{40}Ca (89.28%) and β^+ (10.72%) decays to stable ^{40}Ar emitting a 1460.8 keV gamma-ray [12; 50–52]. The half-life of ^{87}Rb is 4.8×10^{10} yrs and it β^- decays to stable ^{87}Sr but does not emit gamma radiation [52].

The radioactive decay series are ^{237}Np, ^{232}Th, ^{235}U and ^{238}U but only ^{232}Th, ^{235}U and ^{238}U still exist [2; 50–54]. The only isotope of natural thorium is ^{232}Th while ^{235}U and ^{238}U are isotopes of natural uranium [2; 12; 50–52; 54; 55]. These radionuclides (^{232}Th, ^{235}U and ^{238}U) are unstable and undergo several decay stages (through α and β decays) producing secondary radionuclides before ending with a stable lead isotope as shown in Figs. 2.1 $\rightarrow$ 2.3 [2; 12; 50–54]. Each of these daughters (d) are in secular equilibrium with the parent (p) (i.e. have equivalent activity) if the parent half-life (λ_p) is far greater than the daughter half-life (λ_d) i.e. $\lambda_p \gg \lambda_d$ [52]. This means the parent activity remains the same while the activity of the daughter increases until it is the same as that of the parent [51]. Radon is a gas and its isotopes are present in all the three decays series: ^{220}Rn from ^{232}Th, ^{219}Rn from ^{235}U and ^{222}Rn from ^{238}U [12; 54; 55]. Due to the ^{238}U abundance, ^{222}Rn is more abundant than the

other radon isotopes [55]. Also, ^{222}Rn has a greater chance of dispersing from the sample in which it is found than ^{219}Rn (half-life of 3.96 seconds) and ^{220}Rn (half-life of 55 seconds) because of its long half-life of 3.8 days [12; 50; 52–55].

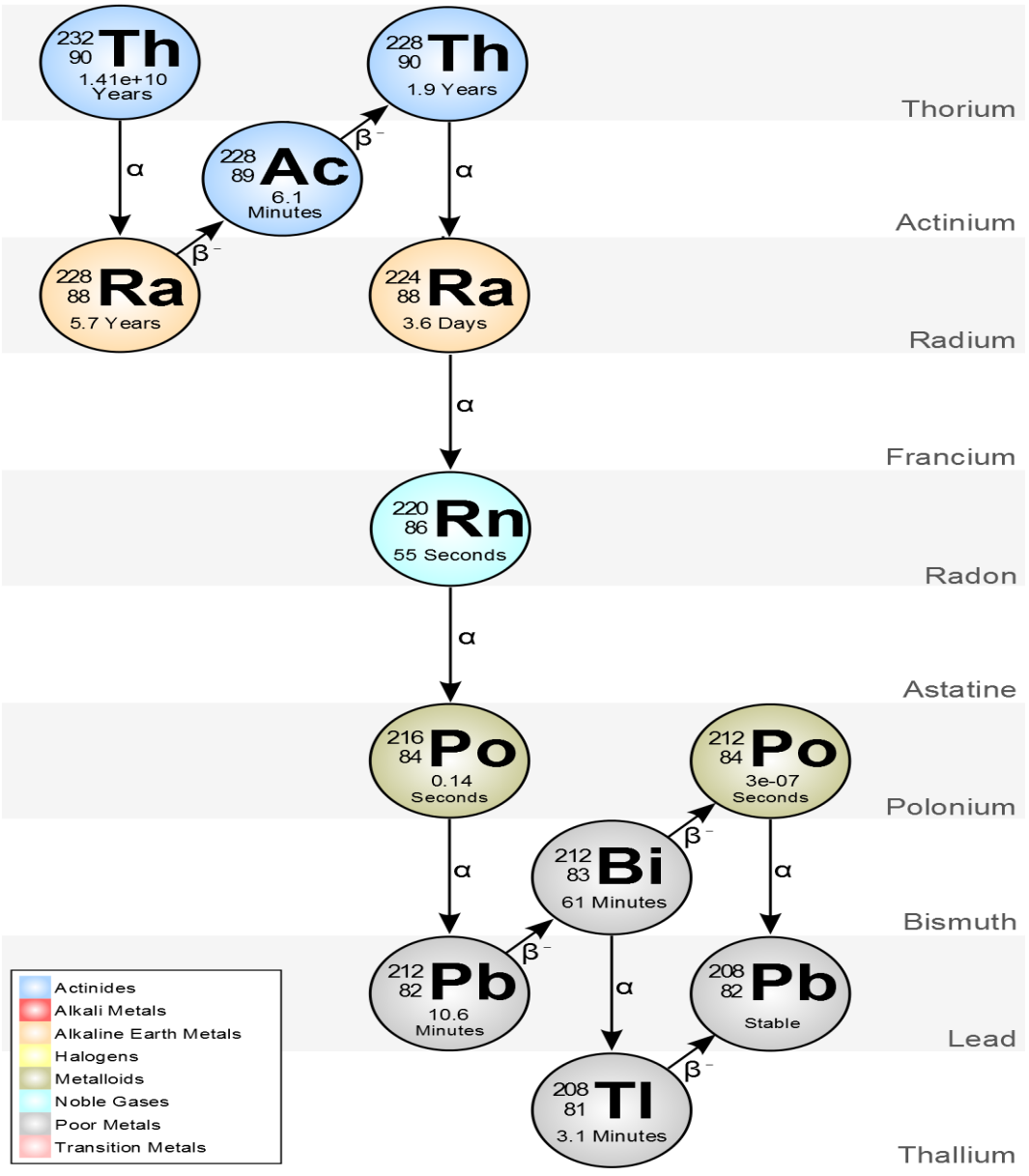

Figure 2.1: ^{232}Th decay series, the gamma-emitters are; ^{228}Ac, ^{224}Ra, ^{212}Pb, ^{212}Bi and ^{208}Tl. Image from reference [56].

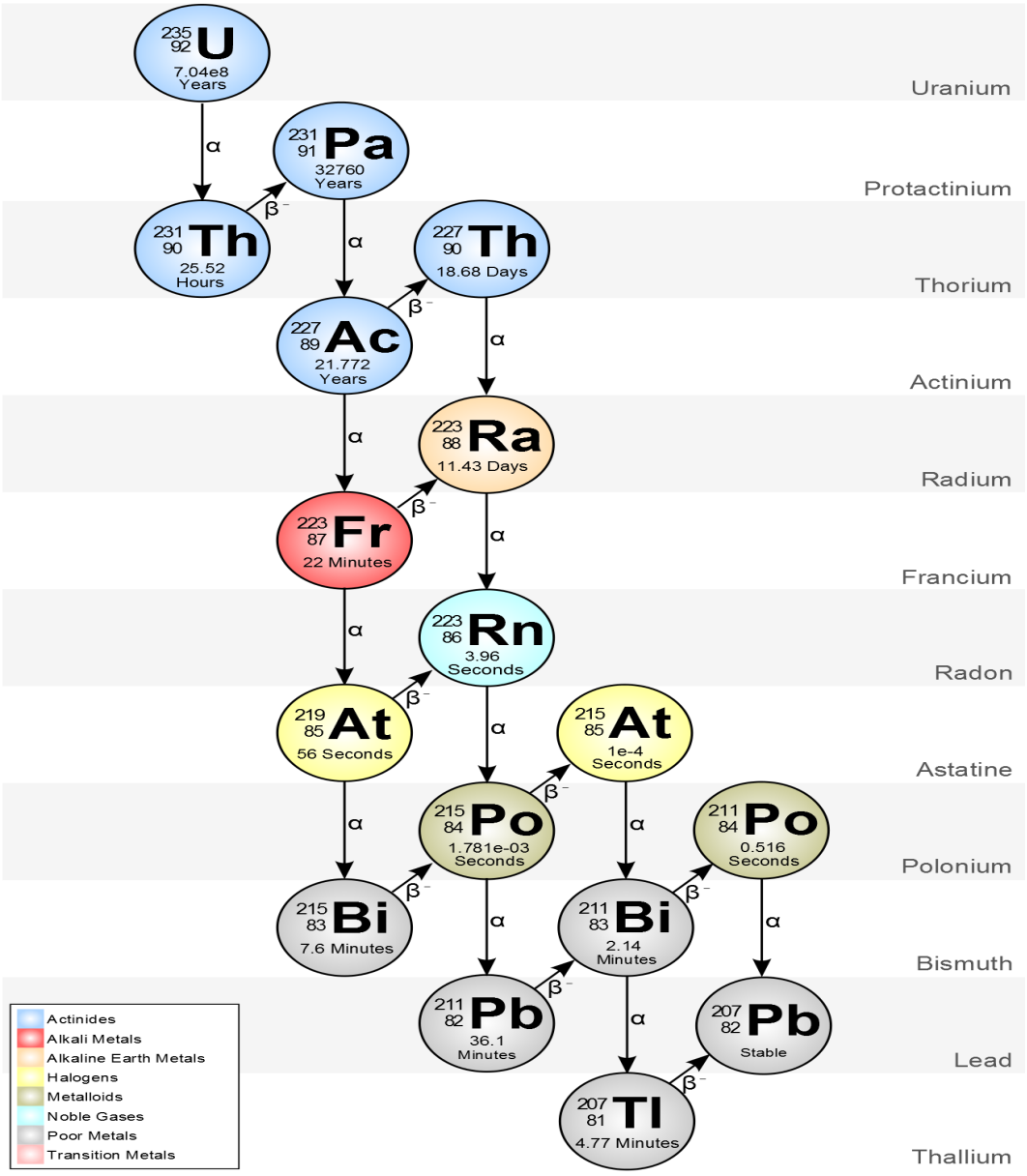

Figure 2.2: ^{235}U decay series, the gamma-emitters are; ^{235}U, ^{227}Th, ^{223}Ra and ^{219}Rn. Image from reference [56].

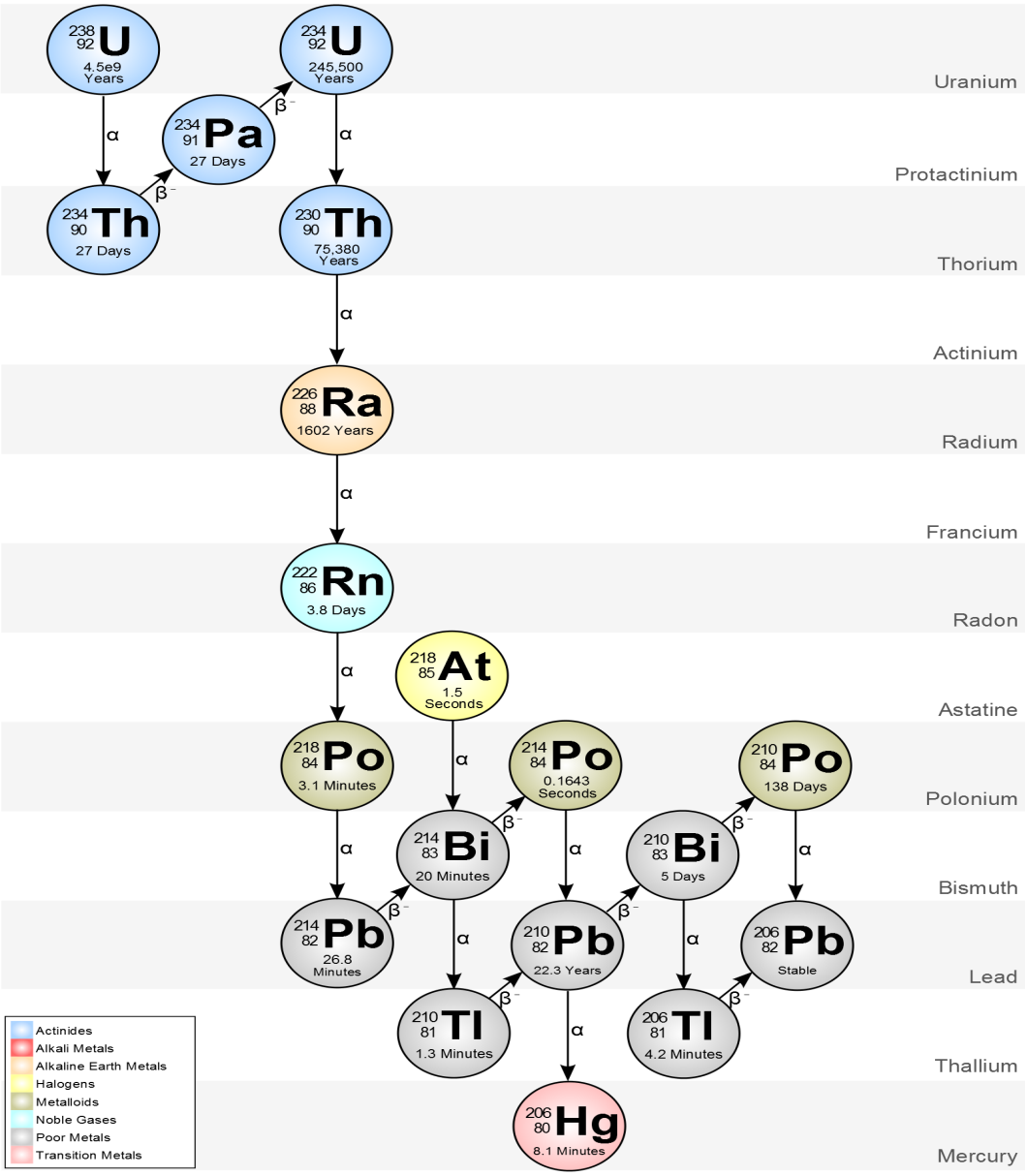

Figure 2.3: ^{238}U decay series, the gamma-emitters are; ^{234}Th, ^{234}Pa, ^{226}Ra, ^{214}Pb, ^{214}Bi and ^{210}Pb. Image from reference [56].

2.1.2 Cosmic Radiation

Primary cosmic radiation are highly energetic particles that emanate from outer space consisting of electrons, heavier nuclei, alpha particles and protons. These primary particles interact with the atmosphere to produce mesons, neu-

trons, electrons, gamma rays and cosmogenic radionuclides [2; 50–54]. Cosmogenic radionuclides are; ^{3}H, ^{7,10}Be, ^{14}C, ^{16}F, ^{22,24}Na, ^{26}Al, ^{28}Mg, ^{31,32}Si, ^{32,33}P, ^{34m,36,38,39}Cl, ^{37,39}Ar, ^{38}S and ^{80}Kr with ^{3}H, ^{7}Be and ^{14}C being the most important [2; 50; 51; 53]. The interaction of neutrons with ^{14}N and ^{16}O produce ^{3}H (12.3 yrs half-life), ^{7}Be (53.4 d half-life) and ^{14}C (5.73×10^{3} yrs half-life), ^{14}C β^{-} decays back to ^{14}N [50; 51].

The interaction of a cosmic ray with constituents of the sea or Earth's crust is small compared to its interaction with the atmosphere. Small amounts of radioactive materials are produced by neutron capture in the Earth's crust or the sea [51].

2.1.3 Anthropogenic Radiation

Anthropogenic radiation stems from artificially produced radiation and increases in natural radiation due to human activities [2; 53]. This includes activities such as uranium mining, mineral processing and metallurgical extraction that producing tailings, waste rocks, heap leach residues and mine water which are released to the environment [2; 50; 53; 55]. Furthermore, combustion of fossil fuels, gas and oil extraction, production of catalysts, special glasses, iron and steel lead to release of radionuclides into the environment [2; 50; 53]. Also, fertilizer production from phosphoric acid, cement and phosphorus production contribute to environmental radionuclides [2; 50; 53; 55]. Testing of nuclear weapons and nuclear power plant operation releases radionuclides such as ^{3}H, ^{14}C, ^{85}Kr, ^{129}I and ^{137}Cs into the environment and significant amounts of radioactive materials can be discharged into the environment in the event of a nuclear accident; for example that of the Chernobyl nuclear power plant explosion in 1986 released at least 5 % of the radioactive reactor core (the

most dangerous of the elements released are ^{131}I, ^{90}Sr and ^{137}Cs) into the atmosphere [50]. Consumer products like smoke detectors and certain ceramics emitting radiation also contribute to the radiation in the environment [2].

2.2 Gamma-ray Interactions with Matter

Gamma rays are electromagnetic radiation with high frequency and short wavelength which emanate from the nucleus. These gamma rays (γ) are emitted by excited nuclei after radioactive transformation by alpha particle (α) emission, beta particle (β^-) emission, positron (β^+) emission or electron capture (EC) [12; 51; 57]. The atomic number (Z), neutron number (N) and mass number (A) remain the same after the emission of one or more gamma rays. The predominant mechanisms of gamma-ray interaction with matter (important in the energy regime of environmental assaying) are photoelectric absorption, Compton scattering and pair production [12; 13; 15; 50; 51; 57; 58]. Other types of interaction of gamma ray with matter are photo-fission, Rayleigh scattering and Thomson scattering [59]. In the case of Rayleigh scattering, the incident photon is scattered by the atom and changes its direction, the target atom recoils to conserve momentums before and after scattering. The recoil energy of the atom is very small and can be negligible because of the large atomic mass.

2.2.1 Photoelectric Absorption

A gamma ray may transfer its energy to a tightly bound orbital electron (mostly from the K shell of the atom, see Fig. 2.4), thereby removing it from the atom creating an ion. This electron kinetic energy is the difference between the incident gamma-ray energy and the electron binding energy

[12; 13; 15; 50; 51; 57; 58; 60]. Photoelectric absorption is dominant at energies of 0.001 MeV to 0.5 MeV and its probability decreases with increase in gamma-ray energy [60]. The photoelectric attenuation coefficient μ_{pe} is [12]:

$$\mu_{pe} = \left\{ c\frac{Z^a}{E_\gamma^b} \right\} \times \rho \times \frac{N_A}{A} \tag{2.2.1}$$

where a and b have value of 3 to 5 respectively, c is a constant, E_γ the incident gamma-ray energy, ρ the absorbing material density, A the atomic mass, Z the atomic number and N_A the Avogadro number.

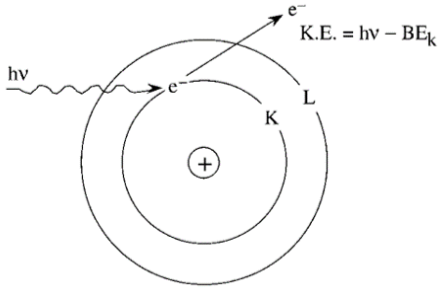

Figure 2.4: Photoelectric absorption. Image from reference [51].

2.2.2 Compton Scattering

Compton scattering occurs when an incident gamma-ray photon interacts with an electron (the incident gamma-ray energy must be greater than the electron binding energy if e^- not free). Then, the gamma ray scatters with a reduced energy equal to the difference between the incident gamma-ray energy and the energy imparted to the recoil electron as shown in Fig. 2.5 [12; 13; 15; 50; 57; 58].

$$E'_\gamma = \frac{E_\gamma}{(1 - cos\theta)\left(\frac{E_\gamma}{m_0 c^2}\right) + 1} \tag{2.2.2}$$

where θ is the scattering angle, E_γ is the incident gamma ray, and E'_γ is scattered gamma ray, m_0 is the rest mass of an electron and c is the speed of light.

The Klein-Nishina formula (Eqn. 2.2.3) gives the angular spread of scattered gamma-ray photons [15; 57].

$$\frac{d\sigma_k}{d\Omega} = Z\left[\frac{1}{1+\beta\left(1-cos\theta\right)}\right]^2\left[\frac{1+cos^2\theta+\beta^2\left(1-cos\theta\right)^2}{1+\beta\left(1-cos\theta\right)}\right] \tag{2.2.3}$$

where $Z = e^4/2m_0^2c^4$, $\beta = hf/m_0c^2$, f is the frequency of the photon, h is the plank's constant and e is the electron.

Compton scattering is dominant at energies of between 0.5 MeV to 1 MeV [51] and its probability increases with decreasing energy and atomic number [15; 57]. The Compton scattering attenuation coefficient μ_{cs} is [12]:

$$\mu_{cs} = \left\{cf\left(E_\gamma\right)\right\}^2 \tag{2.2.4}$$

where c is a constant and f is function.

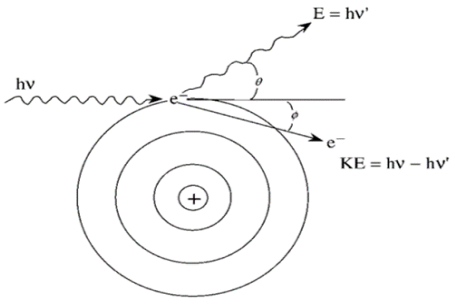

Figure 2.5: Compton scattering with a loosely-bound electron. Image from reference [51].

2.2.3 Pair Production

For the pair production process to occur, the gamma-ray energy must be greater than 1022 keV. The gamma ray interacts with the nucleus producing an electron-positron pair with a kinetic energy equal to the difference between the incident gamma-ray energy and combined rest-mass of the particles as shown in Fig. 2.6 [12; 13; 15; 50; 51; 57; 58]. The slowing down of the positron in the

medium causes it to annihilate producing two annihilation photons [12; 15]. A single-escape peak will appear in the spectrum at an energy equal to the difference between the photopeak energy and electron rest-mass if one annihilation photon is absorbed in the medium and the other escapes [12; 15]. The double-escape peak will appear in the spectrum at an energy equal to the difference between the photopeak energy and two electron rest-masses if both annihilation photons escape the medium [12; 15]. Pair production dominates at gamma-ray energies greater than 10 MeV [12; 60]. The pair production attenuation coefficient is μ_{pp} [12]:

$$\mu_{pp} = \left\{ Z^2 f\left(E_\gamma, Z\right) \right\} \times \rho \times \frac{N_A}{A} \tag{2.2.5}$$

All terms in Eqn. 2.2.5 have definitions as described in Section 2.2.2.

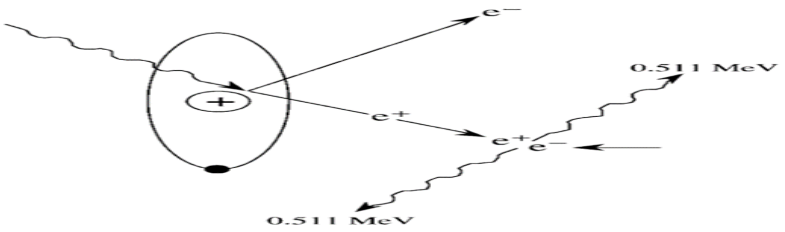

Figure 2.6: Pair production. Image from reference [51].

2.2.4 Attenuation and Mean-free Path

High density (ρ) and high atomic number (Z) materials are usually used to absorb gamma rays as the gamma rays have high penetrating power [15]. However, low ρ and high Z material with thick layers will have the same effect as high ρ and Z material with thin layers since the degree of attenuation depends on the material's density and thickness [61]. When a narrow beam of gamma rays passes through an absorber material of thickness (t), the number of the gamma rays attenuated at a specific energy can be calculated using Eqn.

2.2.6 [12; 13; 15; 51]. Moreover, if the gamma ray must penetrate a shield composed of a series of different materials of thicknesses t_i and attenuation coefficients μ_i before reaching the detector, then Eqn. 2.2.7 is applied.

$$I_f = I_0 e^{-\mu t} \tag{2.2.6}$$

$$I_f = I_0 e^{-\sum_i \mu_i t_i} \tag{2.2.7}$$

where I_0 and I_f are the measured gamma-ray intensities at a specific energy before and after attenuation respectively, t is the absorber thickness in cm, μ is the linear attenuation coefficient in cm^{-1} and $\sum_i \mu_i t_i$ is the total number of mean free-path lengths of attenuating material that an unattenuated gamma ray must traverse without interaction. However, if a broad beam of gamma rays passes through an absorber material of thickness t, then Eqn. 2.2.8 is applied in calculating the final gamma-ray intensity which is a combination of the gamma rays that pass through the absorber material without interaction and some gamma rays scattered in the absorber material and secondary gamma rays [15; 51].

$$I_u = B I_0 e^{-\mu t} \tag{2.2.8}$$

where B is the buildup factor which depends on the absorber material, the absorber material thickness, the gamma-ray energy, and the specific gamma-ray energy attenuation coefficient in the material [12; 15; 51]. The gamma-ray attenuation coefficient (μ) is the summation of the attenuation coefficient due to all gamma-ray interaction mechanisms (see Eqn. 2.2.9 and Fig. 2.7) and it varies with the absorber medium and the gamma-ray energy (see Fig. 2.8) [13; 15; 51].

$$\mu_{Tot} = \mu_{cs} + \mu_{pe} + \mu_{pp} \tag{2.2.9}$$

The mass attenuation coefficient (μ_m) can be converted to linear attenuation coefficient (μ) by using Eqn. 2.2.10 [12; 15].

$$\mu = \mu_m \times \rho \tag{2.2.10}$$

where ρ is the absorber material density in g cm^{-3}.

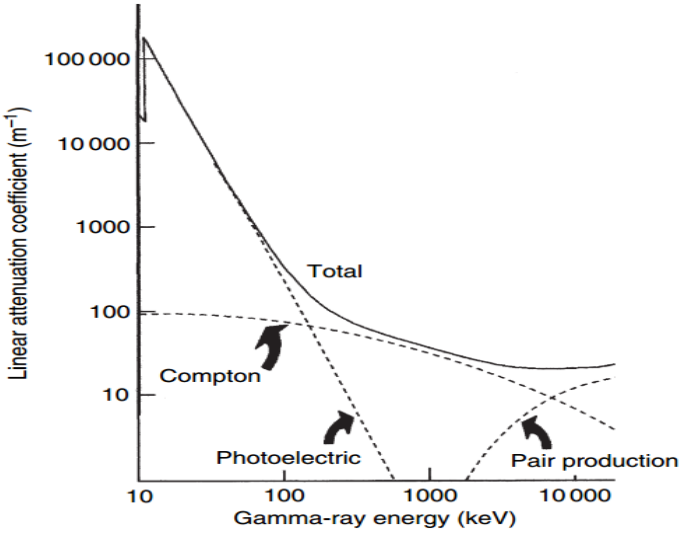

Figure 2.7: The linear attenuation coefficient of germanium and its component parts. Image from reference [12].

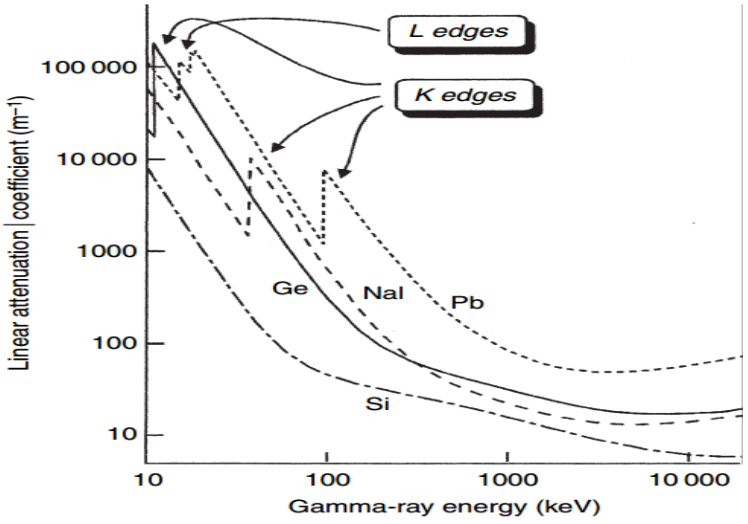

Figure 2.8: Attenuation coefficient of materials as a function of gamma-ray energy. Image from reference [12].

2.3 Radiation Detection

Detection of radiation basically involves the use of a material that stops some of the radiation striking it and produces a measurable signal. Then, the properties of the incident radiation can be established by amplifying and measuring this signal.

2.3.1 Band Structure in Solids

In a crystalline material, there exists a valence band and conduction band with a bandgap between them called the energy-gap. Electrons are confined to certain sites in the valence band and free to move within the crystal in the conduction band. The valence band sites are full of electrons and conduction band, without excitation, is empty. However, when excited, the valence electron moves up to the conduction band creating electron - hole pairs. The application of an external electric field to the material causes a flow of current. The probability of excitation depends on the energy-gap energy [12; 15].

2.3.2 Inorganic Scintillators

Scintillators are materials that become excited and emit prompt visible light after energy absorption. The two type of scintillators are organic and inorganic scintillators. Organic scintillators are mostly used for fast neutron and beta measurement due to their fast light yield while inorganic scintillators are used for gamma-ray measurement because of their good light yield and linearity [15].

Unlike for organic scintillators, small amounts of impurity called activator is added to inorganic scintillator. The activator improves visible photon emission probability by modifying the energy band structure of the pure crystal (i.e.

reduce the energy-gap) [12; 13; 15]. Some examples of inorganic scintillator crystals used in gamma-ray detector are; NaI:Tl, CsI:Tl, CsI:Na, $LaBr_3$:Ce and $LaCl_3$:Ce [12; 13; 15]. The mechanism of scintillation in inorganic crystal detectors are [12; 13; 15; 57; 58];

- gamma ray interacts with crystal material via Compton effect, photo-electric effect and pair production to produce electron - hole pairs;
- valence-band holes are captured by the activator ions;
- the captured holes interact with conduction-band electrons to produce excited activator ions;
- light is emitted following de-excitation of the activator ion;
- the photocathode connected to one end of the detector crystal converts light output (photons) striking its sensitive surface to photoelectrons and an avalanche of secondary electrons produced by the interaction of accelerated photoelectrons with dynodes generates signal pulses.

Photomultiplier Tube (PMT)

A photomultiplier tube is composed of photocathode at its entrance followed by several dynodes then an anode all placed in an evacuated glass tube [12; 15; 58]. When a scintillation pulse light output strikes the photocathode, it emits electrons. The emitted electrons are accelerated towards the first dynode with the aid of electric field and secondary electrons are emitted when the electron hits the dynode. These secondary electrons are accelerated to the next dynode and multiplied until the last dynode. Then, the anode collects the amplified signal which is passed to the measurement circuit. The most commonly used

photocathode materials are Na_2KSb and K_2CsSb with low work function (i.e. low surface barrier to ease the release of photoelectrons). The dynodes are overlaid with either Cs_3Sb, beryllium or magnesium oxides and its secondary emission rate depends on the surface type and the applied voltage [12; 15; 58].

Moreover, Fig. 2.9 shows how a photomultiplier tube is optically coupled to a scintillation crystal in a typical scintillation detector. The reflector prevents loss of light on the front and side of the scintillator crystal by reflecting the light about to escape toward the crystal. During the passage of light from scintillator to PMT, the optical coupling fluid reduces the reflection of light by minimising the change of the refractive index. The PMT is magnetically shielded to prevent interference from the surrounding magnetic field [12; 58].

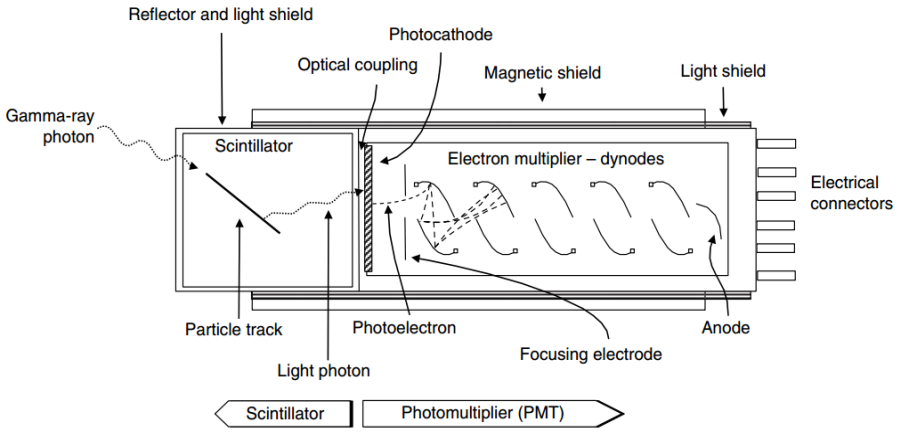

Figure 2.9: A photomultiplier tube optically coupled to a scintillation crystal (scintillation detector). Image from reference [12].

2.3.3 Semiconductor

Semiconductor materials have small energy-gaps (≈ 1 eV) between the valence band and conduction band [15; 58]. The small energy gap increases the number of charge carriers and increase in charge carrier improves energy resolution. A

completely pure semiconductor is called an intrinsic semiconductor while an extrinsic semiconductor has small amounts of impurity or dopants which increase the conductivity of the material [15; 58]. There are two type of extrinsic semiconductor depending on the valence electron of the impurity added (i.e. excess electron or hole). If one of the atoms of the pure semiconductor material is replaced with a donor atom (i.e. having one valence electron higher than that of the pure semiconductor), it is called n-type semiconductor. However, if one of the atoms of the pure semiconductor is replaced with an acceptor atom (i.e. having one valence electron fewer than that of the pure semiconductor), it is called a p-type semiconductor [15; 58]. Increase in temperature or interaction of ionizing radiation with the sensitive volume (thermal excitation) moves electrons from the valence band to the conduction band. Following this, electrons - holes pairs are produced (electrons move toward p^+ and holes towards n^-) by applying an electric field [13; 15]. Then, the preamplifier connected to the detector converts the current pulse to a step voltage [13]. The average energy required to create an electron-hole pair is larger than the energy-gap. Germanium and silicon are the most frequently used semiconductor materials [15; 57]. A loss of charge carriers' ion is caused by trapping and recombination of electrons and holes which limit the energy resolution [15].

2.4 Comparison of $LaBr_3$:Ce, NaI:Tl and HPGe Detectors

The $LaBr_3$:Ce detectors have good timing resolution compared to NaI:Tl and HPGe detectors due to it shorter scintillation decay time of 16 ns, which make it more useful at high count rates [12]. The NaI:Tl detectors typically, have

a decay time of 250 ns whereas in HPGe detectors 100 ns is required for a charge carrier to travel a distance of 1 cm (which may be of the order of detector thickness) [12; 15]. The time resolution of HPGe detectors are limited by slow charge collection process and variability in pulse shape. It is evident that the energy resolution of HPGe detectors are better than those of $LaBr_3$:Ce and NaI:Tl detectors due to the small energy required to produce a photoelectron (3 eV compared to an order of 100 eV for scintillator) and the fact that electrical signal generation does not require many steps [12; 15]. The intrinsic detection efficiency of $LaBr_3$:Ce detector is higher than those of NaI:Tl and HPGe detectors because of its higher density and effective atomic number. The $LaBr_3$:Ce, NaI:Tl and HPGe detectors have density and effective atomic number of; 5.08 g cm^{-3} and 162, 3.67 g cm^{-3} and 64, 5.32 g cm^{-3} and 32, respectively. The HPGe detector needs to be operated at liquid nitrogen temperature due to it small energy-gap to reduce current leakage, which can reduce its energy resolution [15]. Because of the size and weight of the dewar containing the liquid nitrogen, $LaBr_3$:Ce and NaI:Tl detectors are more portable than HPGe detectors.

2.5 Gamma-ray Spectrometry

Gamma-ray spectrometry is the quantitative study of the energy spectra of gamma ray interaction with a detector. The various features of a gamma-ray spectrum is shown in Fig. 2.10.

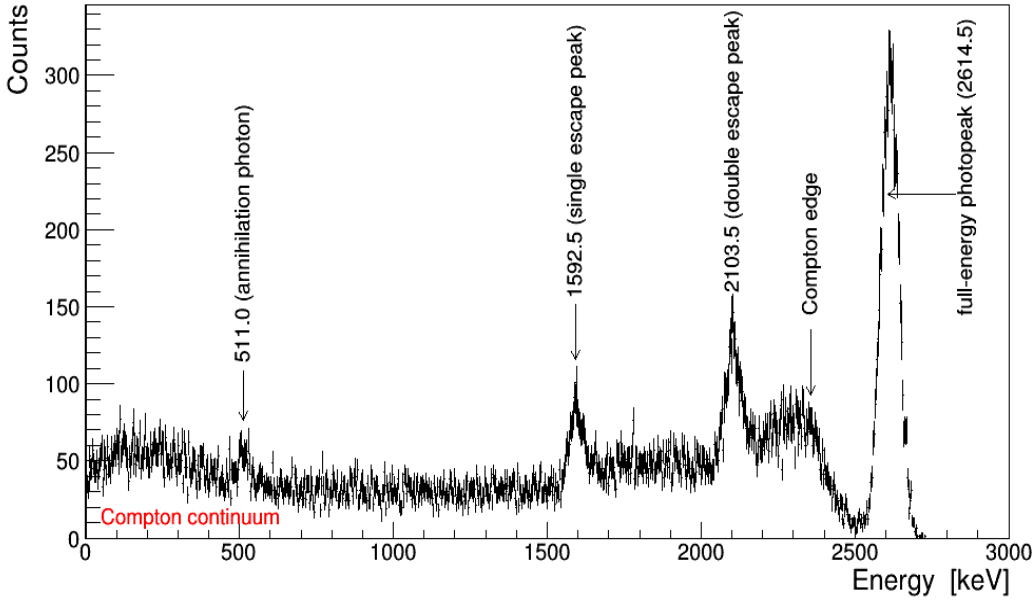

Figure 2.10: Simulated gamma-ray spectrum from the interaction of 2614.5 keV gamma-ray energy with 2" × 2" $LaBr_3$:Ce detectors (see Appendix A for details).

2.5.1 Energy Resolution

The energy resolution (R) of a detector is the detector's ability to distinguish photons of different energies [12; 15; 58]. The full-width-at-half-maximum ($FWHM$) is defined as the width of the distribution at a level that is just half the maximum ordinate of the peak after background or continuum subtraction. For a Gaussian peak $FWHM = 2.35\sigma$ [15; 58], where σ is the standard deviation. The energy resolution of a detector depends on the energy of the radiation, size and inherent quality of a detector [15]. The energy resolution is affected by potential sources of fluctuation in the response of a detector such as statistical noise from the discrete nature of the measured signal, random noise within the detector and instrumentation system and any drift of the detector operating characteristics during measurement [15; 58]. Good energy resolution becomes important if the measured energy spectrum contains closely spaced or

overlapping peaks. To resolve two peaks, the difference between the energies should be greater than or equal to the sum of their $FWHM$ [12; 15; 58]. The peak width ($FWHM$) increases with increase in gamma-ray energy (see Fig. 2.11). The energy resolution R is defined as follows:

$$R = \frac{FWHM}{E_\gamma} \times 100 \tag{2.5.1}$$

where E_γ is the gamma-ray energy i.e. the peak centroid energy.

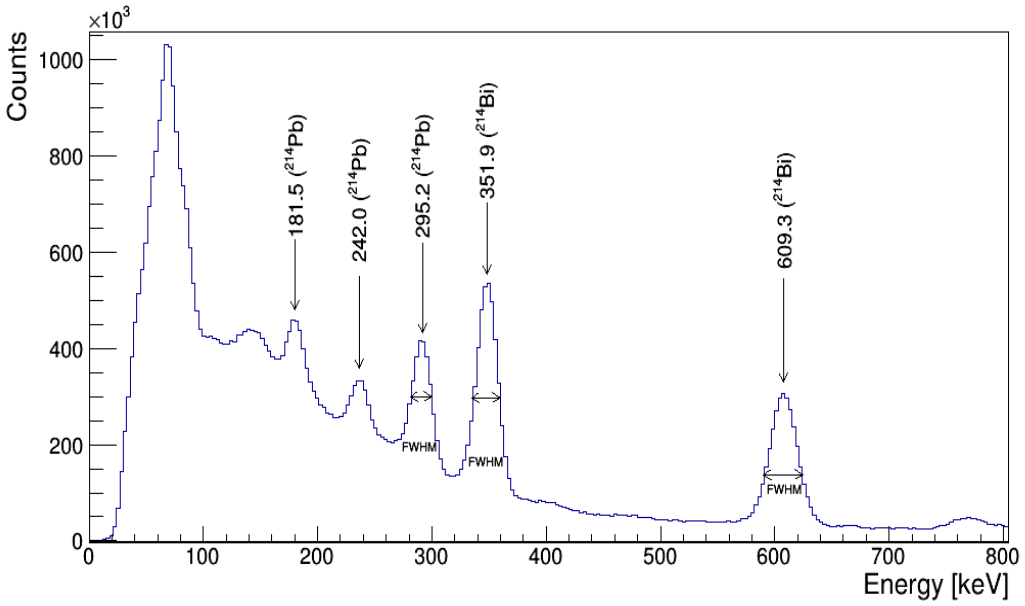

Figure 2.11: Spectrum showing the peaks width from measured uranium ore using $LaBr_3$:Ce detectors (see section 5.2 for details).

2.5.2 True Coincidence Summing

True coincidence summing (TCS) occur when two photons emitted by a decaying nuclide reaches a detector simultaneously and the detector records the sum of the two energies [12]. This depends on the resolving time of the spectrometer, geometry and lifetimes of the nuclear levels. A simple example is ^{60}Co which β^- decays to ^{60}Ni (see Fig. 2.12). If the 1173.2 keV and 1332.5 keV gamma-ray energies are emitted simultaneously and reaches the detector

at the same time, the detector will record 2405.7 keV gamma-ray energy. This results in loss of counts from the full-energy gamma-ray peaks of 1173.2 keV and 1332.5 keV thereby a loss of detection efficiency with these energies. The extent of TCS depend on the geometry and the magnitude of TCS increases with decrease in source-to-detector distance. It is important to note that some degree of summing occurs at any source-to-detector distance, though beyond a certain distance, TCS losses will be negligible in practice which depends upon the detector size. The number of TCS events per second is directly proportional to the sample activity. The probability of summing of two photons emitted concurrently (P) can be estimated as follows [12]:

$$P = \frac{(R - D)^2}{2R^2} \tag{2.5.2}$$

where $R = \sqrt{(r^2 + D^2)}$ and $D = d + d_0$, with r being the detector radius, d the measured source-to-detector distance, d_0 the distance between detector face and the detector cap.

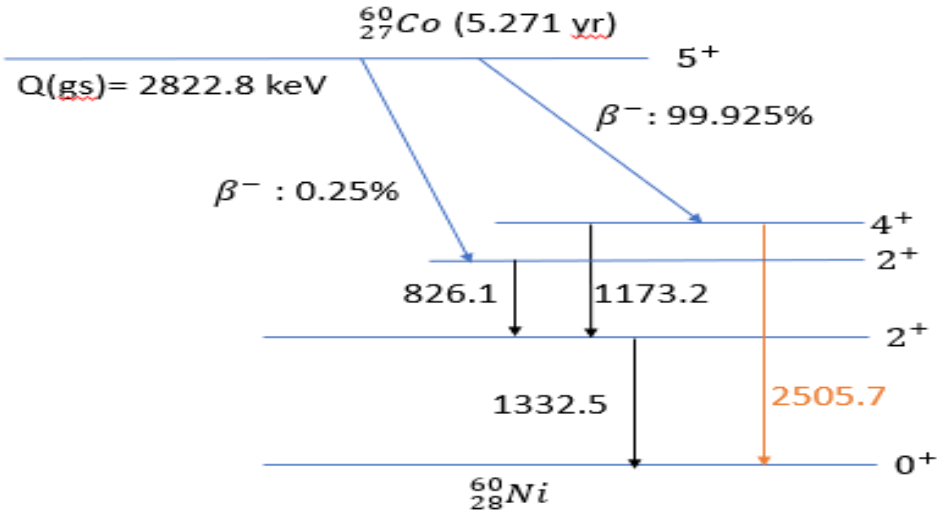

Figure 2.12: Gamma-ray decay scheme of ^{60}Co to ^{60}Ni illustrating true coincidence summing. Adapted from Browne and Tuli [62].

2.5.3 Detection Efficiencies and Activity Concentration

The absolute full-energy peak detection efficiency ($\mathcal{E}(E_\gamma)$) is the ratio of the net counts detected in the full-energy peak area to that emitted by the source of specific gamma-ray energy for a given detection-system live time L_t [12; 13]. The absolute full-energy peak detection efficiency value is the most important parameter in gamma-ray spectrometry because it relates the number of gamma rays emitted by a source to the number of detected events within the photopeak region for a specific energy [12], especially in radionuclide activity concentration determination. It depends on the energy, the source-to-detector geometry and detector material [12; 13]. According to the inverse square law the efficiency increases with a decrease in distance (d) (i.e. $\mathcal{E}(E_\gamma) \quad \alpha \quad 1/d^2$) [12; 13]. The absolute full-energy peak detection efficiency for a gamma ray $\mathcal{E}(E_\gamma)$ (singles mode) can be calculated as follows:

$$\mathcal{E}(E_\gamma) = \frac{C_n}{AP_\gamma M_s L_t} \tag{2.5.3}$$

where C_n is net counts in the full-energy of specific gamma-ray energy, L_t is the data acquisition live time in seconds, A is the source activity concentration in Bq kg^{-1}, M_s is the sample mass in kg and P_γ is the probability of emission of the specific gamma ray.

The absolute full-energy peak detection efficiency of measuring two gamma-ray energies simultaneously $\mathcal{E}(E_{\gamma_c})$ (coincidence mode) is defined as:

$$\mathcal{E}(E_{\gamma_c}) = \frac{2nN_c}{mAP_{\gamma_c} M_s L_t} \tag{2.5.4}$$

or

$$\mathcal{E}(E_{\gamma_c}) = \mathcal{E}(E_{\gamma_1}) \cdot \mathcal{E}(E_{\gamma_2}) \tag{2.5.5}$$

where N_c is the coincidence peak area counts in one of the gamma ray, n is the number of detectors used, m is the number of combinations of the

detectors taking two detectors at a time, $P_{\gamma c} = P_{\gamma 1} P_{\gamma 2}$, $\mathcal{E}(E_{\gamma_1})$ and $\mathcal{E}(E_{\gamma_2})$ are the gamma-ray detection efficiencies from the singles measurement. If the measuring geometry is such that the true coincidence summing is significant, then Eqn. 2.5.5 becomes invalid because the TCS will not cancel out when calculating activity concentration and Eqn. 2.5.4 is applied.

The activity concentration is the measure of the decay rate of radioisotope source per mass in Bq kg^{-1} [15; 57]. The activity concentration of radionuclides measured in singles mode A is given as [12]:

$$A = \frac{C_n}{\mathcal{E}(E_\gamma) P_\gamma M_s L_t} \tag{2.5.6}$$

The activity concentration of radionuclides measured in coincidence mode A_c can be calculated as follows [60]:

$$A_c = \frac{2nN_c}{m\mathcal{E}(E_{\gamma_c}) P_{\gamma_c} M_s L_t} \tag{2.5.7}$$

Self-absorption Correction

The self-absorption correction factor (C_d) is required to determine the absolute activity concentration of radionuclides in a sample having different composition and density from the standard source. However, for photon energies greater than 100 keV, the differences in chemical composition do not amount to a significant problem in environmental sample due to similar mass attenuation coefficients for natural materials [63; 64]. The techniques used in determining the self-absorption correction factor are; analytical, experimental and Monte Carlo simulations [63; 64]. Irrespective of the method used, the self-absorption correction factor C_d is calculated as follows:

$$C_d = \frac{\mathcal{E}(E_\gamma, standard)}{\mathcal{E}(E_\gamma, sample)} \tag{2.5.8}$$

where $\mathcal{E}(E_\gamma, standard)$ and $\mathcal{E}(E_\gamma, sample)$ are the detection efficiencies of the standard source and sample at a given energy.

The activity concentrations (Eqns. 2.5.6 and 2.5.7) are multiplied by the self-absorption correction factor C_d in Eqn. 2.5.8 to obtain the absolute activity concentration of radionuclides in a sample.

2.5.4 Peak-to-Total Area Ratio and Minimum Detectable Activity

The peak-to-total ratio (PTR) is the ratio of the net counts (C_n) in a peak to the total counts (C_T) in the spectrum which include both the photopeak itself and Compton continuum (Eqn. 2.5.9) [65]. The PTR is used to evaluate the performance of a spectrometer. A ^{137}Cs source is often used to determine the PTR due to its single gamma-ray energy of 661.7 keV [65]. However, the 1173.2 and 1332.5 keV peaks of ^{60}Co are also used [12].

$$PTR = \frac{C_n}{C_T} \tag{2.5.9}$$

The minimum detectable activity (MDA) gives the least activity concentration that can be measured with certain degree of confidence (in this case 95 %) [12]. Two concepts are included in calculating the MDA of a radionuclide; Critical Limit (L_c) is the level above which a net count is valid to a degree of confidence and Detection Limit (L_D) is the least net count that can be measured significantly [12]. The MDA is dependent on the counting live time, the energy resolution, the full-energy peak detection efficiency, the degree of confidence and the background count rate which depends on the experimental geometry condition and the measurement environment [12; 58]. Achieving a more sensi-

tive analysis requires the MDA values to be low. A lower MDA value can be achieved by decreasing the background counts, increasing counting time and detection efficiency, and use of a detector with good energy resolution [12]. The MDA in singles mode of measurement can be calculated as follows [12]:

$$MDA = \frac{2.71 + 3.29\sigma_B}{\mathcal{E}(E_\gamma)P_\gamma M_s L_t} \tag{2.5.10}$$

where σ_B is the uncertainty in the background counts. The values 2.71 and 3.29 are from the degree of confidence and the detection limit.

The MDA in coincidence mode of measurement is estimated as follows [12; 66]:

$$MDA = \frac{L_D}{\mathcal{E}(E_{\gamma_c})P_{\gamma c} M_s L_t} \tag{2.5.11}$$

where L_D is the detection limit. It is important to note that L_D depends on the background counts for the data acquisition period. If the total background count for a specific gamma-ray peak in a time is greater than 25 counts, the approximation to a Gaussian distribution will be valid and $L_D = 2\sigma_{Bc}$ [66]. However, if the total background count for a specific gamma-ray peak in a time is low i.e. less than 25 counts, even though the count distribution will be Poisson, the approximation to a Gaussian distribution will not be valid. This means that $L_D = 2\sigma_{Bc}$ will not be valid and the L_D value can be taken from Gilmore [12] for Poisson distribution (for 95 % confidence interval) associated with background count within the data acquisition counting time. For instance, if the total background count acquired during time t for 583.2 keV peak of ^{208}Tl is 10 counts, the L_D will be 23 counts [12]. All terms in Eqns. 2.5.10 and 2.5.11 have definitions as described in Section 2.5.3.

2.5.5 Dead Time

Dead time (τ) is defined as the minimum time separation between events in which the detector can accept events [15]. There is always a probability of a true event being lost because it occurs rapidly after a preceding event due to the random nature of radioactive decay. At high counting rates, the events losses can become critical and correction must be made for these losses. The common techniques for measuring dead time are based on the fact that the observed rate varies nonlinearly with the true rate. The two experimental methods of determining the dead time of a system are; the two-source method and the decaying source method [15]. The two-source method is based on observing the count rate individually and in combination. The observed count rate from the sum of the two sources counted individually will be higher than the rate from combined sources because the count losses are nonlinear. The dead time is estimated from this difference using Eqn. 2.5.12. The decaying source method uses the known exponential decay of a short-lived radioisotope source observed counting rate to calculate the dead time using Eqn. 2.5.13. It is important to note that there is little practical effect on the statistical counting uncertainties if the dead time losses are small (less than 20 %) [15]. The dead time of a counting system τ can be calculated as follows:

$$\tau = \frac{m_1 m_2 - \sqrt{m_1 m_2 \left(m_{12} - m_1\right)\left(m_{12} - m_2\right)}}{m_1 m_2 m_{12}} \tag{2.5.12}$$

or

$$\tau = \frac{n_0 + m e^{\lambda t}}{m n_0} \tag{2.5.13}$$

where m_1, m_2 and m_{12} are the observed count rate of source 1, source 2 and combined sources after background subtraction respectively, n_0 is the true rate at the beginning of the measurement, λ is the decay constant of the measured isotope, m is the observed rate and t is the data acquisition time.

2.5.6 Gamma-ray Energies Emitted by NORM Radionuclides

The most significant gamma-rays energies emitted by the NORM nuclides are shown in Table 2.1. The half-life of ^{7}Be is 53.2 days and it emits only a 477.6 keV gamma ray. This gamma ray is present in a gamma-ray spectrum of environmental air filter and natural water only because it is continuously generated by spallation reactions of charged particles on oxygen and nitrogen in the atmosphere. The gamma-ray energy emitted by ^{40}K is 1460.8 keV, it is present in the background spectrum and must be corrected for possible interference with the 1459.9 keV peak of ^{228}Ac. For uranium and thorium series nuclides, most of the gamma rays are subjected to TCS and/or low emission probability. The 2614.5 keV peak of ^{208}Tl has a very large TCS error because of its final transition to the ground state [12]. If the samples are measured relative to standard sources of the same geometry and distance for each radionuclide, the TCS will be the same and cancel out when calculating activity concentration. However, if the detection efficiency curve needs to be known and radionuclide efficiency calculated from fit parameter, the TCS will not cancel out when calculating activity.

Table 2.1: The most significant gamma-rays emitted by the NORM radionuclides [12].

Nuclide	Gamma-ray Energy (keV)	Emission Probability (%)	Comments (Note; this is subjective to how the radiation is measured i.e. HPGe, NaI:Tl, $LaBr_3$:Ce, the size of the detector and its relation to the source).
^{7}Be	477.6	10.44 (4)	–
^{40}K	1460.8	10.66 (13)	Probable interference from ^{228}Ac
^{235}U series			
^{235}U	143.8	57.2 (8)	^{230}Th interference, correction needed.
	163.3	10.96 (8)	—
	185.7	5.08 (8)	44.8 % of composite peak - ^{223}Ra, ^{226}Ra and ^{230}Th interference, correction needed.
	205.3	5.01 (8)	Many interferences. Not recommended.
^{227}Th	236.0	12.6 (6)	—
	256.2	6.8(4)	—
^{223}Ra	269.5	13.7 (4)	Interference from ^{228}Ac.
^{219}Rn	271.2	10.8 (7)	Interference from ^{228}Ac and ^{223}Ra.
	401.8	6.4(5)	—
^{238}U series			
^{238}U	49.6	0.0697 (26)	Unusable - significant interference from ^{227}Th.
^{234}Th	63.3	4.8 (6)	—
	92.4	2.81 (26)	92.4 and 92.8 measured together.
	92.8	2.77 (26)	Significant interference from ^{228}Ac when present. X-ray interference.
^{234m}Pa	258.2	0.075 (3)	Significant interference from ^{214}Pb.
	766.4	0.391 (9)	Interference from ^{214}Pb and ^{211}Pb.
	1001.0	1.021 (15)	No interference. Slight summing is possible.
^{226}Ra	186.21	3.555 (19)	57.1 % of composite peak - ^{235}Ra and ^{230}Th interference,

			correction needed.
^{214}Pb	242.0	7.268 (22)	Interference from ^{224}Ra and deconvolution from 238.6 keV of ^{212}Pb needed.
	295.2	18.414 (36)	Insignificant interference from ^{212}Bi.
	351.9	35.60(7)	—
^{214}Bi	609.3	45.49 (19)	Subject to TCS.
	1120.3	14.91 (3)	Subject to TCS.
	1238.1	5.831 (14)	Subject to TCS.
	1764.5	15.31 (5)	—
	2204.2	4.913 (23)	—
^{210}Pb	46.5	4.25 (5)	Slight interference from ^{231}Pa.
^{232}Th series			
^{232}Th	63.8	0.27 (2)	Unusuable - significant interference from ^{234}Th.
^{228}Ac	338.3	11.27 (19)	Subject to TCS, slight interferences from ^{223}Ra and ^{214}Bi.
	911.2	25.8 (4)	Subject to TCS.
	964.8	4.99 (9)	Subject to TCS, interference from ^{214}Bi.
	969.0	15.8 (3)	Subject to TCS.
^{212}Pb	238.6	43.6(3)	Deconvolution from 242.0 keV of ^{214}Pb needed.
	300.1	3.18 (13)	Subject to TCS, slight interference from ^{231}Pa.
^{208}Tl	510.7	22.6 (2)	Subject to TCS and difficulty resolving from 511 keV annihilation peak.
	583.2	85.0 (5)	Subject to TCS.
	860.6	12.5 (2)	Subject to TCS.
	1620.7	1.51 (3)	—
	2614.5	99.7 (2)	Subject to TCS.

Chapter 3

Literature Review

Some previous studies undertaken with a low-level gamma-ray spectrometry setups and $LaBr_3$:Ce-based spectrometry systems will be reviewed and summarised in this chapter.

3.1 Low-level Gamma-ray Spectrometry Setup

Ramadhan and Abdullah [67] studied background reduction by Pb/Cu shield using a 3" × 3" well NaI:Tl detector. The background was measured without shielding, with a 4π 60 mm thick Pb shield surrounding the detector and additional 2 mm thick electrolytic Cu inner lining of Pb. The background counts in the 20 - 2160 keV region was reduced 28.7 times with the Pb and 29.0 times with the Pb+Cu shield.

Lutter *et al.* [7] described the Pacman spectrometer located 225 m deep in the HADES underground laboratory Belgium to reduce muon flux (4 orders of magnitude lower compared to the ground level). The spectrometer consists of two HPGe detectors (Ge10 and Ge11) and two NaI:Tl detectors (N6 and

N7). The detectors are shielded with 75 mm thick Pb (50 Bqkg^{-1} of ^{210}Pb), 60 mm thick Pb (20 Bqkg^{-1} of ^{210}Pb), 35 mm thick Pb (2.0 Bqkg^{-1} of ^{210}Pb) and 35 mm thick electrolytic Cu from outside to inside (see Fig. 3.1). The inner volume of the shield is 70 litres, this was to allow for bigger detector placement. The Ge10 is an n-type HPGe detector with crystal dimensions of 67.0 mm diameter and 68.5 mm height and Ge11 is a p-type HPGe detector with crystal dimensions of 80.0 mm diameter and 70.5 mm height. The N6 is cylindrical with crystal dimensions of 102 mm diameter and 102 mm height, and N7 is annular with crystal dimensions of 228 mm outer diameter, 109 mm inner diameter and 228 mm height. The spectrometer has two configurations as shown in Fig. 3.2. The N6 and N7 were used to form an active Compton suppression shield and the total background counts was reduced by a factor of two by the active shield. Due the Ge10 position, endcap, holder and thick dead layer, the effect of the active shield was less.

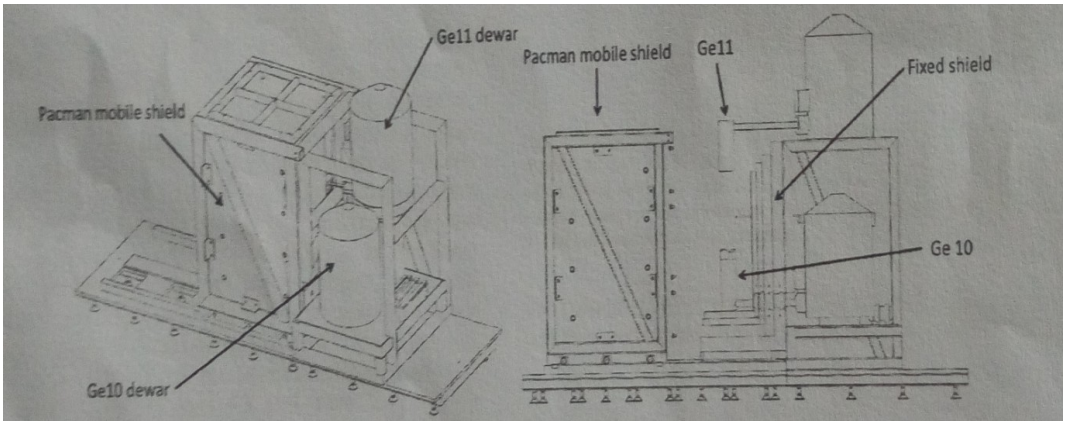

Figure 3.1: Schematic drawing of the Pacman shield with HPGe detectors Ge10 and Ge11 [7].

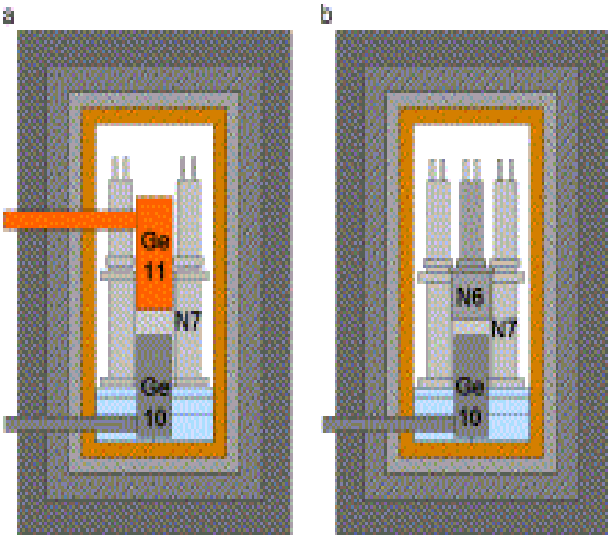

Figure 3.2: Two different configurations of Pacman spectrometer: (a) The anticoincidence with Ge10 is set by Ge11 + N7 and (b) The anticoincidence with Ge10 is set by N6 + N7 [7].

Hansman [68] described the shield for a 9" × 9" well type NaI:Tl detector for gamma-ray spectrometry. The detector was shielded from the inside to the outside with a 4π 1 mm thick electrolytic Cu, 2 mm thick Sn and 150 mm thick Pb. The shield was placed on 1 mm thick steel plate on the laboratory floor. The space between the detector and the inner volume of the shield is 20 mm. The background outside and inside the shield was measured, the background count rate in the 280 - 3000 keV region was reduced 132.7 times by the shield.

The technical details and performance of the Sandwich spectrometer for ultra low-level γ-ray spectrometry was reported by Wieslander *et al.* [6]. The spectrometer is located 500 m deep (water equivalent) in the HADES underground laboratory Belgium to reduce muon flux produced by the cosmic rays in the atmosphere. The spectrometer consists of two p-type HPGe detectors (Ge-6 and Ge-7) with an active muon shield and a Pb/Cu shield. The Ge-6 has crystal dimensions of 78.0 mm diameter and 84.0 mm height, and the Ge-7 crystal

dimensions are 80.5 mm diameter and 66.5 mm height. The shield is 145 mm thick Pb (20 Bq kg^{-1} of ^{210}Pb), 40 mm thick Pb (2.5 Bq kg^{-1} of ^{210}Pb) and 35 mm thick electrolytic Cu from the outer part to the inner part. The Cu is to attenuate the X-rays generated in the Pb shielding by interactions of the gamma rays. The activity of ^{60}Co and ^{228}Th in electrolytic Cu was estimated based on the fact that the Cu was stored above the ground for less than three weeks to be less than 15 mBq kg^{-1} and 20 mBq kg^{-1} respectively. For the active muon shield, two plastic scintillators were placed on top of the Pb shield as depicted in Fig. 3.3. The summed background of the two detectors in the 40 - 2400 keV region with and without muon filter are 868 day^{-1} and 992 day^{-1} respectively.

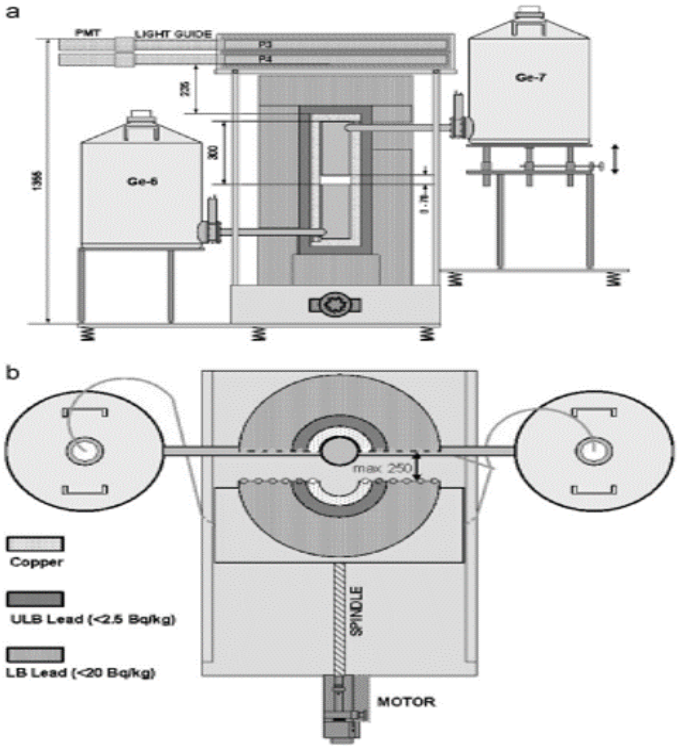

Figure 3.3: The Sandwich spectrometer set-up including dimensions: (a) side view and (b) top view [6].

Kohler *et al.* [8] presented the D6 low-level gamma-ray spectrometer located at a depth of 110 m water equivalent in the Felsenkeller underground laboratory Dresden. The spectrometer consists of a coaxial p-type HPGe detector with a crystal diameter of 78 mm and a length of 75 mm, and is passively shielded. The passive shield from inside to outside is: 50 mm of Cu, 50 mm of low-activity Pb (2.7 ± 0.6 Bq kg^{-1} of ^{210}Pb) and 100 mm Pb (3.3 ± 0.4 Bq kg^{-1} of ^{210}Pb) as shown in Fig. 3.4. The Cu was used to attenuate the bremsstrahlung continuum and the X-rays induced by the betas from the ^{210}Bi decay ($E_{\beta max}$ = 1.2 MeV) in the Pb. The decision thresholds for ^{226}Ra and ^{228}Ra are in the order of some mBq L^{-1}, which shows that the spectrometer is suitable for the effective surveillance of water for human consumption.

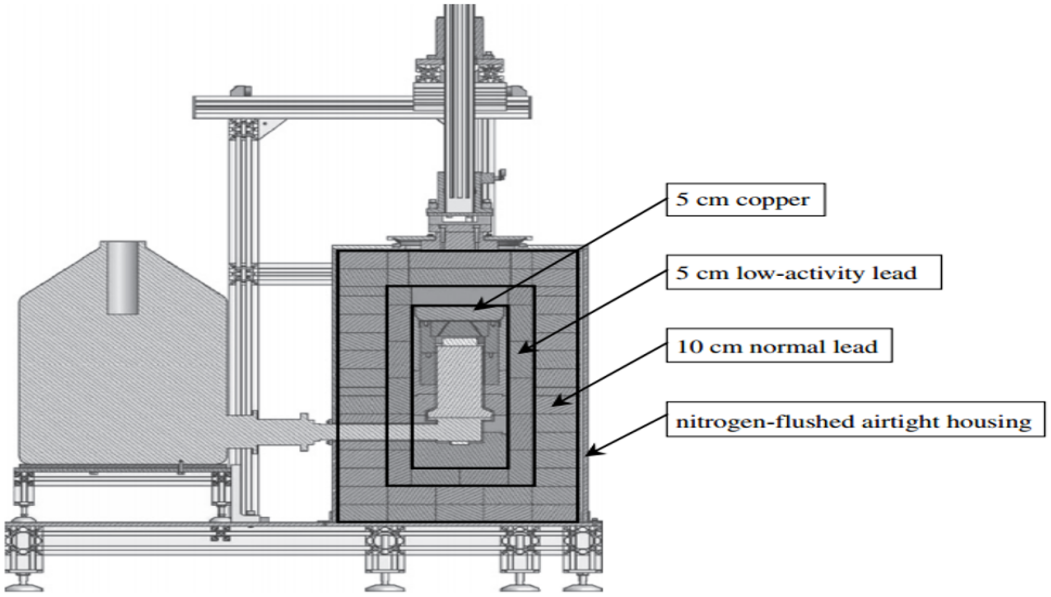

Figure 3.4: Schematic view of the shielding of the detector D6 [8].

Sykora *et al.* [5] presented a report on the single (small) and coincidence (large) low-level gamma-ray spectrometer. Both the large and small spectrometer has the same shield but different inner volume. The shield from the inside to the

outside is: 10 mm $(C_5O_2H_8)_n$ (Perspex), 1 mm Cd, 1 mm electrolytic Cu, 100 mm $(C_2H_4)_n + H_3BO_3$ (polyethylene with boric acid), 100 mm Cu and 100 mm Pb with a 120 mm thick Fe on the top. An extra Cu shield with a dimension of 120×200×300 mm^3 was placed inside the shield, the inner dimensions of the large and small spectrometer are 800×900×1720 mm^3 and 380×380×620 mm^3, respectively. A HPGe detector is used inside the small shield for single measurements whereas a HPGe and NaI:Tl detectors are used in coincidence to measure cascade emitting radionuclides. The background counts were reduced by two orders of magnitude with both the large and small shield.

Mrda *et al.* [69] measured background without shielding using a Gamma-X HPGe (GMX) detector. The detector was surrounded from the inside to the outside with 0.5 mm thick Cu, 3.5 mm thick Sn and 120 mm thick Pb. The inside of the shield was flushed with nitrogen and the background inside the shield measured. The intensity of 511 keV line and the continuum below 511 keV was enhanced by the oversized Pb thickness. However, the spectrometer with shield was able to shield most of the background gamma rays.

Kozak *et al.* [9] presented the ultra-low background gamma spectrometer E made up of coaxial HPGe. The spectrometer has both passive and active shields (see Fig. 3.5). The passive shield from inside to outside: 10 mm Cu, 50 mm of 2500-year-old Pb, 2 mm of Cd, 100 mm of standard Pb and 80-120 mm of C_nH_{2n+2} (paraffin) for external neutron moderator. The inner volume of the shield was flushed with liquid nitrogen vapour, to reduce the radon daughter's contribution to the spectra. A multiwire proportional counter was used for active shield which was situated on the upper side of the shield, between the neutron moderator and commercial Pb. This is a Cosmic-Rays Muon Veto Detector, which works in anti-coincidence mode with a germanium detector.

The background counts in the 80 - 3000 keV region was reduced by a factor of two by the active shield.

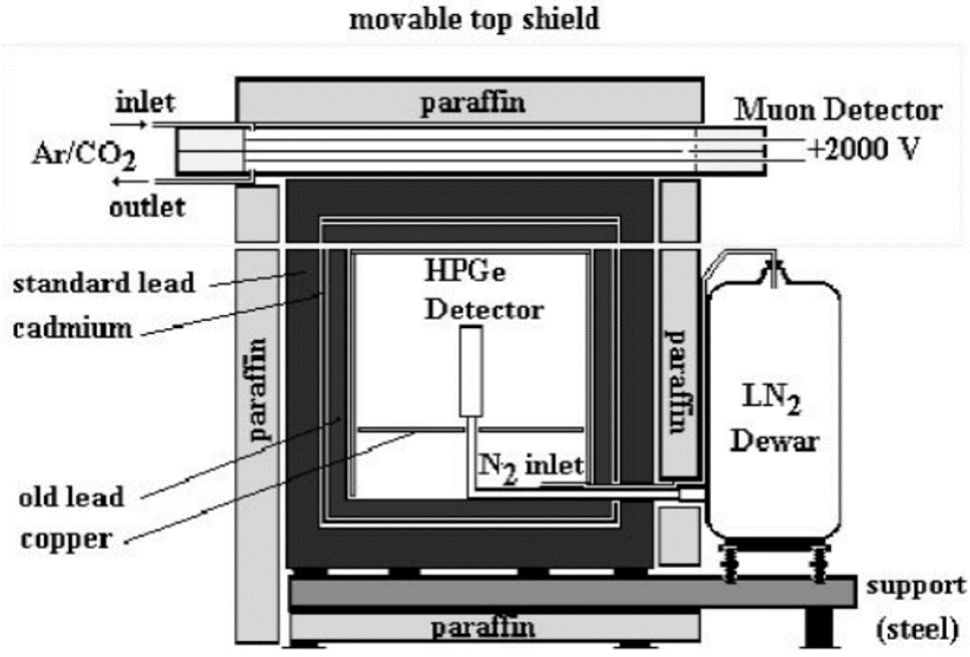

Figure 3.5: A scheme of construction of ultra low-level gamma spectrometer shield [9].

3.2 $LaBr_3$:Ce-based Spectrometry Systems

Drescher *et al.* [17] studied the performance of $LaBr_3$:Ce detectors relative to HPGe detectors for gamma-gamma coincidence in high count-rate scenario. The detection system is made up of two 1.5" × 1.5" $LaBr_3$:Ce detectors compared with two HPGe detectors (55.9 × 57.5 mm^2 n-type) in singles and coincidence. XIA LLC Digital Gamma Finder Pixie-4 was used for data acquisition. Coincident gamma-ray pairs from ^{152}Eu and ^{133}Ba radionuclides were identified in a measured sample that is dominated by ^{137}Cs. The Compton continuum from ^{137}Cs peak was reduced and the signal-to-noise ratio improved using the

$\gamma - \gamma$ coincidence compared to single detector measurements. The performance of $LaBr_3$:Ce detectors was (400 kHz) multiple times higher than that achieved with HPGe detectors (150 kHz) at high count rates. The capability of $LaBr_3$:Ce detectors to perform gamma-gamma coincidence measurements in very high count rate scenarios, can be of potential benefit to nuclear safeguards in-situ measurements of spent nuclear fuel.

Roy *et al.* [70] developed an active and passive computed tomography system that localized and quantifies Pu-239 in a waste drum. A $LaBr_3$:Ce detector and external gamma-ray source were used to determine the attenuation map of waste drum contents at different selected energies i.e. transmission (active). Several $LaBr_3$:Ce detectors were used to measure the emission (passive) and record the spectra of gamma rays emitted from within the drum. Then, the transmission and emission data were coupled to quantitatively assay drum contents for ^{239}Pu. The results show that the three-dimensional distribution of ^{239}Pu as well as the mass/quantity assayed matches well with the true distribution.

Berdnikova *et al.* [71] studied the intrinsic background of a $LaBr_3$:Ce detector with a crystal diameter of 5 mm and a height of 10 mm attached to a silicon photomultiplier with an active area of 3 $\times$ 3 mm^2 in comparison with LYSO and $CeBr_3$ detectors. The $LaBr_3$:Ce detector energy resolution was found to be 4 % for 661.7 keV and a background count rate of $\approx$ 0.39 cps in the energy range of (140 $\pm$ 3σ) keV. The background count rate exhibited by the $LaBr_3$:Ce detector was lower than those of LYSO and $CeBr_3$ detectors.

Ulyanov *et al.* [72] tested a $LaBr_3$:Ce detector with a crystal size of 28 $\times$ 28 $\times$ 20 mm^3 coupled to a custom built 4 $\times$ 4 array of silicon photomultipliers

over energy range of 30 - 9300 keV. The silicon photomultipliers were initially calibrated using 20 ns duration light pulses generated by a light emitting diode. The detector showed a linear response to gamma-ray energies in the 0.1 - 9.3 MeV region on the application of corrections for the non-linearity of the silicon photomultipliers. The energy resolution was found to be 4 % FWHM at 662 keV. The position resolution was found to be 8 mm FWHM at 356 keV in the detector plane and 11 mm FWHM for the depth. The detector was found capable of measuring the positions of the gamma-ray interaction points and can be used as a building block of a larger calorimeter system that is capable of measuring gamma-ray energies up to tens of MeV.

Dhibar *et al.* [34] simulated the response of a 3.5" × 6" $LaBr_3$:Ce detector using GEANT4. The low energy Electromagnetic Physics package was used in Physics list class. General particle source module and the radioactive decay component were used to simulate the decay components of point radioactive sources; ^{60}Co, ^{94}Nb, ^{24}Na, ^{46}Sc and ^{22}Na. The geometrical details of wooden table supporting the source and detector were also used in the simulations. The secondary production threshold for gamma rays, electrons and positrons in their range were taken to be 0.001 mm for simulating all possible physics processes. The simulations were carried out for about 10^6 events considering the source on the detector surface. The experimental measurements were carried out with the same detector as in the simulation. The $LaBr_3$:Ce aluminium casing and reflector material thicknesses were 0.8 mm and 5 mm, respectively with Hamamatsu R10233 PMT attached. The measured and simulated results of ^{60}Co and ^{22}Na were found to be in good agreement.

Bailey [73] performed airborne surveys to characterise environmental radionuclide content for mineral exploration, as well as for emergency scenarios such

as major releases or lost sources. $LaBr_3$:Ce and NaI:Tl detectors were used for an aerial survey of a uranium mine in the western United States. Analyses of the survey data were performed with RadAssist software and applying International Atomic Energy Agency (IAEA) airborne gamma-ray mapping guidelines. The data for the survey were corrected for cross-over i.e. spectral interference from higher energy photons as a result of Compton scattering, height attenuation, cosmic rays and radon contribution to signal. The radiation survey contours produced by the $LaBr_3$:Ce detector were comparable to that of NaI:Tl detector. The $LaBr_3$:Ce detection system contained 1/16th the scintillating volume and had a total system weight that was 1/4th that of the NaI:Tl system. $LaBr_3$:Ce demonstrated a clear advantage over NaI(Tl) detectors in system mobility, and weight factors in airborne gamma-ray spectroscopy.

Mazumdar *et al.* [74] presented the results of the investigation on the performance of $LaBr_3$:Ce detector (3.5" $\times$ 6" and 9460 mm^3). GEANT4 simulations and measurements were performed using gamma rays from radioactive sources and in-beam reactions of few hundred keV to 22500 keV energies. A highly linear response was observed by extracting the energy signal from a lower dynode and operating the PMT at a low voltage. The overall performance of the $LaBr_3$:Ce detector was found to be highly satisfactory and ideal for high energy gamma-ray measurements.

Galli *et al.* [41] measured the time resolution of a 3" $\times$ 3" $LaBr_3$:Ce detector by means of a nuclear reaction facilitated by a Cockcroft-Walton accelerator that produces coincident gamma rays in the 4.4 - 11.6 MeV energy range. Preliminary results allowed them to extrapolate the properties of a segmented gamma-ray detector in the 50 - 100 MeV energy range.

Duval and Arnold [75] replicated the in-situ gamma measurements of 20 natural sedimentary samples by Arnold *et al.* [40] using $LaBr_3$:Ce and NaI:Tl probes. For both types of detectors, gamma dose-rates were calculated using the "threshold" technique and compared with results obtained previously by Arnold *et al.* [40] using the "windows" technique. The results obtained using these two techniques show that gamma dose-rates are consistent at yhe 1σ level, and the $LaBr_3$:Ce and NaI:Tl probes results agreed. The threshold approach offers an improvement in the precision with which gamma dose rates can be determined using the $LaBr_3$:Ce probe compared to the energy window approach. The potential of an alternative threshold approach (the "energy threshold" approach) was also tested for both probe types, and the gamma dose rates results agreed with those obtained using the standard threshold and energy windows techniques. The results provide new insights into methods and instrumentation used for assessing in-situ gamma dose rates in ESR and luminescence dating. The $LaBr_3$:Ce probes can reliably be used for portable gamma dosimetry in low-level activity sedimentary environments (500 - 1500 mGy/a) provided that their non-negligible internal background activities (equivalent to 758 mGy/a) were accurately assessed and subtracted from gamma-ray spectra measured in the field. The results also suggested that there may be some minor merit in applying an internal background subtraction procedure to NaI:Tl gamma-ray spectra when using the threshold technique, in spite of the lower intrinsic activities of NaI:Tl detectors.

Michetti-Wilson [44] characterised the $LaBr_3$:Ce detectors for picosecond lifetime measurements. The experiments were performed in three categories. The first being a table-top setup in which two $LaBr_3$:Ce detectors, both outside of the array were used in tandem; this was used to test the effect of passive

suppression on the timing resolution of said detectors. The second setup implemented the detectors mounted in the 8π array to investigate the potential of active Compton suppression and to measure the timing resolution of a single detector. The final category pertains to the further testing of the DANTE system. It included the first two categories, which tested the prompt response of this system, but goes further on to look at the ability of the DANTE to measure the half-life of the 121 keV excited state in ^{152}Sm. The tests of active suppression performed with a ^{60}Co source demonstrated the shields are remarkably successful at removing Compton events. Applying this suppression to a measurement of the energy spectra from ^{60}Ni, an average of 61 % of the unwanted events were successfully removed in the Compton region. The timing resolution of these detectors demonstrated their exceptional ability, an average prompt time-response of 248.5 ps (FWHM) was measured in $LaBr_3$:Ce detectors with fast-plastic coincidence measurement, gated on the 1332 keV excited state in ^{60}Ni. The most likely candidate for the trouble encountered in making measurements was due to the complexity of the DANTE time signal processing. A broken symmetry between detector-detector timing signals was observed with both ^{60}Co and ^{152}Eu sources measurements. There was a large-scale time-shift observed in both measurements combined with the disparity between timing resolutions in a $LaBr_3$:Ce - $LaBr_3$:Ce prompt coincidence (as in passive suppression). It was highly evident that the method of time-signal processing was operating at a sub-par level.

Arnold *et al.* [40] investigated the use of a $LaBr_3$:Ce detector for measuring individual activity concentrations of ^{40}K, ^{238}U and ^{232}Th using predefined "energy windows" from gamma-ray spectra. Reference materials with well-constrained radioisotope concentrations (the Oxford calibration blocks) were

measured with the $LaBr_3$:Ce detector and the results compared with that obtained for a NaI:Tl detector of the same geometry. The results shows that the $LaBr_3$:Ce detector has a non-negligible intrinsic activity that needs to be accurately quantified prior to measuring any gamma-ray spectra in the field. The energy resolution of the $LaBr_3$:Ce detector was improved compared to the NaI:Tl detector by a factor of two or more, for the main indicator isotope photopeak's in the ^{238}U and ^{232}Th decay series and ^{40}K. The signal-to-noise ratio for the $LaBr_3$:Ce detector showed a 25 - 35 % improvement over that of the NaI:Tl detector. The $LaBr_3$:Ce detector was linear over the full-energy spectral range for the ^{40}K, ^{238}U and ^{232}Th decay series. Natural sedimentary samples (20) from the Lower Tejo River basin, Portugal, and the Duero River basin, Spain were measured using $LaBr_3$:Ce and NaI:Tl detectors and the results yield consistent radioisotope concentrations and estimated gamma dose rates. The results were encouraging and suggested that $LaBr_3$:Ce detectors can provide suitable estimates of individual radioisotope concentrations in low-level activity environments (0.5 - 1.5 Gy/ka), provided that their intrinsic activity is adequately measured and subtracted from field spectra. The comparison also reveals that subtraction of the intrinsic activity from $LaBr_3$:Ce spectra produces a significant reduction in the precision with which radionuclide concentrations can be determined using the 'energy windows' approach. This shortcoming necessitates longer counting times in natural sedimentary environments and overshadows the practical advantages that $LaBr_3$:Ce detectors might otherwise offer for luminescence and Electron Spin Resonance (ESR) dating applications.

Saizu and Cata-Danil [76] used $LaBr_3$:Ce (1.5" × 1.5") and NaI:Tl (2" × 2") detectors for the gamma-ray measurement of ^{131}I in thyroid. Due to the ^{138}La

present in the $LaBr_3$:Ce detector crystal, the background count rates in the 300-700 keV region was observed to be higher in $LaBr_3$:Ce detector background spectra than that obtained with NaI:Tl detector. The count rates for the energy interval corresponding to the region of interest; around the 364.5 keV peak of ^{131}I presented a slight difference. The result show that the energy considered was not affected by the ^{138}La radionuclide with a consistent contribution. The excellent energy resolution of the $LaBr_3$:Ce detector, significantly higher than that of the NaI(Tl) was confirmed. This suggested that a $LaBr_3$:Ce detector be used for in-vivo measurements of ^{131}I activity retention in the thyroid by gamma spectrometry.

Schaart *et al.* [45] studied the timing performance of SiPMs in combination with $LaBr_3$:Ce(5 %). Measurements were performed with two $3 \times 3 \times 5$ mm^3 $LaBr_3$:Ce crystals, each coupled to a 3×3 mm^2 SiPM. A ^{22}Na was placed at various positions between the two detectors and measured. A coincidence resolving time (CRT) of ≈100 ps FWHM for 511 keV annihilation photon pairs was achieved, corresponding to a TOF positioning resolution of ≈15 mm FWHM. This was the best CRT reported for SiPM-based scintillation detectors to date. It was concluded that SiPM-based scintillation detectors can provide timing resolutions at least as good as detectors based on PMTs.

Favalli *et al.* [27] investigated the applicability of the $LaBr_3$:Ce detector to prompt gamma neutron activation analysis (PGNAA). An Am-Be neutron source was surrounded by a cylindrical shield of tungsten (W 95%, Fe 3.5%, Ni 1.5%) to attenuate the gamma rays from the neutron source. The neutron source was clad with cadmium in order to avoid the interactions of thermal neutrons with the source. A second cylinder of polyethylene was arranged around the tungsten shield in order to thermalize the neutrons produced by

the Am-Be source. The test sample (NH_4Cl) was placed outside the cylinder and close to the detector. Additional polyethylene blocks were placed around the sample to achieve a higher thermal neutron flux. The results show that the detector promises to be a suitable detector for the PGNAA application due to excellent properties such as high energy resolution, high efficiency and elimination of cooling requirements as for HPGe detectors.

Tatisscheff *et al.* [77] presented the first gamma-ray imaging results obtained by coupling a $LaBr_3$:Ce crystal with a position-sensitive 8 by 8 multi-anode photomultiplier tube to form a simple Auger camera module. The readout of the 64 signals was carried out with the most recent evolution of the MultiAnode ReadOut Chip (MAROC) which was initially designed for the luminometer of the ATLAS detector. Measured charge distributions were compared with detailed GEANT4 simulations that included the tracking of the optical photons produced in the scintillation crystal. The depth of interaction (d.o.i.) of 662 keV gamma rays inside the crystal was derived from the charge distributions using an artificial neural network. For an irradiation at detector centre a mean standard deviation of 1.69 mm d.o.i. was obtained. Such a position-sensitive gamma-ray detector could form an innovative building block for a future space calorimeter.

Nilsson [35] reported on the use of $LaBr_3$:Ce detector for mobile gamma spectrometry. The $LaBr_3$:Ce(5 %) has a crystal size of 76 $\times$ 76 mm^2 and coupled to a XP5700 PMT. The energy linearity of the PMT, energy calibration drift, energy resolution, internal contamination was tested. Several methods of compensating for the internal contamination were explored. Two of those methods were found to work well for usage in a static measurement setup and a mobile setup respectively. A test to study if it was possible to use the $LaBr_3$:Ce

detector in a multi-detector system was performed and yielded positive results.

Alzimami [78] investigated the possibility of using $LaBr_3$:Ce and $LaCl_3$:Ce instead of the conventional NaI:Tl scintillator for optimization of imaging process in a SPECT system. measurements and simulations results shows that the relatively new lanthanum cerium-doped scintillators have the potential to replace NaI(Tl) as the scintillator of choice in single photon imaging. The $LaBr_3$:Ce has excellent energy and timing resolution, superior intrinsic spatial resolution and higher detection efficiency. The superior performance of 3D ordered-subsets expectation maximization (OSEM) in image contrast and spatial resolution compared to Filter Back Projection (FBP) particularly for low count statistics studies were clearly demonstrated. It was concluded that 3D OSEM become a clinically practical alternative to FBP and probably the best choice of image reconstruction technique in SPECT. Furthermore, the preliminary results demonstrate the potential for improving spatial resolution in SPECT imaging using a combination of $LaBr_3$:Ce detectors and 3D OSEM image reconstruction algorithms.

Crespi *et al.* [79] studied the line-shape of the signals from $LaBr_3$:Ce and $LaCl_3$:Ce detectors coupled to PMT. The possibility of discriminating the type of interacting radiation was investigated making use of Pulse Shape Analysis (PSA) techniques. The study was performed by measuring the self-activity present in lanthanum halide crystals in coincidence with gamma rays in a HPGe crystal. A small but significant difference between alpha and gamma induced signals was directly observed for both the crystals. It was possible to emphasize the differences in the pulse shape of gamma rays and alpha particles using a simple PSA algorithm. This resulted in a rather clear identification of these two types of radiations.

Weisshaar *et al.* [38] investigated the use of $LaBr_3$:Ce for an in-beam gamma-ray spectroscopy with fast ion beams. The Doppler broadening of the gamma-ray line measured with a finite-size detector in the laboratory fundamentally limits the achievable energy resolution in such experiments. With the good intrinsic energy resolution of $LaBr_3$:Ce (3 % FWHM at 662 keV) and its favorable stopping power, it could be a nearly ideal scintillator for gamma-ray spectroscopy applications with fast beams. Results from in-beam gamma-ray measurements using two $LaBr_3$:Ce detectors suggested that an array of $LaBr_3$:Ce can provide a viable tool for many experiments. Also, the excellent timing properties of $LaBr_3$:Ce can be used to significantly reduce background events in the gamma-ray spectra.

3.3 Summary

The important information on the low-level detection systems reviewed are summarised in Tab. 3.1. It is evident that passive shielding for low-level gamma-ray spectrometry are performed using Pb with a thickness ranging from 60 mm to 185 mm depending on the activity of ^{210}Pb in the Pb. The inner part of the Pb shield is lined with one or combination of the following materials; Cu, Cd, Sn to absorb the X-rays and bremsstrahlung from the Pb. In some cases, polyethylene or paraffin material is used for external neutron moderation. Occasionally, the spectrometer is located underground to reduce muon flux from cosmic rays or an active shield is added to the passive shielding. However, lead is expensive and requires the use of other materials for inner lining thereby increasing the cost of shielding. It is important to investigate an alternative shielding material which could serve the purpose with less cost. The summary of the $LaBr_3$:Ce-based detection systems reviewed and their

applications are given in Tab. 3.2. Several peer-reviewed studies have been reported with $LaBr_3$:Ce detectors, as of now there is no peer-reviewed article or thesis on the use of $LaBr_3$:Ce scintillator detector for NORM measurements of soil/ore samples in the laboratory (ex-situ).

Table 3.1: Important information on the low-level detection systems reviewed.

Author	Detectors used	shielding (mm) from outside to inside	location
Ramadhan and Abdullah [67]	1 NaI:Tl	60 Pb + 2 Cu	ground-level laboratory
Lutter *et al.* [7]	2 HPGe + 2 NaI:Tl	75 Pb + 60 Pb + 35 Pb + 35 Cu	underground laboratory
Hansman [68]	1 NaI:Tl	150 Pb + 2 Sn + 1 Cu	ground-level laboratory
Wieslander *et al.* [6]	2 HPGe	145 Pb + 40 Pb + 35 Cu	underground laboratory
Kohler *et al.* [8]	1 HPGe	100 Pb + 50 Pb + 50 Cu	underground laboratory
Sykora *et al.* [5]	1 HPGe + 1 NaI:Tl	120 Fe + 100 Pb + 100 Cu + 100 $(C_2H_4)_n$ + H_3BO_3 + 1 Cu + 1 Cd + 10 $(C_5O_2H_8)_n$	ground-level laboratory
Mrda *et al.* [69]	1 HPGe	120 Pb + 3.5 Sn + 0.5 Cu	ground-level laboratory
Kozak *et al.* [9]	1 HPGe	80-120 C_nH_{2n+2} + 100 Pb + 2 Cd + 50 Pb + 10 Cu	ground-level laboratory

Table 3.2: $LaBr_3$:Ce-based detection systems reviewed and their applications.

Author	Detector	Purposed
Drescher *et al.* [17]	2 $LaBr_3$:Ce + 2 HPGe	Compared the performance of $LaBr_3$:Ce detector to HPGe detector in high count-rate scenario in singles and coincidence modes
Roy *et al.* [70]	$LaBr_3$:Ce	Active and passive computed tomography system development
Berdnikova *et al.* [71]	$LaBr_3$:Ce + LYSO + $CeBr_3$	Studied the intrinsic background of a $LaBr_3$:Ce detector in comparison to that of LYSO and $CeBr_3$ detectors
Ulyanov *et al.* [72]	$LaBr_3$:Ce	Tested $LaBr_3$:Ce detector for possible use in calorimeter system
Dhibar *et al.* [34]	$LaBr_3$:Ce	Compared the GEANT4 simulations of $LaBr_3$:Ce detector response with experimental measurements
Bailey [73]	$LaBr_3$:Ce + NaI:Tl	Performed airborne surveys to characterise environmental radionuclide content for mineral exploration
Mazumdar *et al.* [74]	$LaBr_3$:Ce	Investigated the performance of $LaBr_3$:Ce by performing experimental measurements and GEANT4 simulations
Galli *et al.* [41]	$LaBr_3$:Ce	Time resolution measurements
Duval and Arnold [75]	$LaBr_3$:Ce + NaI:Tl	Replicated Arnold *et al.* [40] measurement by using the "threshold" technique
Michetti-Wilson [44]	2 $LaBr_3$:Ce	Characterised the $LaBr_3$:Ce detectors for picosecond lifetime measurements
Arnold *et al.* [40]	$LaBr_3$:Ce + NaI:Tl	Evaluated $LaBr_3$:Ce detector performance for luminescence and Electron Spin Resonance (ESR) dating applications in comparison with NaI:Tl detector by using the "windows" technique of measurement
Saizu and Cata-Danil [76]	$LaBr_3$:Ce + NaI:Tl	Compared the results of using $LaBr_3$:Ce detector for in vivo measurement of ^{131}I activity retention in the thyroid to that of NaI:Tl detector gamma spectrometry
Schaart *et al.* [45]	2 $LaBr_3$:Ce	Timing performance of SiPMs in combination with $LaBr_3$:Ce crystal
Favalli *et al.* [27]	$LaBr_3$:Ce	Investigated the applicability of the $LaBr_3$:Ce detector to prompt gamma neutron activation analysis (PGNAA)
Tatisscheff *et al.* [77]	$LaBr_3$:Ce	Measurements and GEANT4 simulations performed to determine the depth of interaction (d.o.i.) of gamma rays inside the crystal
Nilsson [35]	$LaBr_3$:Ce	Investigated the use of $LaBr_3$:Ce detector for mobile gamma spectrometry
Alzimami [78]	$LaBr_3$:Ce + $LaCl_3$:Ce	Investigated the possibility of using $LaBr_3$:Ce and $LaCl_3$:Ce for optimization of imaging process in a SPECT system
Crespi *et al.* [79]	$LaBr_3$:Ce + $LaCl_3$:Ce	Studied the line-shape of the signals from $LaBr_3$:Ce and $LaCl_3$:Ce detectors
Weisshaar *et al.* [38]	2 $LaBr_3$:Ce	Investigated the use of $LaBr_3$:Ce for an in-beam gamma-ray spectroscopy with fast ion beams

Chapter 4

GEANT4 Monte Carlo Simulations

4.1 Introduction to Monte Carlo Methods

Monte Carlo methods can be used to solve a complex problem using sequences of random numbers. Probability density functions (pdfs) are used to describe the physical system to be simulated by Monte Carlo [80]. Monte Carlo methods have found application in the fields of game theory, computer science, physics, finance, etc. The common Monte Carlo programs for radiation transport modelling are; MCNPX [81], FLUKA [82] and GEANT4 [83].

FLUKA is written in FORTRAN language (FORTRAN 77) which can be considered to be outdated and lacks many of the attributes of using modern approaches, and MCNPX, a trademark of Los Alamos National Security (LLC, Los Alamos National Laboratory) requires a license. The GEANT4 is an object-oriented detector simulation toolkit written in C++ language. It is an open source and developed at CERN. It is used to simulate the interac-

tions of particles with matter. It includes complete range of functionality like tracking, geometry, physics processes and hits [83–85].

4.2 GEANT4 Implementation

The GEANT4 toolkit modular and hierarchical structure is shown in Fig. 4.1. It allows geometrical setup of the detector together with its material to be modelled, and to define the sensitive part of the detector which records the information (hits) needed to simulate the detector responses (digitisation). Primary particles can be defined internally or from external sources and a set of physics processes is available to model the particles behaviour in GEANT4 toolkit. The interaction of the primary and secondary radiation can be tracked over a wide energy range depending on the user application requirement [85; 86]. The geometry and tracks can be visualised using the graphical system interface of choice in the GEANT4 toolkit. The GEANT4 required implementation classes are: Geometry, Primary Particle Generation and Physics Lists [83].

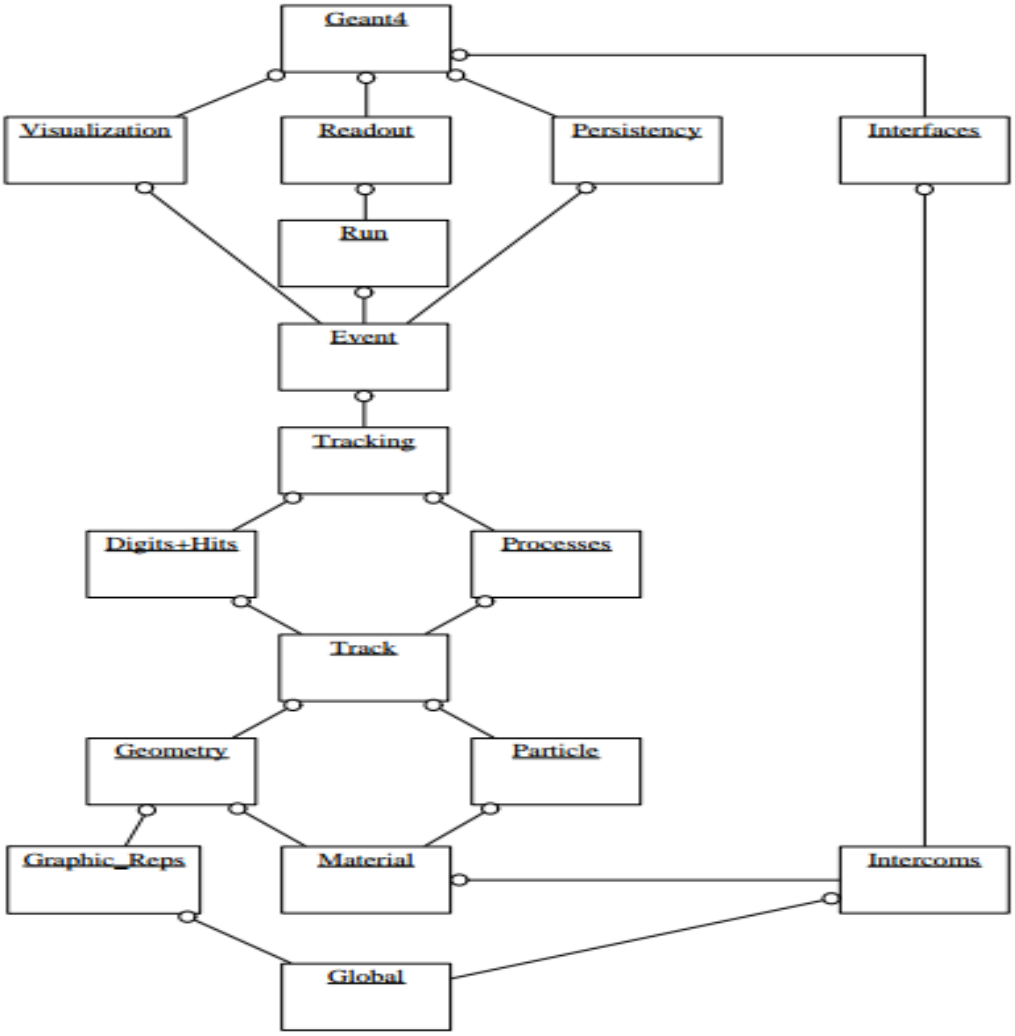

Figure 4.1: The GEANT4 toolkit top Level category diagram. Image from reference [83].

4.2.1 Geometry Representation

The experimental geometry is recreated using three-dimensional primitive Constructive Solid Geometry (CSG) of GEANT4's G4VUserDetectorConstruction class. For complex geometry, two or more CSG solids are combined using the Boolean operations: union, subtraction and intersection [83; 84]. This is important as it allows each part of the detector to be created and placed in the right position using the G4PVPlacement of GEANT4, and all parts put

together and positioned as one object. The constructed geometry is assigned materials.

The GEANT4 database contains elements, isotope composition and materials derived from the NIST database. The material can be invoked from the materials available internally or through user definition by providing the elemental composition, the effective atomic number and density of the material directly in the G4Material class. The detector's sensitive volume is defined (i.e. the readout) using the G4VPrimitiveScorer. The G4VPrimitiveScorer have several concrete classes like G4PSTrackLength and G4PSPassageTrackLength for tracking particle length, G4PSEnergyDeposit and G4PSDoseDeposit for deposited energy and dose respectively. Each detector is assigned a unique identification name for easy readout using G4SDManager of the G4MultiFunctionalDetector. The G4PSNofSecondary is used to filter and record only secondary particles of interest.

The GEANT4 visualization supports diverse graphic system such as OpenGL, Qt, OpenInventor, HepRApp and DAWN. The OpenGL, Qt and OpenInventor uses a graphics library compiled with GEANT4, while HepRApp and DAWN involve a separate application. G4VisAttributes of GEANT4 is used to set the geometry part visible or not. The visualization control is defined in G4VisManager class of GEANT4 or by the default G4VisExecutive.

4.2.2 Primary Particle Generation

The GEANT4 caters for many types of particles; gamma, proton, electron, leptons, baryons, gluon/quarks leptons mesons and nuclei(ions) contents built-in. Their properties like mass, magnetic moment, lifetime and decay modes, electric charge, spin, isospin and parity are defined. Primary particles in

GEANT4 are described by three special classes which are free from any other: G4ParticleDefinition, G4DynamicParticle and G4Track. G4ParticleDefinition defines a particle and contains information about particle's name, mass, spin, lifetime, and decay modes. G4DynamicParticle describes a particle interacting with materials and contains information which describes the particles dynamics like energy, momentum, polarization, time and "particle definition" information. G4Track describes a particle traveling in space and time and holds information like time, position, step and dynamic particle information [84]. Primary particles can be defined using the G4ParticleGun in G4VUserPrimaryGeneratorAction or user conversion code defined using the G4GeneralParticleSource module by interfacing to the physics generators through the special classes. The G4GeneralParticleSource module allows a source with arbitrary energy, spatial and angular distribution to be defined at run time [83]. To define a nuclide in G4GeneralParticleSource, the atomic mass (A), atomic number (Z), and the direction of propagation or spatial and angular distribution are specified. The G4GeneralParticleSource module does not rely on specific choices of physics generators and it is independent of the specific solution adopted for storing the simulation results.

4.2.3 Physics Lists and Models

Physics processes in GEANT4 are grouped into seven categories: electromagnetic, hadronic, decay, photolepton-hadron, optical, parameterization, and transportation. The interaction of particles with material is characterised by these processes. Each of these processes must implement virtual methods of G4VProcess; GetPhysicalInteractionLength (GPIL) which determine when an interaction should occur and DoIt describes the interaction. The GPIL method

calculates the probability of interaction using the process cross-section information and gives the step length between two space-time points. Following this, the DoIt method executes the interaction details, changing the particle's energy, momentum, direction and position, and produces secondary tracks if required. GEANT4 allows the user to choose or create processes to assign to a particle type [84].

The particles, processes, radioactive decay and cut are defined by invoking the ConstructParticle, ConstructProcess, G4RadioactiveDecayPhysics and SetCuts in the G4VModularPhysicsList class. The nuclides decay by invoking the G4NuclideTable. Messenger allows the physics sub-list to be changed without the simulation being re-compiled. There are several Physics models in GEANT4 for each process depending on the user application. For photon interaction with matter e.g. water, require models that account for electromagnetic and hadronic interaction and processes.

4.2.4 Extracting Simulation Results

The unique collection identification name of each detector is used to access the G4THitsMap object from G4HCofThisEvent with the accumulated energy deposited on the defined sensitive volume. GEANT4 outputs the precise energy, the G4RandGauss in the G4UserEventAction class uses given sigma obtained from FWHM to control the width of peaks in the simulated spectrum. The G4AnalysisManager class provides uniform interfaces to the G4tools package and hides the differences between use of G4tools classes for the supported output formats (ROOT, AIDA XML and CSV). The G4AnalysisManager functions with a pointer to the G4RandGauss of each detector and can be used to output the simulation results to the file format of interest.

4.3 Simulations Performed

The GEANT4 version 10.03.p01 toolkit ran on a Linux PC (Intel^R Pentium (R) CPU N3700 @ 1.60GHz, 8.0GB RAM) was used for simulations in this work. Low energy electromagnetic (valid from 250 eV - 100 GeV) and QGSP_BIC_HP (0 eV - 100 TeV) physics models implemented through the G4VModularPhysicsList class were used to model particles interactions with materials for all the simulations in this work. The low energy electromagnetic physics model was used to model photon interactions with materials while the QGSP_BIC_HP was used to model hadronic interaction with material. The secondary production threshold range for gamma rays, electrons, positrons etc. were set to zero for simulating all possible physics processes because the interaction of the secondary particle is important for this work especially the water shield. The program was run in an interactive mode and can be run with or without visualization by commenting out the line below the visualization setting in Fig. 4.2. The visualization was disabled when running the simulation after geometry is recreated correctly to reduce the simulation run time. The execution time differ depending on the particle or nuclide, the geometry and number of primary events generated. The particles or nuclides, number of primary events generated and the simulations execution time are given in Tab. 4.1.

```
# Macro file for the initialization of example B3a #Note in a macro hash indicates a comment
# Set some default verbose
/control/verbose 2
/control/saveHistory
/run/verbose 2
# Initialize kernel
/run/initialize
/gps/source/clear
/gps/source/multiplevertex true

#source 1
/gps/source/add 1
/gps/particle ion
/gps/ion 83 214 #19 40 #81 208 #  #   #
/grdm/nucleusLimits 214 214 84 83 #-18
/gps/position  0. -3.6 0. cm
/gps/pos/type Volume
#Source shape
/gps/pos/shape Cylinder #Sphere
#set radius
/gps/pos/radius 6.3 cm
#Set half-length in xyz of the source
/gps/pos/halfz 4.2 cm
/gps/pos/rot2 0. 1. -1.57735
#confine to a volume
/gps/pos/confine thickness
/gps/ang/type iso

#background source1 gamma 1
/gps/source/add 1066
/gps/particle gamma
/gps/energy 1.4608 MeV
/gps/pos/type Surface
#Set half-length in xyz of the source
/gps/pos/shape  Para
#Set half-length in xyz of the source
/gps/pos/halfx 61.75 cm
/gps/pos/halfy 61.75 cm
/gps/pos/halfz 125.55 cm
/gps/ang/type iso

#background source2 gamma 2
/gps/source/add 1517
/gps/particle gamma
/gps/energy 1.7645 MeV
/gps/pos/type Surface
#Set half-length in xyz of the source
/gps/pos/shape  Para
#Set half-length in xyz of the source
/gps/pos/halfx 61.75 cm
/gps/pos/halfy 61.75 cm
/gps/pos/halfz 125.55 cm
/gps/ang/type iso

#background source3 gamma 3
/gps/source/add 3538
/gps/particle gamma
/gps/energy 2.6145 MeV
/gps/pos/type Surface
#Set half-length in xyz of the source
/gps/pos/shape  Para
#Set half-length in xyz of the source
/gps/pos/halfx 61.75 cm
/gps/pos/halfy 61.75 cm
/gps/pos/halfz 125.55 cm
/gps/ang/type iso

# Visualization setting
/control/execute vis.mac
```

Figure 4.2: Screenshot of code showing how particles and nuclides are defined in G4GeneralParticleSource.

Table 4.1: The simulations number of primary events generated and execution time (without shielding = wos and with the water shield = ws).

Particles/Nuclides	Geometry	number of primary events generated	execution time (hours)
gamma-ray energies: 1460.8 keV, 1764.5 keV, and 2614.5 keV	wos	5.0×10^7	≈ 25
gamma-ray energies: 1460.8 keV, 1764.5 keV, and 2614.5 keV	ws	5.0×10^7	≈ 65
^{40}K	wos and ws	1.0×10^7	≈ 12
^{208}Tl	wos and ws	1.0×10^7	≈ 40
^{214}Bi	wos and ws	1.0×10^7	≈ 52
^{138}La	ws	1.0×10^7	≈ 24

4.3.1 $LaBr_3$:Ce Detector Response

The $LaBr_3$:Ce (5 %) detector was modelled with the geometrical parameters and materials densities given in Tab. 4.2. Most of the geometrical parameters used are from the manufacturer's specifications except for the PMT. The PMT is a complex structure and difficult to model, so an aluminium cylinder of 64 mm diameter and 190 mm length was used for the simulation (see Fig. 4.3). The detector's crystal was made the sensitive volume i.e. the readout.

To evaluate the simulation results and the spectrum response of $LaBr_3$:Ce detector, the measurement using four $LaBr_3$:Ce detectors without shielding was simulated and each detector given a unique identification name (see Fig. 4.4). The Marinelli beaker being a complex shape was modelled using two cylindrical shapes with the Boolean operation; subtraction mention in section 4.2. It is important to note that the beaker was modelled only to the 1 litre volume fill height. The beaker dimensions and material density are given in Tab. 4.2.

Table 4.2: Geometrical description of detectors and water shielding with the materials densities.

	Component	value
Materials	Density of Polypropylene	0.92 g cm^{-3}
	Density of Polyethylene	0.93 g cm^{-3}
	Density of H_2O	1.00 g cm^{-3}
	Density of $LaBr_3$:Ce(5 %)	5.08 g cm^{-3}
	Density of NaI:Tl(0.4 %)	3.67 g cm^{-3}
	Density of Al	2.70 g cm^{-3}
	Density of Air	1.22 g cm^{-3}
	Density of Al_2O_3	3.97 g cm^{-3}
	Density of sources	
	^{40}K (KCl)	1.29 gcm^{-3}
	^{208}Tl (RGTh-1)	1.36 gcm^{-3}
	^{214}Bi (RGU-1)	1.41 gcm^{-3}
Marinelli beaker	Outer - diameter	130.0 mm
	Well - diameter	85.0 mm
	Outer - height	88.0 mm
	Well - height	61.0 mm
	Polypropylene thickness	2.0 mm
$LaBr_3$:Ce detector	$LaBr_3$:Ce crystal diameter	50.8 mm
	$LaBr_3$:Ce crystal length	50.8 mm
	Air reflector thickness	0.4 mm
	Al casing thickness	3.2 mm
	PMT	Treated as aluminium cylinder of diameter 64 mm and length 190 mm
NaI:Tl detector	NaI:Tl crystal diameter	76.2 mm
	NaI:Tl crystal length	76.2 mm
	Al casing entrance window thickness	17 mm
	Al casing wall thickness	1.7 mm
	Al_2O_3 reflector thickness	6.8 mm

	at the front	
	Al_2O_3 reflector thickness	1.2 mm
	from the side	
	PMT	Treated as aluminium
		cylinder of diameter
		82 mm and length 80 mm
Water	Tank outer - diameter	1410 mm
shielding	Tank outer - height	1234 mm
	Polyethylene tank thickness	5 mm
	Pipe outer - diameter	234 mm
	Pipe outer - length	1456 mm
	Polyethylene pipe thickness	17 mm
jerry can	can length	137.5 mm
	can width	20.0 mm
	can height	117.5 mm
	can thickness	2.0 mm

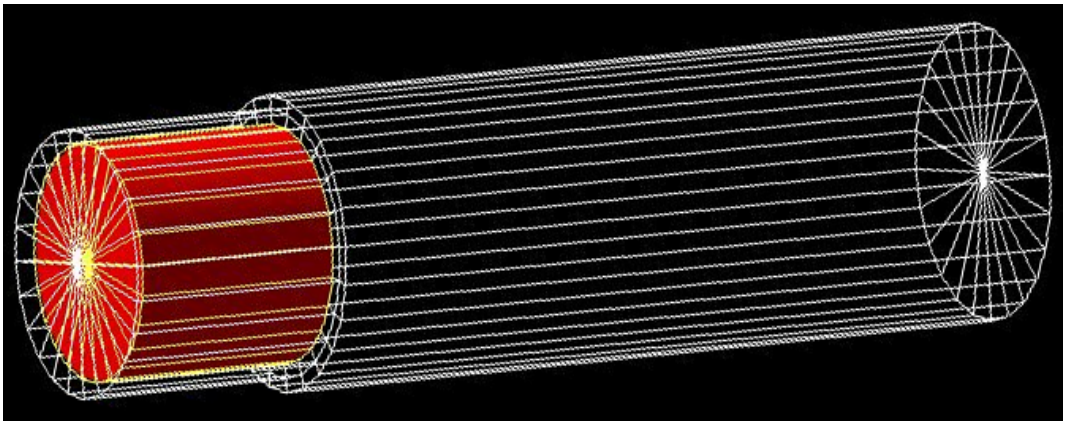

Figure 4.3: The GEANT4 modelled $LaBr_3$:Ce detector geometry, the red is the crystal, yellow the reflector and white the aluminium casing and PMT.

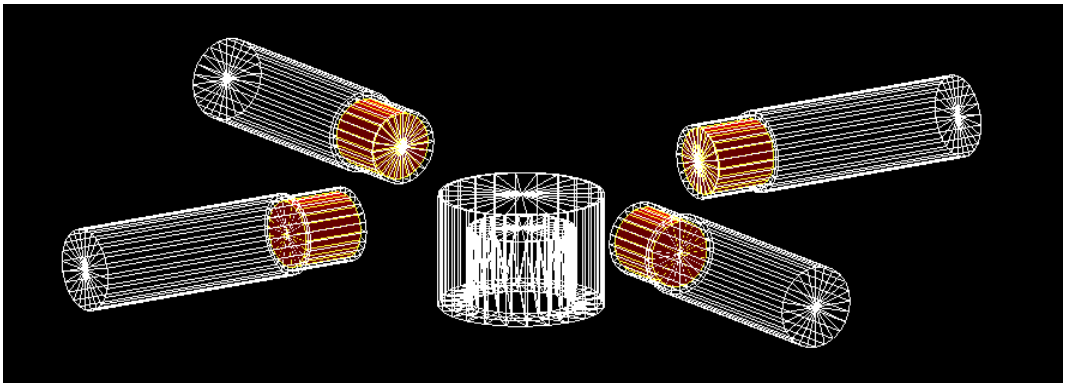

Figure 4.4: The GEANT4 modelled geometry of four $LaBr_3$:Ce detectors placed at 165 mm equidistant from Marinelli beaker (1 litre) centre containing a radioactive source.

The KCl, RGU-1 and RGTh-1 reference materials described in section 5.1 were replaced with an isotropic cylindrical source of ^{40}K, ^{208}Tl and ^{214}Bi each with diameter 63 mm and height 42 mm having KCl and SiO_2 as sample composition, respectively. The densities of the sources are given in Tab. 4.2. These sources were defined using the G4GeneralParticleSource, which allows the confinement of the source to the inside of the Marinelli beaker only (see line 26 of Fig. 4.2). The G4GeneralParticleSource also allows one to limit the decay of a radionuclide with several daughters to a certain daughter by specifying the atomic and mass number of the final daughter (see line 15 of Fig. 4.2). It is worth noting that ^{214}Bi was restricted to only β^- decay to ^{214}Po. The simulations were repeated using the densities of IAEA-375 soil and beach sand and SiO_2 [63] as soil composition. This was done to enable the calculation of self-absorption correction factor due to difference in sources and sample composition and density. The unique identification name of each detector was linked to a G4THitsMap object from G4HCofThisEvent with the accumulated energy deposited on the defined sensitive volume.

The measured energy resolution of the detector from standard sources mea-

surements were fitted in LibreOffice Calc using 3^{rd} degree polynomial of the form:

$$FWHM = a_0 + a_1E + a_2E^2 + a_3E^3 \tag{4.3.1}$$

where E is the gamma-ray energy in keV, and a_0 (in keV), a_1, a_2 (in keV^{-1}) and a_3 in (keV^{-2}) are the fitting parameters. The parameters from measured energy resolution of the $LaBr_3$:Ce detector in Eqn. 4.3.1 are shown in Fig. 4.5. The FWHM was divided by 2.35 to obtain the sigma and the sigma use in the G4RandGauss (see Fig. 4.6), to control the width of peaks in the simulated spectrum. The G4AnalysisManger function with a pointer to the G4RandGauss of each detector was used to plot the spectra as shown Fig. 4.6 and output to ROOT.

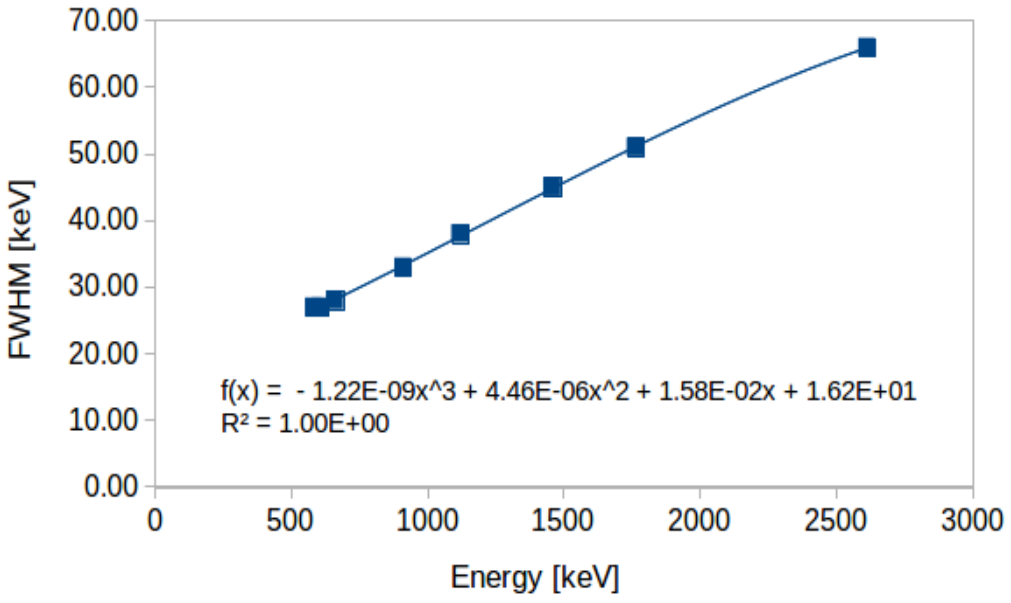

Figure 4.5: Plot of the measured peak FWHM ($LaBr_3$:Ce detector) against energy fitted with a 3^{rd} degree polynomial and the fit parameters.

```
110
111  //Hits collections
112  const G4double eThreshold2 = 0.*keV;
113  G4int nhit2 = 0;
114   G4THitsMap<G4double>* evtMap2 = (G4THitsMap<G4double>*)(HCE->GetHC(fCollID_detector2));
115   std::map<G4int,G4double*>::iterator itr2;
116  for (itr2 = evtMap2->GetMap()->begin(); itr2 != evtMap2->GetMap()->end(); itr2++) {
117    G4double edep2 = *(itr2->second);
118     if (edep2 > eThreshold2) nhit2++;
119
120  //Introduce the gaussian distribution
121  G4double totedep2 = edep2/keV;
122  G4double sigma2 =  (16.2 - (0.0158*totedep2) + (0.00000446*(totedep2*totedep2)) - (0.00000000122*
   (totedep2*totedep2*totedep2*totedep2)))/2.35;
123  G4double gaus2Energy =G4RandGauss::shoot(totedep2, sigma2);
124  gaus2Energy*=keV;
125
126  //Insert gaussian distributed energy into histogram
127    analysisManager->FillH1(1,gaus2Energy);
128  }
129
```

Figure 4.6: Screenshot showing how energy deposited in the detector is collected, peaks width made Gaussian and spectrum plotted.

4.3.2 Water Shield Design

Prior to the final water shielding simulation model and design, different thicknesses of water placed in a polyethylene container were investigated to find out the thickness of water required to shield the 2614.5 keV background gamma ray from reaching the detectors (see Appendix A). The focus was on the 2614.5 keV gamma ray because it is the maximum full-energy peak centroid in the gamma-ray spectrometry spectrum of NORMs as seen in Tab. 2.1. Polyethylene containers were chosen because it has almost the same attenuation coefficient as water (Fig. A.1). Modular shielding was the initial plan which involved stacking of polyethylene containers filled with water. However, obtaining a water container that is strong, stable and stackable without an airgap poses a challenge. This led to the idea of using a modified water tank.

For the final shielding, a pipe was inserted horizontally at the centre of a cylin-

drical tank (their geometries and materials densities are given in Tab. 4.2). The inside of the pipe is the measurement volume i.e. it housed the detector and the sample, and the tank was filled with water. A horizontal cylindrical segment made of polyethylene of radius 20 mm and length 700 mm was placed inside the measurement volume to support the sample and detectors. Eight jerry cans (dimensions and material density given in Tab. 4.2) were filled with water. Four jerry cans were placed on both ends of the pipe (see Fig. 4.7) to shield the measurement volume from the surrounding gamma rays. Two $LaBr_3$:Ce detectors were placed inside the measurement volume on the cylindrical segment 165 mm equidistant from the centre. Thereafter, surface isotropic gamma rays of 1460.8 keV, 1764.5 keV and 2614.5 keV were placed 5 mm away from the water shield in Fig. 4.7 all moving inward, and the energy deposited in the detectors recorded. Also, the shield was removed while keeping other parameters constant and the energy deposited on the detectors recorded to enable calculation of gamma-ray attenuation by the water.

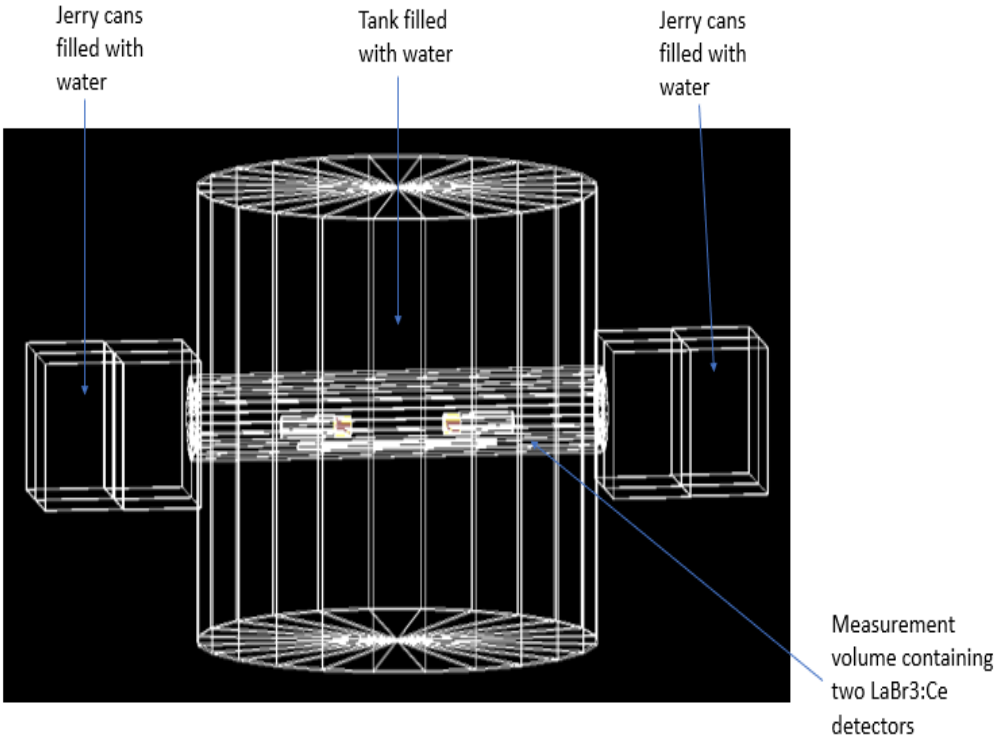

Figure 4.7: The modelled water shield geometry with two $LaBr_3$:Ce detectors placed 165 mm equidistant from the centroid on a cylindrical segment inside the measurement volume.

4.3.3 NaI:Tl Detector Response

The NaI:Tl (0.4 %) detector was modelled with the geometrical parameters and materials densities given in Tab. 4.2. The detector reflector material is Al_2O_3 powder with an indefinite thickness; this was replaced with an estimated effective Al_2O_3 layer with definite thickness. It is important to note that only the Al_2O_3 reflection layer in front of the NaI:Tl crystal was estimated. This is because it has more effect on the efficiency than the other layer surrounding the crystal as the sample is placed in front of the detector. The PMT was modelled using an aluminium cylinder with a diameter 82 mm and length 80 mm. The detector's crystal was made the sensitive volume i.e. the readout.

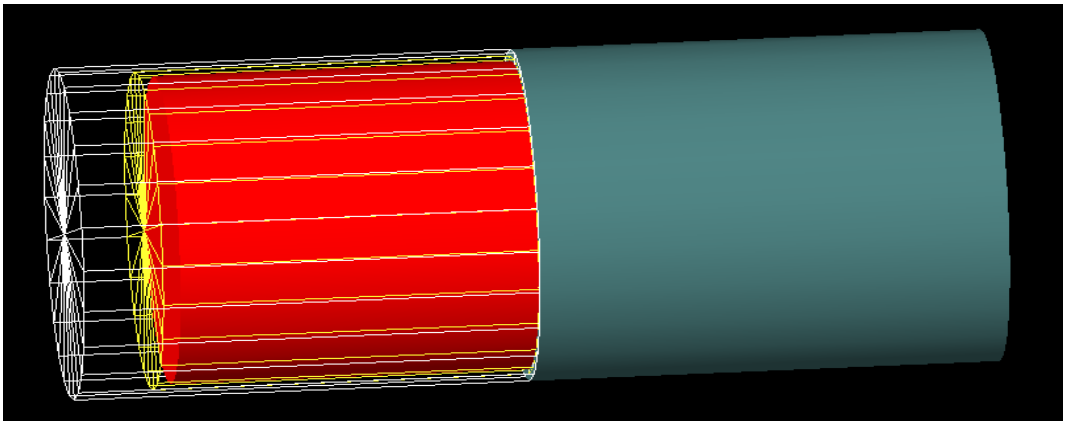

Figure 4.8: The GEANT4 modelled NaI:Tl detector geometry, the red is the crystal, yellow the reflector and white the aluminium casing and grey the PMT.

Thereafter, the NaI:Tl detector spectrum response and simulation results were evaluated. The $LaBr_3$:Ce detectors inside the measurement volume in Fig. 4.7 were replaced by the NaI:Tl detector in Fig. 4.8. The ^{40}K, ^{208}Tl and ^{214}Bi each placed inside the Marinelli beaker described above were used to simulate the detector's efficiency. The NaI:Tl detector was placed at 90 mm from the Marinelli beaker centre. To enable quantification of the $LaBr_3$:Ce detector internal activity as experimentally measured using NaI:Tl detector, a ^{138}La source was defined using the G4GeneralParticleSource with a dimension of 50.8 $\times$ 50.8 mm^2 and placed inside a $LaBr_3$:Ce detector crystal. The $LaBr_3$:Ce detector's face was placed 25 mm from the NaI:Tl detector and energy deposited in the NaI:Tl detector recorded. Similarly, the energy deposited in the NaI:Tl detector with and without the shielding in place was collected as per $LaBr_3$:Ce detectors.

The unique identification name of the detector was linked to a G4THitsMap object from G4HCofThisEvent with the accumulated energy deposited in the defined sensitive volume. The measured energy resolution of the NaI:Tl de-

tector from standard sources measurements were fitted in LibreOffice Calc using 3^{rd} degree polynomial in Eqn. 4.3.1. The parameters from measured energy resolution of the NaI:Tl detector in Eqn. 4.3.1 are shown in Fig. 4.9. The FWHM was divided by 2.35 to obtain the sigma and the sigma used in the G4RandGauss to control the width of peaks in the simulated spectrum. The G4AnalysisManger function with a pointer to the G4RandGauss of the detector was used to plot the spectra and output to ROOT.

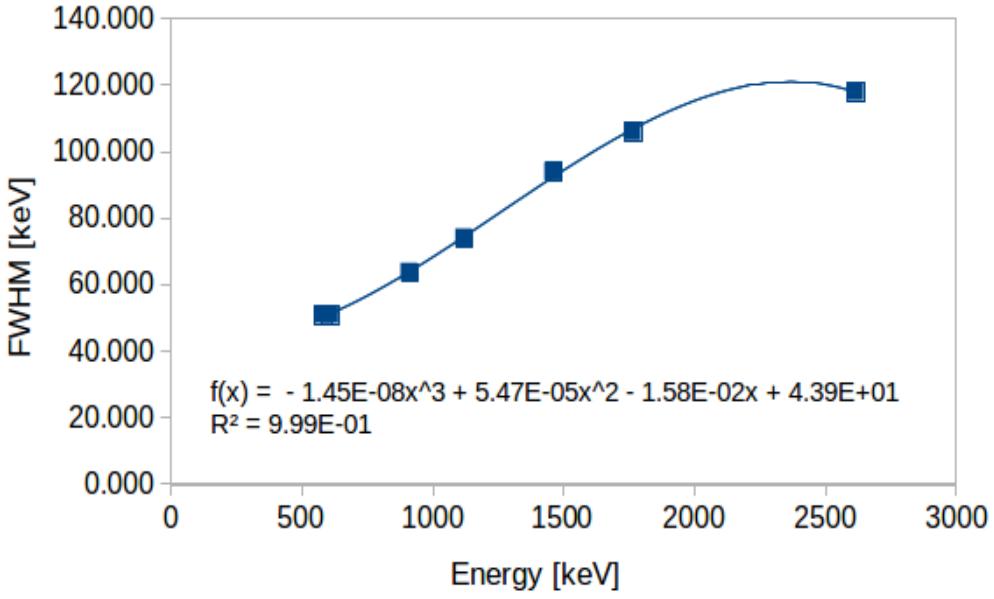

Figure 4.9: Plot of the measured peak FWHM (NaI:Tl detector) against energy fitted with a 3^{rd} order polynomial and the fit parameters.

Chapter 5

Experimental Methods

All experimental measurements were performed at the iThemba Laboratory for Accelerator Based Sciences (LABS), Cape Town, South Africa. The list of all measurements, measurement dates and locations within the iThemba LABS are given in Tab. 5.1.

5.1 Samples/Reference Materials Selection

The samples selected for this research are listed in Tab. 5.2. The KCl is 99.5 % pure from the Merck company for calibrating ^{40}K [87]. The RGU-1, RGTh-1 and IAEA-375 soil are from the International Atomic Energy Agency (IAEA). The RGU-1 was prepared for the IAEA at Centre for Mineral and Energy Technology (CANMET), Canada as agreed by the Canadian Certified Reference Materials Project (CCRMP) in 1984. The RGU-1 is intended for use in calibrating laboratory gamma-ray spectrometers for determining uranium. RGU-1 was prepared by dilution of uranium reference ore BL-5 (1) of CCRMP (7.09 % U) with a silica matrix of negligible U and Th content. The homogeneity of RGU-1 was assessed by an X-ray fluorescence and a neutron activation

Table 5.1: List of all measurements (d is the distance from the centre of the Marinelli beaker to detector's front face).

Measurement series	Date Start	Stop	Detectors	Geometry d (mm)	Location (iThemba LABS)	Notes
S01	15/10/18	26/10/18	4 $LaBr_3$:Ce	165	N-line vault	without shielding investigation
S02	14/06/19	10/07/19	2 $LaBr_3$:Ce	165	outside beside N-line vault	without and with water shield investigation
S03	11/07/19	24/07/19	NaI:Tl	90	outside beside N-line vault	$LaBr_3$:Ce detector internal activity and gamma-ray investigation
S04	22/01/19	01/02/19	HPGe	on top of the detector	ERL	for validation of $LaBr_3$:Ce results
S05	30/05/18	13/06/18	2, 4 and 8 $LaBr_3$:Ce	100, 150 and 240	N-line vault	geometry investigation
S06	10/05/17	14/05/17	8 $LaBr_3$:Ce	240	N-line vault	dead time investigation

technique by analysing in triplicate for the 16 bottles selected from the stock of 972 bottles (500 g bottle). The observed difference between the mean values was not statistically significant. The recommended activity concentration and uncertainty for the radionuclides present in this material are given in Tab. 5.2. This was established using the certified values for these radionuclides in BL-5 and uncertainty in the dilution by weighing. The RGTh-1 was prepared for IAEA at CANMET in November 1986 for calibrating gamma-ray spectrometer for determining thorium. RGTh-1 is a blend of sub 74 μm particles of CCRMP reference britholite ore OKA-2 with essentially non-radioactive silica of similar size distribution. The homogeneity of the material was tested by gamma-ray measurement of a sampling representing 5 % of the stock of 1012 500 g bottles. Analysis of the variance of the data detected show no significant difference between bottles. The recommended activity concentration and uncertainty for the radionuclides present in this material are given in Tab. 5.2. This was established using the certified values for the radionuclides in OKA-2, the measured values for the minor contributions from silica, and the dilution ratio of the preparation. The estimated uncertainties are at 95 % confidence interval. The IAEA-375 is a topsoil to the depth of 20 cm collected on the field of the collective farm "Staryi Vishkov", Novozybkov district, Brjansk region, Russia, in July 1990. Approximately 500 g of dried soil was milled, sieved, homogenised and placed in bottles. The soil was measured by several laboratories using techniques such as; gamma-ray spectrometry (low and high resolution), XRF, alpha spectrometry, NAA, AAS, etc. The results from the participating laboratory were compared by the IAEA. The results which deviated significantly from the population were considered to be outliers and rejected if they failed any one of the following statistical tests at the significance level of a =

0.05: Dixon's, Grubb's, coefficient of skewness and coefficient of kurtosis. The recommended certified activity concentration of the radionuclides present in this soil as at 31 December 1991 are given in Tab. 5.2 and the uncertainties are at 95 % confidence interval. Beach sand is a soil sample collected from Zanzibar [88].

Table 5.2: Samples/Reference materials, the radionuclides present in the reference materials and their activity concentrations.

Sample	mass (kg)	Radionuclides	Activity concentration (Bq kg^{-1})
Potasium chloride (KCl)	1.29	^{40}K	16259 (100)
Uranium ore (RGU-1)	1.41	U	4940 (26)
		Th	< 4.06
		^{40}K	< 0.62
Thorium ore (RGTh-1)	1.36	Th	3248 (64)
		U	77.81 (4.94)
		^{40}K	6.26 (3.13)
IAEA-375 soil	1.50	^{40}K	417.0 - 432.0
		^{238}U	19.0 - 29.8
		^{232}Th	19.2 - 21.9
		^{125}Sb	74.0 - 79.0
		^{134}Cs	454.0 - 472.0
		^{137}Cs	5200.0 - 5360.0
Beach sand (Bs)	2.66	—	—

5.1.1 Marinelli beaker

The iThemba LABS Environmental Radioactivity Laboratory (ERL) Marinelli beaker (Fig. 5.1) is manufactured by AEC-Amersham with dimensions of 130 mm diameter, 85 mm well diameter, 135 mm height, 61 mm well height and 2 mm thickness. The Marinelli beaker is used for radioactive sample analysis in gamma-ray spectroscopy applications [89]. Each of the samples described

in section 5.1 was placed in the Marinelli beaker filled up to the 1 L mark (88 mm). The Marinelli sample geometry was chosen to enable comparison between the high purity germanium (HPGe) and $LaBr_3$:Ce detectors results.

Figure 5.1: Marinelli beaker (1 litre volume) used to house the sample.

5.2 Measurement using Four $LaBr_3$:Ce Detectors without Shielding

Prior to the measurement with four $LaBr_3$:Ce detectors, different experimental geometries using the available eight $LaBr_3$:Ce (5 %) detectors at iThemba LABS were studied to ascertain the best experimental geometry for this work (see Appendix B.1). These detectors were manufactured by Saint-Gobain with a crystal size of 2" $\times$ 2" and R2083 photomultiplier tubes (PMTs) attached to them. For this work, measurements were performed using four $LaBr_3$:Ce detectors (L1, L2, L3 and L4) at 165 mm equidistant from the sample without shielding (Fig. 5.2). Each of the samples selected in section 5.1 was measured

in singles and coincidence modes and the counting time given in Tab. 5.3. An empty Marinelli beaker was used to measure the beaker and surrounding background contribution (background).

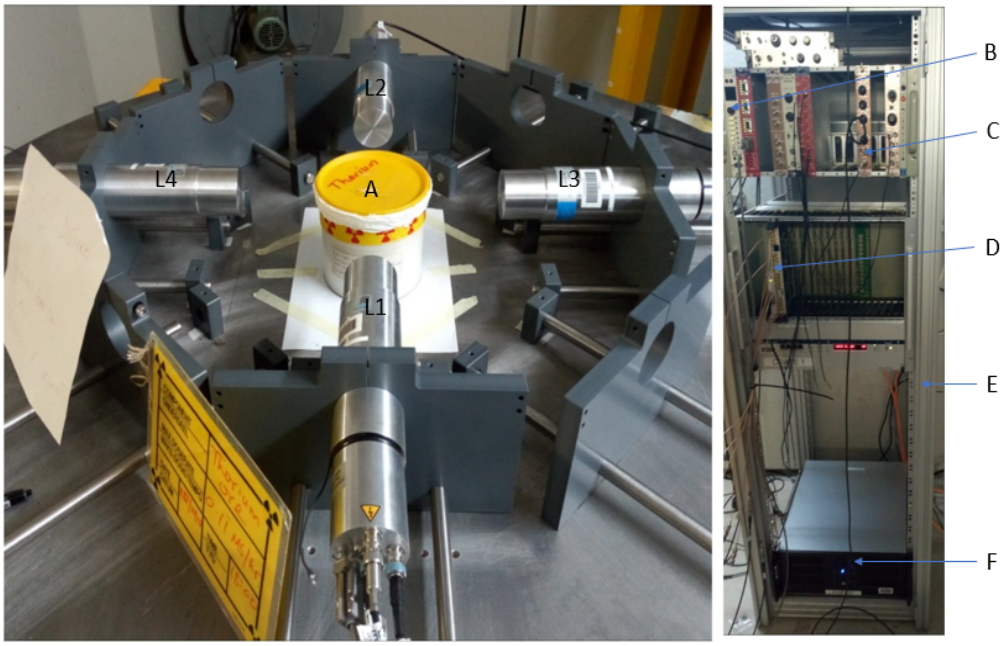

Figure 5.2: $LaBr_3$:Ce detectors (L1 - L4) placed 165 mm equidistant from the Marinelli beaker centre containing the sample without shielding and the associated electronics (A = sample, B = High voltage, C = Preamplifier, D = Pixie-16, E = Crate and NIM bin and F = CPU).

Table 5.3: Samples/Reference materials (sources) and measurement time using four $LaBr_3$:Ce detectors without shielding.

Samples/Sources	Live time (seconds)
KCl	172793
RGU-1	172796
RGTh-1	172764
IAEA-375 soil	172787
Beach sand	172983
Background	57594
^{137}Cs and ^{60}Co	7200

5.2.1 Electronics and Data Acquisition System

The iThemba LABS digital data acquisition system used for this study is MIDAS installed on a Linux PC [90]. This software accesses all the data read out from the hardware electronics through a single Peripheral Component Interconnect (PCI) bridge (PXI-8360). All the hardware electronic modules and Pixie-16 500 MHz were housed in a crate and NIM bin. The detectors were connected to a high voltage model NHS 62 20n supplied by CAEN SPA, Italy and set to -1260 V, -1233 V, -1236 V and -1290 V for L1, L2, L3 and L4, respectively. The detectors PMT anodes were integrated with a preamplifier (model 474 by ORTEC) to provide the signals.

Both anode (slow) and first dynode or cathode (fast) signal from the detectors PMT were connected to the XIA Pixie-16 module. Fig. 5.3 shows a schematic diagram of $LaBr_3$:Ce detector connected to the electronics. RG58 cables and RG175/lemo connectors were used for energy signal and fast signal connections, respectively. The XIA Pixie-16 module is a 16-channel all digital signal processing unit, which accepts the input signal from the preamplifier. The data acquisition of each of the 16-channels of the Pixie-16 module are independently gated by the Channel Gate Inputs (0-15). The slow and fast signals from detectors L1 to L4 were connected to channel 0 to 3 and 8 to 11 respectively i.e. 2 ns samples. A field-programmable gate array (FPGA) captures 5 ADC samples at the rate of 100 MHz (i.e. every 10 ns). Furthermore, full constant fraction discriminator (CFD) timing data are calculated from the differences between the delayed and non-delayed sums, providing the zero-crossing point. Data were read out in list-mode i.e. event by event which allows zero dead-time data acquisition by counting only when events are processed, and data taken. These data consist of event ID, time stamp (48-bit), CFD time (16-bit)

and (calculated) energy (16-bit) [91]. The digital signal processing settings for both slow and fast signals used for this work are given in Tab. 5.4 $\longrightarrow$ 5.6.

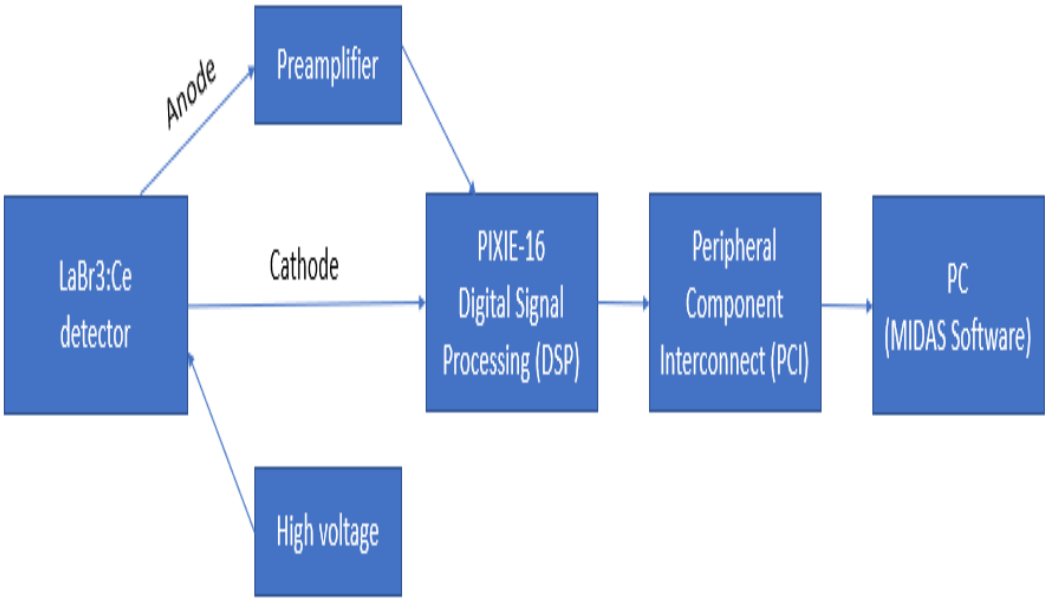

Figure 5.3: Schematic diagram showing connection of $LaBr_3$:Ce detector anode (slow) and cathode (fast) outputs to the electronics.

Table 5.4: Digital signal processing (DSP) parameters used for both anode and cathode (first dynode) signals.

Parameter/Action	Slow signal	Fast signal
Trigger type	Local	Local
Good channel	Enable	Enable
Trigger polarity	Positive	Negative
CFD trigger mode	Enable	Enable
Energy sums	Enable	Enable
Input relay	Enable	Enable
Pileup rejection	Enable	Disable

Table 5.5: Digital signal processing (DSP) parameters settings used for each detector PMT anode signal channel.

Parameter	Channel			
	L1	L2	L3	L4
Trigger threshold	200.00	300.00	300.00	300.00
Fast risetime (10 ns)	0.02	0.10	0.10	0.10
Fast flat top (10 ns)	0.10	0.10	0.10	0.10
Energy risetime (10 ns)	1.00	0.50	0.50	0.50
Energy flat top (10 ns)	0.80	0.50	0.50	0.50
Peak sample (10 ns)	1.80	0.98	0.98	0.98
Peak separation (10 ns)	1.00	1.00	1.00	1.00
Delay constant (ns)	35.67	34.93	34.93	36.10
CFD delay	5.00	5.00	5.00	5.00
CFD scale	1:5	1:5	1:5	1:5
CFD threshold	50.00	50.00	50.00	50.00

Table 5.6: Digital signal processing (DSP) parameters settings used for each detector cathode (first dynode) signal channel.

Parameter	Channel			
	L1	L2	L3	L4
Trigger threshold	500.00	350.00	350.00	350.00
Fast risetime (10 ns)	0.10	0.02	0.02	0.02
Fast flat top (10 ns)	0.10	0.01	0.01	0.01
Energy risetime (10 ns)	0.60	0.20	0.20	0.20
Energy flat top (10 ns)	0.60	0.10	0.10	0.10
Peak sample (10 ns)	1.80	0.98	0.24	0.24
Peak separation (10 ns)	1.00	0.50	0.50	0.50
Delay constant (ns)	34.93	0.03	0.03	0.03
CFD delay	5.00	5.00	5.00	5.00
CFD scale	1:5	1:5	1:5	1:5
CFD threshold	50.00	50.00	50.00	50.00

5.3 Measurement using High-Purity Germanium (HPGe) Detector

The ERL is a low-background laboratory, which houses a planar high purity germanium (HPGe) detector. The HPGe detector (GC4520 model) manufactured by Canberra, France has a crystal diameter of 62.5 mm and length of 59.9 mm. The detector crystal has a mounted liquid nitrogen (LN2) Dewar (vertical dipstick type) for continuous cooling. The detector is enclosed with 100 mm thick lead and 2 mm inner copper lining to attenuate the X-rays from the lead as shown in Fig. 5.4. The detector was reverse biased with a high voltage (SILENA MOD 7716) of +3500 V. The detector was connected to an amplifier (model 572 by ORTEC) with the following ADC settings: gain: 1.2, coarse gain: 20 and shaping time: 6 μs, and the amplifier was linked to a Multi-Channel Analyzer (MCA). The Palmtop MCA (model serial: 0202 by ATOMKI) was connected to the computer and ATOMKI Palmtop software MCA [92] installed on the computer was used to acquire data. The schematic diagram of HPGe detector connected to the electronics is shown in Fig. 5.5.

Figure 5.4: High purity germanium (HPGe) detector coupled to a liquid nitrogen (LN2) Dewar and enclosed in a lead shielding with inner copper lining, and the associated electronics: A = Lead shielding, B = dewar containing liquid nitrogen, C = Crate and NIM bin, D = High voltage, E = Amplifier, F = HPGe detector and G = Sample.

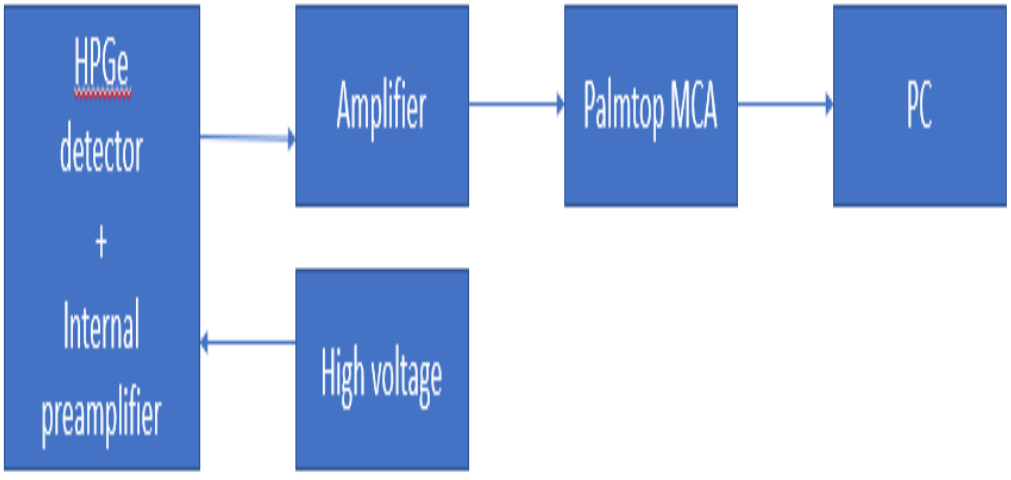

Figure 5.5: Schematic diagram of HPGe detector connected to the electronics.

5.4 Measurement using $LaBr_3$:Ce and NaI:Tl Detectors inside the Water Shield

The criteria considered in the final design of the water shield were; strength of the polyethylene material that will carry the required volume of water, the modality for filling water in and out of the shield without damaging the detector, connection of electronics cables to the detectors and changing of sample, detector and sample support to ensure consistency in the source-to-detector distance.

A water tank with a pipe inserted horizontally at height 600 mm from the tank base was supplied by the local company J.J.A.D Marine and Industrial Installation, Cape Town, South Africa. The dimensions of the tank and the inserted pipe are given in Tab. 5.7. The tank has a lid on top through which the tank can be filled with water and an outlet tap just above the base for emptying. The pipe has a cover on both ends made with polyethylene. The pipe cover has a hole through which detector cables pass. The tank was placed on the floor outside beside the N-line vault at iThemba LABS (see Appendix B), a pump was used to transfer tap water from a mobile water tanker to the tank. The tank was filled to the 1234 mm height such that 500 mm height water is below and above the measurement volume. Eight jerry cans with the dimensions of each given in Tab. 5.7 were also filled with tap water and four placed on both ends of the pipe as shown in Fig. 5.6. The jerry cans are moveable as seen in Fig. 5.7 to enable change of sample. A horizontal cylindrical segment made of polyethylene of radius 20 mm and length 700 mm was constructed to support the sample and detectors (see the upper part of Fig. 5.6). As seen in the upper part of Fig. 5.6, the detectors are supported to avoid movement

in the event of sample change, the Marinelli beaker placement area was also carved to support it. This was placed inside the pipe (measurement volume) for measurement with the water shield. The reference materials and sample selected in section 5.1 were each measured using two $LaBr_3$:Ce detectors (L2 and L3) placed 165 mm equidistant from the sample. An empty Marinelli beaker was also measured to gauge the background and beaker contributions to the spectrum. These measurements were performed inside the water shield and outside the shielding on a table for the purpose of checking the gamma-ray attenuation.

Likewise, because of the internal activity of the $LaBr_3$:Ce detector observed, the same measurements were repeated using a 3" × 3" NaI:Tl detector (model 12MBHA20/3A-X DX-642 by Harshaw scintillation crystal) placed at 90 mm from the beaker centre. The NaI:Tl detector was also used to measure the $LaBr_3$:Ce detector internal activity, the distance between the $LaBr_3$:Ce detector and NaI:Tl detector front face was 25 mm. See Tab. 5.8 for the reference materials/samples measured and the measurement time. The electronics and data acquisition system are the same as that of section 5.2.

Table 5.7: Water shield and associated material geometries.

Material	Tank	Pipe	Jerry can	cylindrical segment
Diameter (mm)	1410.0	234.0	—	—
Height (mm)	1800.0	—	117.5	—
Length (mm)	—	1456.0	137.5	700
thickness (mm)	5.0	17.0	2.0	—
radius (mm)	—	—	—	20.0
width (mm)	—	—	20.0	—

Table 5.8: Samples/Reference materials measuring time using $LaBr_3$:Ce and NaI:Tl detectors without shielding (wos) and inside the water shielding (ws).

Sample/Sources		Live time (seconds)		
	$LaBr_3$:Ce (wos)	$LaBr_3$:Ce (ws)	NaI:Tl (wos)	NaI:Tl (ws)
KCl	86404	86400	—	86398
RGU-1	86391	86400	—	86400
RGTh-1	86309	86400	—	86400
IAEA-375	—	172799	—	86400
Beach sand	—	172809	—	86400
Background	43200	43200	43200	43200
^{60}Co	3600	3600	—	10800
$LaBr_3$:Ce detector	—	—	—	86399

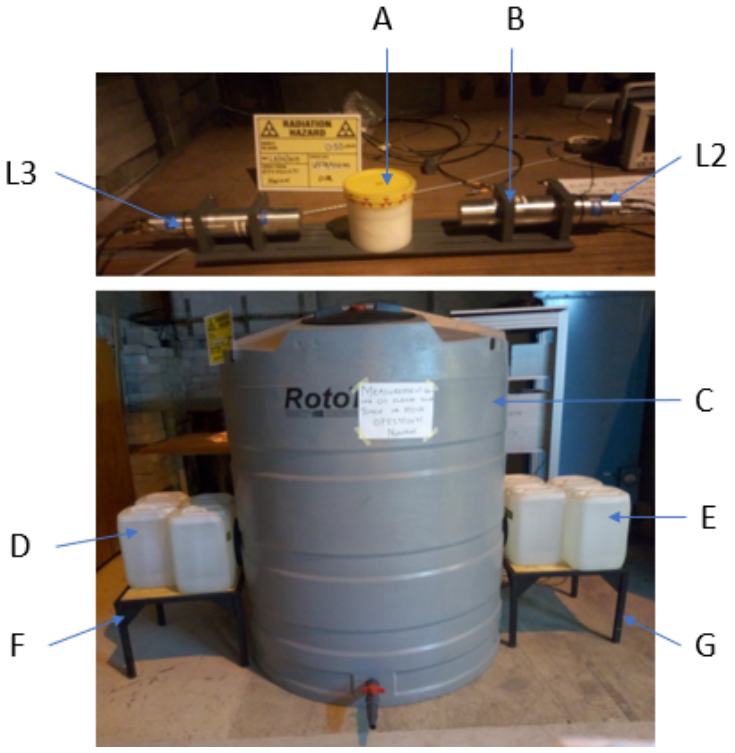

Figure 5.6: The water shielding (lower), and two $LaBr_3$:Ce detectors and Marinelli beaker placed on a cylindrical segment all placed on a table outside the shielding (upper): A = Sample, B = Detectors support, C = Tank, D and E = jerry cans, F and G = jerry cans support, and L2 and L3 = $LaBr_3$:Ce detectors.

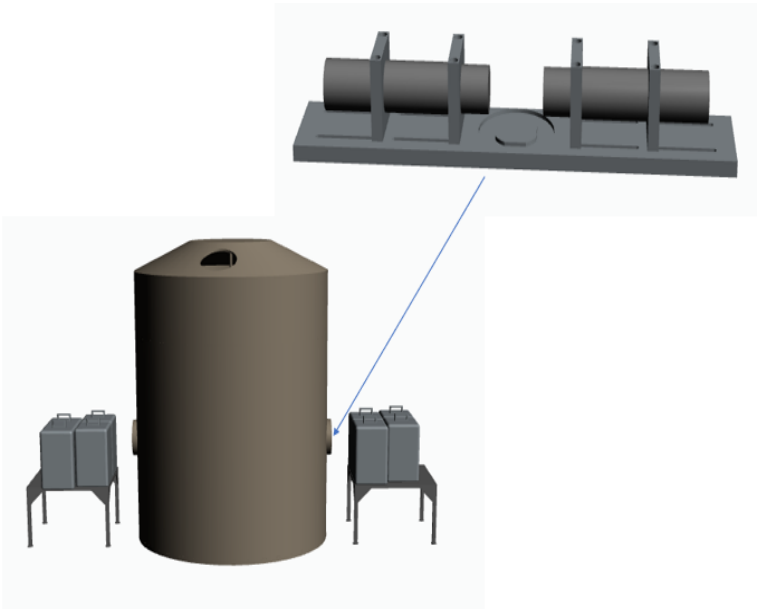

Figure 5.7: CAD drawing of water shield design with the jerry cans moved to show the location of the measurement volume (lower) and the two $LaBr_3$:Ce detectors placed on a cylindrical segment which is placed inside the measurement volume (upper).

5.5 Background/Scattered Gamma ray Reduction using Time-of-flight and Measurement of Two Photons in Coincidence

The time resolution of the $LaBr_3$:Ce detector ($\approx$ 370 ps FWHM) together with the digital data acquisition system (measured to be 5(2) ps) allow for resolving time differences at the sub-nanosecond level. The application of gamma ray time-of-flight enables the gamma rays from the sample to be differentiated from background/scattered gamma rays. The application of gamma ray time-of-flight for background gamma ray reduction is possible only when the

radionuclide to be measured is a cascade emitter. The $LaBr_3$:Ce detectors (2" × 2") are 165 mm equidistant (d) from the Marinelli beaker centre in Fig. 5.2. In Fig. 5.8, the gamma rays from the measured sample travels the same distance to all the detectors (blue lines). The gamma rays from the sample will not originate from the beaker centre alone since it is a volume sample. Therefore, the gamma rays from the measured sample travels a distance 165 ± 65 mm to all the detectors. Compton scattered gamma rays from one detector to another is dependent on the experimental geometry (red lines in Fig. 5.8). The distance covered by Compton scattered gamma rays from one detector to another at 90° (e.g. L1 to L3) and 180° (e.g. L1 to L2) are 230 ± 90 mm and 330 ± 130 mm, respectively. Using the distance covered by the gamma rays and speed of light (3.0×10^8 m s^{-1}), the time-of-flight can be estimated. The time-of-flight of gamma rays from the measured sample is 550 ± 217 ps. The time-of-flight of Compton scattered gamma rays for detectors at 90° and 180° are 767 ± 300 ps and 1100 ± 433 ps, respectively. This means that the time-of-flight of gamma rays from the sample is shorter than that of the Compton scattered gamma rays. Furthermore, the Compton scattered gamma rays for detectors at 180° takes a longer time to get to the detector than for detectors at 90° due to the longer distance covered. This is the reason for the two types of time difference spectra in Fig. 5.9, the centroid peak is the true coincidence peak containing the coincident events of interest while the peaks on either side of the centroid peak are associated with Compton scattered events between the detectors. However, when coincidence between detectors at 180° measured using $LaBr_3$:Ce detectors without shielding in Fig. 5.9 is compared to that measured using $LaBr_3$:Ce detectors inside the water shield in Fig. 5.10, the time-of-flight of gamma rays from the sample is the

same. This is because the detectors, sample geometry and source-to-detector distance is the same. However, the latter has more random coincidence events and wider spectrum spread than the former due to the gamma rays Compton scattered in the water shield. This can be explained using Fig. 5.11. Some of the gamma rays from the background and sample (blue lines) will Compton scatter in the water shield (red lines). Depending on the energy of the gamma ray some will be completely absorbed in the water shield while some will scatter back into the detector (see Fig. 5.12). However, these background/scattered gamma-ray events can be significantly reduced by setting a time gate smaller than the scattered gamma-ray time-of-flight in generating the gamma-gamma coincidence events (see Chapter 6).

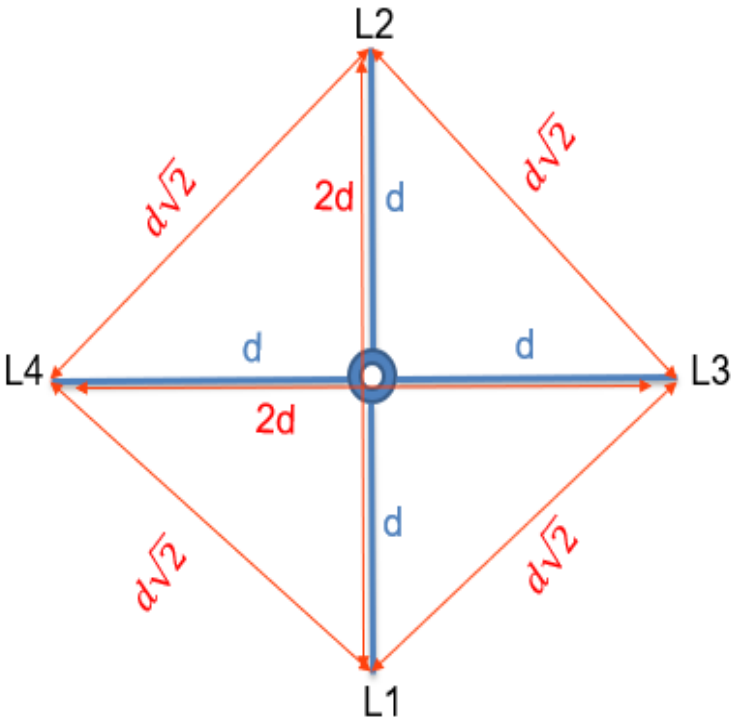

Figure 5.8: Illustration of the distance (d = 165 mm) between sample and detector front surfaces plus the Marinelli beaker radius; and between the detectors (L1 to L4).

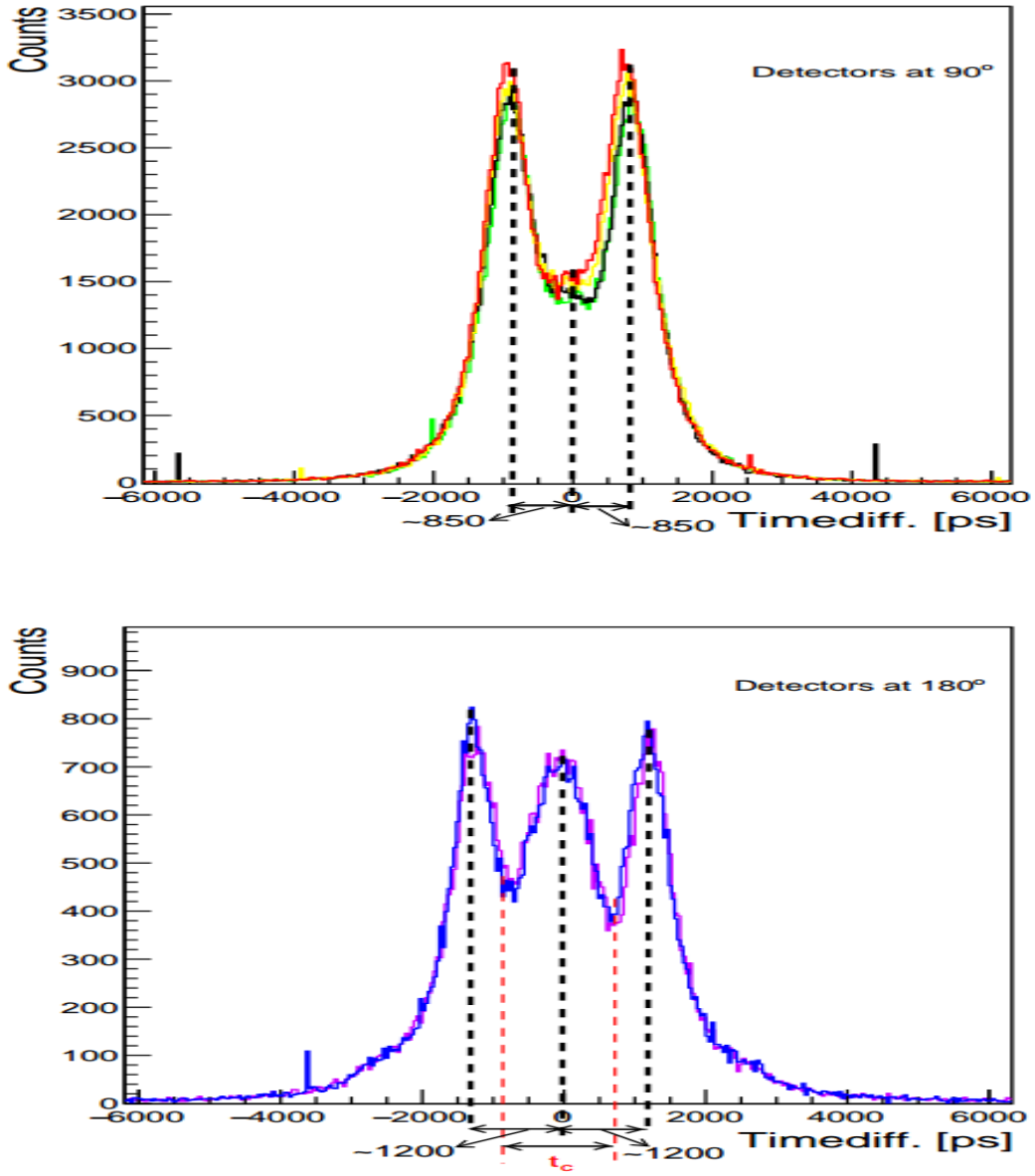

Figure 5.9: Time difference spectra for the two combinations of four $LaBr_3$:Ce detectors at 90° (upper: black, red, green and yellow) and 180° (lower: blue and purple) measured without shielding (t_c is the time-of-flight of gamma rays from the sample). The spike is the timestamp which was latched by the fast filter trigger when fast filter crosses over the trigger threshold which does not affect the results. That is, if a zero-crossing point cannot be found within a certain period after the fast trigger, a forced CFD trigger will be issued and a flag will be set in an event header word to indicate that the recorded CFD time for this event is invalid, but the event will still have a valid timestamp.

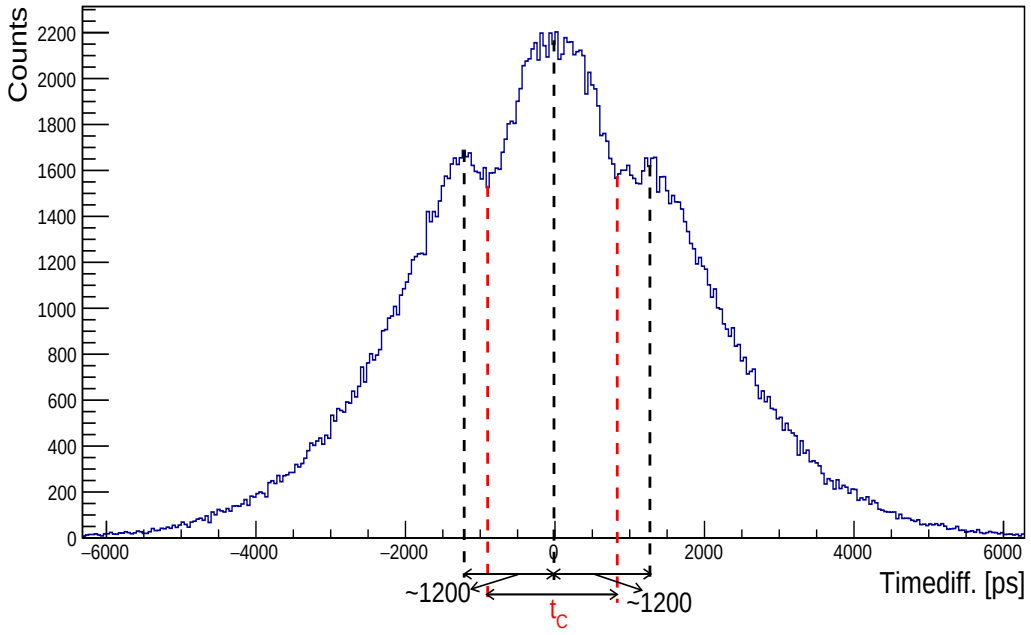

Figure 5.10: Time difference spectra for the two combinations of two $LaBr_3$:Ce detectors at 180° measured inside the water shield.

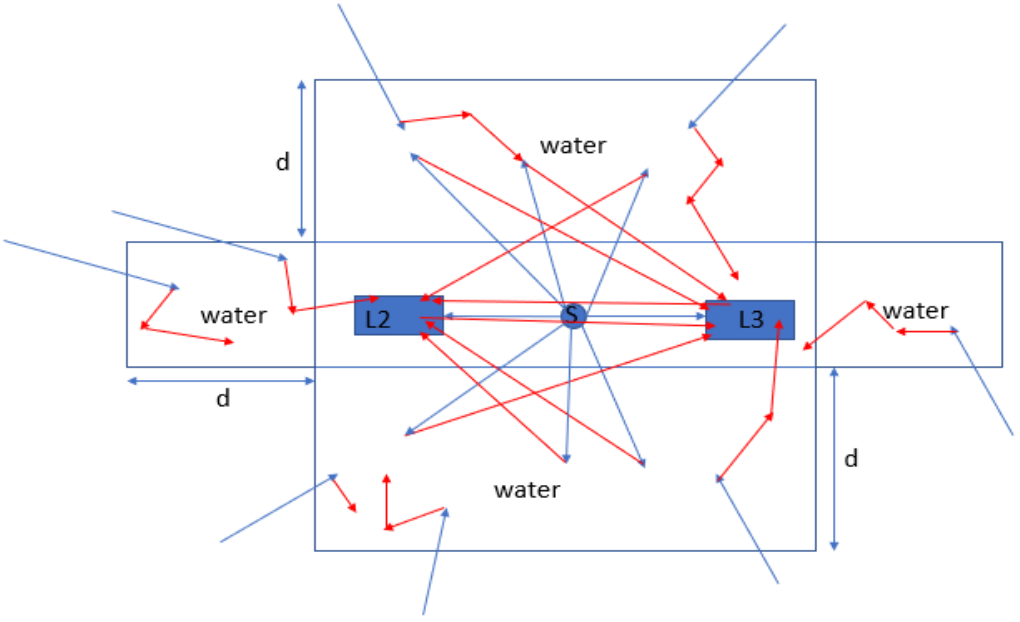

Figure 5.11: Illustration of gamma rays scattering in the water shield of thickness d = 500 mm (the detectors (L2 and L3) are 165 mm equidistant from Marinelli beaker centre).

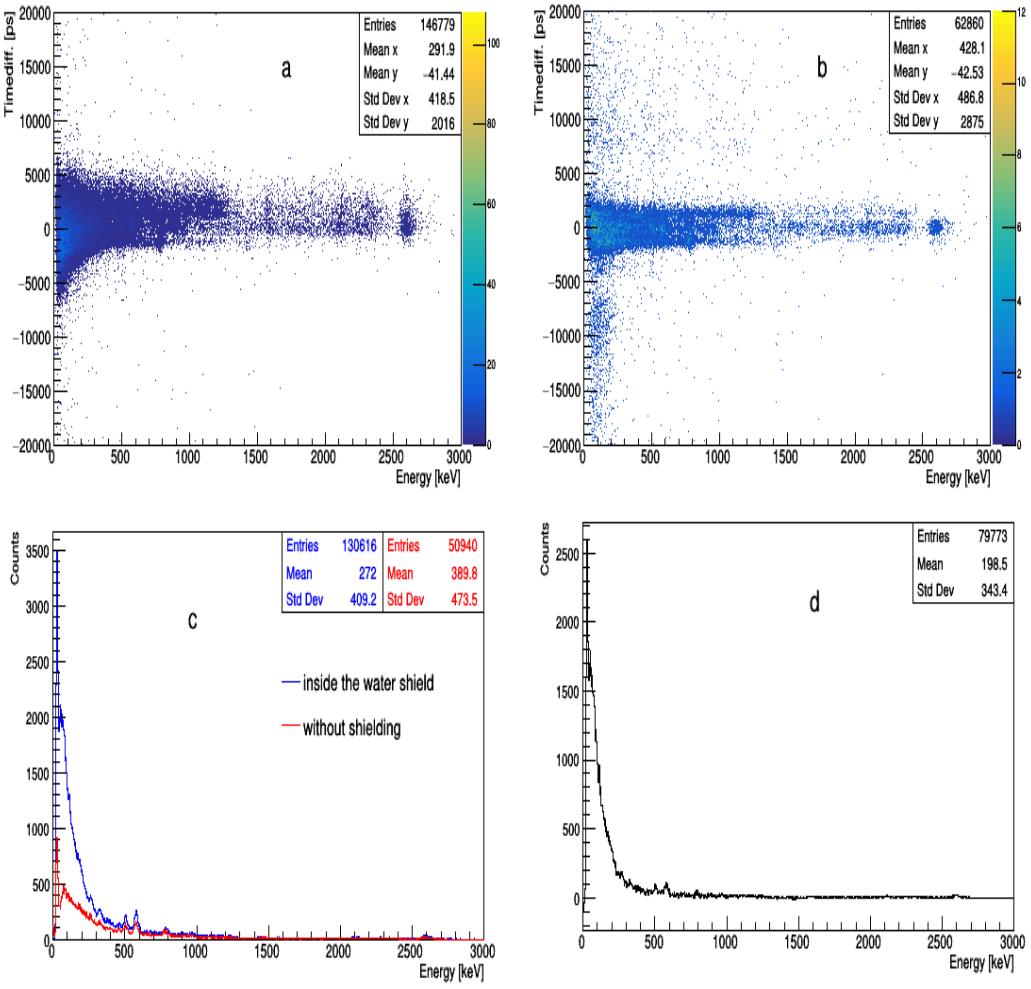

Figure 5.12: Plot of time difference against energy for RGTh-1 measured using two $LaBr_3$:Ce detectors (a) inside the water shield and (b) without shielding, (c) Projection of x-axis of (a) (upper=blue) and (b) (lower=red), and (d) upper spectrum minus lower spectrum in (c).

5.6 Dead Time Measurement

The two-source method was used to measure the dead time of the system using ^{22}Na (1274.5 keV) and ^{137}Cs (661.7 keV) point sources. The measurement was performed using eight $LaBr_3$:Ce detectors placed 240 mm equidistant from the source. The ^{22}Na and ^{137}Cs sources were measured separately and together,

the counting time for each is given in Tab. 5.9. Background was measured for 3596 seconds. The background spectrum was normalized to the source counting time and subtracted from the source spectrum. The measured source spectra after background subtraction are shown in Fig 5.13 and the net counts in the 1274.5 keV and 661.7 keV peaks region were extracted using the method described in section 6.5. The count rates are given in Tab. 5.9 and dead time was calculated using Eqn. 2.5.12. The dead time was found to be 0.0033 % which is insignificant.

Table 5.9: Radioactive source measuring times and count rates.

sources	source activity kBq	counting time (seconds)	count rates (cps)
^{22}Na	691.69	5400	39.6
^{137}Cs	71.59	5389	362.0
^{22}Na + ^{137}Cs		7200	39.3 + 361.4 = 400.6

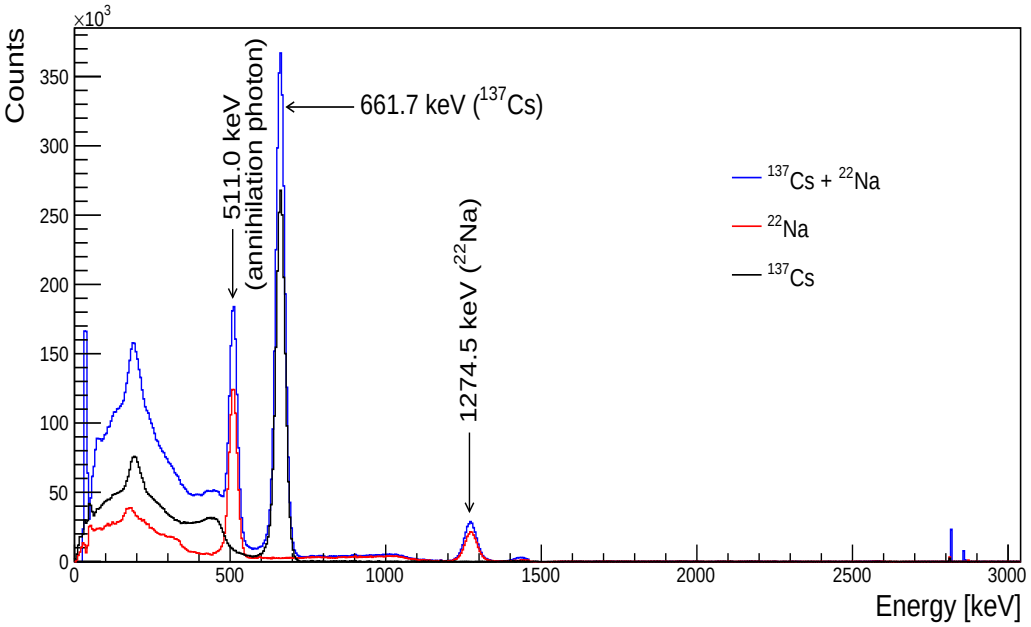

Figure 5.13: Spectra of ^{22}Na and ^{137}Cs measured separately for 1.5 hours and together for 2.0 hours after background subtraction.

Chapter 6

Data Analysis

In this Chapter, the analysis of the acquired list-mode data (see Chapter 5) is described in detail. The list-mode data gives the advantage of enabling the re-processing of the raw data offline. The data were sorted into channel, time and energy. The sorted data were used to plot energy and time spectra using ROOT software [93] for each detector channel. The flowchart of data analysis in singles and coincidence modes is shown in Fig. 6.1. The analysis chain for measurement series S01 given in Tab. 5.1 will be presented as an exemplar case. Other measurement series data were analysed in the same way and some of the spectra can be seen in Appendix B.3.

6.1 Spectrum Energy Calibration

Before sample measurements, the detection system was energy calibrated. This entails measuring a radioactive source with known associated gamma-ray energies. These gamma-ray energies are then correlated with the peak channel in a spectrum to obtain a function mostly linear or quadratic [12]. The 661.7 keV, 1173.2 keV, 1332.5 keV peaks of ^{137}Cs and ^{60}Co point sources plus the

1460.8 keV and 2614.5 keV peaks present in the background spectra were used to energy calibrate all the spectra offline. Firstly, the peaks in the spectrum were each fitted with a Gaussian line-shape in ROOT [93], as shown in Fig. 6.2, to obtain the channel mean (centroid). Secondly, the known energies were plotted against the channel means using LibreOffice Calc as shown in Fig. 6.3. Thirdly, the data were fitted with a linear function to obtain the fitting parameter. Finally, the fitted parameters were inputted into the ROOT code written for energy calibration. Some spectra before and after energy calibration are shown in Fig. 6.4. Also, the energy calibration was used to "gain-match" the $LaBr_3$:Ce detectors to enable data comparison/summing.

Figure 6.1: Flowchart of data analysis in singles and coincidence modes.

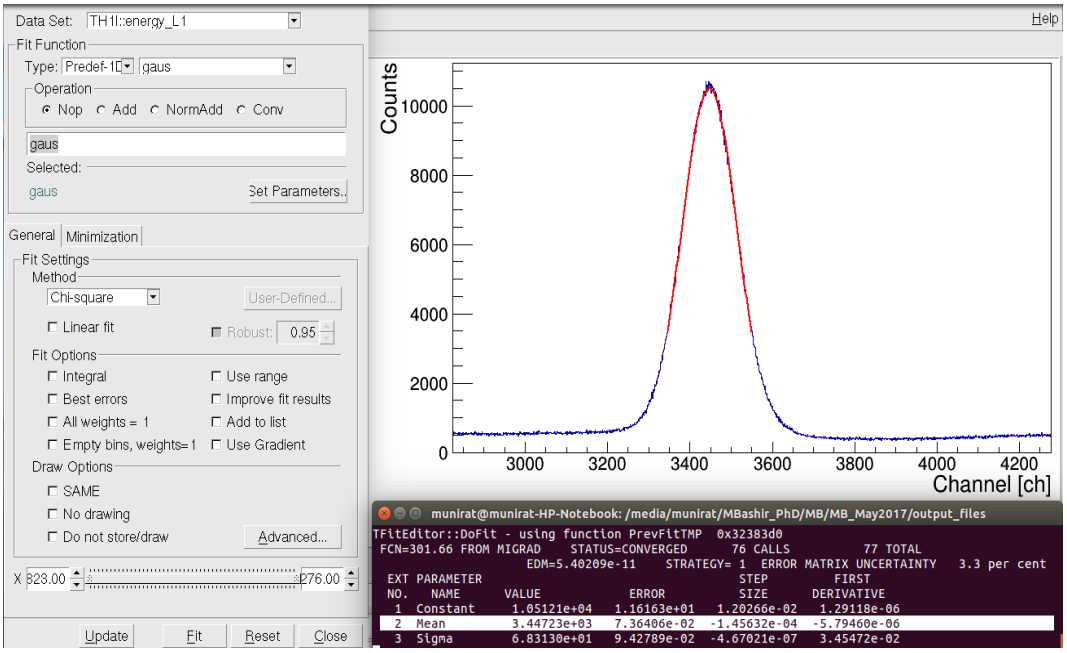

Figure 6.2: Fitting of spectrum peak with a Gaussian line-shape in ROOT to obtain the centroid: The ROOT fit panel is on the left side, fitted peak on the upper right side and the centroid value on the lower right side of the figure.

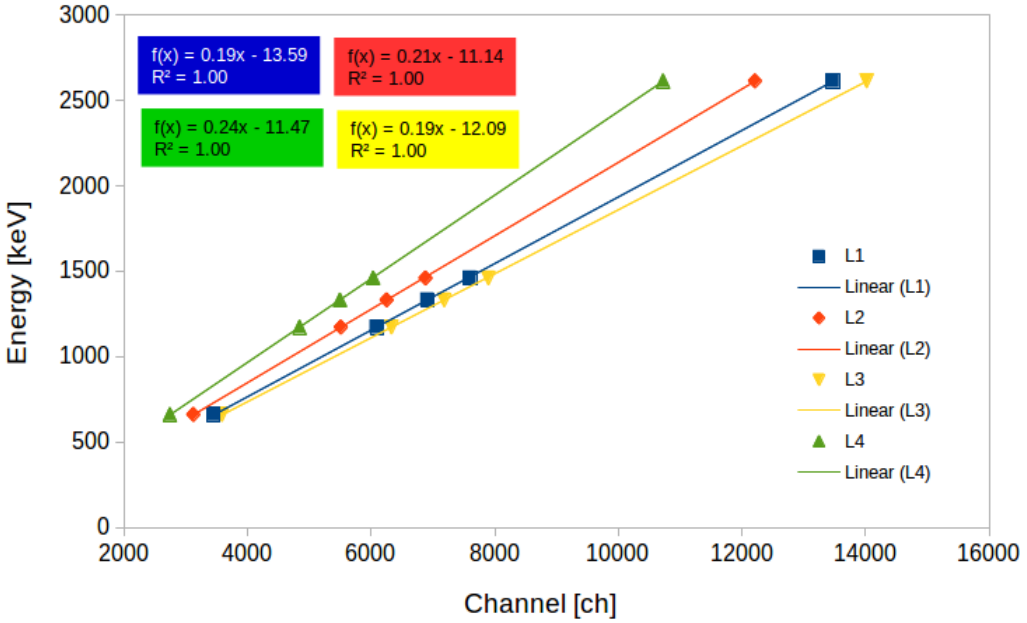

Figure 6.3: Plot of energy vs channel for each of the four detectors (L1 - L4) each fitted with a linear function and their fitting parameters shown.

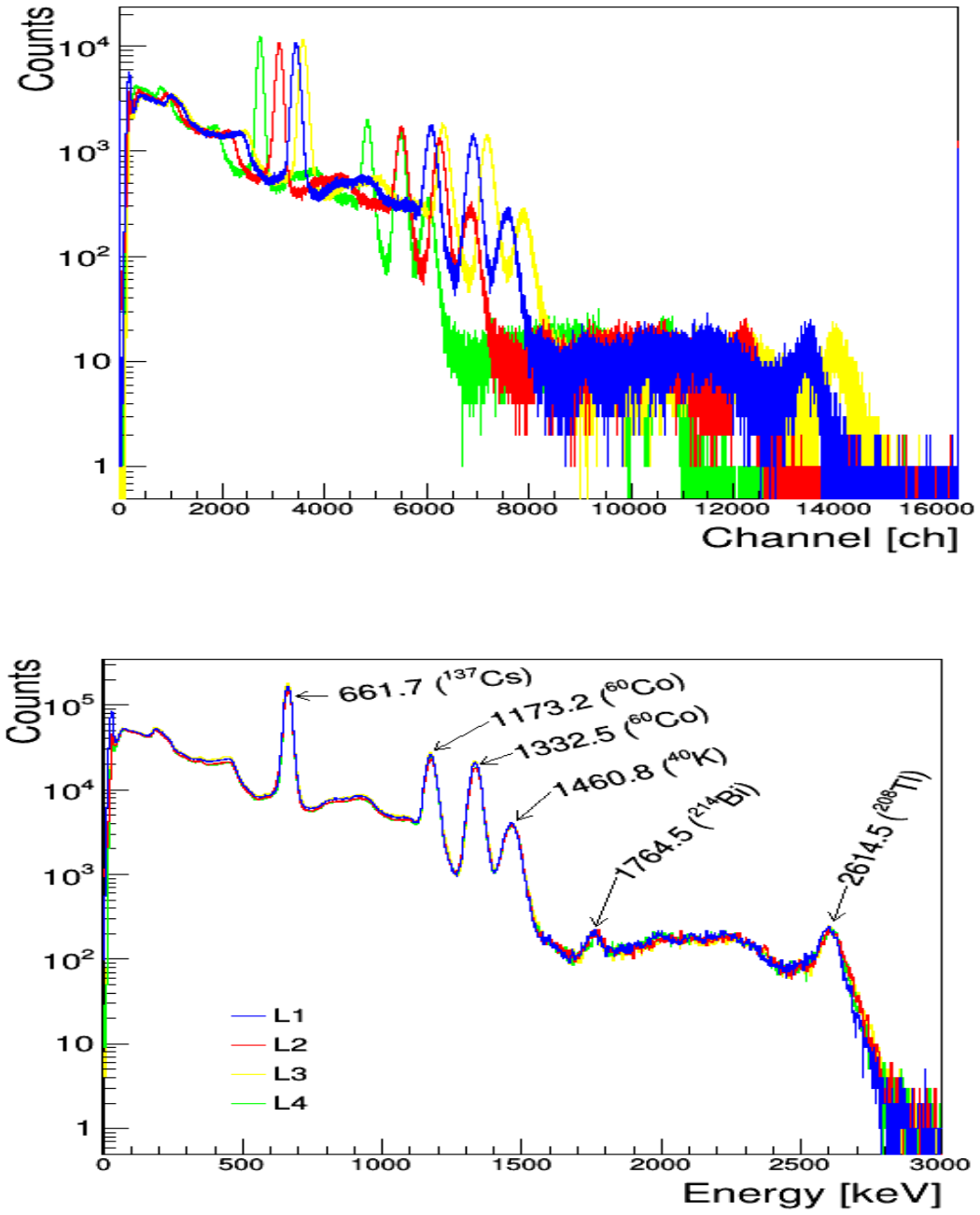

Figure 6.4: Spectra before (upper) and after (lower) energy calibration using ^{60}Co and ^{137}Cs sources plus background radiation measured with four $LaBr_3$:Ce detectors.

6.2 Time Spectra

The acquired time-stamped data (± 10 ns plus ± 2 ns CFD time and CFD granular of 20ps/bin, see Chapter 5) were used to plot the time difference between gamma-ray events associated with any two $LaBr_3$:Ce detectors within the time window of ± 10000 ps (Fig. 6.5). The time window was defined in the sorting code such that one $LaBr_3$:Ce detector signal is taken as the clock start and the other $LaBr_3$:Ce detector signal taken as the clock stop. For instance, taking $LaBr_3$:Ce detector L1 signal as the clock start and detector L2 signal as the clock stop; if a gamma-ray energy event arrives at $LaBr_3$:Ce detector L1 at time 5000 ps and another gamma-ray event arrives at $LaBr_3$:Ce detector L2 at time 12000 ps, then the time difference between the events in the two detectors is 7000 ps. The events will be registered as coincident events because it is within the time window of 10000 ps.

The time difference spectra were calibrated by subtracting the peak mean (centroid) time in Fig. 6.5 (left) from the time of each bin. As seen from Fig. 6.5 (right), the peaks in all the spectra are centred at zero. The centroid peak in Fig. 6.5 is the true coincidence peak which contain the coincident events of interest, while the peaks on either side of the centroid peak are random coincidence [60] due to background radiation from terrestrial and/or Compton scattering.

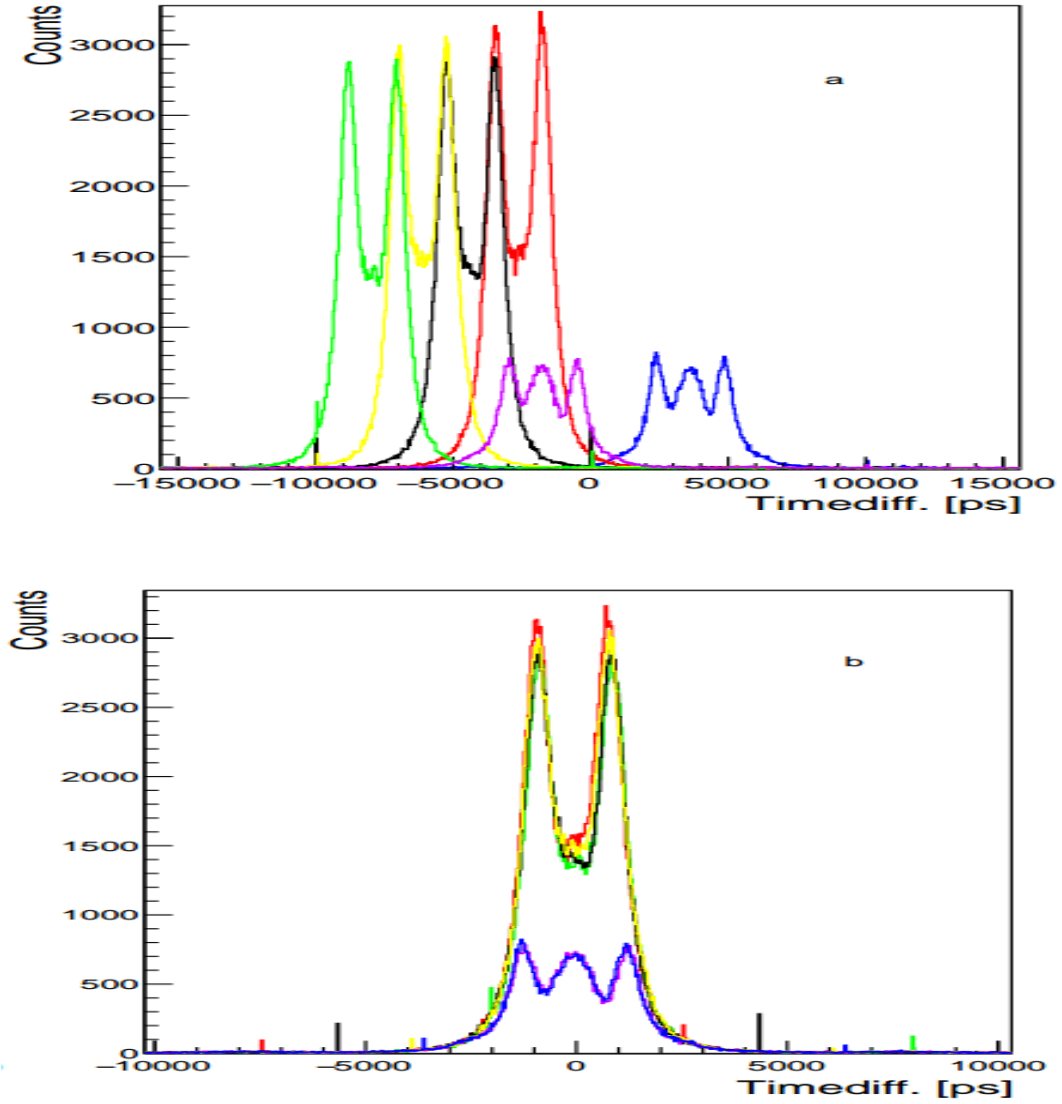

Figure 6.5: Time difference spectra (a) before and (b) after calibration for six of the two combinations of four detectors (black, red, green and yellow colour spectra are for detectors at 90^o whereas blue and purple colour spectra are for detectors at 180^o).

6.3 Time Gated Gamma-Gamma Spectra

The time gate t_c in Fig. 5.9 was set on the data to generate gamma-gamma spectra for any two detectors in coincidence within that time. The spectra for all the two combinations of four $LaBr_3$:Ce detectors were summed for each

sample measured and background. Correction for the background radiation contribution to the counting rates was made [60; 94] by normalizing the background gamma-gamma spectrum in Fig. 6.6 to the samples counting time. Then, the normalized background gamma-gamma coincident spectrum was subtracted from that of the sample. The beach sand gamma-gamma spectra after background subtraction measured using four $LaBr_3$:Ce detectors without shielding is shown in Fig. 6.7. The two-dimensional gamma-gamma matrix corresponds to gamma rays in the decay cascade being detected in coincidence and random coincidence.

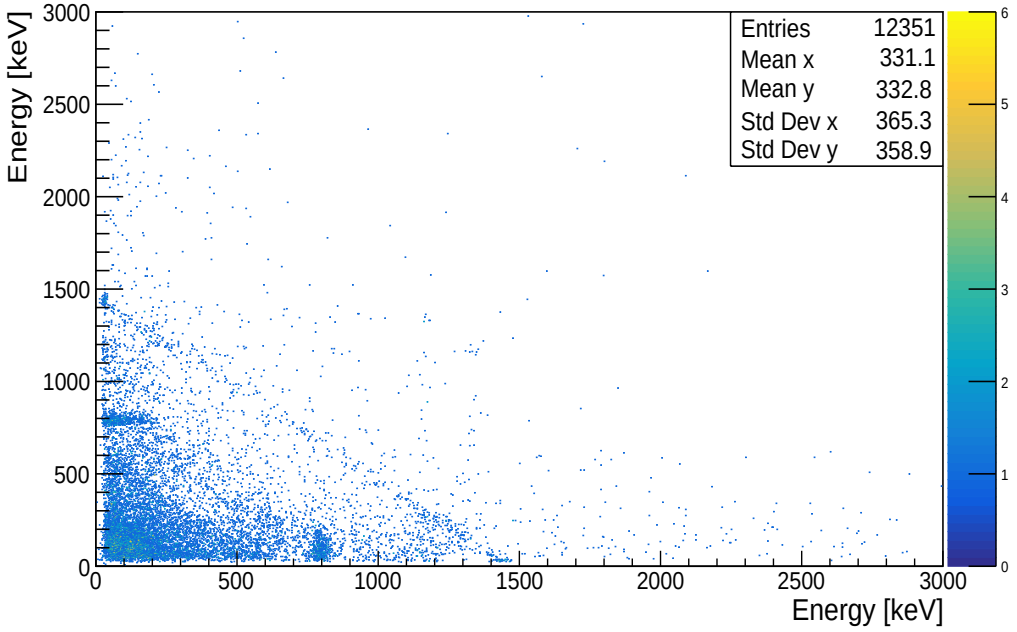

Figure 6.6: Summed total gamma-gamma spectra for background generated using the time gate t_c measured for 57594 seconds using four $LaBr_3$:Ce detectors without shielding. The colour scale shows the events intensities.

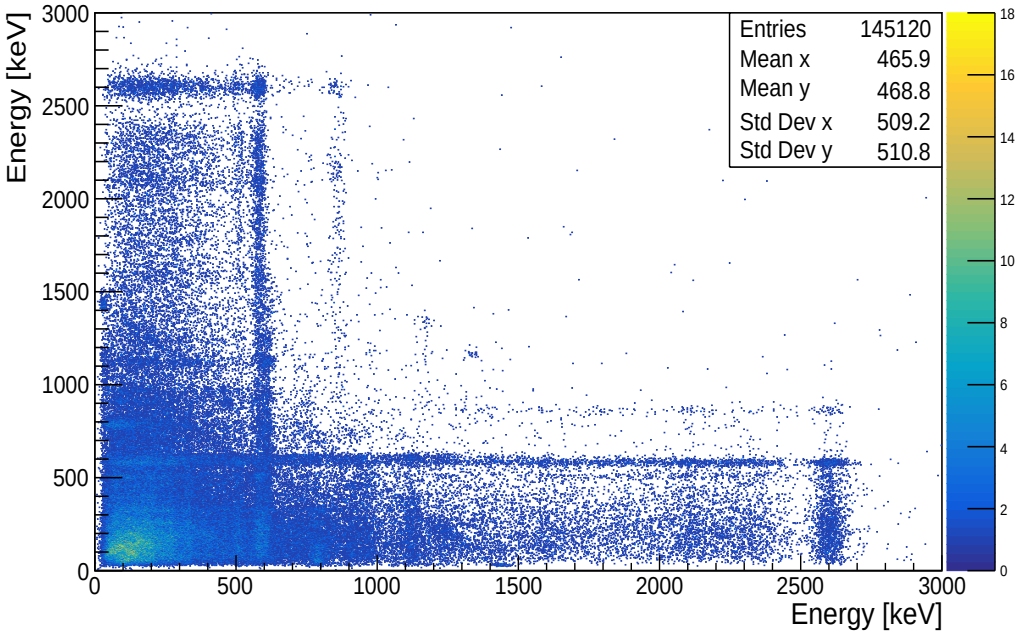

Figure 6.7: Summed total gamma-gamma spectra after background subtraction for beach sand generated using the time gate t_c measured using four $LaBr_3$:Ce detectors without shielding. The colour scale shows the events intensities.

Furthermore, a total time gate (from -5000 ps to 5000 ps) was also set on the background, IAEA-375 soil and beach-sand data measured using four $LaBr_3$:Ce detectors to check the sensitivity of the time gate t_c (see appendix B.2). Also, the width of the peaks on either side of the centroid peak of Fig. 5.9 were set on the beach-sand data measured using four $LaBr_3$:Ce detectors to generate the gamma-gamma matrix in Fig. B.11 to show the background/scattered events contribution.

6.4 Gamma-ray Spectra

In singles mode of measurement, the spectra from all the detectors were summed for each measured sample and background. The background spec-

trum in Fig. 6.8 was normalized to the sample counting time and subtracted from the sample spectrum to obtain the background subtracted spectrum in Fig. 6.9. The 1460.8 keV peak of ^{40}K is negative in Fig. 6.9, this means that the counts in this peak region for background is higher than in the sample. This could be due to self-absorption in the sample.

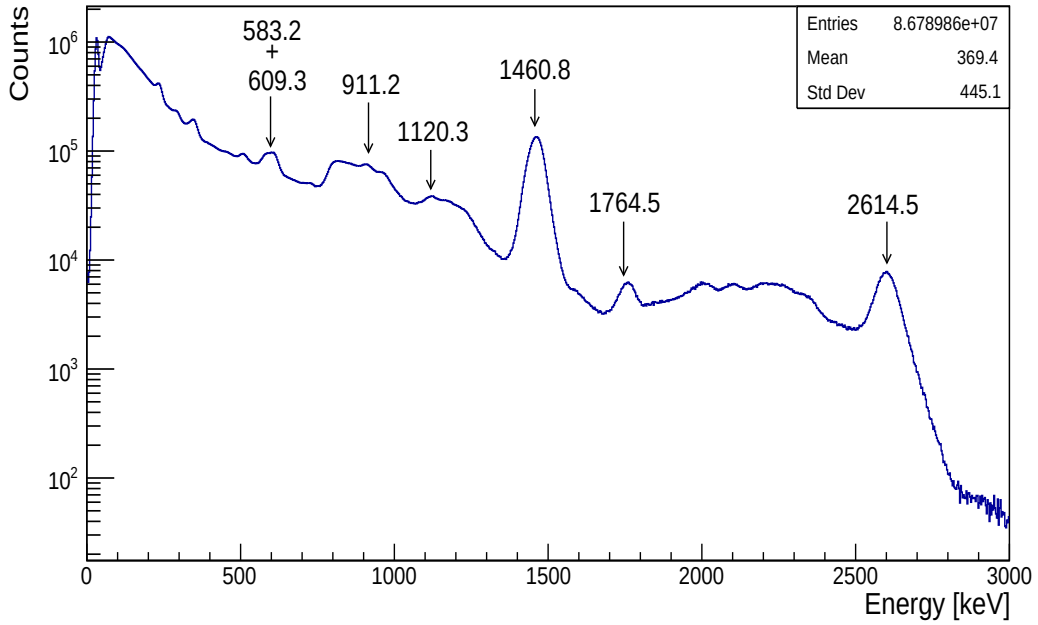

Figure 6.8: Summed total background gamma-ray spectra measured for 57594 seconds using four $LaBr_3$:Ce detectors without shielding (wos) in singles mode.

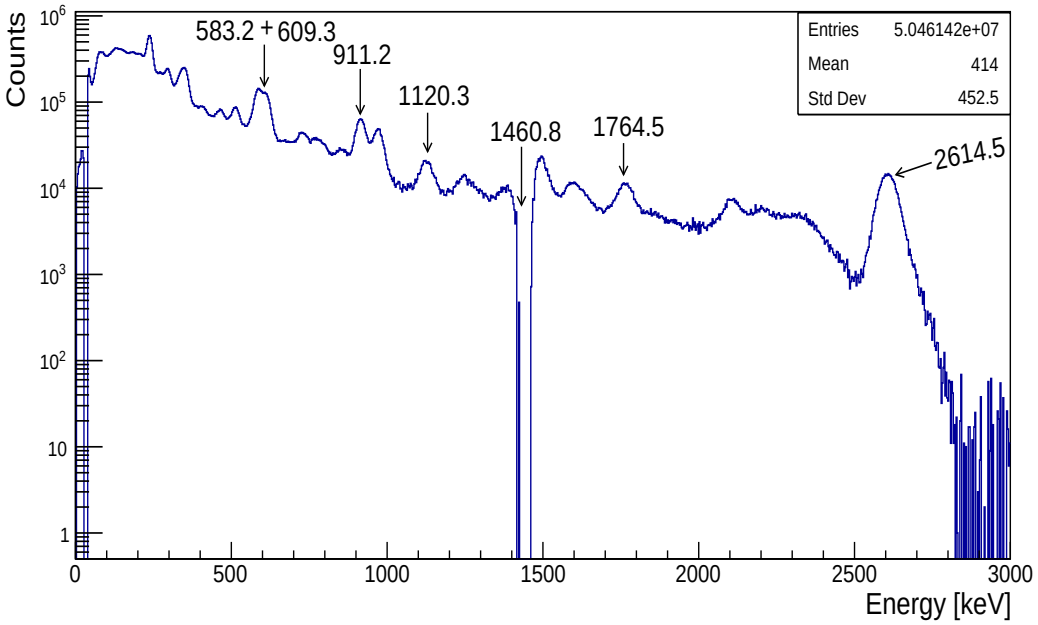

Figure 6.9: Summed total gamma-ray spectra after background subtraction for beach sand measured using four $LaBr_3$:Ce detectors without shielding (wos) in singles mode.

In coincidence mode, only gamma rays from β^- decay of ^{214}Bi and ^{208}Tl have energies and intensities suitable for gamma-gamma coincidence measurements of ^{238}U and ^{232}Th series radionuclides for the studied experimental geometries. The coincidences between gamma-ray energies 609.3 keV and 1120.3 keV from ^{214}Bi were used for the ^{238}U series radionuclides measurement, and 583.2 keV and 2614.5 keV gamma-ray energies from ^{208}Tl were used for the ^{232}Th series radionuclides [95; 96]. These gamma-ray energies were in coincidence with other gamma-ray energies (see Figs. 6.10 and 6.11) but were not considered in this work.

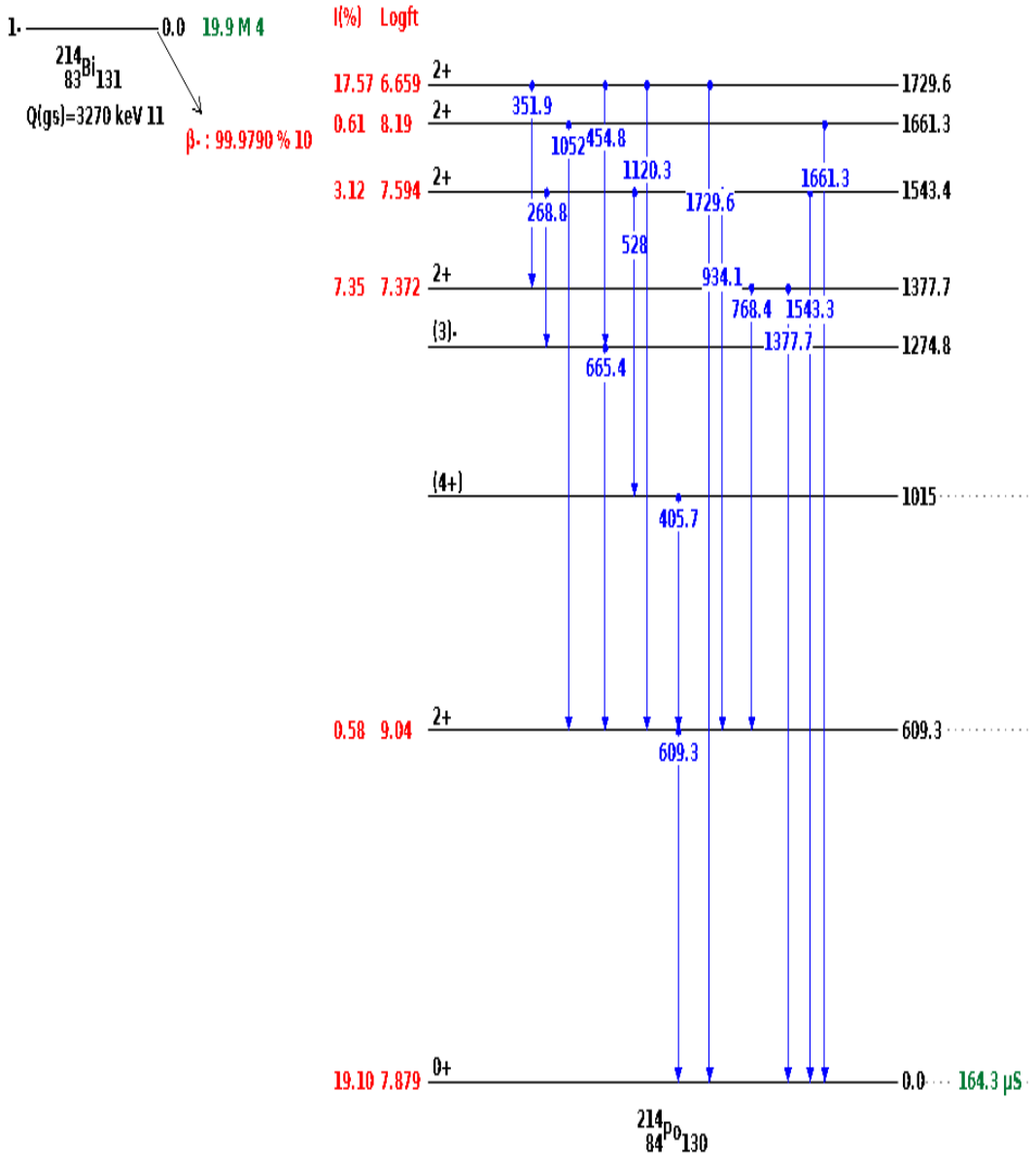

Figure 6.10: Gamma-ray decay scheme of ^{214}Po from decay of ^{214}Bi - the most intense gamma rays. Image from reference [95].

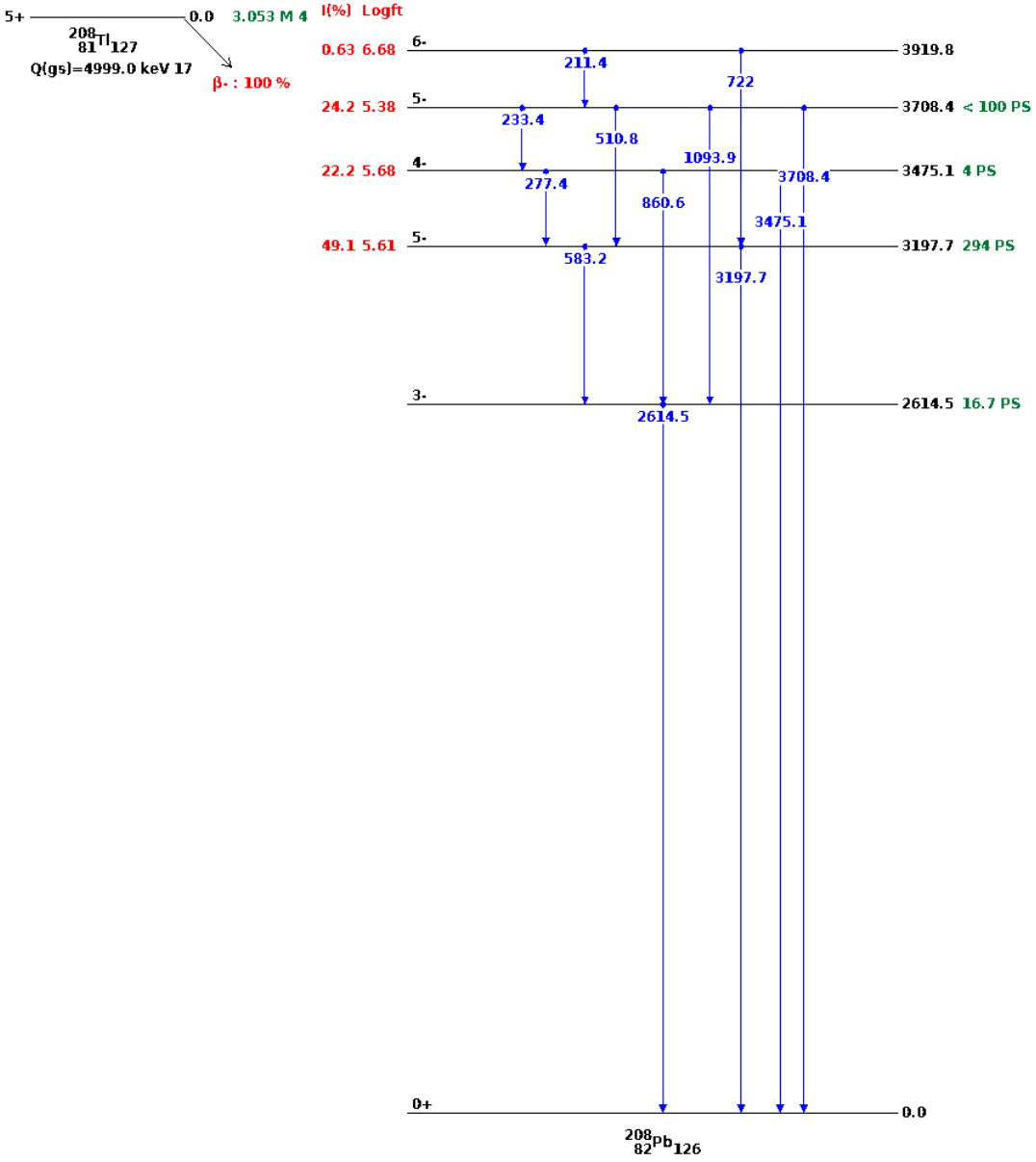

Figure 6.11: Gamma-ray decay scheme of ^{208}Pb from decay of ^{208}Tl - the most intense gamma rays. Image from reference [96].

For the ^{238}U series, the energies peak width gate (the red lines region in Fig. 6.12) were set on the data using the ProjectionX and Y functions in ROOT. As seen in Fig. 6.13, when a gate is set on 609.3 keV, the 1120.3 keV $2_5^+ \rightarrow 2_1^+$ transition is seen and the 609.3 keV $2_1^+ \rightarrow 0_1^+$ transition is absent from

the decay of ^{214}Bi to ^{214}Po. Similarly, when a gate is set on 1120.3 keV, the 609.3 keV $2_1^+ \rightarrow 0_1^+$ transition is seen and the 1120.3 keV $2_5^+ \rightarrow 2_1^+$ transition is absent from the decay of ^{214}Bi to ^{214}Po.

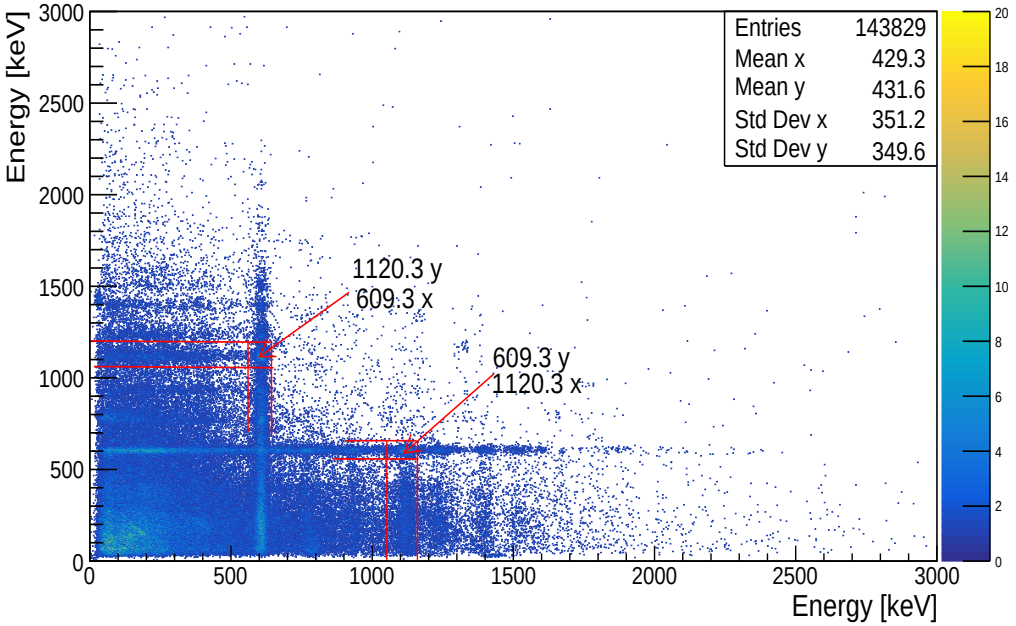

Figure 6.12: Summed total gamma-gamma spectra after background subtraction for RGU-1 generated using the time gate t_c measured using four $LaBr_3$:Ce detectors without shielding (wos). The red lines region is the energies: 609.3 keV and 1120.3 keV of ^{214}Bi peak width on the vertical (y) and horizontal (x) axes. The colour scale shows the events intensities.

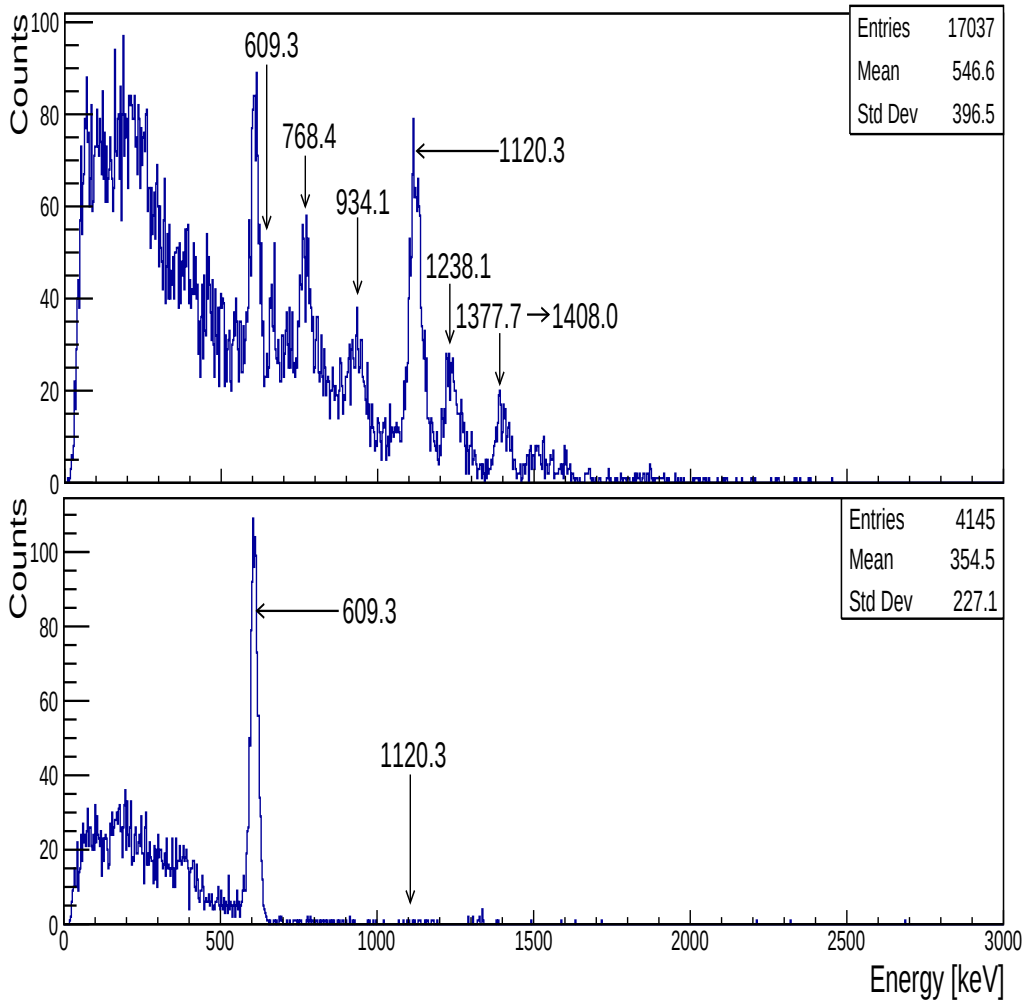

Figure 6.13: Energy gated spectra: 609.3 keV (upper) and 1120.3 keV (lower) for RGU-1 measured using four $LaBr_3$:Ce detectors without shielding (wos).

In addition, the ProjectionX and Y functions in ROOT were used to set energies peak width gate (the red lines region in Fig. 6.14) on the data for the ^{232}Th series. From the decay of ^{208}Tl to ^{208}Pb, when a gate is set on 583.2 keV, the 2614.5 keV $3^-_1 \rightarrow 0^+_1$ transition is seen and the 583.2 keV $5^-_1 \rightarrow 3^-_1$ transition is absent. Similarly, when a gate is set on 2614.5 keV, the 583.2 keV $5^-_1 \rightarrow 3^-_1$ transition is seen and the 2614.5 keV $3^-_1 \rightarrow 0^+_1$ transition is absent (see Fig. 6.15).

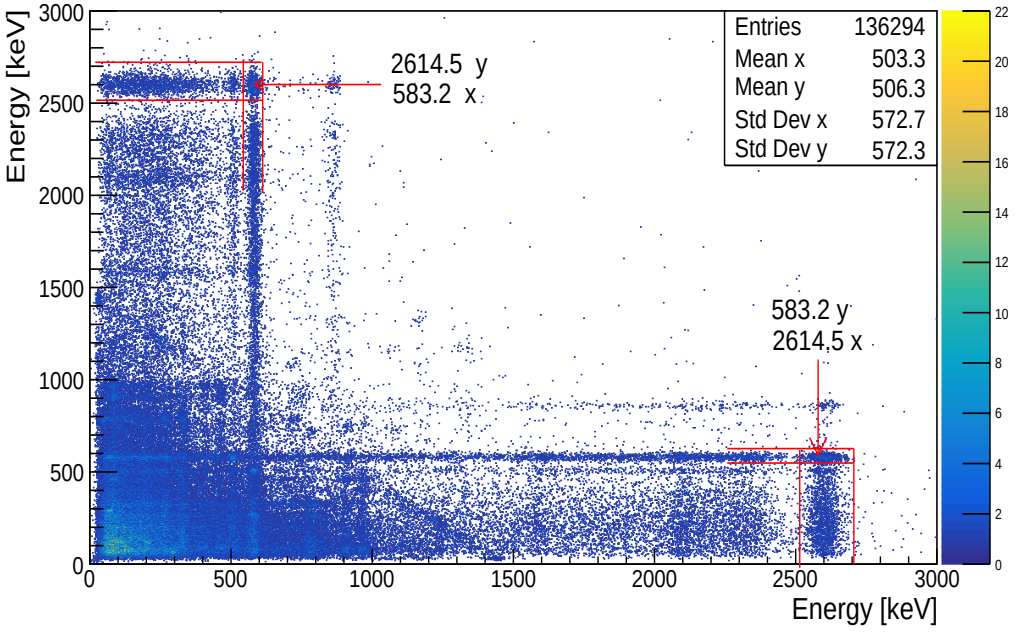

Figure 6.14: Summed total gamma-gamma spectra after background subtraction for RGTh-1 generated using the time gate t_c measured using four $LaBr_3$:Ce detectors without shielding (wos). The red lines region is the energies: 583.2 keV and 2614.5 keV of ^{208}Tl peak width on the vertical (y) and horizontal (x) axes. The colour scale shows the events intensities.

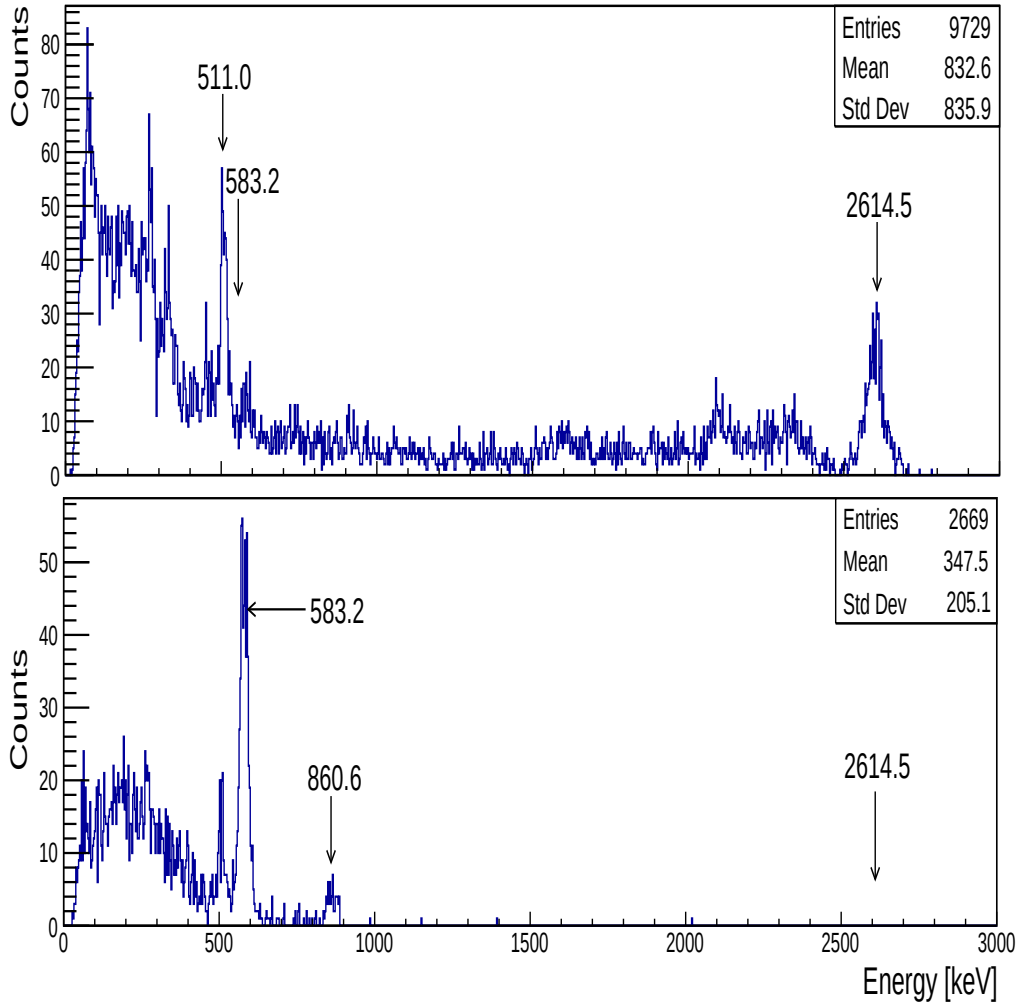

Figure 6.15: Energy gated spectra: 583.2 keV (upper) and 2614.5 keV (lower) for RGTh-1 measured using four $LaBr_3$:Ce detectors without shielding (wos).

6.5 Peak Area Determination

The peak net counts in the gamma-ray spectra were determined using the Covell method [12; 13; 15]. The counts C_{b_i} in the initial bin (b_i), C_{b_f} in the final bin (b_f), and C_g ($\sum_{b_i}^{b_f} C$) in the peak of interest region as shown in Fig. 6.16 were extracted using the integral function in ROOT [93]. The peak net counts (C_n) for the energies of interest were calculated using Eqn. 6.5.1 and

the uncertainty on C_n (σ_{C_n}) computed using Eqn. 6.5.2 [12; 13; 15]. The overlapping 583.2 keV and 609.3 keV peaks in some spectra were resolved and fitted using Radware gf3 [97] to determine their net counts (see Fig. 6.17).

$$C_n = C_g - (b_f - b_i)\left(\frac{C_{b_i} + C_{b_f}}{2}\right) \tag{6.5.1}$$

$$\sigma_{C_n} = \sigma_B + \sqrt{C_g + (b_f - b_i)^2\left(\frac{C_{b_i} + C_{b_f}}{4}\right)} \tag{6.5.2}$$

where σ_B is the uncertainty on the peak counts in the background spectrum.

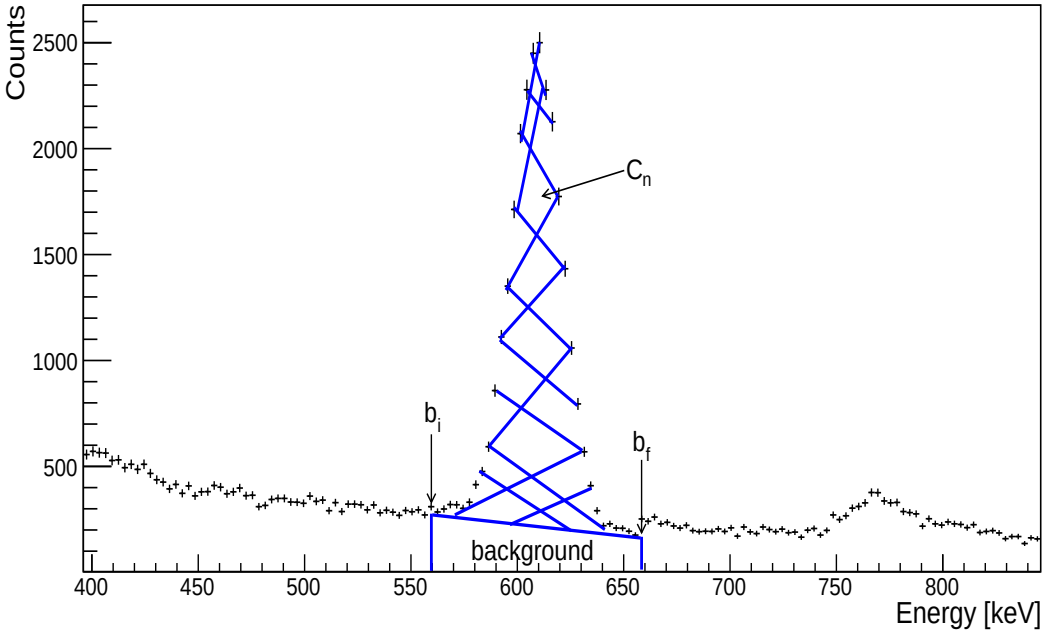

Figure 6.16: Spectra showing how peak net count (the blue lines detract from the information being given in the spectrum) was extracted and calculated using Covell method.

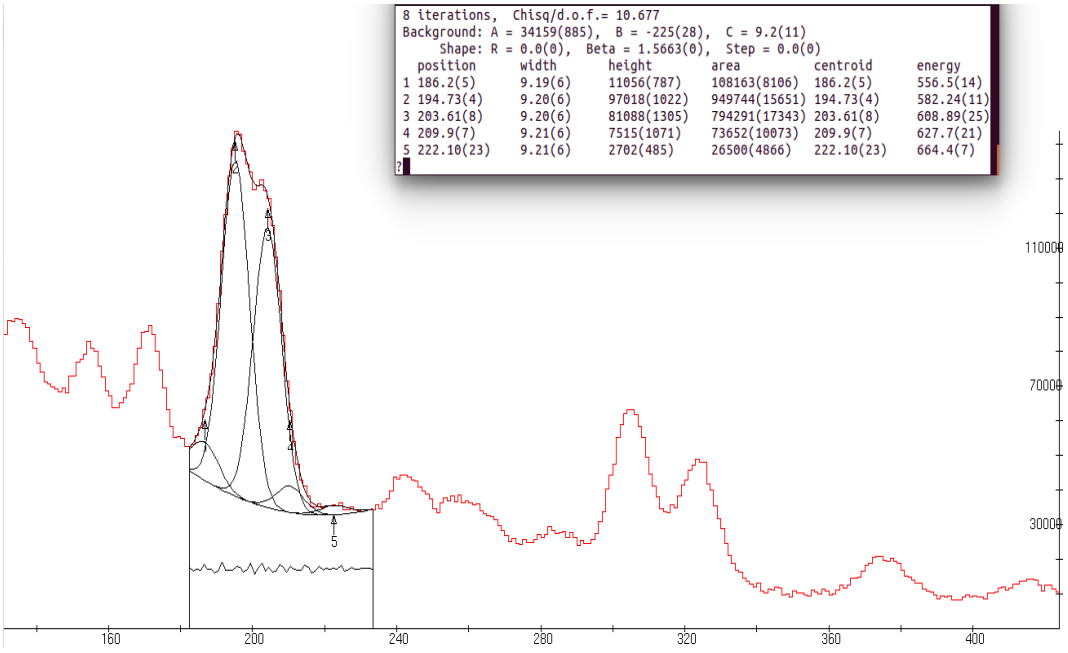

Figure 6.17: Fitting and resolving of 583.2 keV and 609.3 keV peaks in beach-sand spectrum measured using $LaBr_3$:Ce detectors without shielding (555.1 keV and 627.2 keV from ^{228}Ac and 665.4 keV from ^{214}Bi).

6.6 Absolute Full-energy Peak Efficiency Evaluation

The net counts for energy of interest were extracted from the measured and simulated standard sources spectra using the method described in section 6.5. The singles absolute full-energy peak detection efficiency at a gamma-ray energy was calculated using Eqn. 2.5.3 and the uncertainty on the detection efficiency $\sigma_{\mathcal{E}(E_\gamma)}$ estimated using Eqn. 6.6.1:

$$\sigma_{\mathcal{E}(E_\gamma)} = \mathcal{E}(E_\gamma) \times \sqrt{\left(\frac{\sigma_{C_n}}{C_n}\right)^2 + \left(\frac{\sigma_{P_\gamma}}{P_\gamma}\right)^2 + \left(\frac{\sigma_A}{A}\right)^2} \tag{6.6.1}$$

where σ_{P_γ} and σ_A are the given uncertainties on probability of emission of the specific gamma-ray energy and standard sources activity concentration. The uncertainties on the other parameters in Eqn. 2.5.3 are assumed to be

negligible.

The simulated absolute full-energy peak detection efficiency ε_γ for energies of interest were calculated using Eqn. 6.6.2 and the uncertainty $\sigma_{\varepsilon_\gamma}$ estimated using Eqn. 6.6.3.

$$\varepsilon_\gamma = \frac{N_p}{P_\gamma N} \tag{6.6.2}$$

$$\sigma_{\varepsilon_\gamma} = \varepsilon_\gamma \times \sqrt{\left(\frac{\sigma_{N_p}}{N_p}\right)^2 + \left(\frac{\sigma_{P_\gamma}}{P_\gamma}\right)^2 + \left(\frac{\sqrt{N}}{N}\right)^2} \tag{6.6.3}$$

where N_p is the net counts in the full-energy peak of E_γ and σ_{N_p} the uncertainty on it, and N is the number of decay nuclide or primary gamma ray generated.

In coincidence mode, two methods were used in calculating the gamma-ray detection efficiency: the first method used Eqn. 2.5.4 and the uncertainty estimated using Eqn. 6.6.4. This entails extracting the net counts in the energy gated gamma-ray spectra of the sources. The net counts in the 609.3 keV and 1120.3 keV peak region of Fig. 6.13 were averaged and used to calculate the coincidence detection efficiency of ^{238}U series radionuclides. In the same way, the net counts in the 583.2 keV and 2614.5 keV peak region of Fig. 6.15 were averaged and used to calculate the coincidence detection efficiency of ^{232}Th series radionuclides. Eqn. 2.5.5 was used in the second method and uncertainty computed using Eqn. 6.6.5. Here the product of the singles gamma-ray detection efficiency of the two photons measured simultaneously was taken. That is the product of singles detection efficiency at 609.3 keV and 1120.3 keV gamma-ray energies for ^{238}U, and at 583.2 and 2614.5 keV gamma-ray energies for ^{232}Th. The emission probability of the gamma-ray energies used in this

work are given in Tab. 6.1. The uncertainties on the other parameters in Eqn. 2.5.4 are assumed to be negligible.

$$\sigma_{\mathcal{E}(E_{\gamma_c})} = \mathcal{E}(E_{\gamma_c}) \times \sqrt{\left(\frac{\sigma_{C_n}}{C_n}\right)^2 + \left(\frac{\sigma_{P_{\gamma_c}}}{P_{\gamma_c}}\right)^2 + \left(\frac{\sigma_{A_c}}{A_c}\right)^2} \tag{6.6.4}$$

$$\sigma_{\mathcal{E}(E_{\gamma_c})} = \mathcal{E}(E_{\gamma_c}) \times \sqrt{\left(\frac{\sigma_{\mathcal{E}(E_{\gamma_1})}}{\mathcal{E}(E_{\gamma_1})}\right)^2 + \left(\frac{\sigma_{\mathcal{E}(E_{\gamma_2})}}{\mathcal{E}(E_{\gamma_2})}\right)^2} \tag{6.6.5}$$

Table 6.1: Gamma-ray emission probability for the energies used [98].

Series/Nuclide	Energy keV	Emission probability per decay $\times 10^{-2}$
^{40}K	1460.8	10.66 (13)
^{238}U/^{214}Bi	609.3	45.16 (33)
^{238}U/^{214}Bi	1120.3	14.78 (11)
^{238}U/^{214}Bi	1764.5	15.17 (12)
^{232}Th/^{208}Tl	583.2	30.55 (17)
^{232}Th/^{228}Ac	911.2	25.80 (103)
^{232}Th/^{208}Tl	2614.5	35.85 (7)

6.7 Energy Resolution and Attenuation Evaluation

Equally important in radiation spectroscopy is energy resolution (R) of a detector. The peaks of interest were fitted with Gaussian plus polynomial functions in ROOT [93] as shown in Fig. 6.18 to obtain the sigma (σ). Eqn. 2.5.1 was used to calculate the energy resolution.

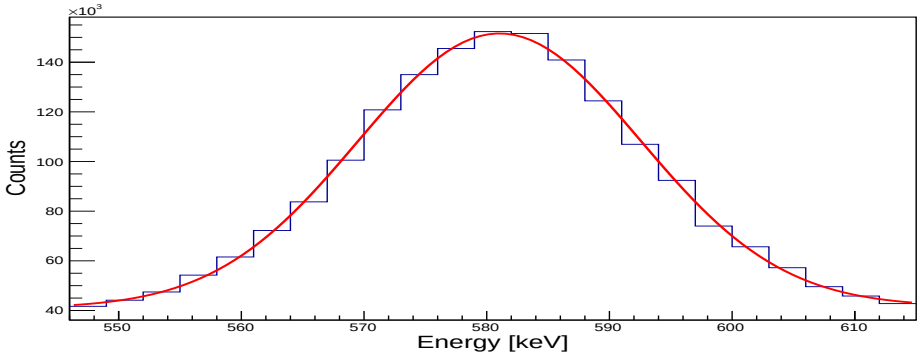


```
root [1] .x fit.c
 FCN=443.9 FROM MIGRAD    STATUS=CONVERGED      260 CALLS         261 TOTAL
                     EDM=8.43904e-10    STRATEGY= 1      ERROR MATRIX ACCURATE
  EXT PARAMETER                                   STEP         FIRST
  NO.   NAME      VALUE            ERROR          SIZE      DERIVATIVE
   1  p0           1.09963e+05   1.90125e+02   1.40612e+00  -7.73106e-08
   2  p1           5.81063e+02   2.22427e-02   2.77073e-04   2.04034e-03
   3  p2           1.14693e+01   2.86295e-02   1.31986e-04  -3.32836e-04
   4  p3           4.21307e+04   1.98135e+03   5.97822e-01  -5.48524e-08
   5  p4          -6.30354e-01   3.35998e+00   1.02531e-03  -1.81210e-05
```

Figure 6.18: The gaussian plus 1^{st} order polynomial fit (upper) and the fit parameter (lower) (where p0 is the amplitude, p1 the peak centroid energy, p2 the sigma, p3 the y-axis intercept and p4 the slope of the polynomial).

For attenuation evaluation, the net peak counts in the peak of interest were extracted from the measured and simulated gamma-ray spectra without shielding I_0 and with water shield I_f. These counts were used in Eqn. 6.7.1 to calculate the attenuation (%).

$$attenuation(\%) = \left(\frac{I_0 - I_f}{I_0}\right) \times 100 \tag{6.7.1}$$

6.8 Peak-to-Total Ratio and MDA Evaluation

The net counts of 1173.2 keV (1113 - 1257 keV) and 1332.5 keV (1263 - 1397 keV) peaks of ^{60}Co in Fig. 6.19 were extracted and summed. The total counts in the spectrum (0 - 3000 keV) was also extracted using the integral function in ROOT [93]. The summed total peaks net counts were divided by the total spectrum counts to obtain the peak-to-total area ratio (Eqn. 2.5.9).

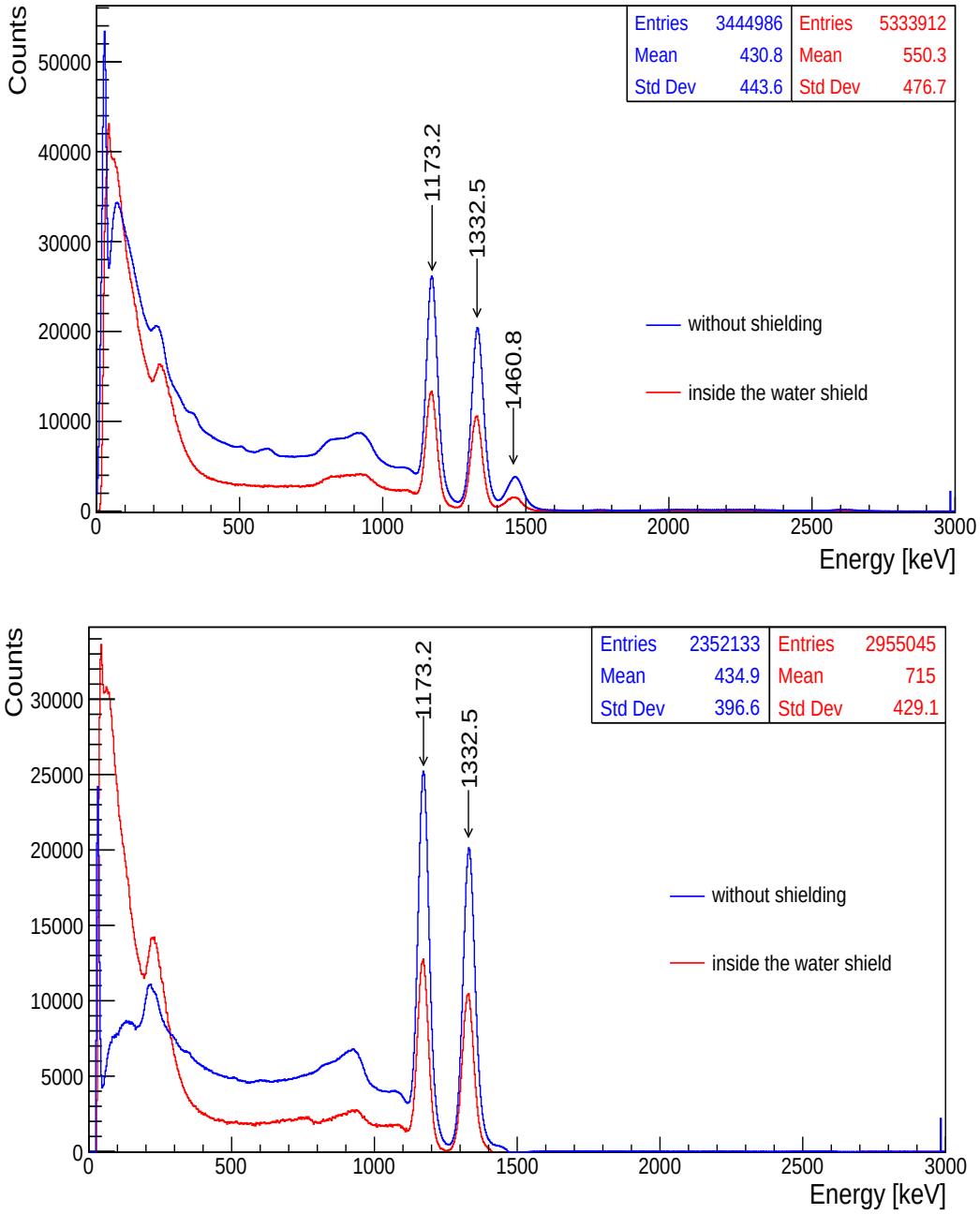

Figure 6.19: Summed total spectra for ^{60}Co before (upper) and after (lower) background subtraction measured for 3600 seconds using two $LaBr_3$:Ce detectors with the water shield and without shielding.

Furthermore, the MDA in singles mode and when two gamma-ray energies are measured in coincidence were calculated. In singles mode, the C_g $(\sum_{b_i}^{b_f} C)$

in the peak of interest region were extracted from the singles background spectrum in Fig. 6.8 and normalized to the counting time of IAEA-375 soil. The uncertainty associated with the peak counts was used in Eqn. 2.5.10 to calculate the MDA.

In coincidence mode, the C_g ($\sum_{b_i}^{b_f} C$) in the peak of interest region were extracted from the energy gated background gamma-ray spectra in Figs. 6.20 and 6.21 and normalised to the IAEA-375 soil counting time. The background counts were less than 25 counts and approximation to Gaussian distribution becomes invalid. The detection limit (L_D) values were taken from Gilmore [12] for the Poisson distribution (for 95 % confidence interval) associated with the background count rate.

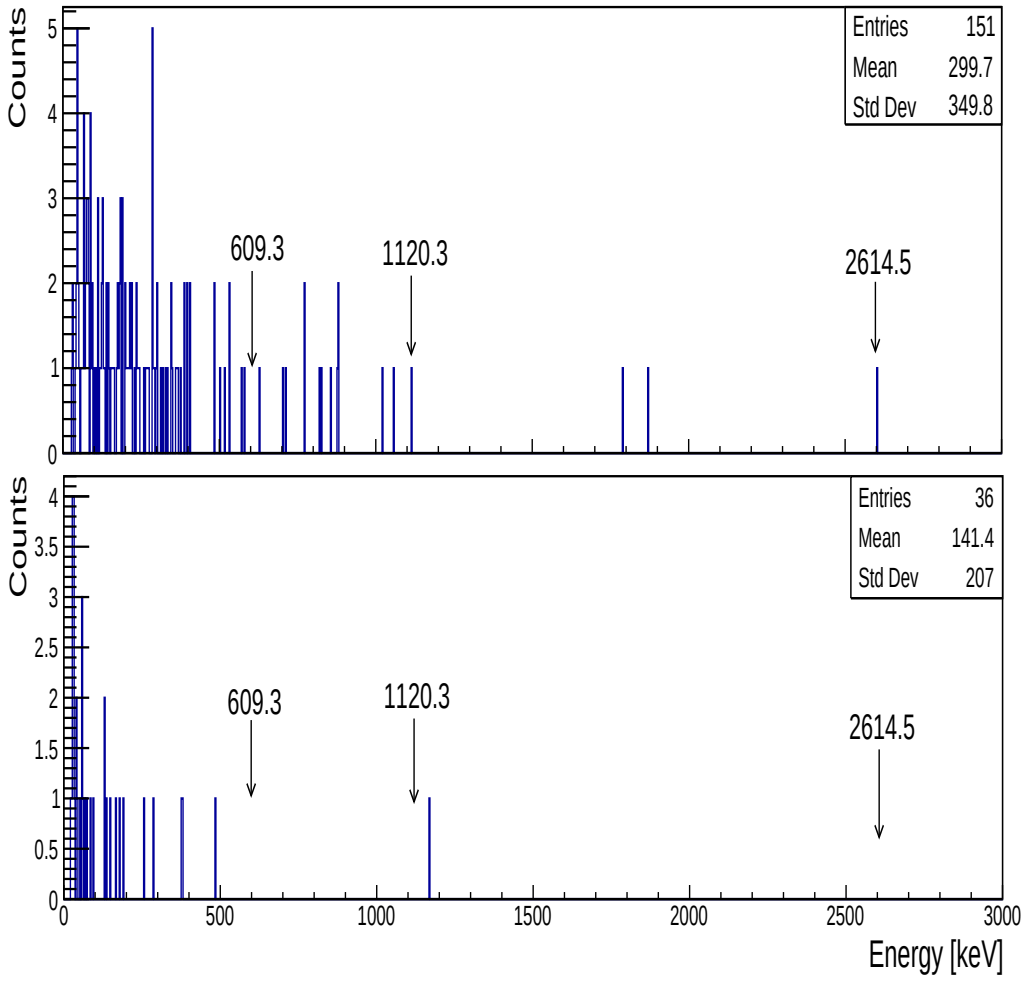

Figure 6.20: Energy gated spectra: 609.3 keV (upper) and 1120.3 keV (lower) for the background measured for 57594 seconds using four $LaBr_3$:Ce detectors without shielding.

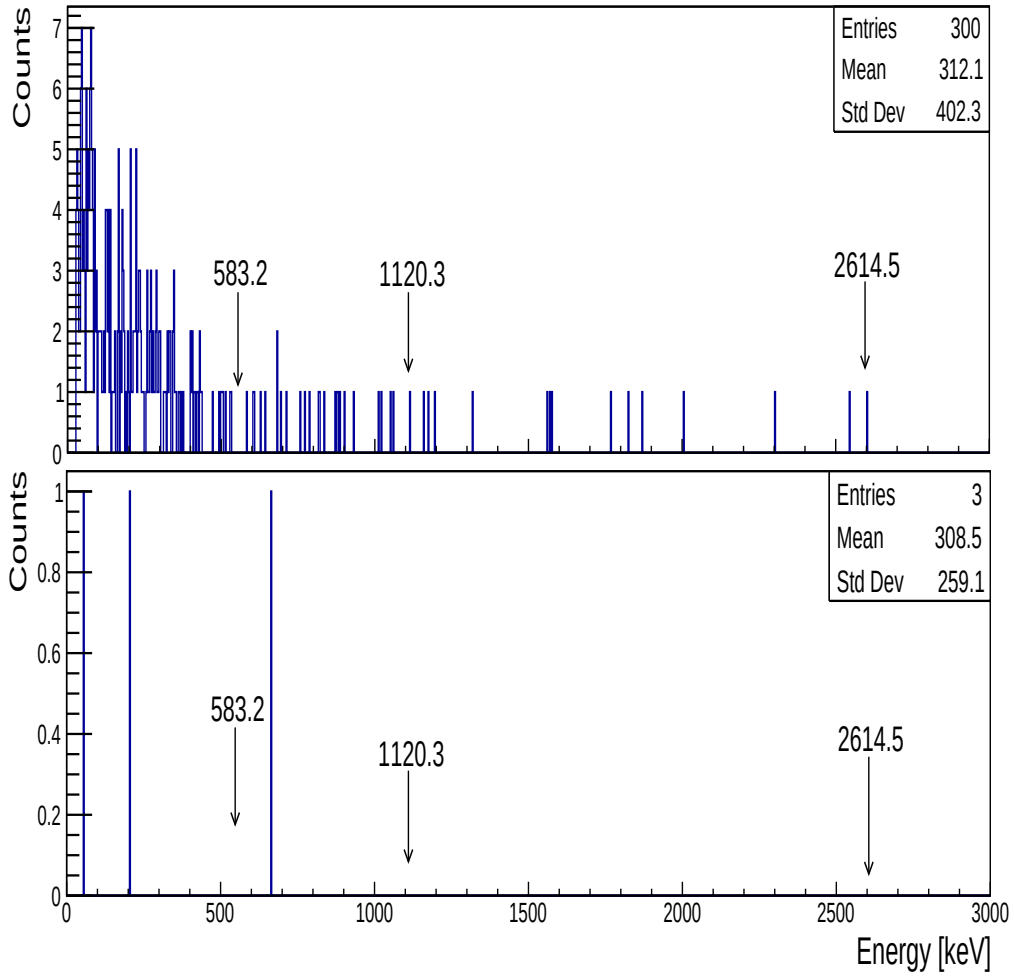

Figure 6.21: Energy gated spectra: 583.2 keV (upper) and 2614.5 keV (lower) for the background measured for 57594 seconds using four $LaBr_3$:Ce detectors without shielding.

6.9 Activity Concentration and Self-absorption Correction Factor Evaluation

The activity concentration of ^{40}K, ^{238}U, ^{232}Th in IAEA-375 soil and beach sand were calculated in singles and coincidence modes. In singles mode, the net counts in the peaks of interest were extracted from the IAEA-375 soil and

beach-sand spectra (see Appendix B.3) and used in using Eqn. 2.5.6 to calculate the activity concentration. The uncertainty on the activity concentration σ_A was estimated using Eqn. 6.9.1. The uncertainties on the other parameters in Eqn. 2.5.6 are assumed to be negligible.

$$\sigma_A = A \times \sqrt{\left(\frac{\sigma_{C_n}}{C_n}\right)^2 + \left(\frac{\sigma_{P_\gamma}}{P_\gamma}\right)^2 + \left(\frac{\sigma_{\mathcal{E}}(E_\gamma)}{\mathcal{E}(E_\gamma)}\right)^2} \tag{6.9.1}$$

In coincidence mode the energy-gated gamma-ray spectra of IAEA-375 soil and beach sand were used. The net counts in the 609.3 keV and 1120.3 keV peaks region were extracted and averaged. The average counts were used in Eqn. 2.5.7 to calculate the activity concentration of ^{238}U in the samples. Similarly, the net counts in 583.2 keV and 2614.5 keV peak region were extracted and averaged. The average counts were used to calculate the activity concentration of ^{232}Th in the samples. The uncertainty on the activity concentration σ_{A_c} was estimated using Eqn. 6.9.2. The uncertainties on the other parameters in Eqn. 2.5.7 are assumed to be negligible.

$$\sigma_{A_c} = A_c \times \sqrt{\left(\frac{\sigma_{N_c}}{N_c}\right)^2 + \left(\frac{\sigma_{P_{\gamma c}}}{P_{\gamma_c}}\right)^2 + \left(\frac{\sigma_{\mathcal{E}(E_{\gamma c})}}{\mathcal{E}(E_{\gamma_c})}\right)^2} \tag{6.9.2}$$

The self-absorption correction factor (C_d) is needed to obtain the absolute activity concentration of radionuclide in the sample due to standard sources and sample difference in density. The net counts in the peak of interest were extracted from the simulated standard sources and sample spectra (see Fig. 6.22 $\rightarrow$ 6.24). The counts were used in Eqn. 2.5.8 to calculate the C_d values given in Tab. 6.2.

The activity concentration calculated in singles and coincidence modes above were multiplied by the self-absorption factors (C_d) in Tab. 6.2 for each energy

and sample to obtain the absolute activity concentration of radionuclides in IAEA-375 soil and beach sand. It is important to note that, for the activity concentration in coincidence mode only the C_d value for 583.2 keV and 609.3 keV was used for ^{232}Th and ^{238}U, respectively.

Table 6.2: Self-absorption correction factor (C_d) for IAEA-375 soil and beach sand.

Energy (keV)	Density Sources	Density IAEA-375	Density Beach sand	C_d IAEA-375	C_d Beach sand
583.2	1.36494	1.50263	2.65830	1.06	1.36
609.3	1.40912	1.50263	2.65830	1.06	1.33
911.2	1.36494	1.50263	2.65830	1.05	1.23
1120.3	1.40912	1.50263	2.65830	1.00	1.21
1460.8	1.29080	1.50263	2.65830	1.03	1.26
1764.5	1.40912	1.50263	2.65830	1.00	1.20
2614.5	1.36494	1.50263	2.65830	1.01	1.20

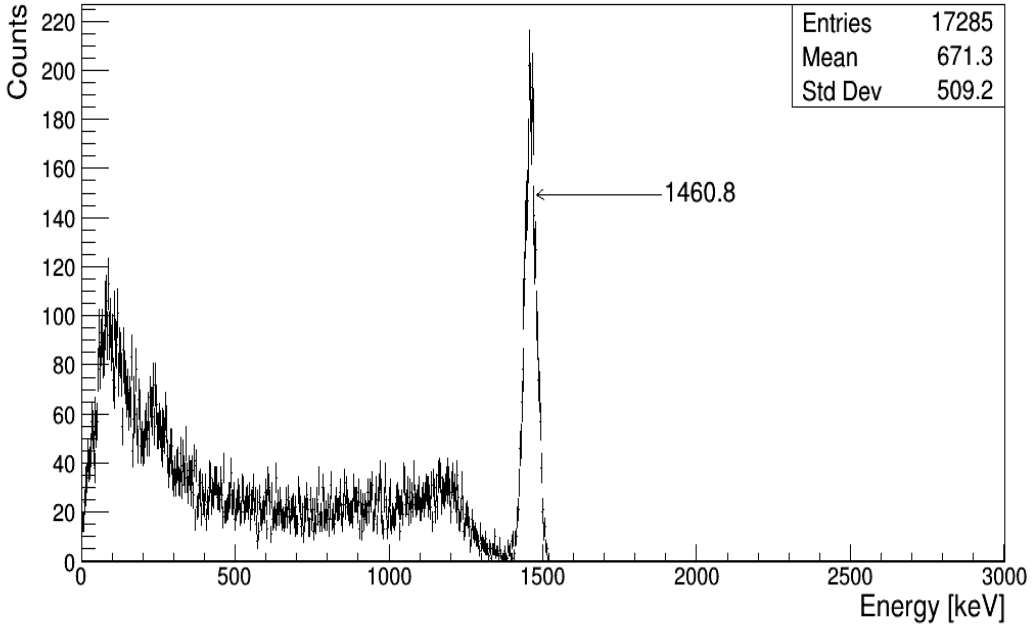

Figure 6.22: The simulated spectra of standard source (^{40}K) with composition of KCl and density of 1.29 g cm^3.

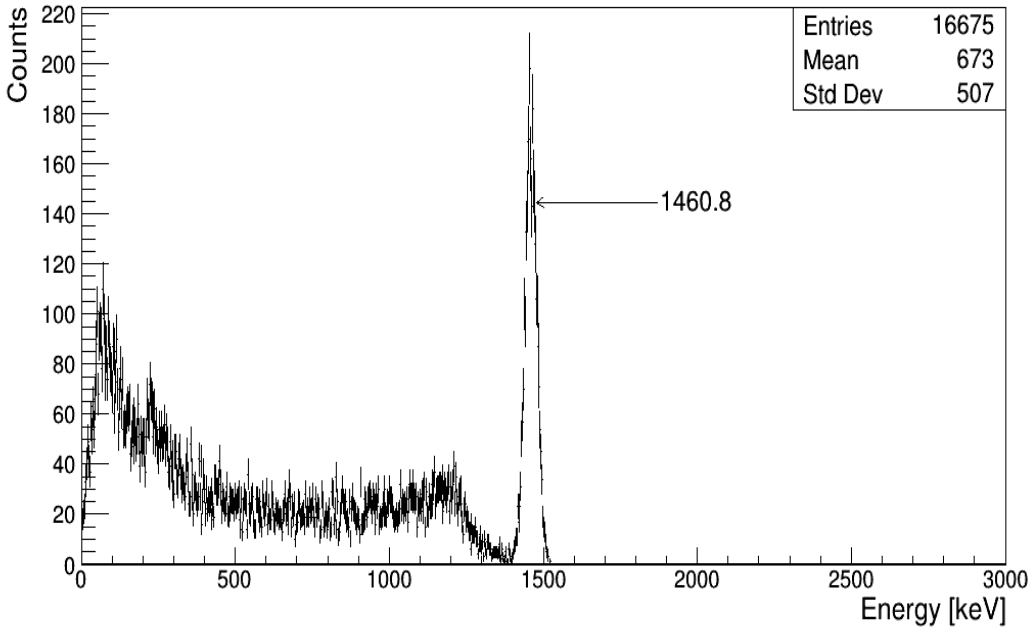

Figure 6.23: The simulated spectra of IAEA-375 soil (^{40}K) with composition of SiO_2 and density of 1.50 g cm^3.

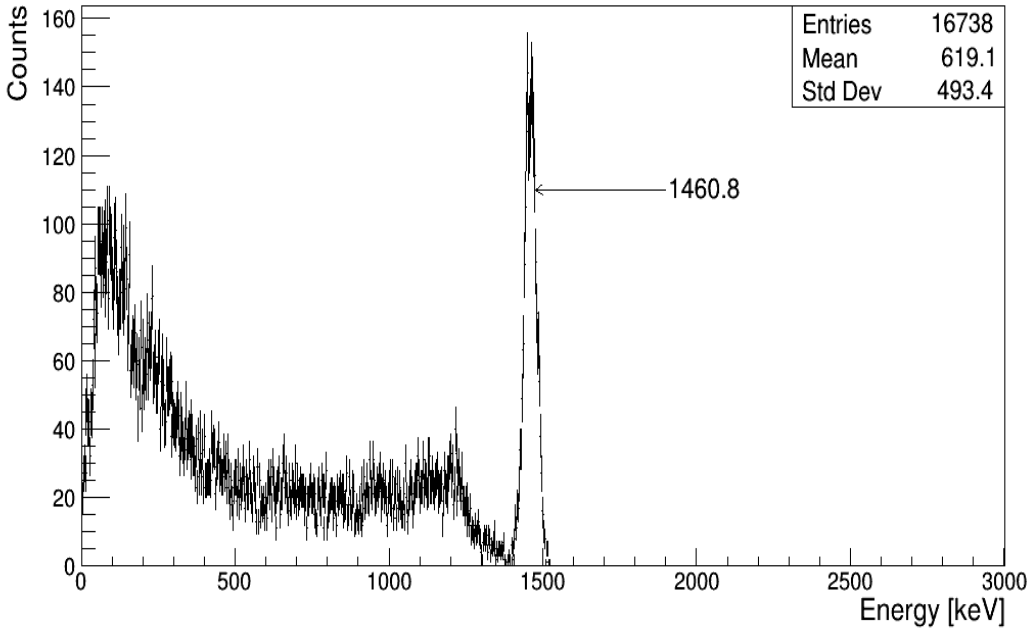

Figure 6.24: The simulated spectra of beach sand (^{40}K) with composition of SiO_2 and density of 2.66 g cm^3.

Chapter 7

Results and Discussion

All the result uncertainties are quoted at 1σ level and formulated as combined standard uncertainties according to the BIPM Guide to the Expression of Uncertainty in Measurement (GUM) [99]. The results from this work were published in Proceedings of SAIP 2017 and Applied Radiation and Isotopes (see Appendix C).

7.1 Energy Resolution

A superior detector energy resolution means being able to differentiate two gamma rays of close energies i.e. the difference between the gamma-ray peaks centroid of close energies should be greater than or equals to the sum of their peak FWHM [12; 15; 58]. Energy resolution becomes important if there are several closely spaced gamma-ray full-energy peaks in the spectrum [15], which is the case here. The energy resolution of a detector depends on the energy of the radiation, size and inherent quality of a detector [15].

The FWHM increases with increased gamma-ray energy (Tab. 7.1) i.e. the peak width increases with increase in gamma-ray energy. The detectors energy

resolution as a percentage improve with increasing gamma-ray energy i.e. the energy resolution (R) values decrease with increasing gamma-ray energy (see Tab. 7.1). $LaBr_3$:Ce detector was able to resolve most of the peaks of interest except for the gamma-ray peaks centred at 583.2 keV and 609.3 keV (see Fig. 6.9). This is because the difference between the two energies is less than the sum of their FWHM as seen in Tab. 7.1, though these peaks could be resolved using Radware gf3 [97] (see section 6.5). Furthermore, the energy resolution of $LaBr_3$:Ce detector; L1 to L4 measured by the manufacturer at 661.7 keV peak of ^{137}Cs are 3.8 %, 3.9 %, 3.8 % and 3.8 %, respectively [100]. There is a negligible difference between energy resolution of the four $LaBr_3$:Ce detectors measured by this work at 661.7 keV peak of ^{137}Cs (4.1 %) and the manufacturer (an average of 3.8 %). This difference could be due to the difference in measurement conditions like electronic noise and statistical uncertainty, explained in chapter 2, which affect detector's energy resolution. Moreover, comparing the energy resolution of $LaBr_3$:Ce detector to those of HPGe and NaI:Tl detectors, the energy resolution of a HPGe detector is lower than that of $LaBr_3$:Ce detector by an order of magnitude (see Fig. 7.1) due to the HPGe crystal small band gap energy which means less energy required to generate electron-hole pairs (information carriers) [15]. The $LaBr_3$:Ce detector energy resolution is lower by a factor of two than that of a NaI:Tl detector. However, the crystal size of NaI:Tl detector is bigger than that of $LaBr_3$:Ce detector and detectors with smaller crystal size have better energy resolution. Ciupek *et al.* [31] reported that the energy resolution value of 1.5" × 1.5" $LaBr_3$:Ce detector is better by a factor of 2.3 than that of NaI:Tl detector of the same size. Similarly, Fig. 7.2 shows that difference between the measured FWHM and the simulated FWHM is 0.01 for the energies of interest.

Table 7.1: FWHM (keV) and energy resolution (%) of $LaBr_3$:Ce, NaI:Tl and HPGe detectors.

Energy (keV)	$LaBr_3$:Ce FWHM (keV)	R (%)	NaI:Tl FWHM (keV)	R (%)	HPGe FWHM (keV)	R (%)
583.2	27.0	4.63	51.0	8.75	4.0	0.72
609.3	27.0	4.43	51.0	8.37	4.0	0.67
911.2	33.0	3.62	63.7	6.99	4.0	0.48
1120.3	38.0	3.39	74.0	6.61	4.0	0.37
1460.8	45.0	3.08	94.0	6.44	5.0	0.29
1764.5	51.0	2.89	106.0	6.01	5.0	0.25
2614.5	66.0	2.52	118.0	4.51	5.0	0.18

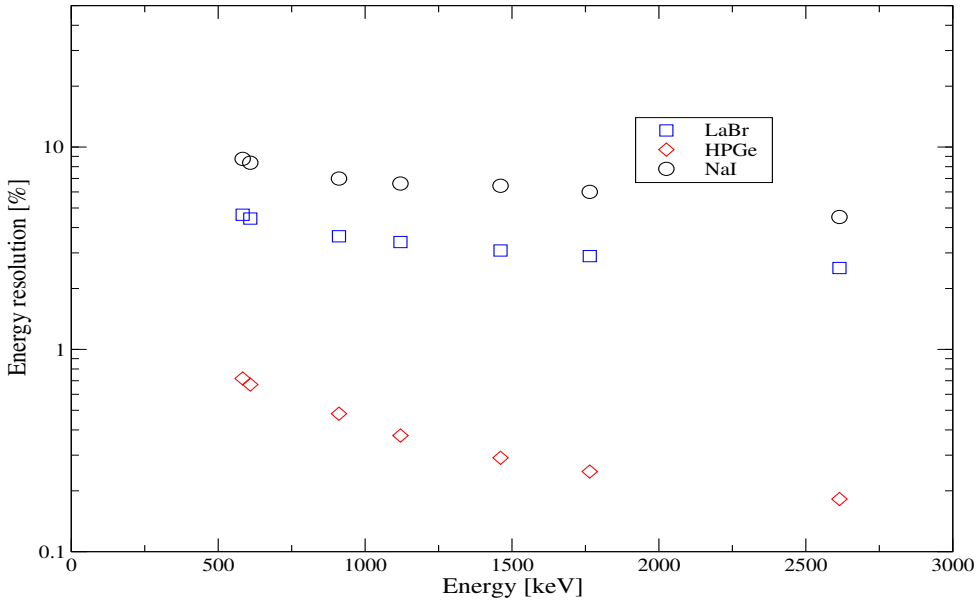

Figure 7.1: Energy resolution of 2" × 2" $LaBr_3$:Ce, 3" × 3" NaI:Tl and 2.5" × 2.4" HPGe detectors.

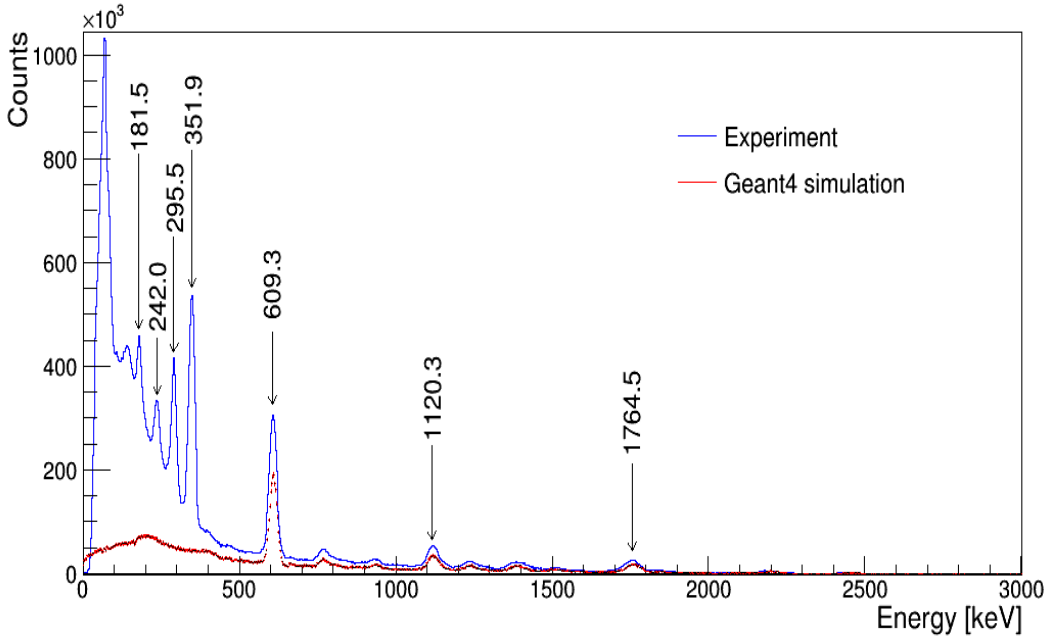

Figure 7.2: Gamma-ray spectra of uranium ore after background spectrum subtraction measured (blue) and simulated ^{214}Bi source which only β^- decayed to ^{214}Po (red) using four $LaBr_3$:Ce detectors without shielding.

7.2 Detection Efficiency

The absolute full-energy peak detection efficiency depends on the energy and the source-detector geometry [12; 13]. The absolute full-energy peak detection efficiencies measured in singles and coincidence mode for the different measurement series are given in Tab. 7.2. As observed from this table, the efficiency decreases with increase in energy except for the 911.2 keV gamma-line for the $LaBr_3$:Ce detectors geometry. This could be due to high TCS at this gamma-ray energy. In singles mode, the four $LaBr_3$:Ce detector geometry detection efficiency is a factor of two higher than the two $LaBr_3$:Ce detector geometry, though the source-to-detector distance is the same, the number of detectors used for the former is twice the latter. The detection efficiency of the two $LaBr_3$:Ce detector geometry measured without shielding and inside the water

shield is the same within the measurement uncertainties. This is expected since the number of detectors and source-to-detector distance are the same. The detection efficiency in singles mode measured and simulated using four $LaBr_3$:Ce detector geometry are comparable to within measurement uncertainty see Fig. 7.3. The uncertainties associated with the simulated detection efficiencies are higher than those associated with the measured detection efficiencies due to low statistics. As seen in Tab 7.2, the detection efficiencies measured in singles mode using $LaBr_3$:Ce, NaI:Tl and HPGe detectors vary. This is because of the difference in the measurement geometry and bandgap of the detector material [12; 13].

Furthermore, two methods were used to evaluate the detection efficiency in coincidence mode. As seen in Tab. 7.2, the results of the two methods used to evaluate the detection efficiency in coincidence mode agreed to within 1σ to 2σ level. This is because the true coincidence summing (TCS) for the $LaBr_3$:Ce detector geometry estimated using Eqn. 2.5.2 is insignificant (0.6 % solid angle and 0.006 % chance of summing for this distance).

Moreover, the detection efficiencies in singles mode are more than two orders of magnitude higher than in coincidence mode (see Figs. 7.4 and 7.5). This is because the coincidence detection efficiency is the probability of measuring two gamma rays simultaneously i.e. the product of singles detection efficiencies of two cascade gamma rays detected at the same time. Antovic and Svrkota [19, 20]; Paradis *et al.* [23]; Tillet *et al.* [25] also reported low detection efficiency in coincidence mode of counting compared to singles mode. Equally important is the simulated absolute full-energy peak detection efficiency of gamma-lines associated with ^{138}La decay using the NaI:Tl detector (see Fig. 7.6). The absolute full-energy peak detection efficiency of gamma-lines associated with

^{138}La decay are $(4.90 \pm 0.47) \times 10^{-3}$ and $(3.65 \pm 0.17) \times 10^{-3}$ at 788.7 keV and 1435.8 - 1470.0 keV gamma-ray energies, respectively.

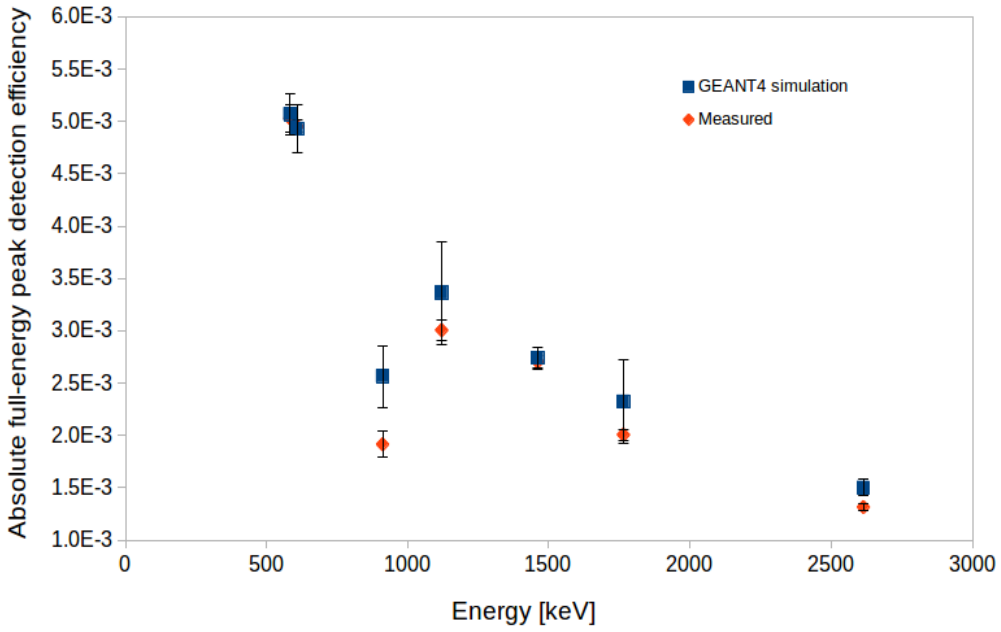

Figure 7.3: Absolute full-energy peak detection efficiencies measured and simulated using four $LaBr_3$:Ce detectors without shielding in singles mode.

Table 7.2: Absolute full-energy peak detection efficiency measured in singles (S) and coincidence (C) modes (d is the distance from the front face of the detector to the centre of Marinelli beaker).

Series/ Nuclide	Energy (keV) Geometry d (mm) Shielding	Mode	4 $LaBr_3$:Ce 165 No	2 $LaBr_3$:Ce 165 No	detection 2 $LaBr_3$:Ce 165 H_2O	efficiency 1 NaI:Tl 90 H_2O	1 HPGe on top of the detector (Pb+Cu)
		S $\times 10^{-3}$					
$^{232}Th/^{208}Tl$	583.2		5.03 ± 0.13	2.76 ± 0.60	2.81 ± 0.06	2.49 ± 0.06	7.87 ± 0.16
$^{238}U/^{214}Bi$	609.3		4.95 ± 0.06	2.72 ± 0.26	2.59 ± 0.03	3.30 ± 0.03	8.56 ± 0.08
$^{232}Th/^{228}Ac$	911.2		1.91 ± 0.12	1.64 ± 0.75	1.64 ± 0.07	3.03 ± 0.14	7.30 ± 0.33
$^{238}U/^{214}Bi$	1120.3		3.01 ± 0.10	1.77 ± 0.24	1.85 ± 0.03	1.78 ± 0.04	5.07 ± 0.05
^{40}K	1460.8		2.70 ± 0.06	1.67 ± 0.23	1.47 ± 0.02	2.09 ± 0.03	4.89 ± 00.7
$^{238}U/^{214}Bi$	1764.5		2.01 ± 0.05	1.35 ± 0.27	1.11 ± 0.02	2.12 ± 0.03	4.52 ± 0.04
$^{232}Th/^{208}Tl$	2614.5		1.32 ± 0.04	0.85 ± 0.17	0.85 ± 0.02	1.04 ± 0.02	2.77 ± 0.06
		C $\times 10^{-6}$					
$^{232}Th/^{208}Tl$	583.2/2614.5[a]		7.65 ± 0.52	2.48 ± 0.69	2.26 ± 0.66		
	583.2/2614.5[b]		6.62 ± 0.26	2.33 ± 0.07	2.38 ± 0.07		
$^{238}U/^{214}Bi$	609.3/1120.3[a]		15.35 ± 0.74	5.85 ± 1.08	5.58 ± 1.06		
	609.3/1120.3[b]		14.89 ± 0.54	4.82 ±0.08	4.79 ± 0.09		

[a] Calculated using Eqn. 2.5.4.
[b] Calculated using Eqn. 2.5.5.

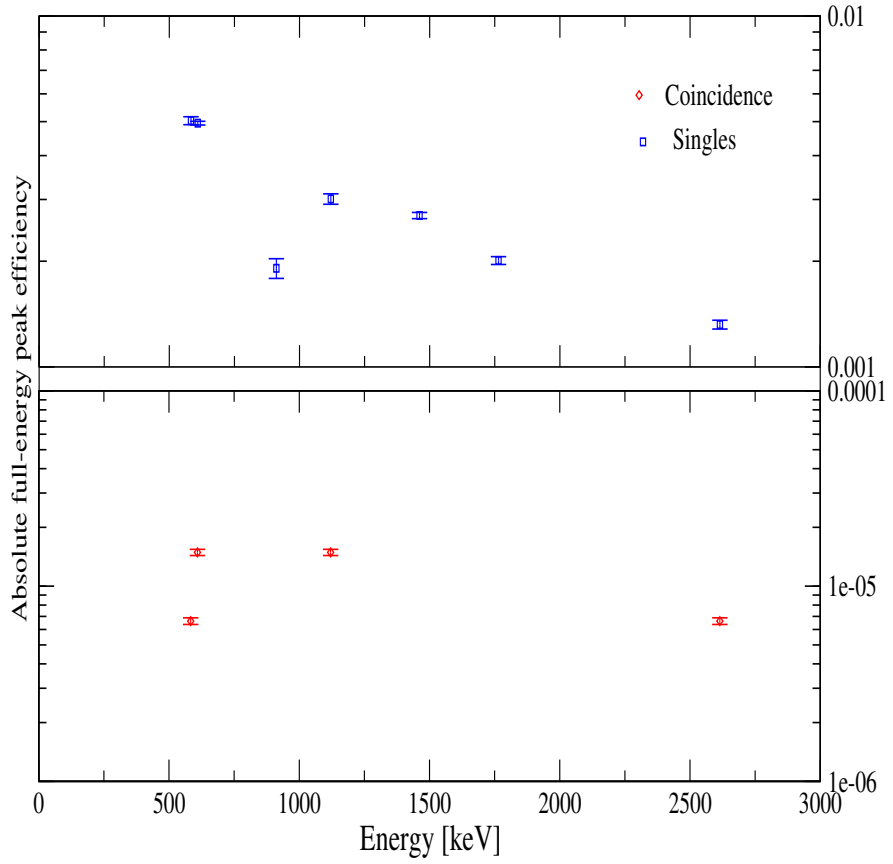

Figure 7.4: Absolute full-energy peak detection efficiencies measured using four $LaBr_3$:Ce detectors without shielding in singles and coincidence modes.

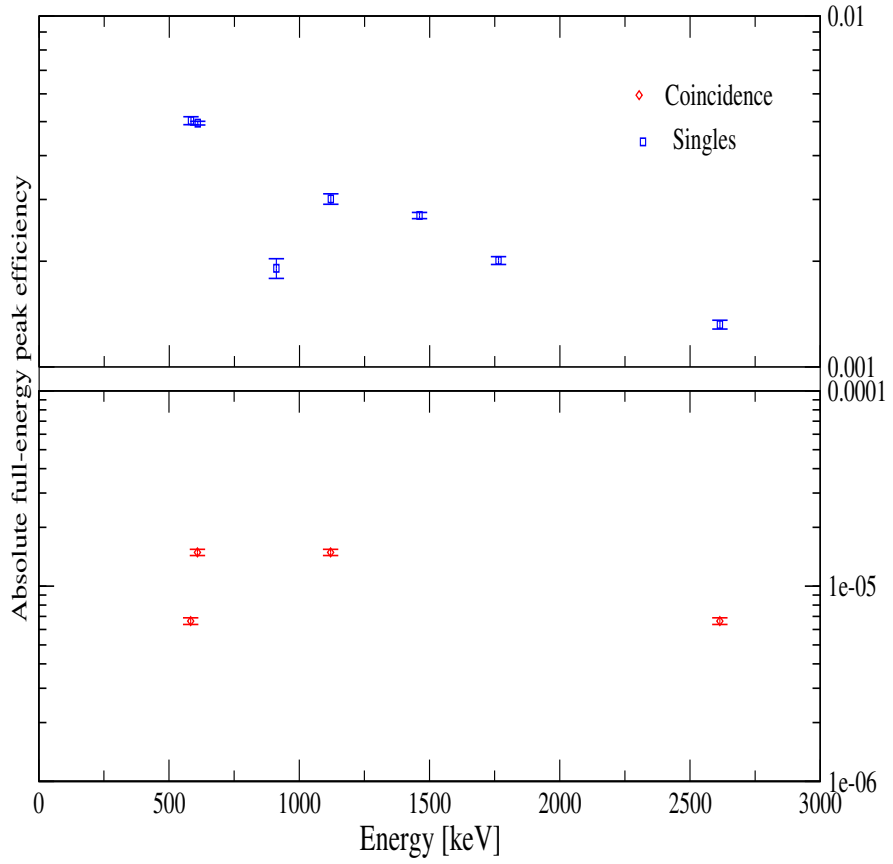

Figure 7.5: Absolute full-energy peak detection efficiencies measured using two $LaBr_3$:Ce detectors inside the water shield in singles and coincidence modes.

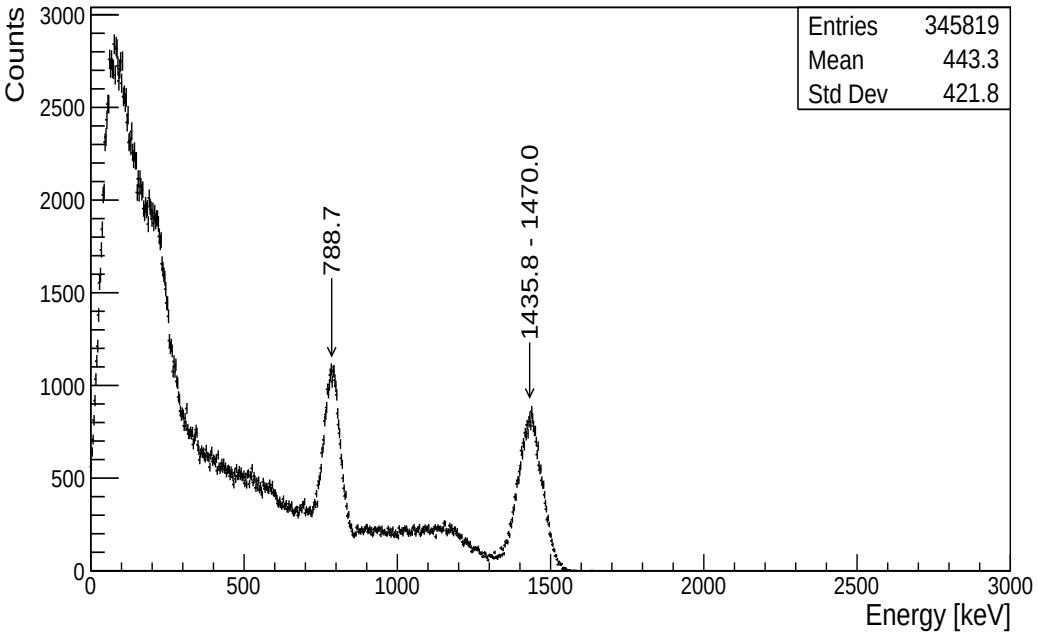

Figure 7.6: The simulated spectra of gamma rays emitted by ^{138}La source placed in the $LaBr_3$:Ce detector crystal collected by NaI:Tl detector (The NaI:Tl detector was placed 2.5 cm from the $LaBr_3$:Ce detector's face).

7.3 Gamma-ray Attenuation with Water: GEANT4 Simulations and Experimental Measurements

Background gamma rays reaching the detector without shielding (I_0) may include gamma rays which undergo scattering with the surrounding material. As shown in Fig. 7.7 $\rightarrow$ 7.11, the simulated background gamma rays without shielding have fewer scattered gamma rays reaching the detector than the measured. Besides, the measurement environment unlike that of the simulated have surrounding materials (see Appendix B) in which the gamma rays can interact with and possibly scatter back into the detector. The background gamma rays interacting with the shield material (water) are broad beam in

nature. The gamma rays that interact with the water without being absorbed (I_f) plus fraction of the scattered gamma rays will reach the detector. Compton scattered high-energy gamma rays partially absorbed by the water shield results in more continuum at low energy (see Fig. 5.12. Fig. 7.7 $\rightarrow$ 7.11 shows that the background gamma-ray counts in both measured and simulated spectra without shielding (blue) is higher than that inside the water shield (red). The difference between the blue and red spectra gives the number of background gamma rays which have been attenuated by the water shield. As observed in Figs. 7.7 and 7.8, the peaks at 1460.8 keV and 2614.5 keV gamma-ray energies appears that there is not much attenuation. This is due to alpha particles, beta particles and gamma rays from ^{227}Ac and ^{138}La present in the $LaBr_3$:Ce detector crystal constantly emitted. This appears in 32.2 keV, 788.7 keV, 1435.8 keV and 1800 - 2700 keV peak region in the measured background spectra. The ^{227}Ac was not simulated which makes only 32.2 keV, 788.7 keV and 1435.8 keV peaks to be present in the simulated background spectra. But when GEANT4 simulations were performed without the internal activity of the $LaBr_3$:Ce detector, the attenuation of 1460.8 keV and 2614.5 keV gamma rays were obvious (Fig. 7.9).

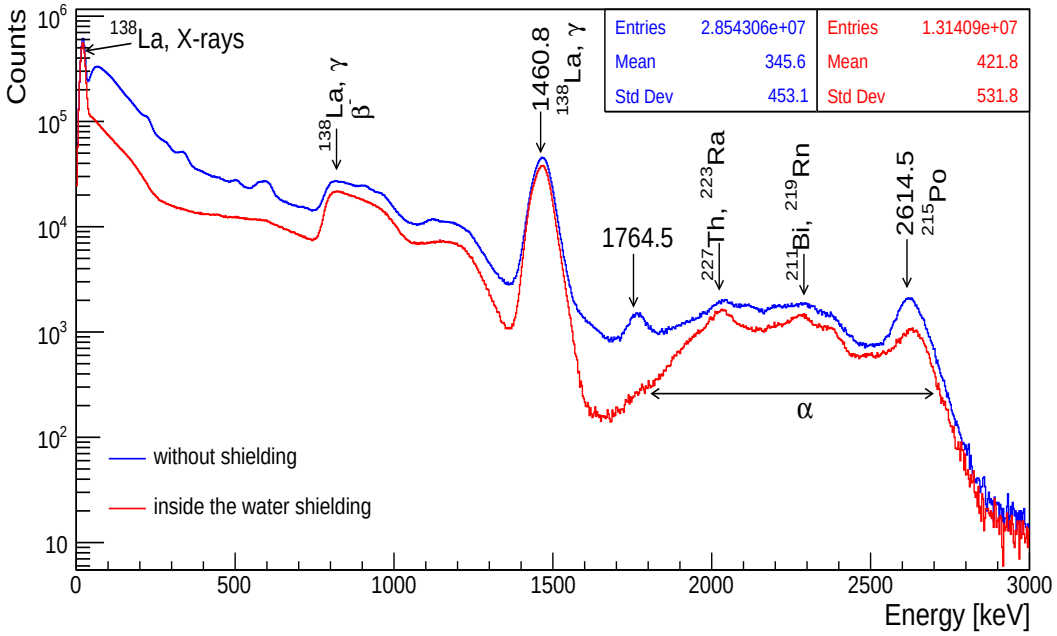

Figure 7.7: Background spectra measured using two $LaBr_3$:Ce detectors outside (on a table) and inside the water shield.

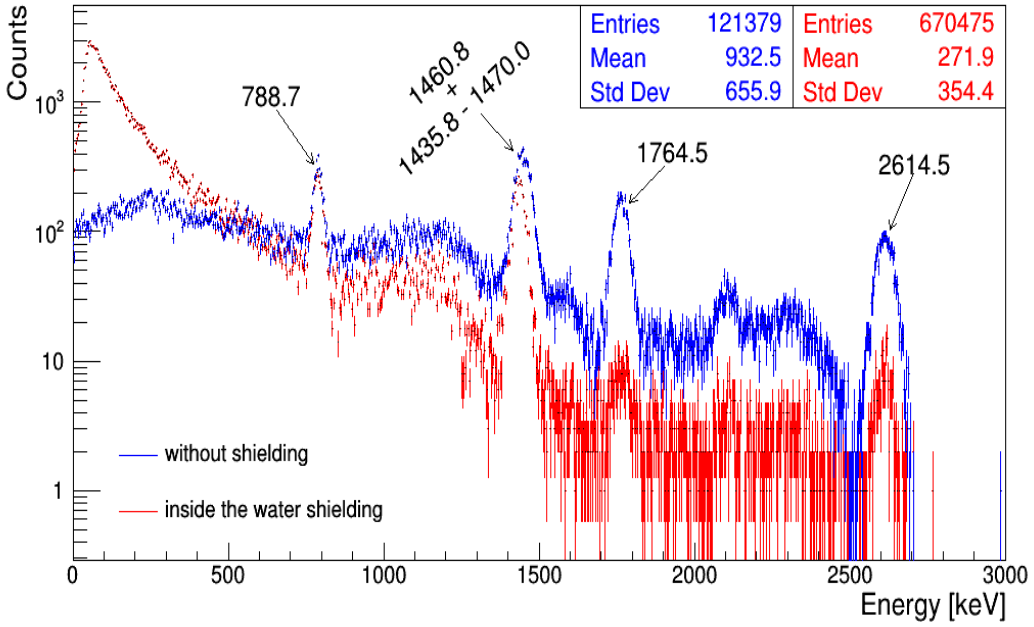

Figure 7.8: Background spectra simulated using two $LaBr_3$:Ce detectors (with ^{138}La internal activity) outside and inside the water shield.

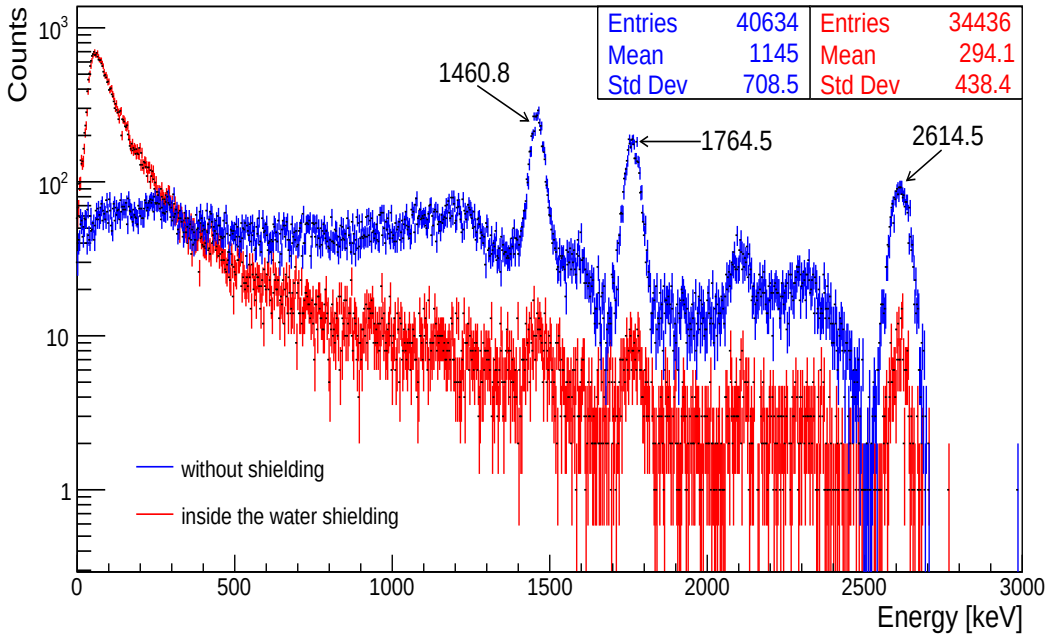

Figure 7.9: Background spectra simulated using two $LaBr_3$:Ce detectors (without the internal activity) outside and inside the water shield.

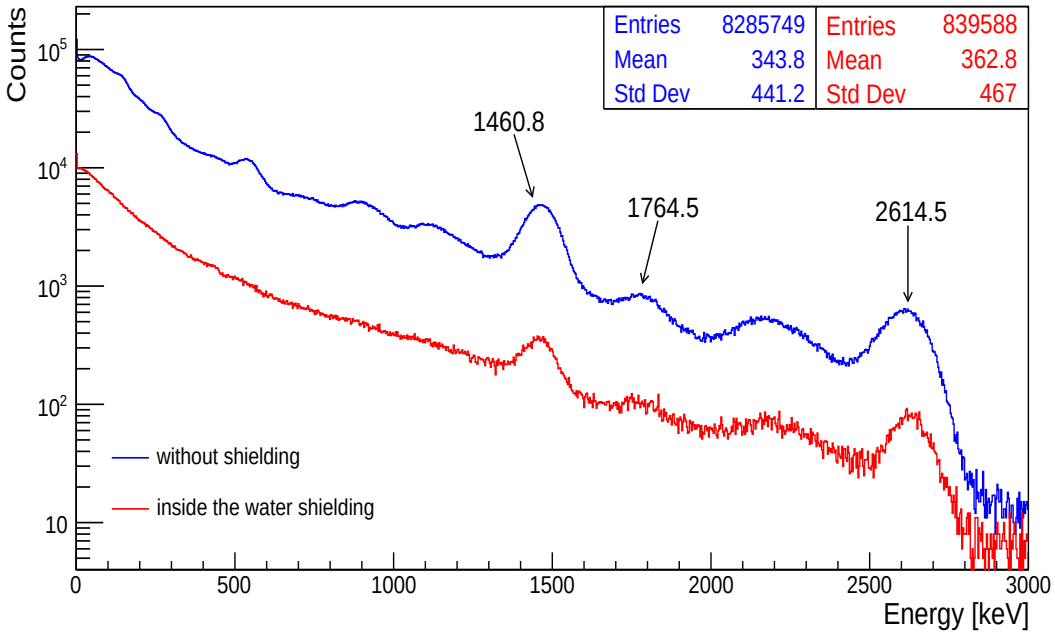

Figure 7.10: Background spectra measured using NaI:Tl detector outside (on a table) and inside the water shield.

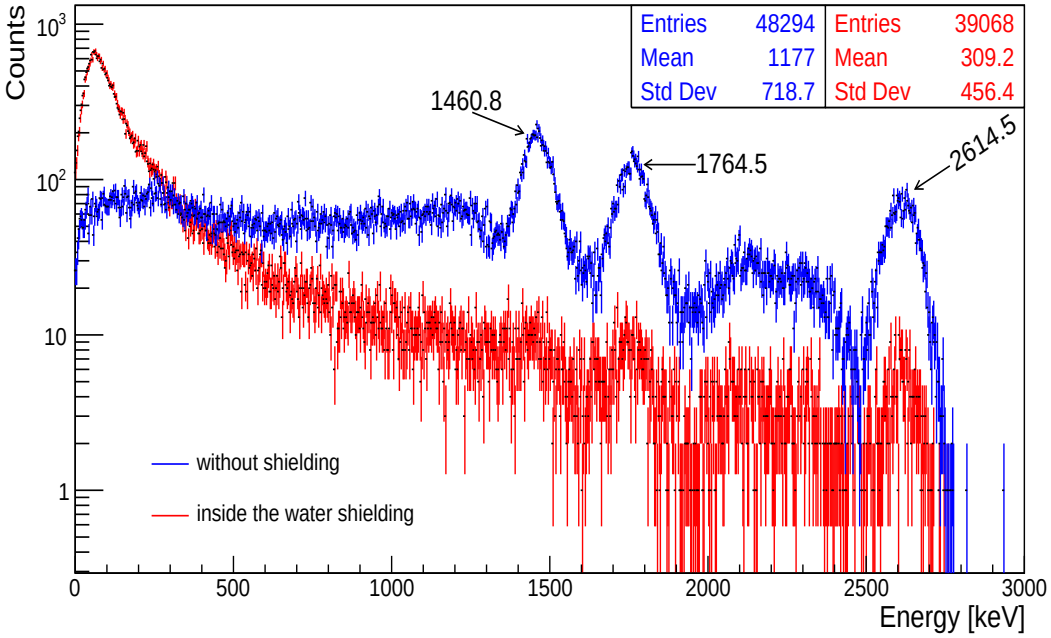

Figure 7.11: Background spectra simulated using NaI:Tl detector outside and inside the water shield.

Moreover, Tab. 7.3 give the ratio between the background counts without shielding and with the water shield as well as the attenuation. Gamma rays of a certain energy; 1460.8 keV and 2614.5 keV appear not to be attenuated when measurements and simulations were performed using $LaBr_3$:Ce detectors with the internal activity. However, when simulations were performed using $LaBr_3$:Ce detectors without the internal activity, 94 % of 1460.8 keV gamma rays was attenuated. Both measured and simulated results using the NaI:Tl detector shows that 94 % of 1460.8 keV gamma rays was attenuated by the water shield. At the same time 92 - 93 % of 1764.5 keV gamma rays was attenuated by the water shield when measured and simulated using $LaBr_3$:Ce and NaI:Tl detectors. In addition, 91 % attenuation of 2614.5 keV gamma rays was achieved when simulations were performed using $LaBr_3$:Ce detectors without the internal activity. Both measured and simulated results using NaI:Tl de-

tector shows that 90 - 91 % of 2614.5 keV gamma rays was attenuated by the water shield. The total background counts (0 - 3000 keV) were reduced by a factor of eight with the water shield which is greater compared to the results of Kozak *et al.* [9] where background counts (80 - 3000 keV) were reduced by a factor of two with 1 cm Cu + 10 cm standard Pb + 5 cm ordinary Pb shield. As shown in Tab. 7.4, the water shield attenuates the 1460.8 keV gamma-ray energy by the same factor as 6 cm Pb + 2 mm Cu shield [67]. Higher thicknesses of lead shield show higher attenuation of gamma rays than the water shield. It is evident that water was able to attenuate gamma rays and the attenuation decreases with increase in gamma-ray energy. This is because the probability of photoelectric absorption decreases with increasing gamma-ray energy [12].

Table 7.3: Attenuation of 1460.8 keV, 1764.5 keV and 2614.5 keV gamma-ray energies with water measured and simulated using $LaBr_3$:Ce and NaI:Tl detectors.

Detector		I_0	I_f	I_f/I_0	Attenuation (%)
1460.8 keV					
2 $LaBr_3$:Ce	Measured	1074440	891651	0.83	17.0
	Simulated[c]	8010	7271	0.91	9.2
	Simulated[d]	3952	251	0.06	93.6
NaI:Tl	Measured	142605	8835	0.06	93.8
	Simulated	5968	362	0.06	93.9
1764.8 keV					
2 $LaBr_3$:Ce	Measured	11902	661	0.06	93.3
	Simulated[c]	1695	130	0.08	92.3
	Simulated[d]	3368	249	0.07	92.6
NaI:Tl	Measured	10965	932	0.08	91.5
	Simulated	4453	338	0.08	92.4
2614.5 keV					
2 $LaBr_3$:Ce	Measured	53349	19914	0.37	62.7
	Simulated[c]	1061	102	0.10	90.3
	Simulated[d]	2174	195	0.09	91.0
NaI:Tl	Measured	27877	2847	0.10	89.8
	Simulated	2978	260	0.09	91.3
NaI:Tl	Measured				
30-450 keV		5521920	535763	0.10	90.3
500-3000 keV		1785900	191537	0.11	89.3
0-3000 keV		10725900	1367520	0.13	87.3

[c] Simulation with ^{138}La internal activity of $LaBr_3$:Ce detector.
[d] Simulation without internal activity of $LaBr_3$:Ce detector.

Table 7.4: Comparison of background spectra counts ratio of the present work with other work. I_0 and I_f are counts in the background spectra measured without and with shielding, respectively.

Reference/Energy (keV)	1460.8	1764.5	2614.5
	I_f/I_0	I_f/I_0	I_f/I_0
3" × 3" NaI:Tl (H_2O) Present work	0.06	0.08	0.09
3" × 3" NaI:Tl (6 cm Pb + 2 mm Cu)[67]	0.06	—	—
HPGe (12 cm Pb + 3.5 mm Sn + 0.5 mm Cu)[69]	0.01	0.008	0.013
9" × 9" NaI:Tl (15 cm Pb + 2 mm Sn + 1 mm Cu)[68]	0.0009	0.001	—

7.4 Peak-to-Total Ratio and Minimum Detectable Activity

The peak-to-total area ratio is used to evaluate the performance of a spectrometer. The PTR was evaluated using the 1173.2 keV and 1332.5 keV peaks of ^{60}Co. The PTR with shielding and without shielding (without background spectrum subtraction) are 0.10 and 0.13, respectively. The PTR without shielding is higher due to the contribution of background gamma rays in that peak region to the peaks counts. The PTR with shielding and without shielding (after background spectrum subtraction) are 0.15 and 0.23, respectively. The PTR results with shield are only marginally improved because of more Compton scattering with the water shield.

The MDA is dependent on the counting live time, the energy resolution, the full-energy peak detection efficiency, the degree of confidence and the background count rate which depends on the experimental geometry condition [12; 58]. A lower MDA value for a given radionuclide means higher chance of detecting low activity concentration of that radionuclide (95 % of probability was considered in this work). It is important to note that the MDA values

vary for diffferent gamma-ray energy peaks even if originating from the same radionuclide. Tab. 7.5 gives the MDA measured in singles and coincidence modes. The MDA for 1460.8 keV gamma-line of ^{40}K measured in singles mode using four $LaBr_3$:Ce geometry is higher than the two $LaBr_3$:Ce detector geometry without shielding. Even though both geometries are without shielding and have same resolution and source-to-detector distance, the detection efficiency and the measured background condition differs (see Appendix B). The MDA for 1460.8 keV measured using two $LaBr_3$:Ce detector geometry without shielding is higher by a factor of 1.5 than that measured inside the water shield. It is obvious that MDA reduction by the water shield is not significant at this gamma-ray energy because the 1435.8 keV gamma-line of ^{138}La present in the detector's crystal increases the MDA. The ^{138}La internal activity of $LaBr_3$:Ce detector measured using a NaI:Tl detector (see Fig. 7.12) is 263.8 $\pm$ 26.8 Bq kg^{-1} which means that the MDA cannot be lower than that activity in this peak region (1460.8 keV). The ^{138}La internal activity of $LaBr_3$:Ce detector (2" $\times$ 2") calculated and measured by this work agrees with that calculated and measured by Zeng *et al.* [101] to within measurement uncertainties.

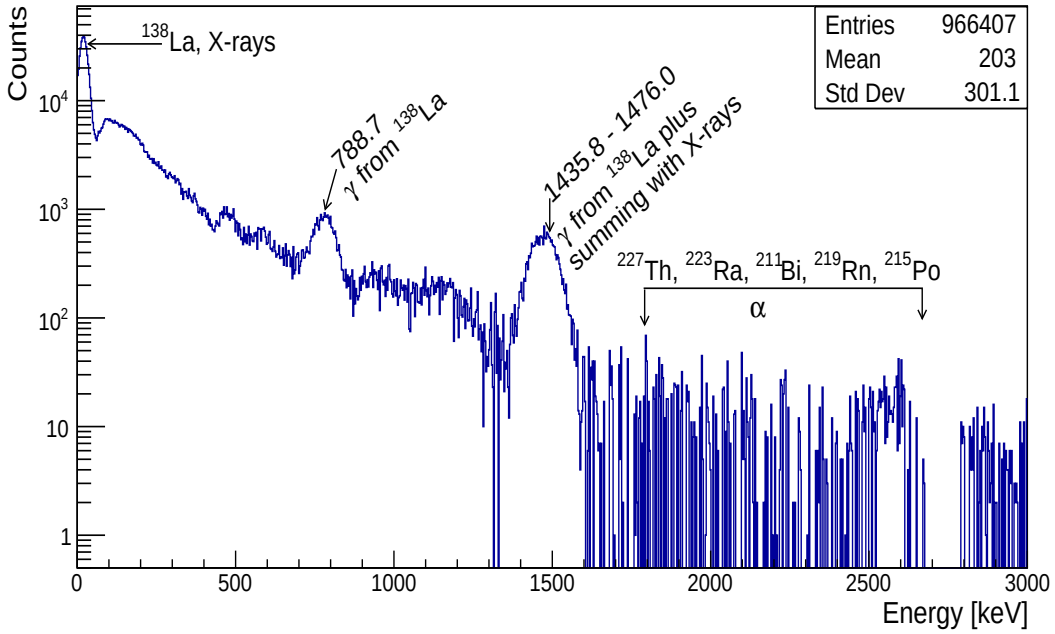

Figure 7.12: Gamma-ray spectra of internal activity of $LaBr_3$:Ce detector after background spectrum subtraction measured using NaI:Tl detector.

Furthermore, the 609.3 keV, 1120.3 keV and 1764.5 keV are gamma-lines associated with ^{238}U series radionuclides, and 583.2 keV, 911.2 keV and 2614.5 keV are gamma-lines associated with ^{232}Th series radionuclides. For the four $LaBr_3$:Ce detector measurement geometry in singles mode, the 583.3 keV and 609.3 keV have the least MDA value and 911.2 keV and 1120.3 keV have the highest MDA for the ^{232}Th and ^{238}U series radionuclides. Comparing the MDA measured in singles and coincidence modes using the four $LaBr_3$:Ce detector geometry (Fig. 7.13), the latter is lower by a factor of 8, 8, 36, 10 than the former for 583.3 keV, 609.3 keV, 1120.3 keV, 2614.5 keV gamma-lines, respectively. The coincidence MDA measured using the four $LaBr_3$:Ce detector geometry is lower than that of Tillet *et al.* [25] for 609.3 keV and 2614.5 keV and higher than that of Antovic and Svrkota [20]. It is important to note that shielding was used in the case of Antovic and Svrkota [20]; Tillet *et al.* [25] and their

detection efficiency was higher than that of this work. For the two $LaBr_3$:Ce detector geometry, the MDA measured in singles mode inside the water shield is lower than that measured without a shield by a factor of 8, 4, 3, 3, 5 and 1 for 583.2 keV, 609.3 keV, 911.2, 1120.3 keV, 1764.5 keV and 2614.5 keV gamma-line, respectively. It can be observed that there is no significant MDA improvement of the 2614.5 keV gamma-line by the water shield due to the αs released by ^{227}Ac which appear in the 1800 - 2700 keV region of the gamma-ray spectrum see Fig. 7.7. In coincidence mode, the MDA measured using the two $LaBr_3$:Ce detectors without shielding and inside the water shield are the same. This is because there is no background counts in the 583.2, 609.3 keV, 1120.3 keV and 2614.5 keV region in Fig. B.17 $\rightarrow$ B.20 and other parameters in which MDA depend on are the same. The application of the gamma-ray time-of-flight method in addition to measuring two photons simultaneously makes the background/scattered gamma-ray contribution insignificant. This shows that shielding does not have effect on the coincidence MDA so long as the gamma-ray time-of-flight method is applied. Fig. 7.14 shows that the MDA in coincidence mode is lower than in singles mode measured using two $LaBr_3$:Ce detectors without shielding by a factor of 4, 4, 15 and 4 for 583.2 keV, 609.3 keV, 1120.3 keV and 2614.5 keV, respectively. There is no significant difference between the singles and coincidence MDA measured using two $LaBr_3$:Ce detectors inside the water shield for 583.2 keV and 609.3 keV gamma-lines because the use of gamma-ray time-of-flight significantly reduce the background contribution. However, the latter is lower than the former by a factor of 5 and 4 for the 1120.3 keV and 2614.5 keV gamma-lines respectively. The coincidence MDA measured for 583.2 keV, 609.3 keV and 2614.5 keV using the two $LaBr_3$:Ce detector geometry is higher than that of Antovic and Svrkota [20]

and almost the same as that of Tillet *et al.* [25] for the 609.3 keV and 2614.5 keV gamma-lines. The coincidence MDA can be improved by increasing the efficiency which can be achieved by decreasing the source-to-detector distance.

In addition, measurements using a NaI:Tl detector inside the water shield in singles mode at source-to-detector distance and counting time smaller than the $LaBr_3$:Ce detector geometry show significant improvement in the MDA values see Tab. 7.5. The MDA for the 1460.8 keV gamma-line of ^{40}K measured using NaI:Tl detector geometry without shielding is higher by a factor of 4 than that measured inside the water shield. The MDA measured using the NaI:Tl detector inside the water shield is lower than that measured without shield by a factor of 10, 10, 9, 12, 13 and 8 for 583.2 keV, 609.3 keV, 911.2 keV, 1120.3 keV, 1764.5 keV and 2614.5 keV gamma-lines, respectively.

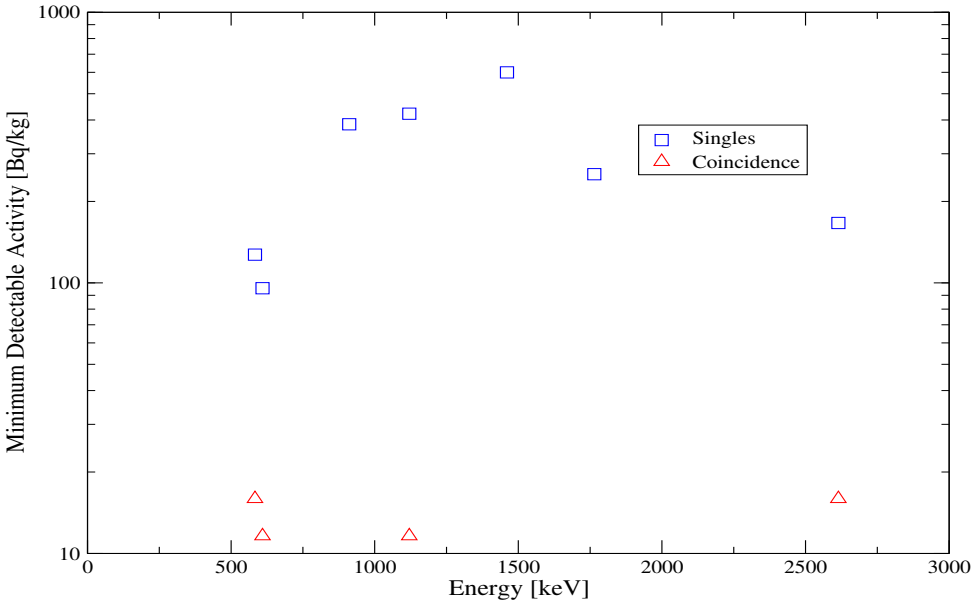

Figure 7.13: MDA measured in singles and coincidence modes using four $LaBr_3$:Ce detectors without shielding.

Table 7.5: MDA measured in singles and coincidence modes using $LaBr_3$:Ce, NaI:Tl and HPGe detectors (d is the distance from the front face of the detector to the centre of Marinelli beaker).

Mode	Series/Nuclide	Energy (keV)	MDA		Bq kg^{-1}			
		Detectors	4 $LaBr_3$:Ce	2 $LaBr_3$:Ce	2 $LaBr_3$:Ce	NaI:Tl	NaI:Tl	HPGe
		Geometry (d in mm)	165	165	165	90	90	on top of the detector
		Shielding	None	None	H_2O	None	H_2O	Pb+Cu
		Counting time (hours)	48	48	48	24	24	24
Singles	^{40}K	1460.8	599.6	563.0	387.6	546.2	145.5	4.4
Singles	^{238}U/^{214}Bi	609.3	95.6	139.9	39.7	312.3	31.9	1.1
	^{238}U/^{214}Bi	1120.3	422.0	536.1	181.2	181.2	14.5	3.0
	^{238}U/^{214}Bi	1764.5	252.2	219.5	43.4	194.0	14.8	2.9
Coincidence	^{238}U/^{214}Bi	609.3/1120.3	11.6	35.9	36.1	—	—	—
Singles	^{232}Th/^{208}Tl	583.2	127.2	191.9	48.7	465.6	47.9	1.9
	^{232}Th/^{228}Ac	911.2	385.7	360.9	114.3	131.1	15.3	1.6
	^{232}Th/^{208}Tl	2614.5	166.5	191.1	160.9	294.1	36.8	0.9
Coincidence	^{232}Th/^{208}Tl	583.2/2614.5	15.9	45.2	44.0	—	—	—

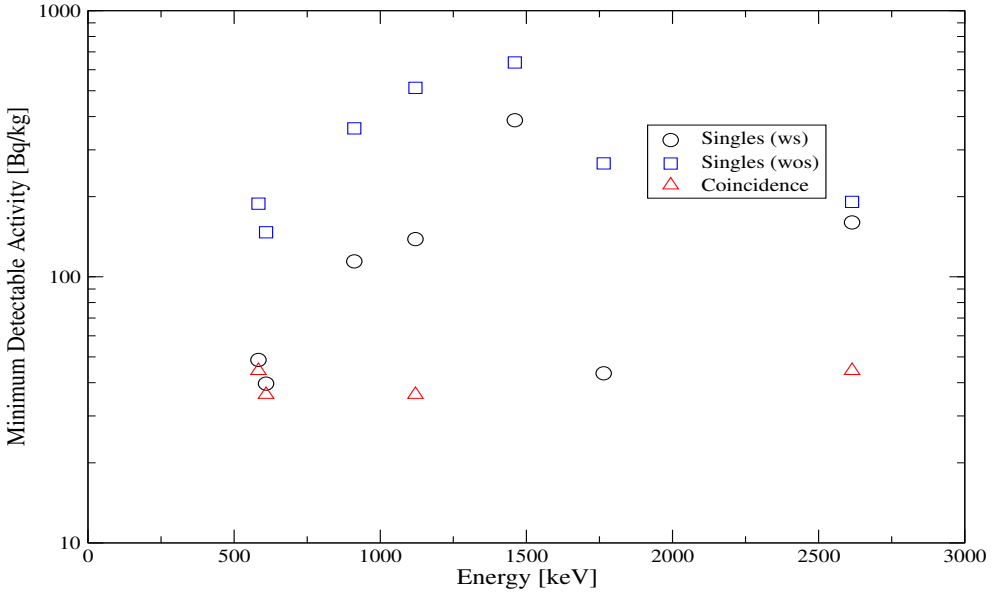

Figure 7.14: MDA measured in singles and coincidence modes using two $LaBr_3$:Ce detector without shielding (wos) and inside the water shield (ws).

7.5 Activity Concentration

The activity concentrations of ^{238}U and ^{232}Th series and ^{40}K radionuclides in IAEA-375 soil and beach sand measured in singles and coincidence modes are given in Tabs. 7.6 and 7.7, respectively. The activity concentrations of ^{238}U and ^{232}Th series and ^{40}K radionuclides in IAEA-375 measured in singles mode using four $LaBr_3$:Ce detectors without shielding and two $LaBr_3$:Ce detectors inside the water shield are all below the MDA. However, the activity concentrations of these radionuclides in IAEA-375 soil were determined when measured using NaI:Tl detector inside the water shield due to the lower MDA values. The IAEA-375 soil also contains some radionuclides that are not NORM nuclide. The peaks centered at 583.2 keV and 609.3 keV gamma-ray energies were not used in evaluating activity concentrations in IAEA-375 soil due to the presence of ^{137}Cs (661.7 keV) in the sample, which makes resolving

of these peaks difficult see Fig. B.31. Similarly, the activity concentrations of ^{238}U and ^{232}Th series radionuclides in IAEA-375 soil were determined in coincidence mode using the four $LaBr_3$:Ce detector without shielding geometry. Although the uncertainties on the activity concentrations were high due to low statistics, the results were comparable to the certified values given in Tab. 5.2 to within measurement uncertainties. The activity concentrations of ^{238}U and ^{232}Th series radionuclides in IAEA-375 soil measured in coincidence mode using the two $LaBr_3$:Ce detector inside the water shield geometry were below the MDA because the geometries efficiency is low.

Moreover, the results in Tab. 7.7 shows that the activity concentration of ^{40}K in beach sand measured using NaI:Tl detector, two and four $LaBr_3$:Ce detectors geometries is below the MDA. The activity concentrations of ^{238}U and ^{232}Th series radionuclides inside beach sand were determined in both singles and coincidence mode using the four $LaBr_3$:Ce detector without shielding and two $LaBr_3$:Ce detector inside the water shield geometries. Similarly, the activity concentrations of ^{238}U and ^{232}Th series radionuclides in beach sand measured in singles mode using NaI:Tl detector inside the water shield were determined. The peaks centered at 911.2 keV and 1120.3 keV gamma-ray energies were not used in calculating activity concentrations in beach sand measured using NaI:Tl detector due to poor resolution. The activity concentration in beach sand is quite high compared to in IAEA-375, which makes gamma-ray energies with low intensity prominent (see Figs. B.31 and B.33). The results of the measured activity concentrations of ^{238}U and ^{232}Th series radionuclides in beach sand measured using $LaBr_3$:Ce and NaI:Tl detectors agree with that measured using the standard HPGe detector system within 1σ to 2σ level.

Table 7.6: Activity concentrations of ^{238}U and ^{232}Th series and ^{40}K radionuclides in IAEA-375 soil measured in singles and coincidence modes using $LaBr_3$:Ce, NaI:Tl and HPGe detectors (NR is peak not resolved).

Mode	Series/Nuclide	Energy	Activity	concentration	(Bq kg^{-1})	
		Detectors shielding	4 $LaBr_3$:Ce None	2 $LaBr_3$:Ce H_2O	NaI:Tl H_2O	HPGe Pb+Cu
Singles	^{40}K	1460.8	<MDA	<MDA	429.9 ± 11.7	434.8 ± 20.1
Singles	^{238}U/^{214}Bi	609.3	<MDA	<MDA	<MDA	21.9 ± 3.0
	^{238}U/^{214}Bi	1120.3	<MDA	<MDA	26.2 ± 3.6	21.9 ± 3.3
	^{238}U/^{214}Bi	1764.5	<MDA	<MDA	20.6 ± 1.0	19.3 ± 1.7
Coincidence	^{238}U/^{214}Bi	609.3/1120.3	24.7 ± 11.7	<MDA	—	—
Singles	^{232}Th/^{208}Tl	583.2	<MDA	<MDA	<MDA	18.5 ± 2.5
	^{232}Th/^{228}Ac	911.2	<MDA	<MDA	18.2 ± 2.6	21.7 ± 3.2
	^{232}Th/^{208}Tl	2614.5	<MDA	<MDA	<MDA	18.7 ± 1.2
Coincidence	^{232}Th/^{208}Tl	583.2/26145	22.5 ± 13.0	<MDA	—	—

Table 7.7: Activity concentrations of ^{238}U and ^{232}Th series and ^{40}K radionuclides in beach sand measured in singles and coincidence modes using $LaBr_3$:Ce, NaI:Tl and HPGe detectors (NR is peak not resolved).

Mode	Series/Nuclide	Energy	Activity	concentration	(Bq kg^{-1})	
		Detectors	4 $LaBr_3$:Ce	2 $LaBr_3$:Ce	NaT:Tl	HPGe
		shielding	None	H_2O	H_2O	Pb+Cu
Singles	^{40}K	1460.8	<MDA	<MDA	<MDA	174 ± 15
Singles	^{238}U/^{214}Bi	609.3	1222 ± 86	1043 ± 50	1148 ± 23	1139 ± 14
	^{238}U/^{214}Bi	1120.3	1105 ±111	1076 ± 26	NR	1115 ± 16
	^{238}U/^{214}Bi	1764.5	1046 ± 78	1045 ± 39	1049 ± 20	1097 ± 16
Coincidence	^{238}U/^{214}Bi	609.3/1120.3	1297 ± 86	1244 ± 214	—	—
Singles	^{232}Th/^{208}Tl	583.2	2143 ± 135	2052 ± 82	2155 ± 53	2263 ± 49
	^{232}Th/^{228}Ac	911.2	1906 ± 175	1952 ± 119	NR	2260 ± 135
	^{232}Th/^{208}Tl	2614.5	1980 ± 71	1933 ± 53	1925 ± 50	2011 ± 40
Coincidence	^{232}Th^{208}Tl	583.2/26145	2393 ± 148	2362 ± 336	—	—

Chapter 8

Summary and Conclusion

The purpose of this research was to design, construct and characterise a low-level radioactivity counting system with NORM samples based on gamma-ray spectrometry with $LaBr_3$:Ce scintillator detectors. This was carried out to ascertain the suitability of using the $LaBr_3$:Ce detector in measuring low-level radioactivity samples and to establish if water can be used as an alternative material for shielding gamma rays from the environment, where measurements are being made.

A passive water shielding to reduce background radiation reaching the detectors was designed with GEANT4 Monte Carlo toolkit simulations, and then constructed. Volume soil samples (Marinelli beaker geometry) were measured in singles and coincidence modes using four $LaBr_3$:Ce detectors without shielding, two $LaBr_3$:Ce detectors without shielding and the same two detectors inside the water shield. The samples were also measured using a NaI:Tl detector inside the water shield and with a standard HPGe detector shielded with lead to compare and validate the results from measurements with the $LaBr_3$:Ce detectors.

The energy resolution of the HPGe detector was as expected lower by an order of magnitude than that of the $LaBr_3$:Ce detector even though the $LaBr_3$:Ce detector was able to resolve most peaks of interest. The energy resolution of $LaBr_3$:Ce detector was found to be also as expected lower by a factor of two than that of a NaI:Tl detector. Furthermore, the results of the measured and simulated absolute full-energy peak detection efficiencies using the four $LaBr_3$:Ce detectors are in good agreement to within measurement uncertainty. The detection efficiencies for the singles mode of measurement were more than two orders of magnitude higher than that for the coincidence mode of measurement. The water shield was able to attenuate 1460.8 keV, 1764.5 keV and 2614.5 keV background gamma rays by 94 %, 92 - 93 % and 90 - 91 %, respectively. This shows that the attenuation decrease with increased gamma-ray energy due to the decrease in the probability of photoelectric absorption with increase in gamma-ray energy [12]. The PTR with water shielding before and after background spectrum subtraction using the 1173.2 keV and 1332.5 keV peaks of ^{60}Co are 0.10 and 0.15, respectively. The PTR results with shield are not much better because of more Compton scattering.

The MDA measured using four $LaBr_3$:Ce detectors without shielding for measurement in coincidence mode was lower by a factor of 8 and 36, and 8 and 10 than for singles mode for ^{238}U (609.3 keV and 1120.3 keV) and ^{232}Th (583.2 keV and 2614.5 keV) series radionuclides, respectively. Activity concentration $\geq$ 11.6 Bq kg^{-1} (for ^{238}U) and $\geq$ 15.9 Bq kg^{-1} (for ^{232}Th) can be measured in 95 % of cases with this measurement geometry in coincidence mode. The MDA measured in singles mode using two $LaBr_3$:Ce inside the water shield is lower than that measured without shielding by a factor of 1.5, 4, 3 and 5, and 8, 3 and 1 for the ^{40}K (1460.8 keV), ^{238}U (609.3 keV, 11203 keV and 1764.5

keV) and ^{232}Th (583.2 keV, 911.2 keV and 2614.5 keV) series radionuclides, respectively. The MDA reduction by the water shield is not significant at 1460.8 keV and 2614.5 keV due to increases in the MDA as a result of the 1435.8 keV gamma-line of ^{138}La and the alpha particles released by ^{227}Ac which appears in the 1800 - 2700 keV region of gamma-ray spectrum of $LaBr_3$:Ce detector. The MDA in coincidence mode is lower than in singles mode measured using two $LaBr_3$:Ce detectors without shielding by a factor of 4 and 15, and 4 for ^{238}U (609.3 keV and 1120.3 keV) and ^{232}Th (583.2 keV and 2614.5 keV) series radionuclides, respectively. The MDAs measured using two $LaBr_3$:Ce without shielding and inside the water shield in coincidence mode are the same. This is because the use of the coincidence method plus photon time-of-flight eliminate the background gamma-ray contribution. Furthermore, the activity concentration of ^{40}K in IAEA-375 soil and beach sand measured using the $LaBr_3$:Ce detectors geometries is below the MDA due to the internal activity of the detector. However, the activity concentration of ^{40}K in IAEA-375 was measured using the NaI:Tl detector inside the water shield. The activity concentrations of ^{238}U and ^{232}Th series radionuclides in IAEA-375 soil measured in singles mode using $LaBr_3$:Ce detectors geometries were below the MDA. The activity concentrations of ^{238}U and ^{232}Th series radionuclides in IAEA-375 soil were determined in singles mode using a NaI:Tl detector inside the water shield and in coincidence mode using the four $LaBr_3$:Ce detectors without shielding. The activity concentrations of ^{238}U and ^{232}Th series radionuclides inside beach sand were determined in both singles and coincidence modes. The results of the measured activity concentrations of ^{238}U and ^{232}Th series radionuclides in beach sand using $LaBr_3$:Ce and NaI:Tl detectors agree with that measured using the standard HPGe detector geometry. The NORM radionuclides activity

concentration in soil measured with the detection system campaign for is given Tab. 8.1.

Table 8.1: The NORM radionuclides activity concentration in soil measured with the detection system campaign for.

Detection	system		Radionuclides	measured	
Detectors	Shielding	Mode	^{40}K	^{238}U	^{232}Th
1 NaI:Tl	water	singles	√	√	√
2 $LaBr_3$:Ce	water	singles	x	√	√
2 $LaBr_3$:Ce	water	coincidence	x	√	√
4 $LaBr_3$:Ce	None	singles	x	√	√
4 $LaBr_3$:Ce	None	coincidence	x	√	√

In conclusion, water performed well in shielding background gamma rays (2614.5 keV energy by above 90 %) during low-level NORM radioactivity measurements. The internal activity of the $LaBr_3$:Ce detector increases the minimum detectable activity (MDA) at 1460.8 keV (^{40}K) and 2614.5 keV (^{208}Tl/^{232}Th), which limits the measurement of radionuclides with low activity concentration in singles mode. However, using the coincidence method plus photon time-of-flight, the scattered/background radiation contribution becomes insignificant. According to UNSCEAR [102], the world average activity concentrations of ^{40}K, ^{238}U and ^{232}Th are 400 Bq kg^{-1}, 35 Bq kg^{-1} and 30 Bq kg^{-1}, respectively. Therefore, using four $LaBr_3$:Ce detectors without shielding in coincidence mode low-level activity concentration $\geq$ 11.6 Bq kg^{-1} and $\geq$ 15.9 Bq kg^{-1} for ^{238}U and ^{232}Th series radionuclides, respectively, can be measured in any soils.

The use of two $LaBr_3$:Ce detectors (with source-to-detector distance smaller than that used in this work to improve detection efficiency) or more in coincidence mode together with the gamma-ray time-of-flight background subtrac-

tion method is recommended when measurement of activity concentrations of cascade emitting radionuclides are of interest. A single HPGe or NaI:Tl detector shielded with water is recommended for gamma-ray spectrometry of radionuclides that are not cascade emitters such as ^{40}K.

Appendices

Appendix A

Investigation of Water Thickness Required to Shield Gamma rays

The mass attenuation coefficient of water and polyethylene for various energies were taken from National Institute for Standard and Technology (NIST) [103]. The mass attenuation coefficients were fitted with a power function in Libre-Office Calc and fit parameters obtained (see Fig. A.1). The fit parameters were used to calculate the mass attenuation coefficient for energies of interest. The calculated mass attenuation coefficient for the energies of interest were converted to linear attenuation coefficient using Eqn. 2.2.10. The linear attenuation coefficient of water and polyethylene for the energies of interest are shown in Fig. A.2. This was done to determine the suitability of using a polyethylene container for the water shield. As observed from Fig. A.2, the difference between the linear attenuation of water and polyethylene is not significant. Polyethylene also happen to be a common water container material and is cheap.

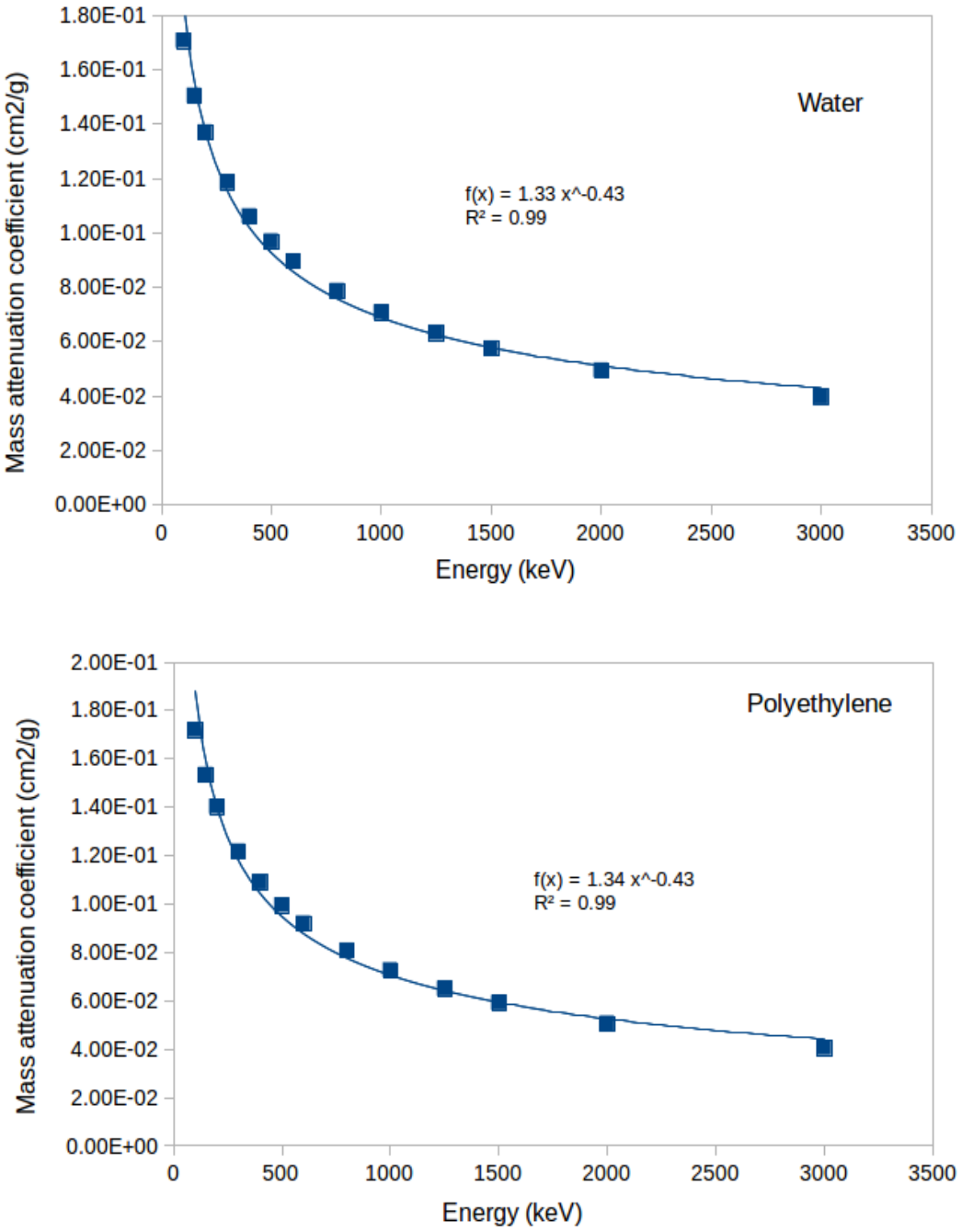

Figure A.1: Interpolated mass attenuation coefficients of water (upper) and polyethylene (lower) from National Institute for Standard and Technology (NIST) [103].

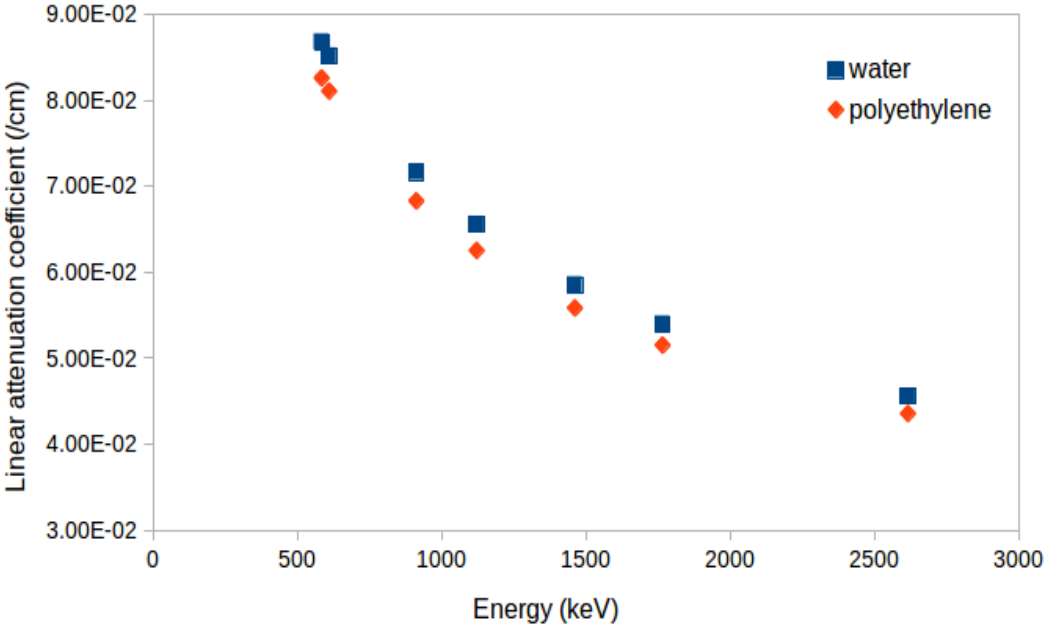

Figure A.2: Linear attenuation coefficients (μ) of water ($\rho = 1$ gcm^{-3}) and polyethylene ($\rho = 0.93$ gcm^{-3}) extracted using the fitting parameters in Fig. A.1.

To investigate the thickness of water required to shield the 2614.5 keV background gamma rays from reaching the detectors, GEANT4 simulations were performed. The Physics lists and models are the same as in Chapter 3. A water thickness of 500 mm was placed around a measurement volume housing two $LaBr_3$:Ce detectors as shown in Fig. A.3. Then, surface isotropic gamma-rays of 2614.5 keV energy were placed at 505 mm from the measurement volume all round moving inward i.e. outside of the water shield and energy deposited in the detectors recorded. Thereafter, keeping other parameters constant except for the water shield thickness, the simulation was repeated for 400 mm, 300 mm, 200 mm and 100 mm thicknesses of water shield. Also, the energy deposited in the detectors, without the shield in place was simulated with other parameters remaining constant and recorded. The counts in the peaks were extracted as described in section 6.5 and the percentage attenuation calculated

using Eqn. 6.7.1. The results of the investigations are shown in Fig. A.4 and Tab. A.1.

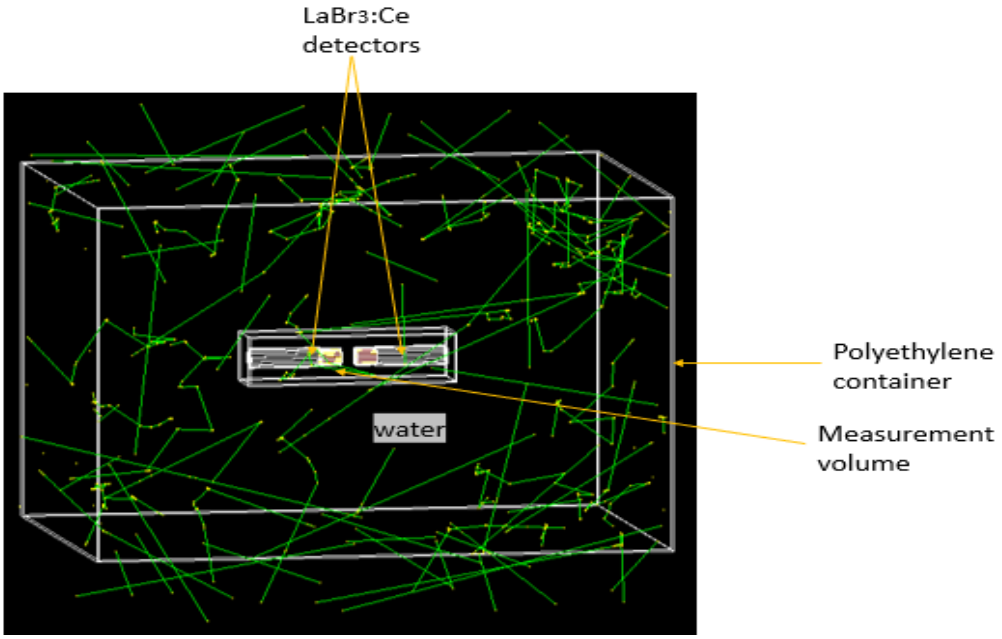

Figure A.3: Two $LaBr_3$:Ce detectors surrounded by 500 mm thick water placed inside a polyethylene container (from GEANT4 simulation).

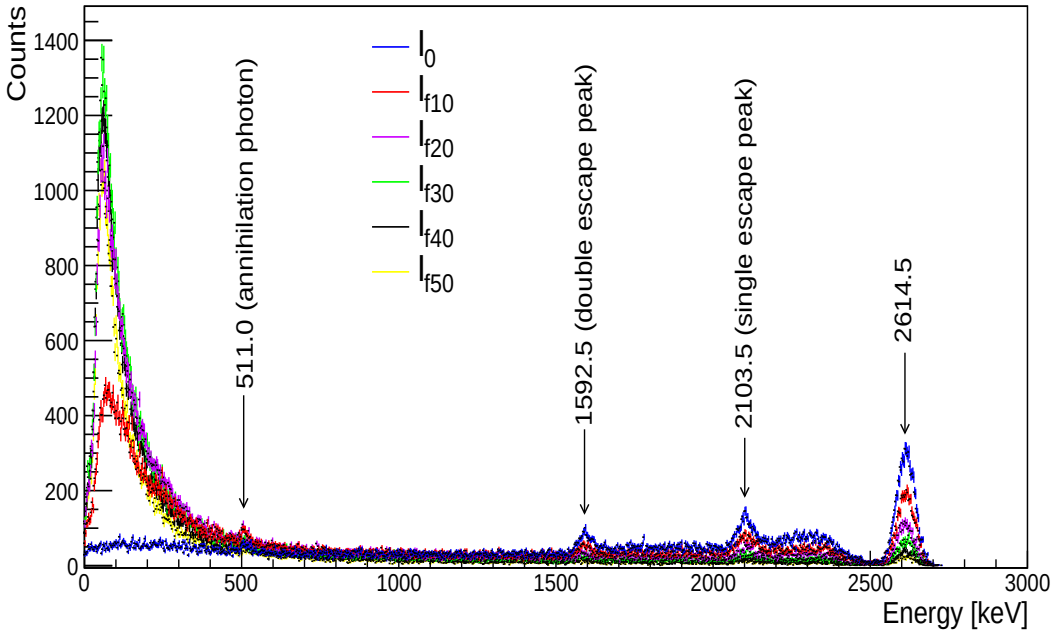

Figure A.4: GEANT4 simulations spectra showing attenuation of 2614.5 keV gamma rays by various thicknesses of water. I_0 is without shielding, I_{f10}, I_{f20}, I_{f30}, I_{f40} and I_{f50} are with water shielding of thickness 100 mm, 200 mm, 300 mm, 400 mm and 500 mm respectively.

Table A.1: Simulation results of attenuation of 2614.5 keV gamma rays by various thicknesses of water.

Thickness (mm)	Counts	I_f/I_0	Attenuation (%)
0 (I_0)	7277	—	—
100 (I_{f10})	4547	0.62	38
200 (I_{f20})	2547	0.35	65
300 (I_{f30})	1559	0.21	79
400 (I_{f40})	991	0.14	86
500 (I_{f50})	623	0.09	91

Appendix B

Measurements Series

Figs. B.1 and B.2 shows pictures of the measurement locations given in Tab. 5.1.

Figure B.1: Pictures showing the inside of the N-line vault at iThemba LABS.

Figure B.2: Pictures showing the outside beside N-line vault at iThemba LABS.

$LaBr_3$:Ce Detector

The activity concentration of ^{138}La in 2" × 2" $LaBr_3$:Ce detector is calculated as follows: mass (m) of 2" × 2" $LaBr_3$:Ce detector of radius r, height h and density ρ is:

$$m = v\rho = \pi r^2 h\rho = 3.14 \times (2.54)^2 \times 5.08 \times 5.08 = 523.1g$$

Therefore, the mass of $LaBr_3$ is 496.9 g and the mass of Ce (5 %) is 26.2 g. Molar mass of $LaBr_3$ = 138.9 g mol^{-1} + (3 × 79.9 g mol^{-1}) = 378.6 g mol^{-1} . Mass of La in 1 mole of $LaBr_3$ is 138.9 g and composition of La by mass is:

$$\frac{138.9}{378.6} = 0.367$$

The mass of La in 2" × 2" $LaBr_3$:Ce detector is $0.367 \times 496.9 = 182.4$ g.

The activity concentration of ^{138}La with 1.05×10^{11} yrs half-life and constitute 9.02×10^{-4} of the total mass of La is:

$$\frac{dN}{dt} = N\lambda = M_{La} f_{La} A_v (0.693/(m w_{La-138} t_{1/2}))$$

$$= 182.4 \times 9.02 \times 10^{-4} \times 6.022 \times 10^{23} \times (0.693/(138 \times 1.02 \times 10^{11} \times 3.16 \times 10^{7}))$$

$$= 153.4 Bq$$

The activity concentration per mass is:
$\frac{153.4}{523.1} = 0.293$ Bq g^{-1} or 293 Bq kg^{-1}.
The gamma-ray decay scheme of ^{138}La present in the $LaBr_3$:Ce detector crystal is shown in Fig. B.3.

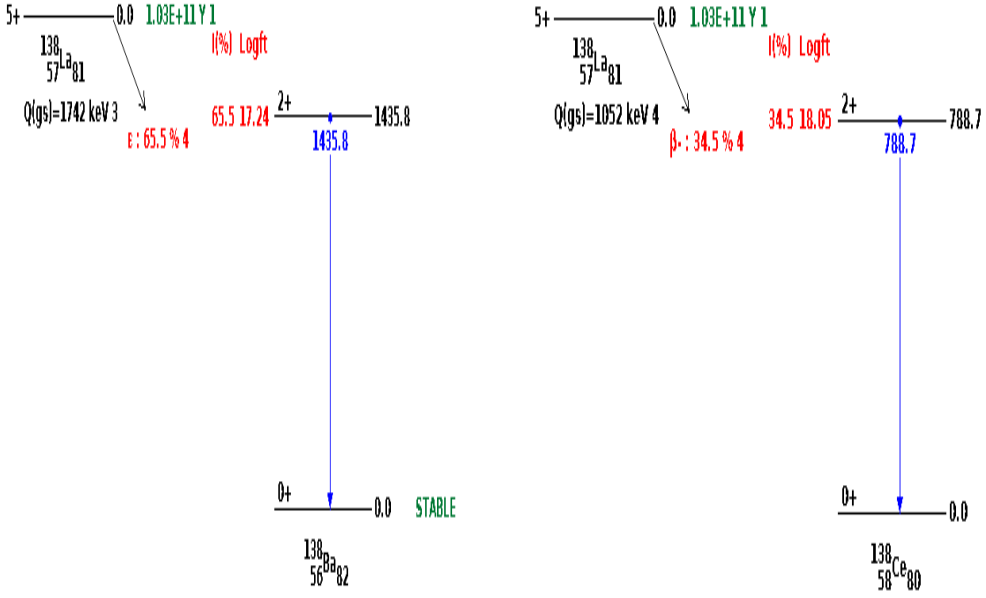

(a) (b)

Figure B.3: Gamma-ray decay scheme ^{138}Ba and ^{138}Ce from decay of ^{138}La. Image from reference [104].

B.1 Investigation of Different $LaBr_3$:Ce Detector Experimental Geometries

Eight detectors at 240 mm, four detectors at 150 mm and two detectors at 100 mm equidistant from the sample were investigated (see Tab. 5.1 for detail). The thorium and uranium ore described in section 5.1 were measured. The background was measured using an empty Marinelli beaker and a ^{60}Co point source was used for energy calibration. The counting time is given in Tab. B.1. The analysis was done as described in Chapter 6. It was evident that the eight detector experimental geometry has the most scattering events while the two detector experimental geometry has the least scattering events due to the distance and angle between the detectors (Fig. B.4 $\rightarrow$ B.6). The scattered gamma-ray time-of-flight increased with the increase in the angle between detectors. The absolute full-energy peak detection efficiencies in singles mode for the three experimental geometries investigated are given in Fig. B.7. The eight detector experimental geometry is more efficient due to the number of the detectors used.

Table B.1: Radioactive sources and background counting time.

Sample	Counting time (seconds)		
	2 $LaBr_3$:Ce	4 $LaBr_3$:Ce	8 $LaBr_3$:Ce
Thorium ore	163218	172767	171806
Uranium ore	153847	172737	173276
Co-60	3602	4310	14818
background	1561	7158	57726

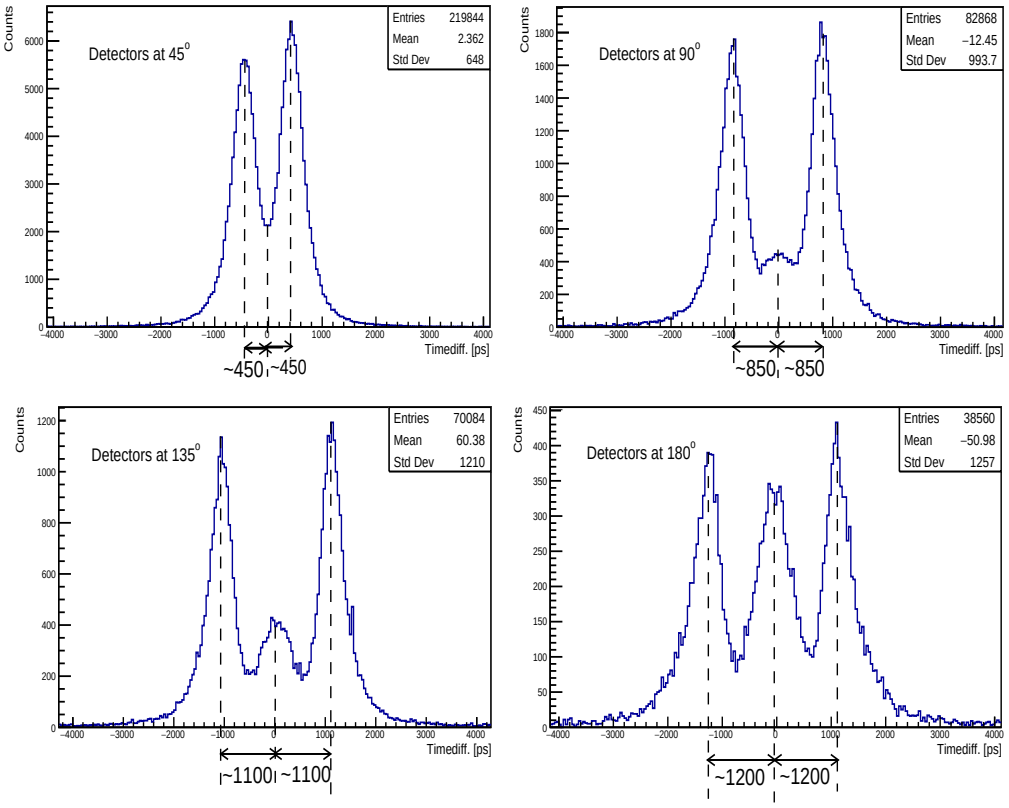

Figure B.4: Time difference spectra between detectors at 45° (upper left), 90° (upper right), 135° (lower left) and 180° (lower right) for the eight $LaBr_3$:Ce detector experimental geometry.

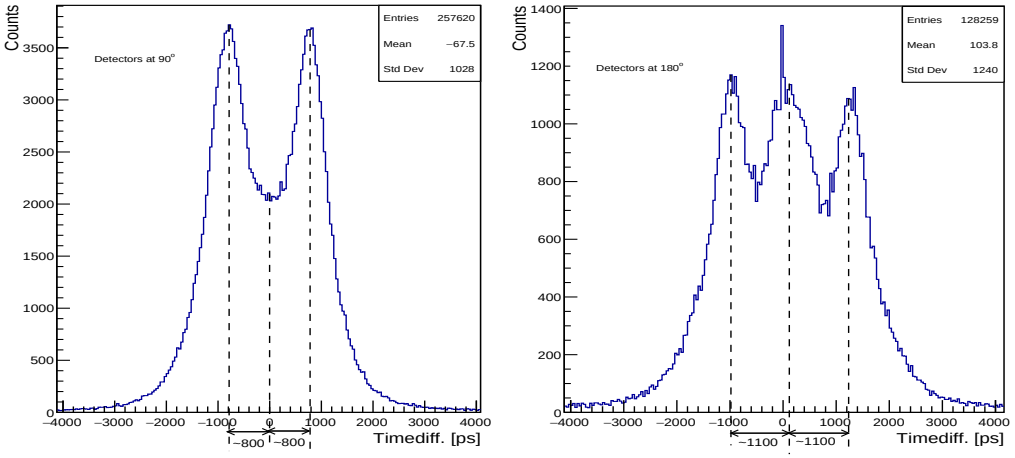

Figure B.5: Time difference spectra between detectors at 90° (left) and 180° (right) for the four $LaBr_3$:Ce detector experimental geometry.

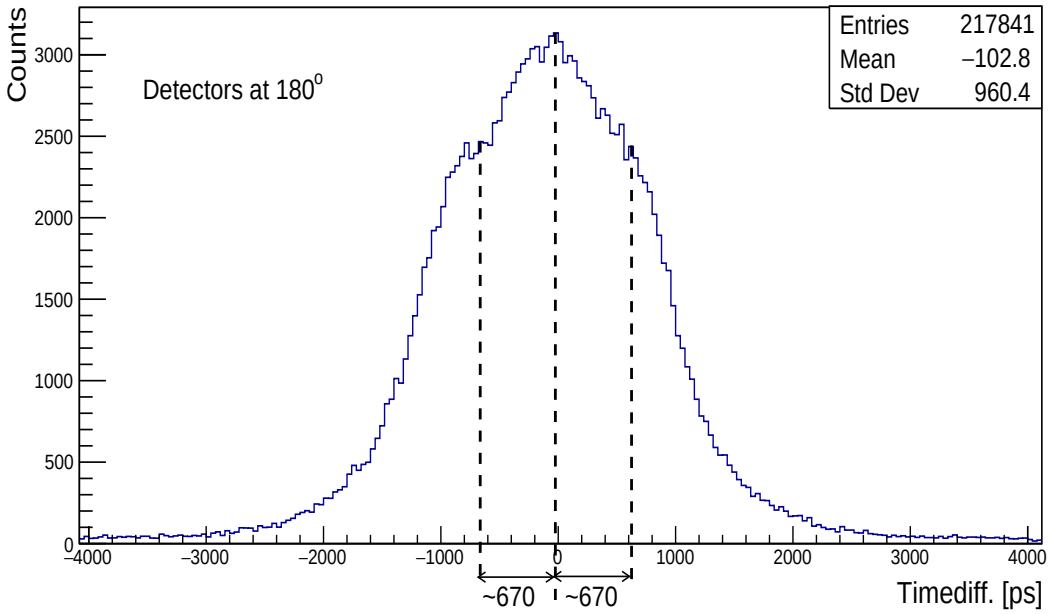

Figure B.6: Time difference spectra between detectors at 180° for the two $LaBr_3$:Ce detector experimental geometry.

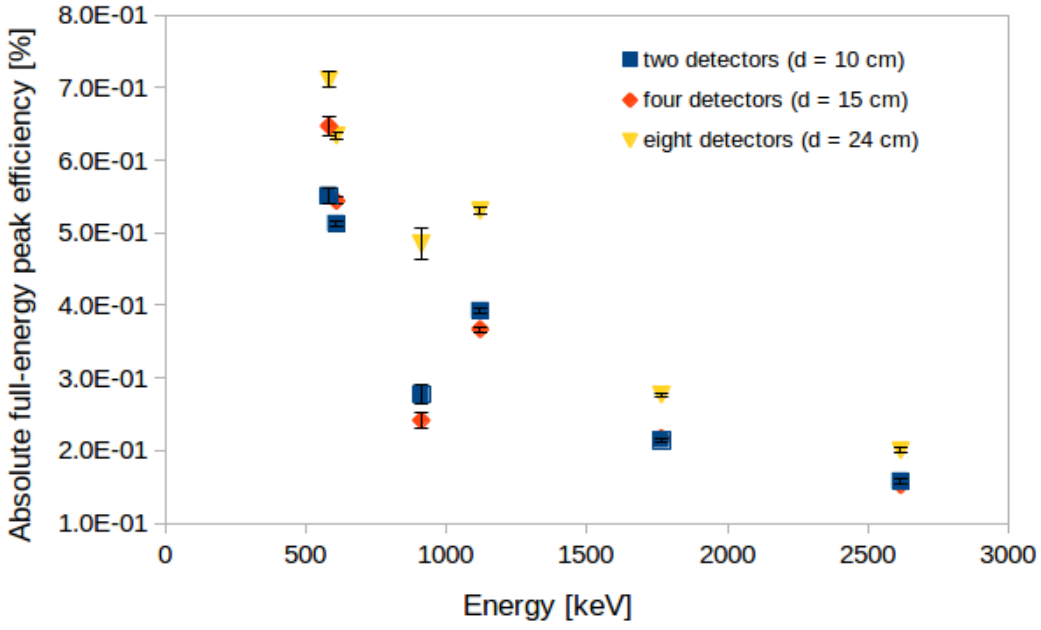

Figure B.7: Absolute full-energy peak detection efficiencies of gamma rays associated with decay of ^{238}U and ^{232}Th series radionuclides in singles mode for the three experimental geometries investigated.

B.2 Time Gate Sensitivity Check

Fig. B.8 → B.10 shows the summed total gamma-gamma spectra for background, and IAEA-375 soil and beach sand after background subtraction generated using the total time gate t_T measured using four $LaBr_3$:Ce detectors without shielding. As observed from these figures, both the true coincident gamma-ray events from the sample and the random coincident events from scattered gamma rays are present. These figures differ from those in section 6.3 because only the gamma-ray time-of-flight was applied to the figures in section 6.3 to separate the true coincidence events from random coincidence events. The summed total gamma-gamma spectra for beach-sand sample generated using the width of the peaks on either side the centroid peak of Fig. 5.9 measured using four $LaBr_3$:Ce detectors without shielding is shown in Fig B.11. Tab. B.2 gives total counts in the gamma-gamma matrix generated using time gates t_c and t_T for IAEA-375 soil and beach sand after background subtraction for the two combination of four detectors in coincidence. The weighted average counts in the energy gated coincidence peaks generated using t_c and t_T measured using four $LaBr_3$:Ce detectors without shielding are given Tab. B.3.

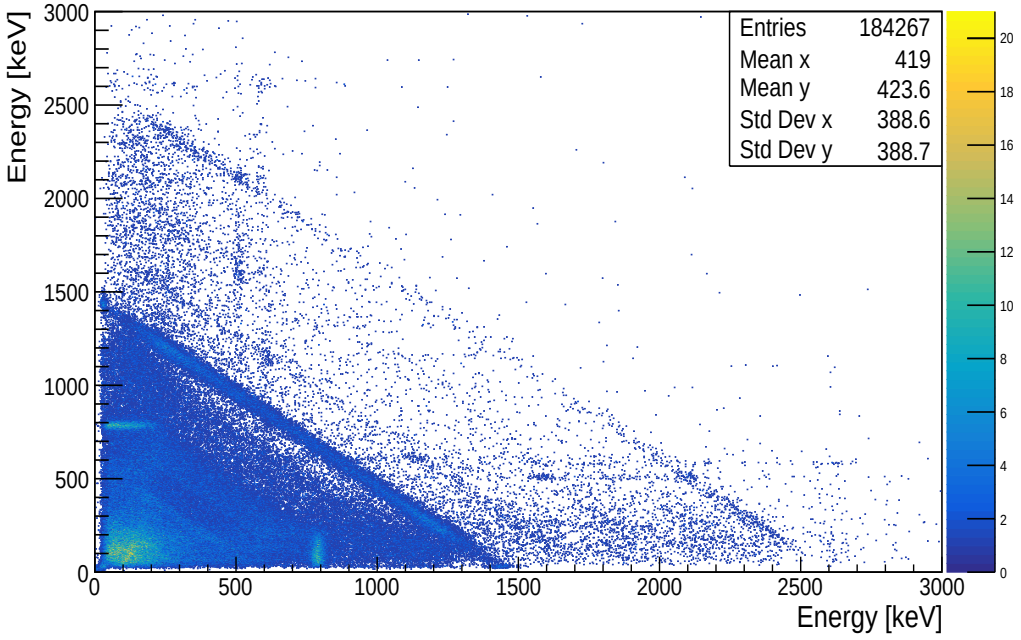

Figure B.8: Summed total gamma-gamma spectra for background generated using the total gate time t_T measured using four $LaBr_3$:Ce detectors without shielding.

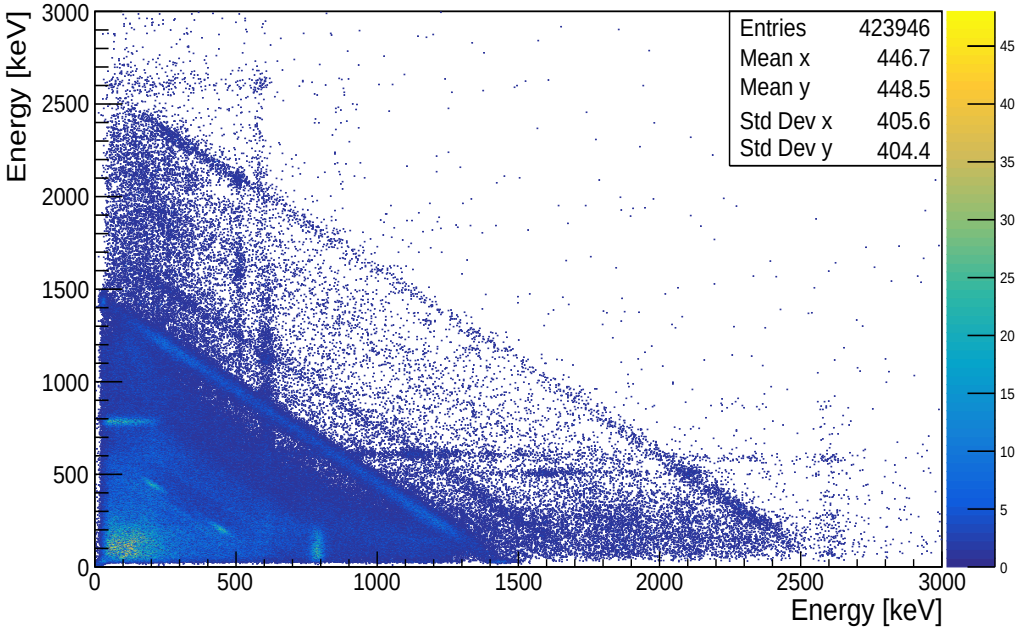

Figure B.9: Summed total gamma-gamma spectra after background subtraction for IAEA-375 soil generated using the total time gate t_T measured using four $LaBr_3$:Ce detectors without shielding.

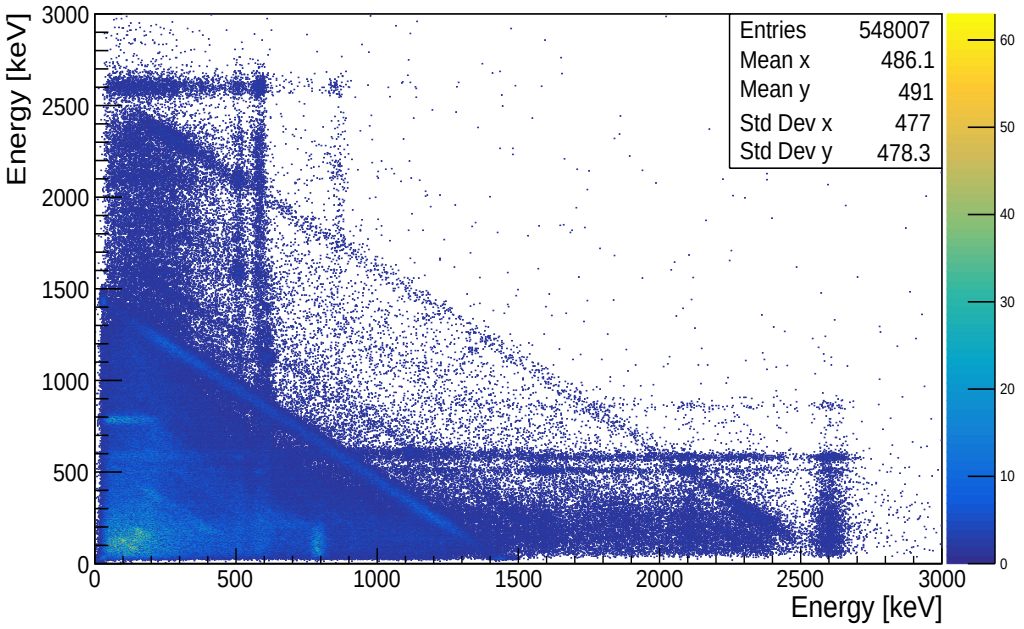

Figure B.10: Summed total gamma-gamma spectra after background subtraction for beach sand generated using the total time gate t_T measured using four $LaBr_3$:Ce detectors without shielding.

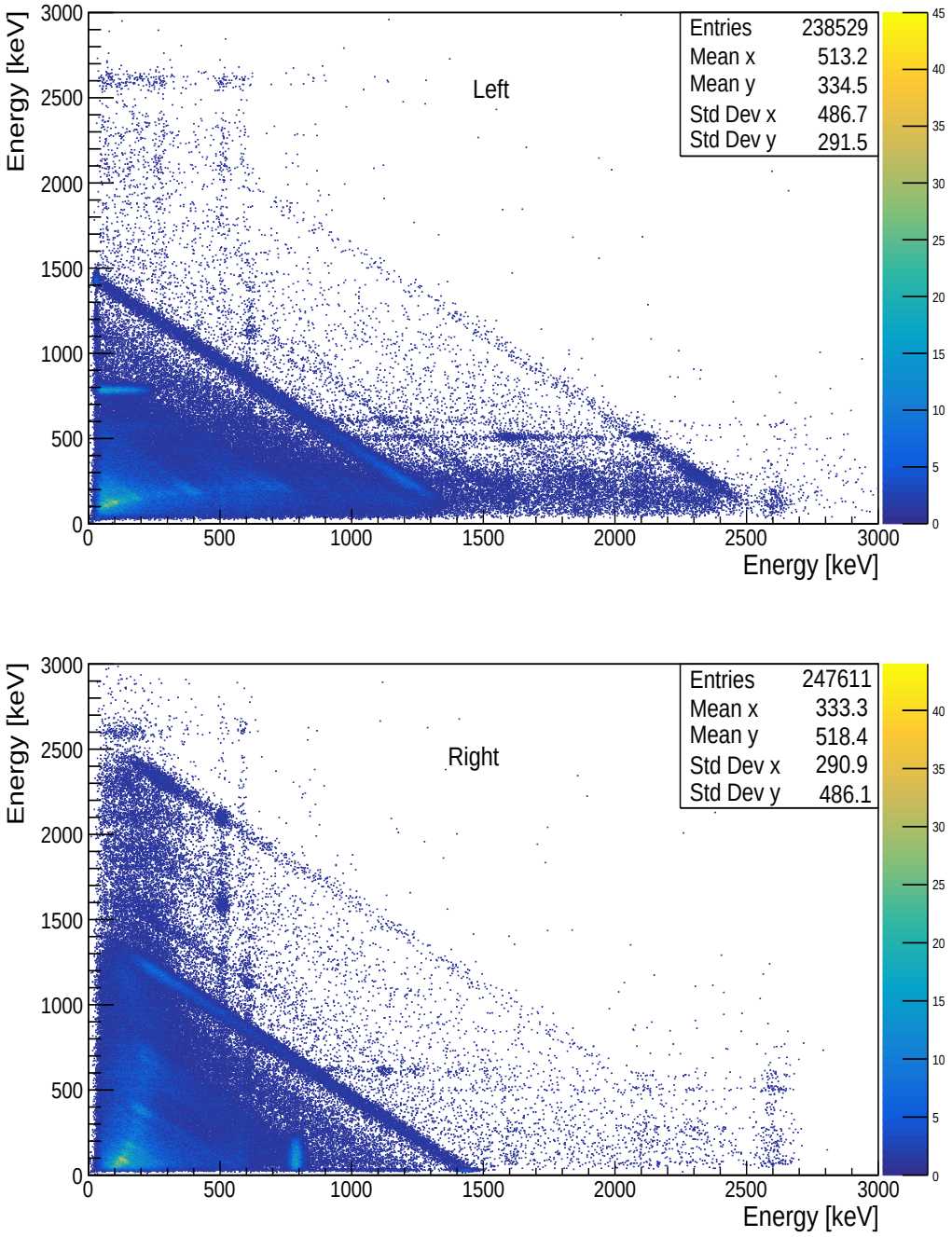

Figure B.11: Summed total gamma-gamma energy spectra for beach sand generated using the width of the peaks on either side of the centroid peak of Fig. 5.9 measured using four $LaBr_3$:Ce detectors without shielding.

Table B.2: Total counts in the gamma-gamma matrix generated using time gates t_c and t_T for two combinations of four detectors in coincidence for IAEA-375 soil and beach sand after background subtraction measured using four $LaBr_3$:Ce detectors without shielding.

Detectors in coincidence	Angle	IAEA-Counts (t_c)	375 Count (t_T)	Beach Counts (t_c)	sand Counts (t_T)
L1-L2	180^o	1338	30416	19949	56935
L1-L3	90^o	2477	118671	29816	152482
L1-L4	90^o	4849	110530	23038	143332
L2-L3	90^o	3937	115331	27561	148511
L2-L4	90^o	2826	108386	23559	141298
L3-L4	180^o	995	29635	21198	57045

Table B.3: Weighted average counts in the energy gated coincidence peaks generated using t_c and t_T measured using four $LaBr_3$:Ce detectors without shielding.

Sample	Series	Nuclide	Counts (t_c)	Counts (t_T)
IAEA-375				
	^{238}U	^{214}Bi	4.5 ± 2.1	5.5 ± 2.3
	^{232}Th	^{208}Tl	3.0 ± 1.7	3.3 ± 1.8
Beach sand				
	^{238}U	^{214}Bi	327.3 ± 18.1	331.3 ± 18.2
	^{232}Th	^{208}Tl	402.5 ± 20.1	424.3 ± 20.6

B.3 Some Spectra from Data Analysis

The data from measurement using the two $LaBr_3$:Ce detectors and NaI:Tl detector were analysed as described in Chapter 6. Some important spectra from the analysed data are shown in Figs. B.12 → B.33.

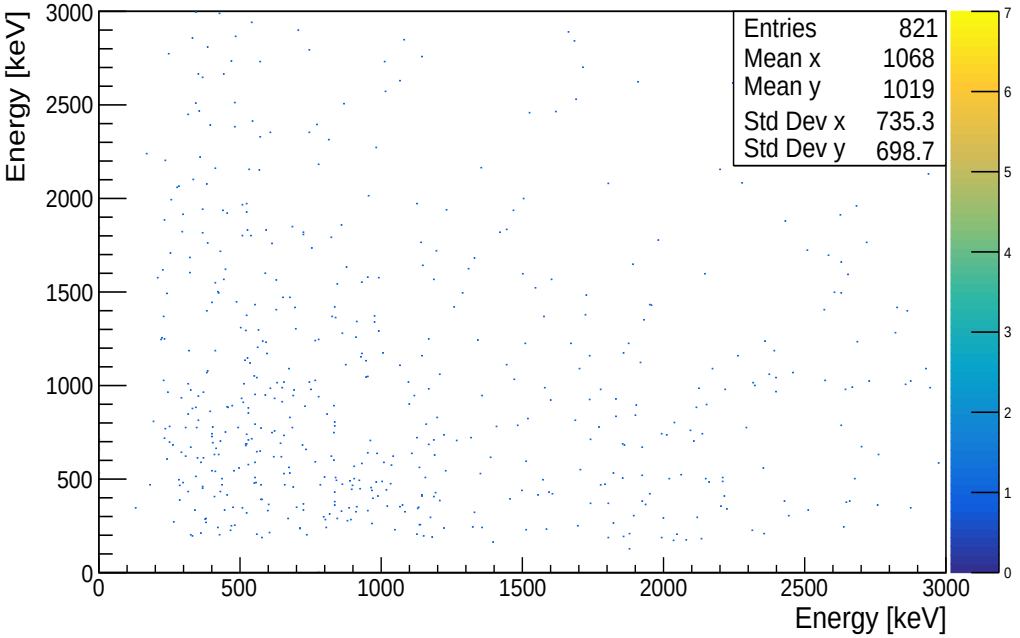

Figure B.12: Gamma-gamma spectra for background generated using the time gate t_c measured for 43200 seconds using two $LaBr_3$:Ce detectors without shielding.

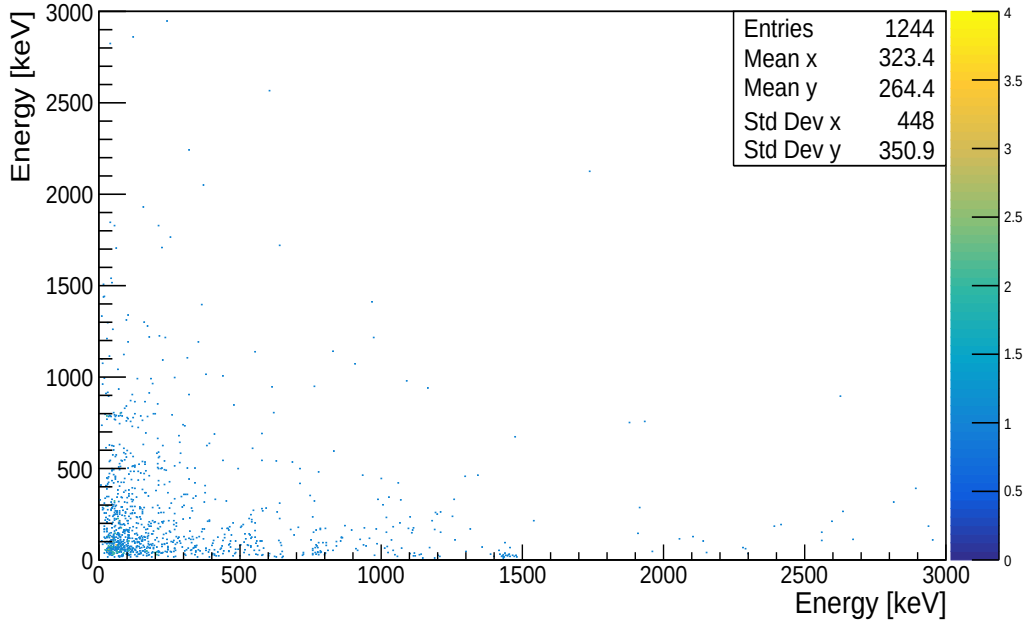

Figure B.13: Gamma-gamma spectra for background generated using the time gate t_c measured for 43200 seconds using two $LaBr_3$:Ce detectors inside the water shield.

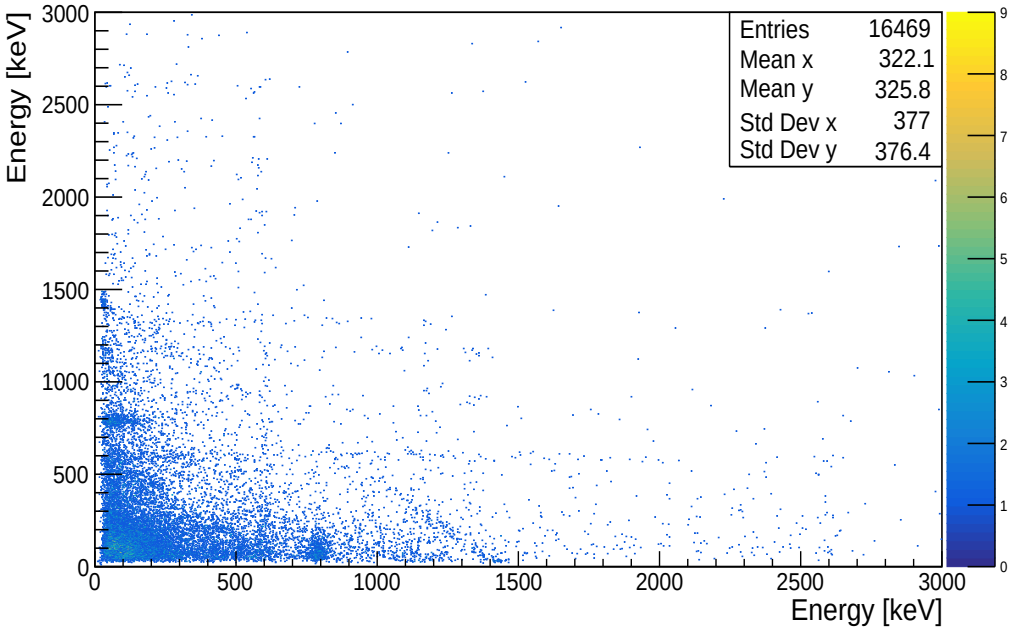

Figure B.14: Summed total gamma-gamma after background subtraction for IAEA-375 soil generated using the time gate t_c measured using four $LaBr_3$:Ce detectors without shielding.

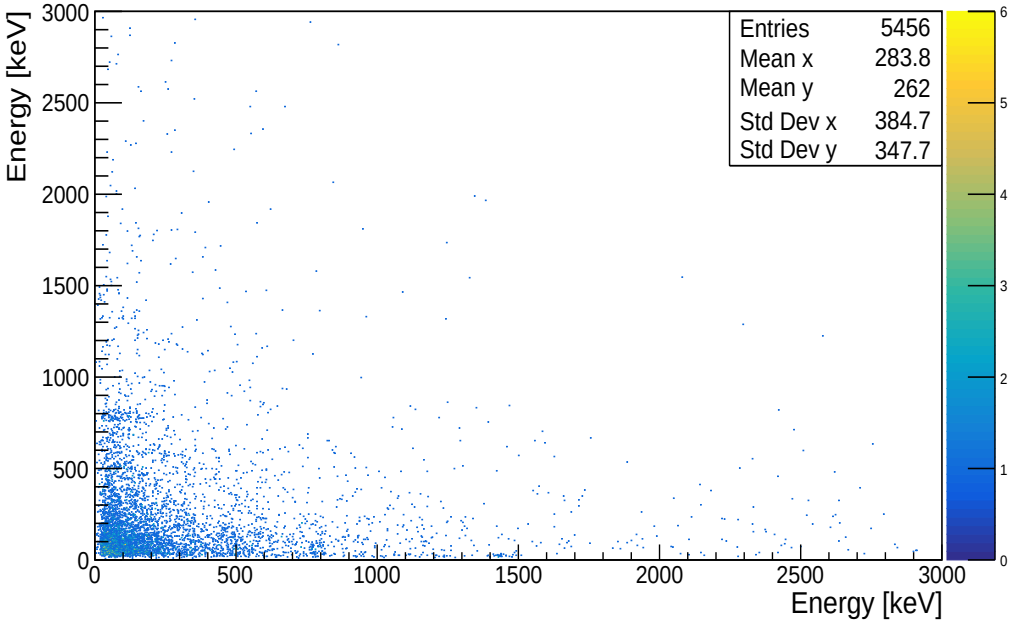

Figure B.15: Gamma-gamma spectra after background subtraction for IAEA-375 soil generated using the time gate t_c measured using two $LaBr_3$:Ce detectors inside the water shield.

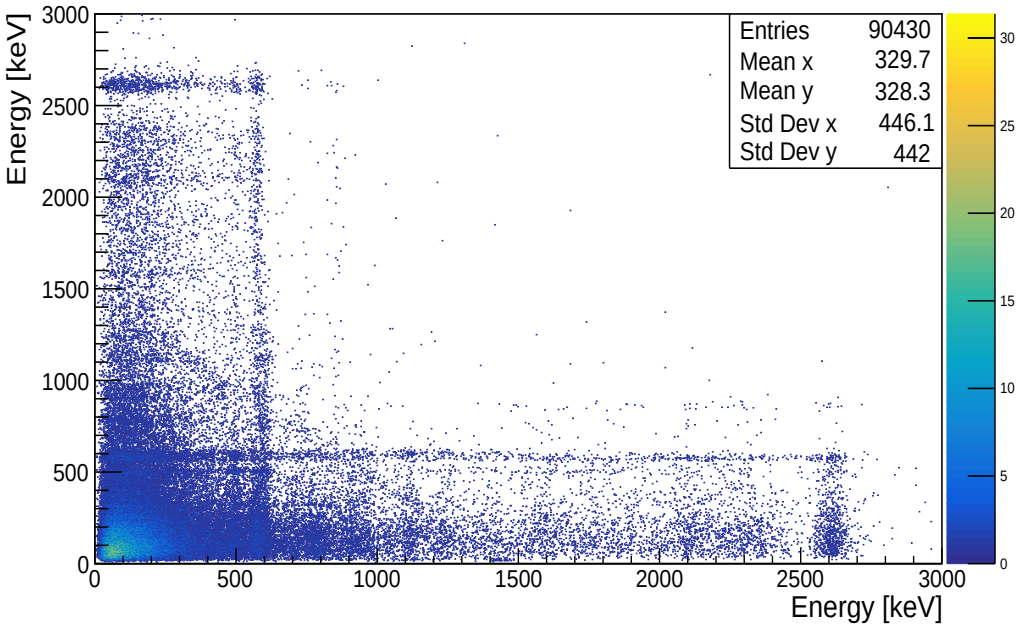

Figure B.16: Gamma-gamma spectra after background subtraction for beach sand generated using the time gate t_c measured using two $LaBr_3$:Ce detectors inside water shield.

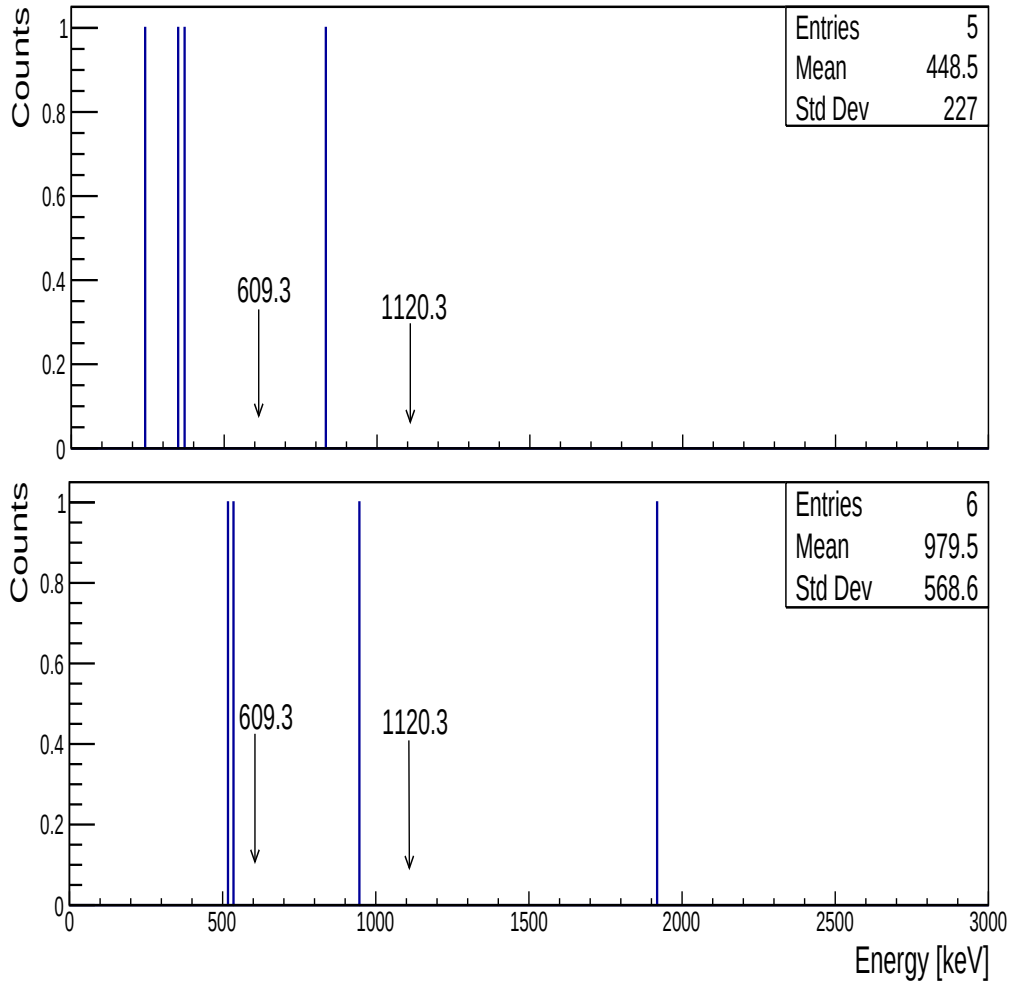

Figure B.17: Energy gated spectra (^{214}Bi): 609.3 keV (upper) and 1120.3 keV (lower) for background measured using two $LaBr_3$:Ce detectors without shielding.

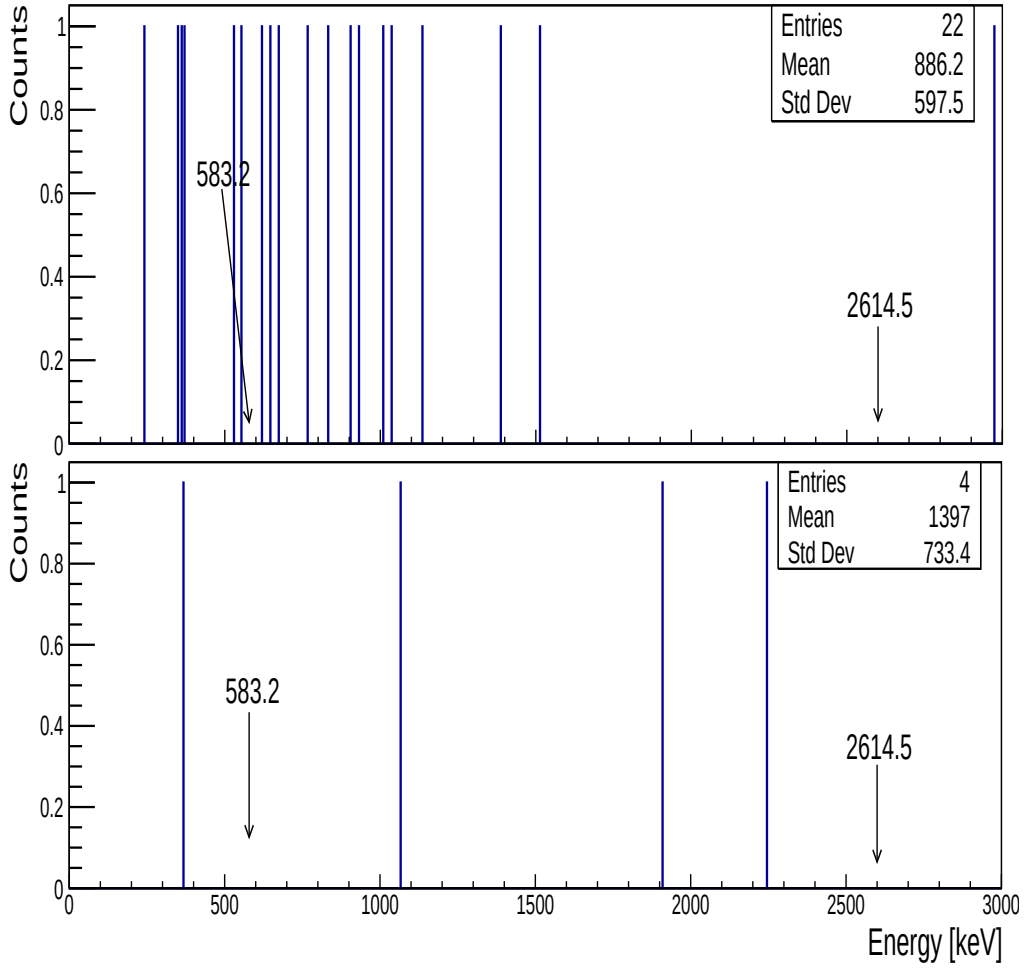

Figure B.18: Energy gated spectra (^{208}Tl): 583.2 keV (upper) and 2614.5 keV (lower) for background measured using two $LaBr_3$:Ce detectors without shielding.

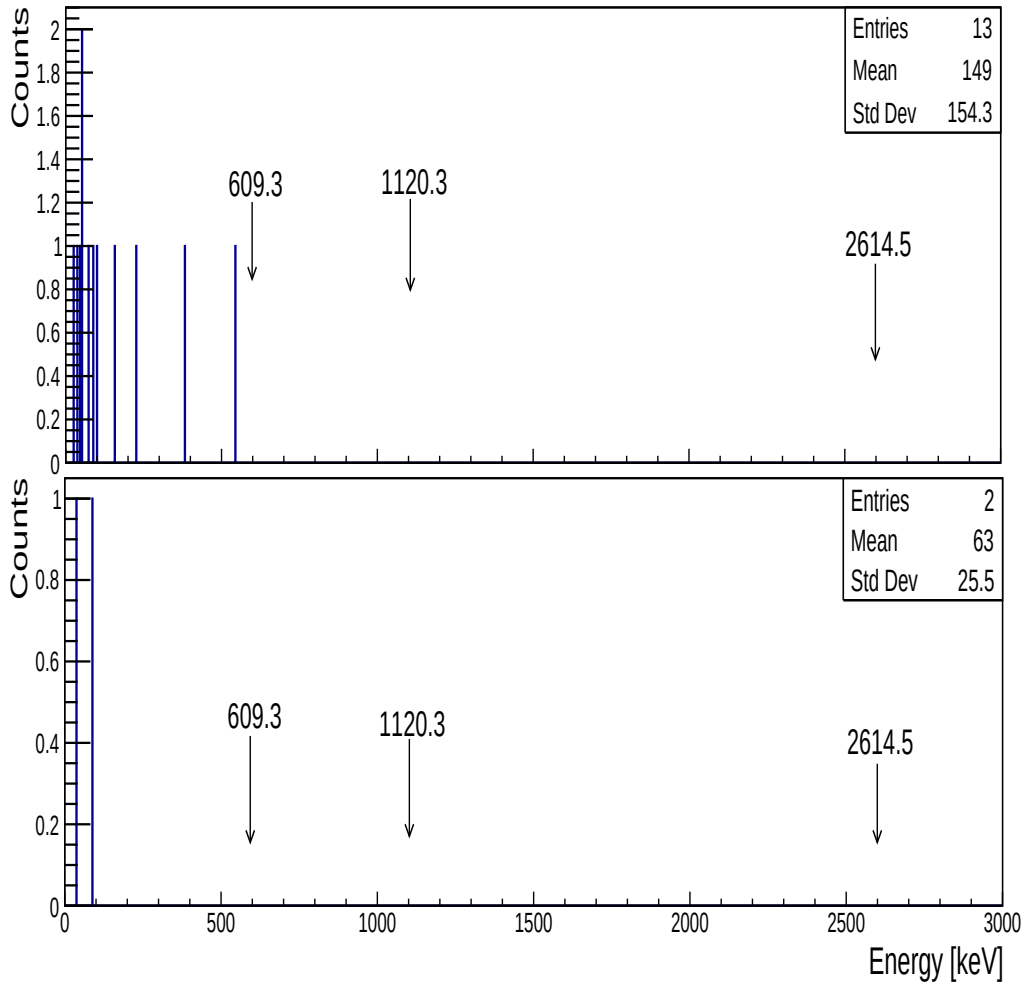

Figure B.19: Energy gated spectra (^{214}Bi): 609.3 keV (upper) and 1120.3 keV (lower) for background measured using two $LaBr_3$:Ce detectors inside the water shield.

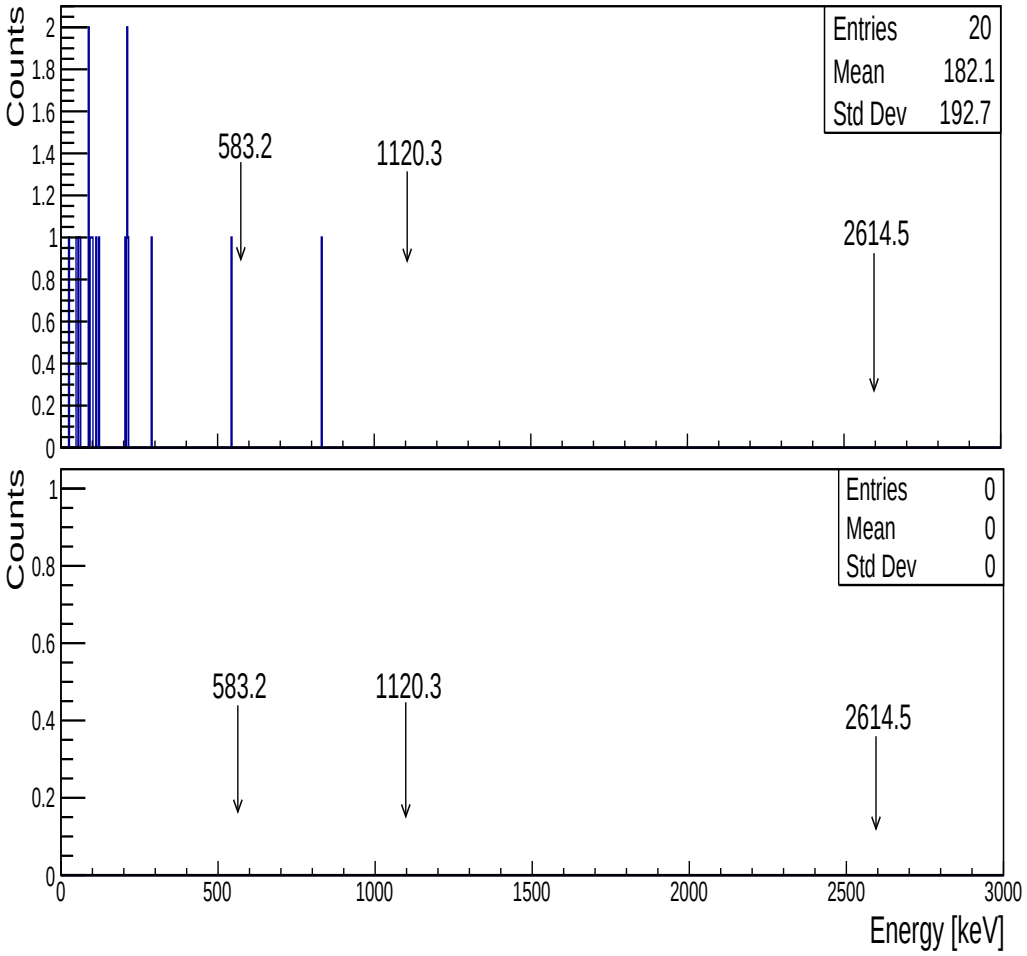

Figure B.20: Energy gated spectra (^{208}Tl): 583.2 keV (upper) and 2614.5 keV (lower) for background measured using two $LaBr_3$:Ce detectors inside the water shield.

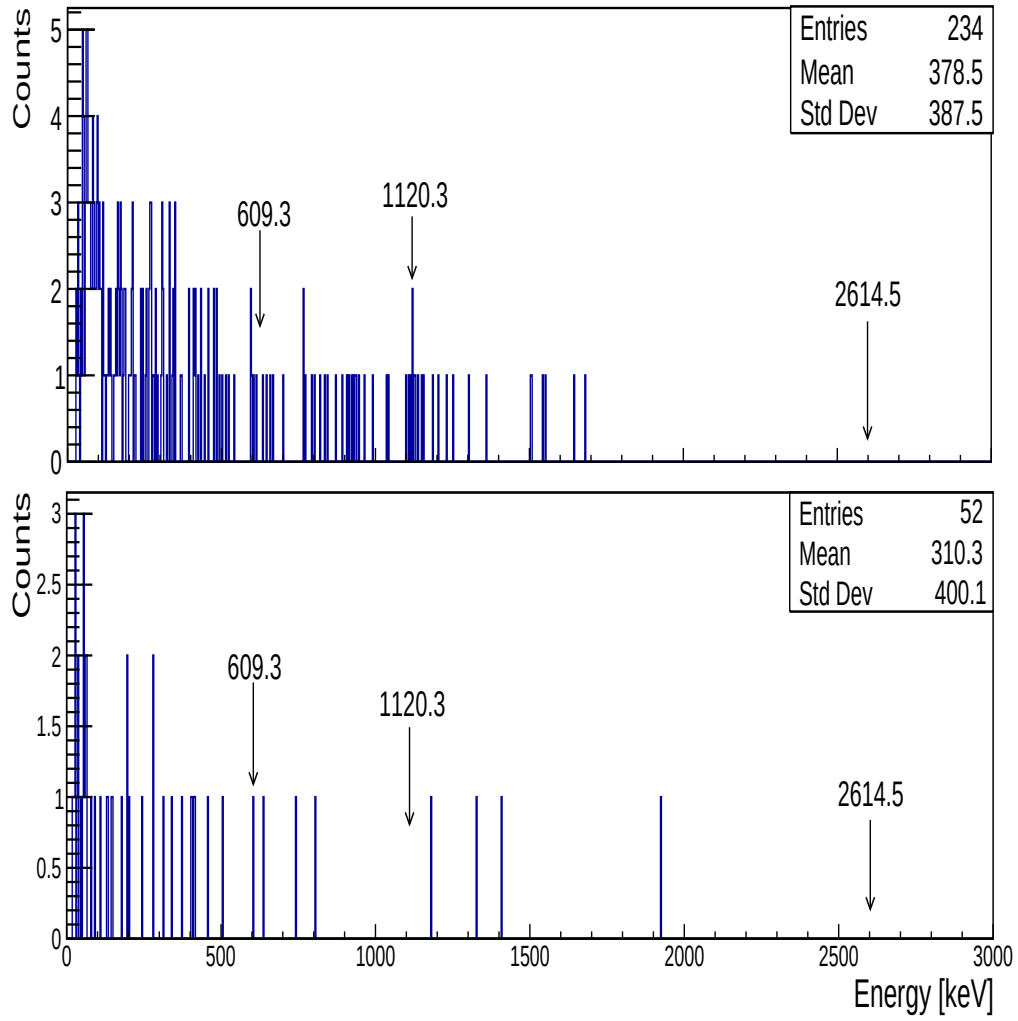

Figure B.21: Energy gated spectra (^{214}Bi): 609.3 keV (upper) and 1120.3 keV (lower) for IAEA-375 soil measured using four $LaBr_3$:Ce detectors without shielding.

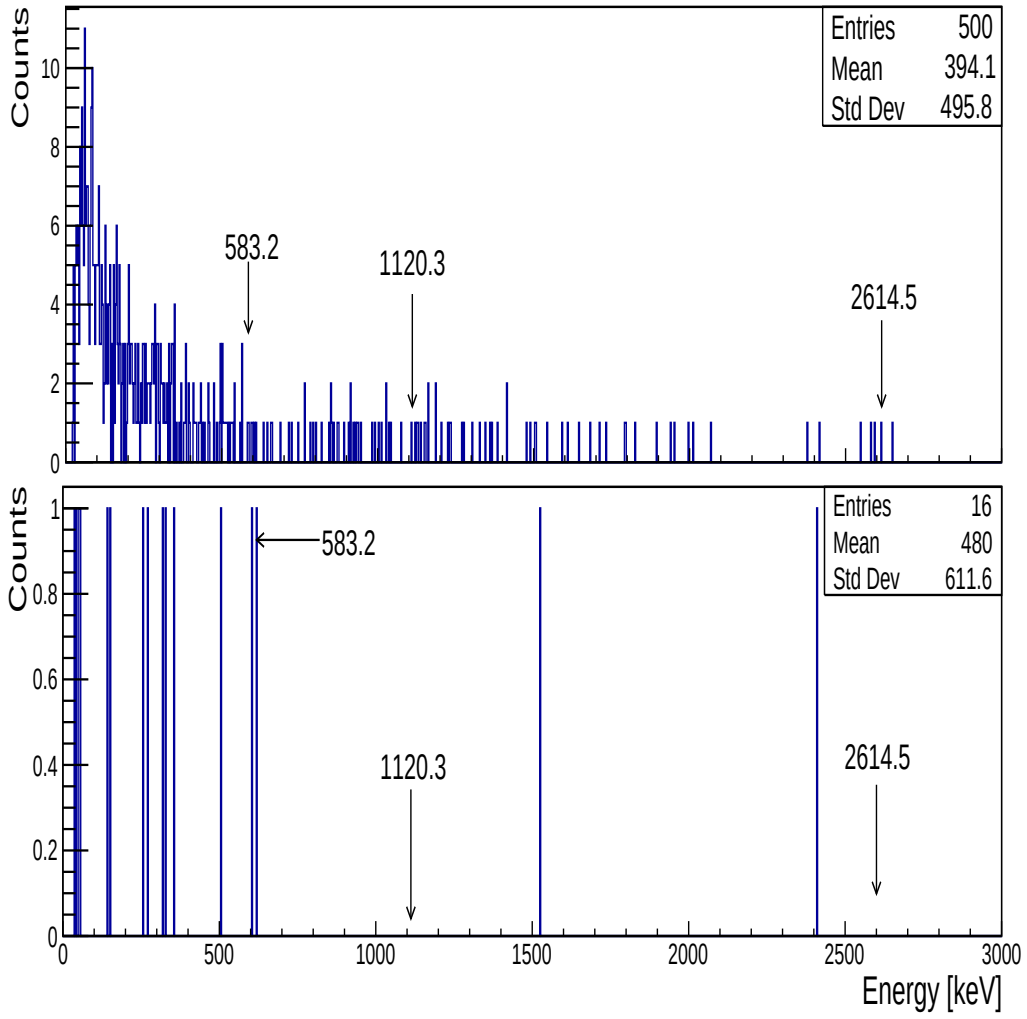

Figure B.22: Energy gated spectra (^{208}Tl): 583.2 keV (upper) and 2614.5 keV (lower) for IAEA-375 soil measured using four $LaBr_3$:Ce detectors without shielding.

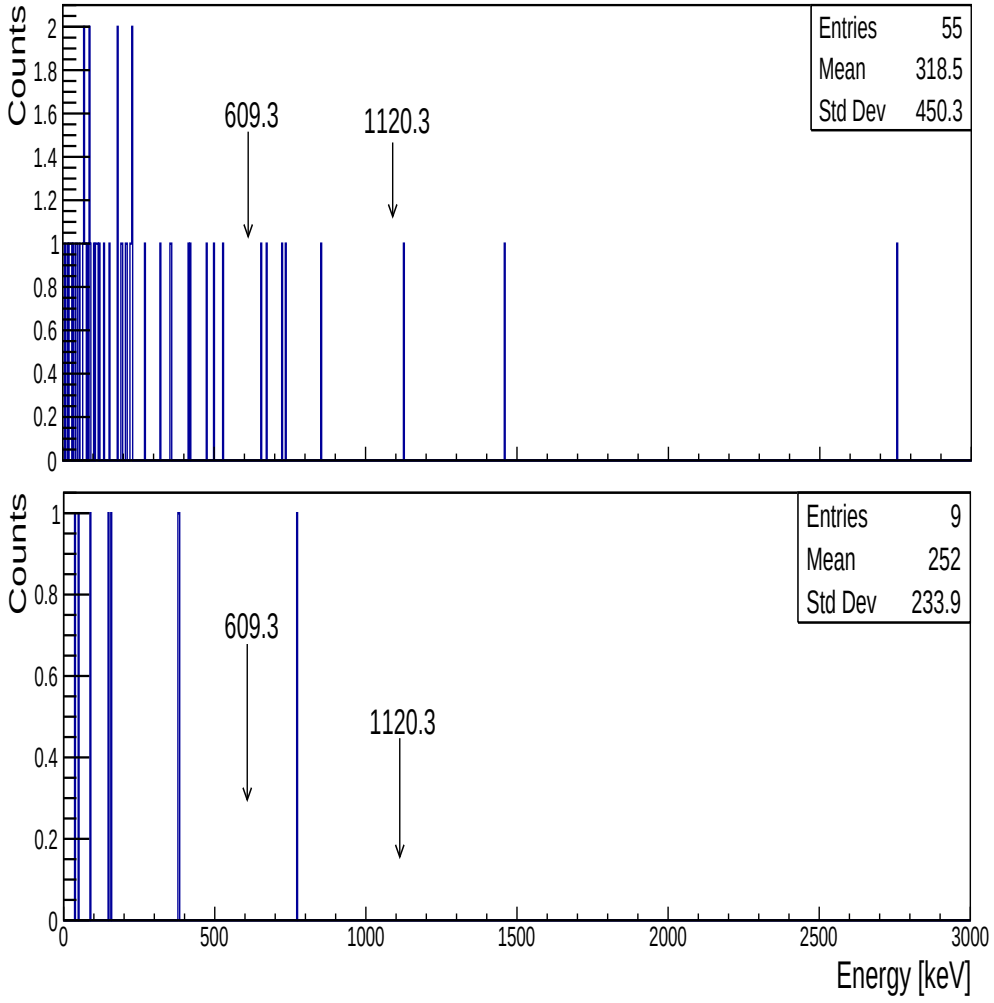

Figure B.23: Energy gated spectra (^{214}Bi): 609.3 keV (upper) and 1120.3 keV (lower) for IAEA-375 soil measured using two $LaBr_3$:Ce detectors inside water shield.

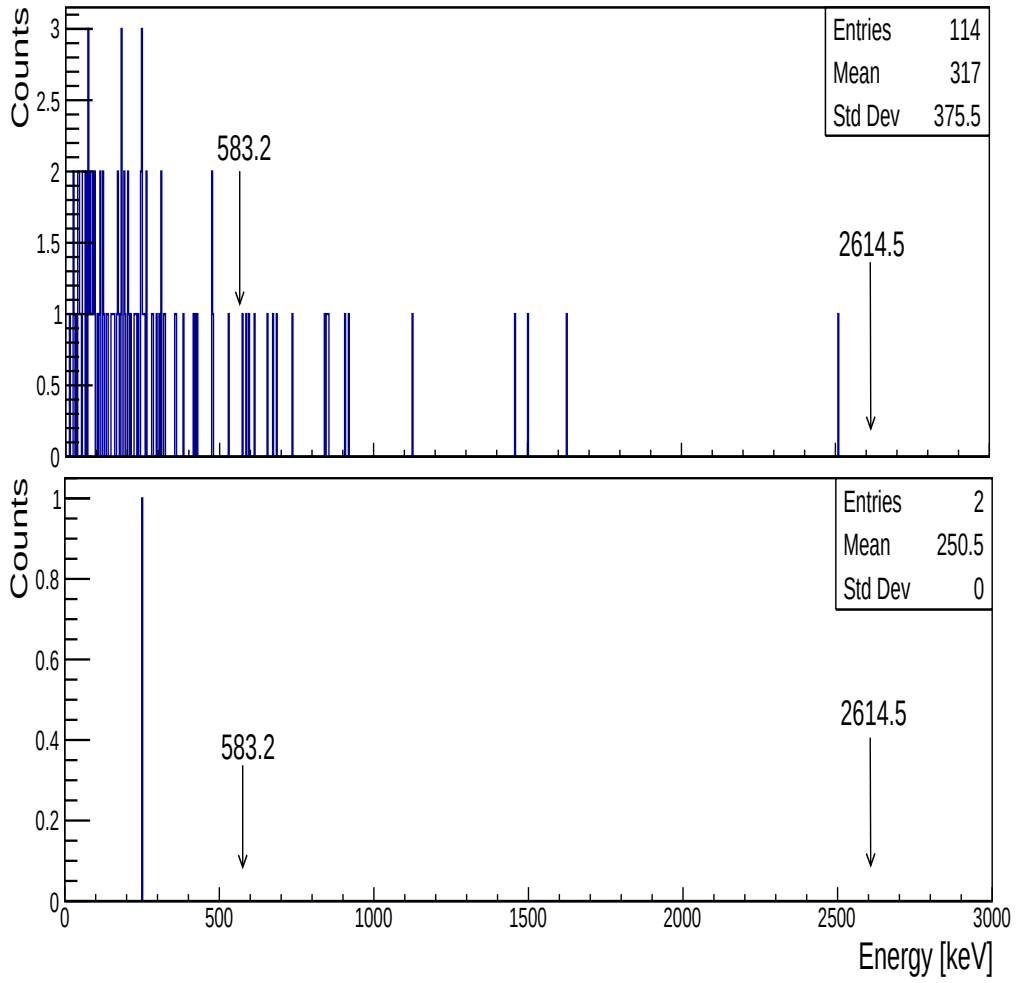

Figure B.24: Energy gated spectra (^{208}Tl): 583.2 keV (upper) and 2614.5 keV (lower) for IAEA-375 soil measured using two $LaBr_3$:Ce detectors inside water shield.

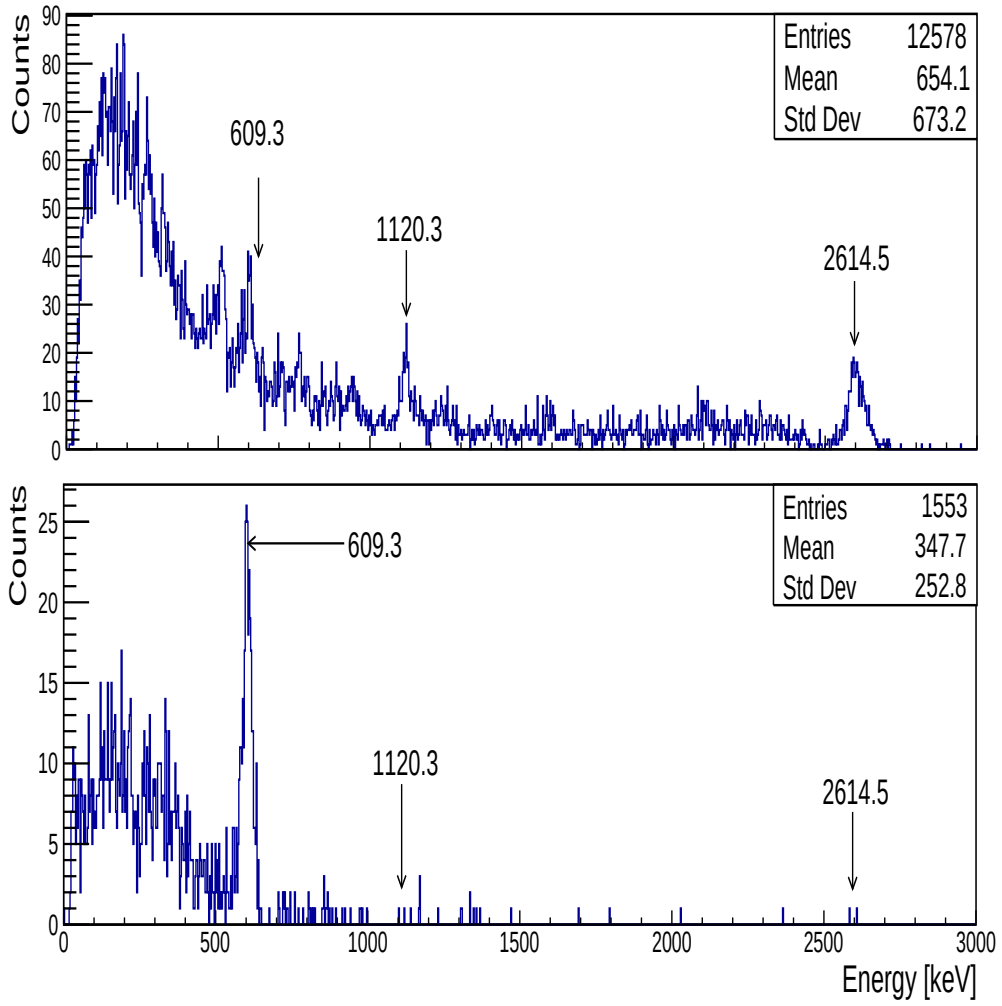

Figure B.25: Energy gated spectra (^{214}Bi): 609.3 keV (upper) and 1120.3 keV (lower) for beach sand measured using four $LaBr_3$:Ce detectors without shielding.

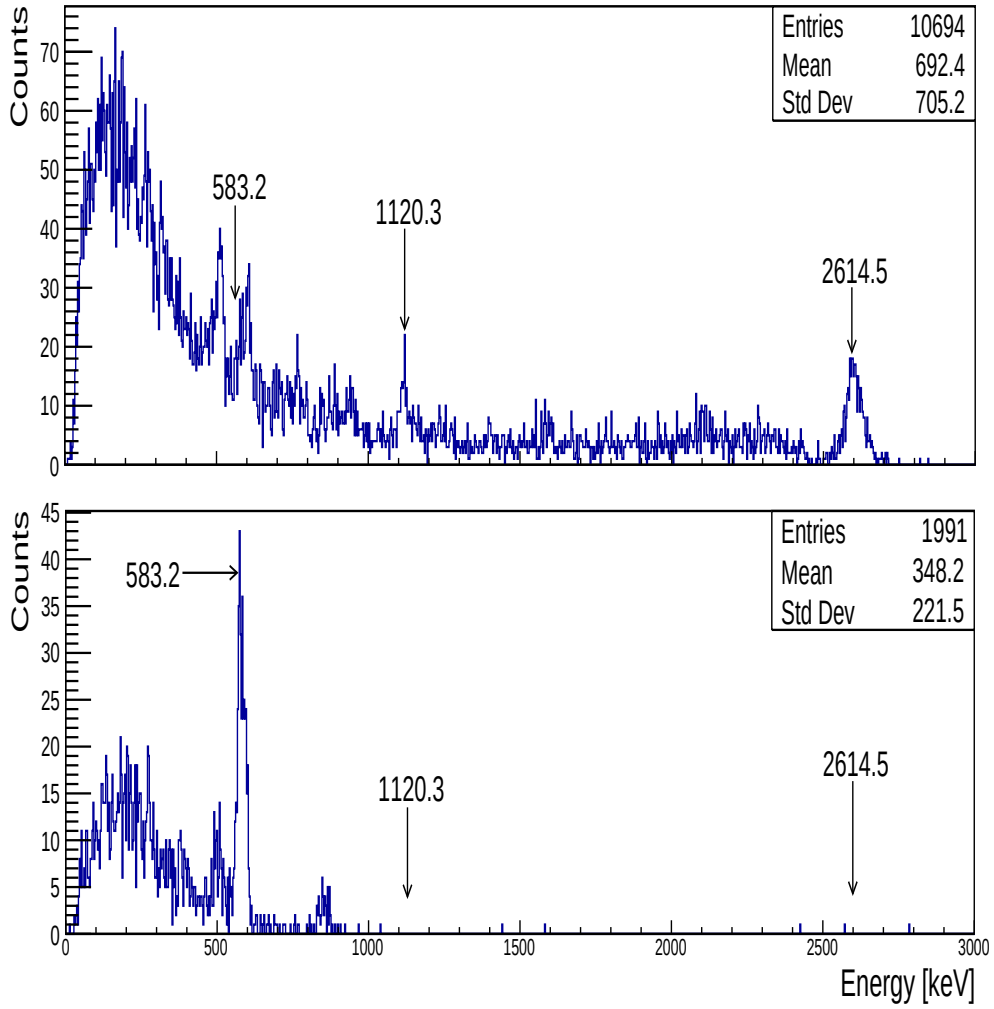

Figure B.26: Energy gated spectra (^{208}Tl): 583.2 keV (upper) and 2614.5 keV (lower) for beach sand measured using four $LaBr_3$:Ce detectors without shielding.

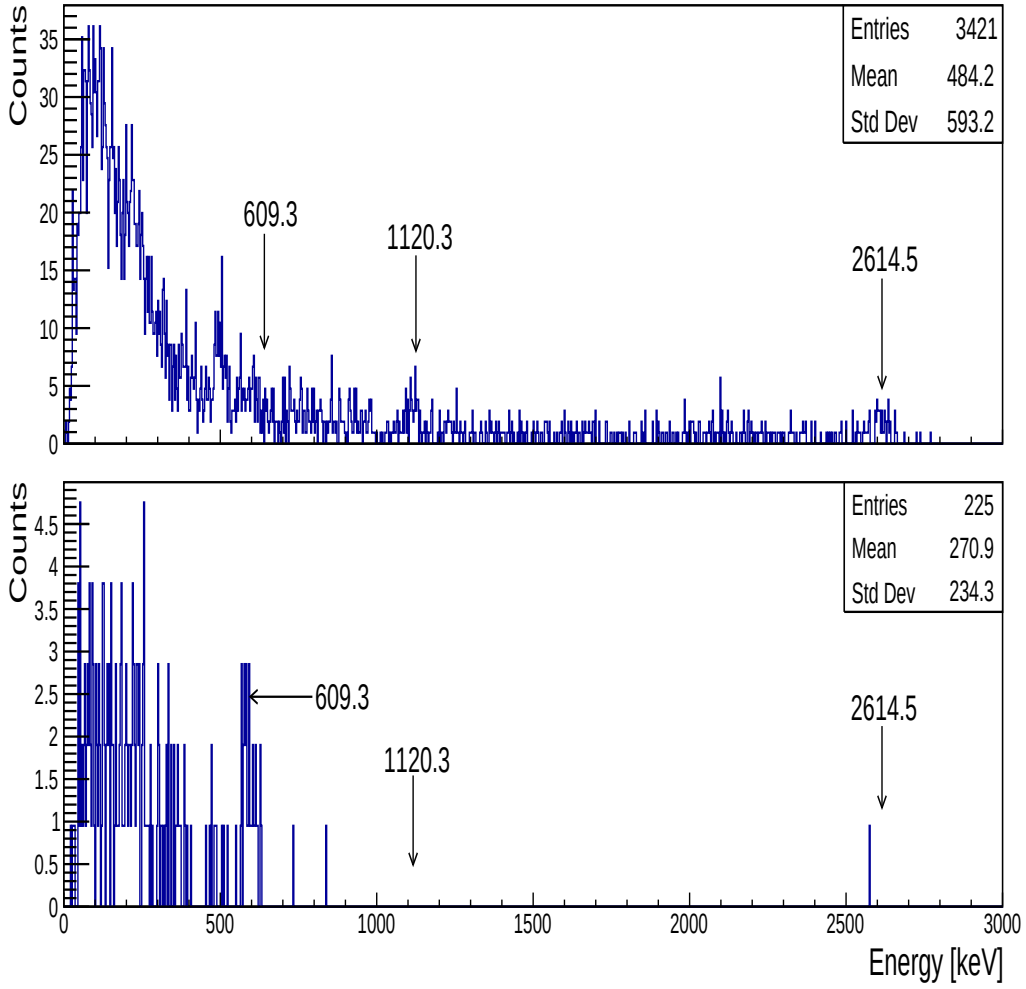

Figure B.27: Energy gated spectra (^{214}Bi): 609.3 keV (upper) and 1120.3 keV (lower) for beach sand measured using two $LaBr_3$:Ce detectors inside water shield.

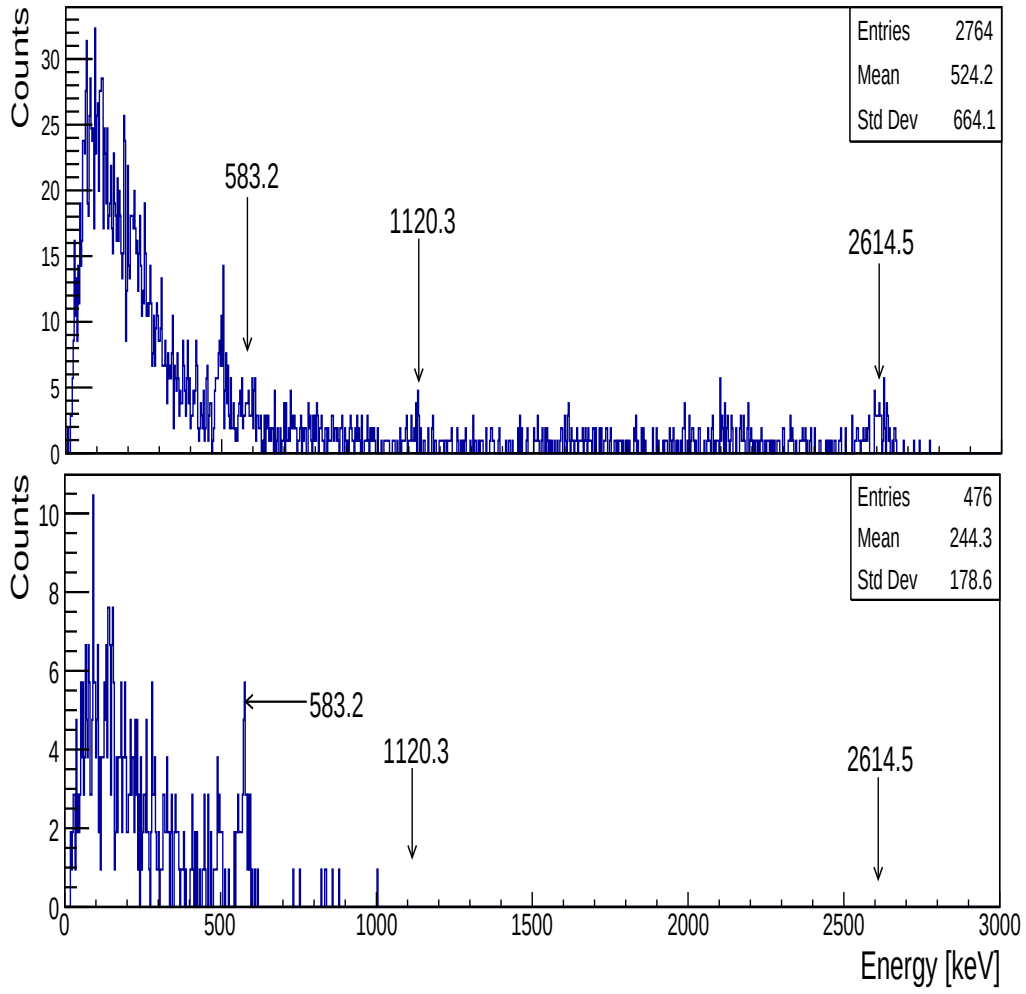

Figure B.28: Energy gated spectra (^{208}Tl): 583.2 keV (upper) and 2614.5 keV (lower) for beach sand measured using two $LaBr_3$:Ce detectors inside water shield.

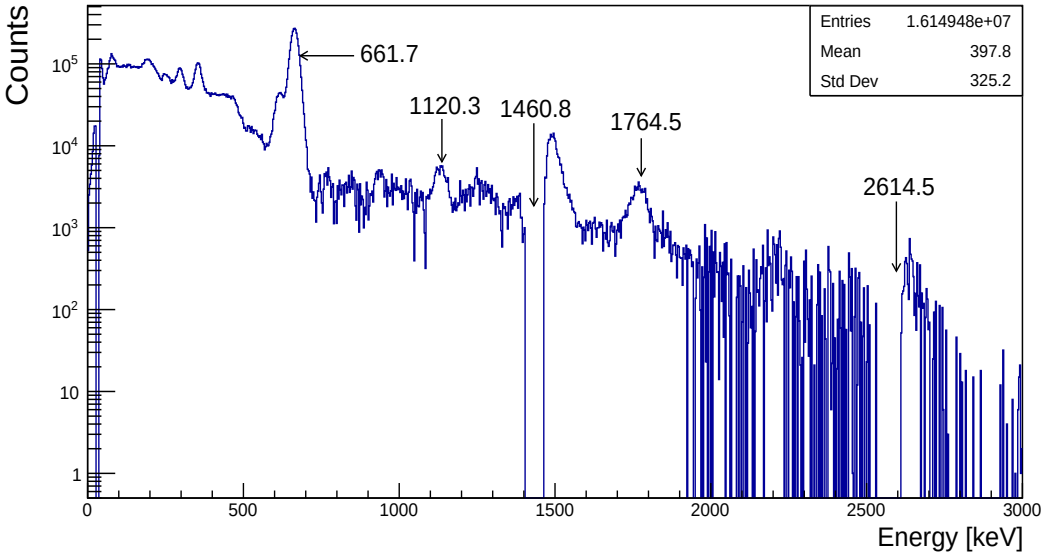

Figure B.29: Summed total gamma-ray spectra after background subtraction for IAEA-375 soil measured using four $LaBr_3$:Ce detectors without shielding.

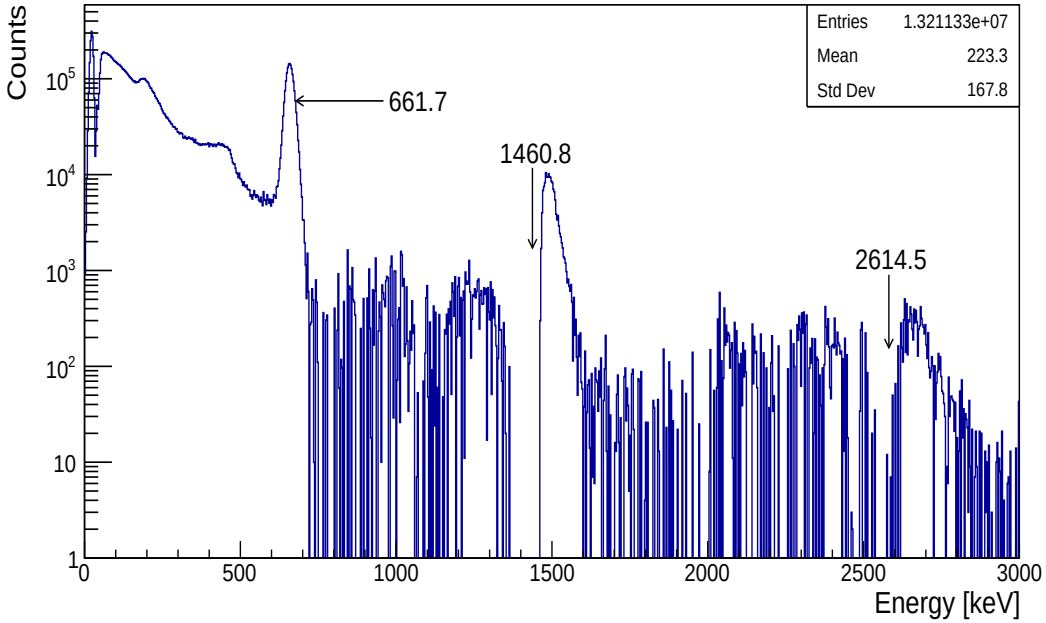

Figure B.30: Summed total gamma-ray spectra after background subtraction for IAEA-375 soil measured using two $LaBr_3$:Ce detectors inside the water shield.

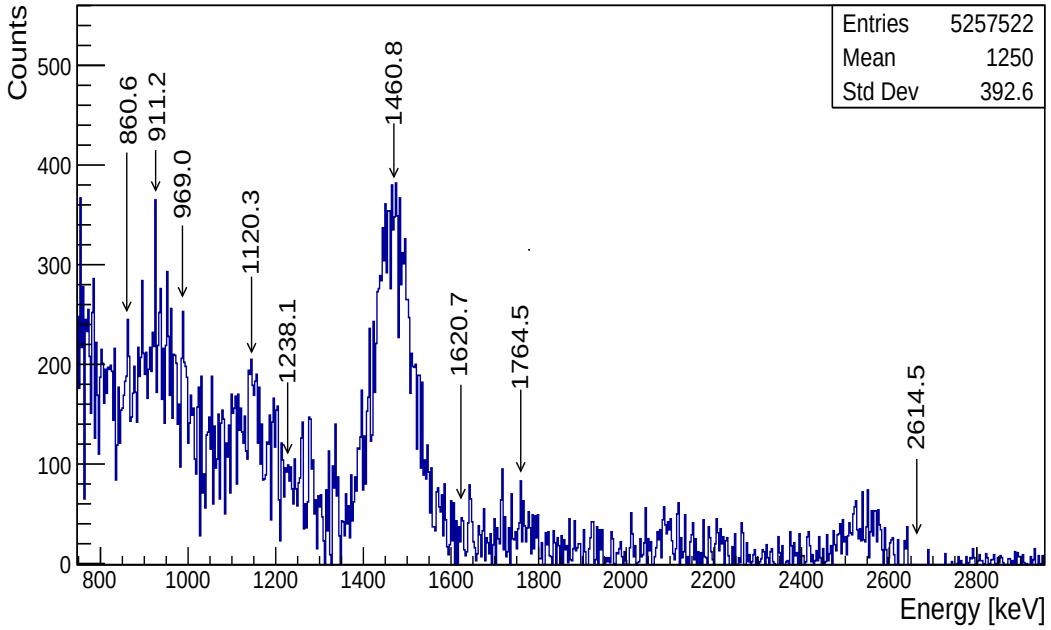

Figure B.31: Gamma-ray spectrum after background subtraction for IAEA-375 soil measured using NaI:Tl detector inside the water shield.

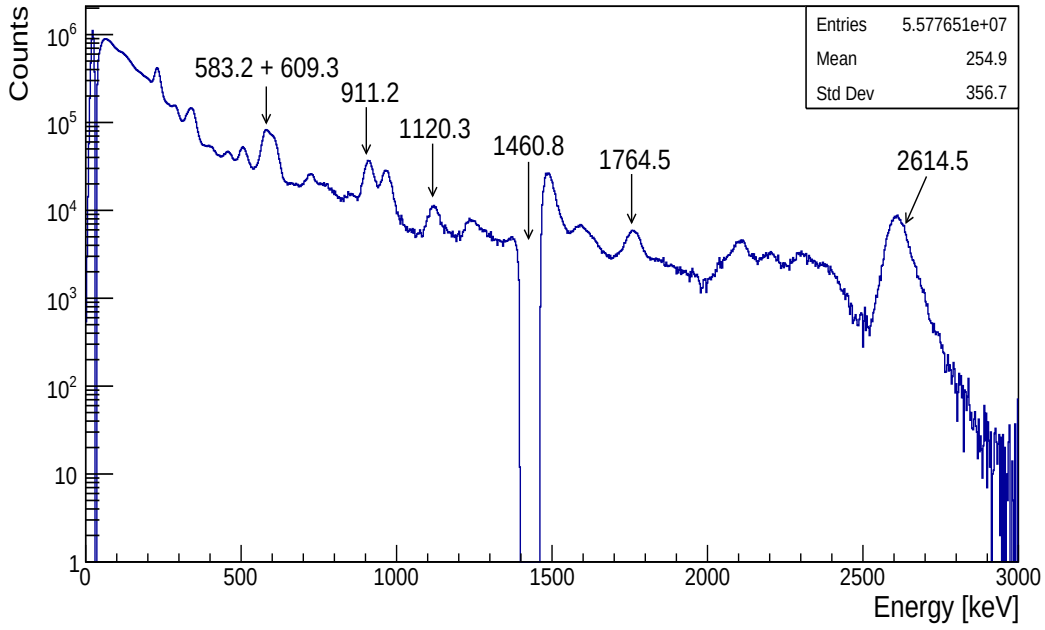

Figure B.32: Summed total gamma-ray spectra after background subtraction for beach sand measured using two $LaBr_3$:Ce detectors inside the water shield.

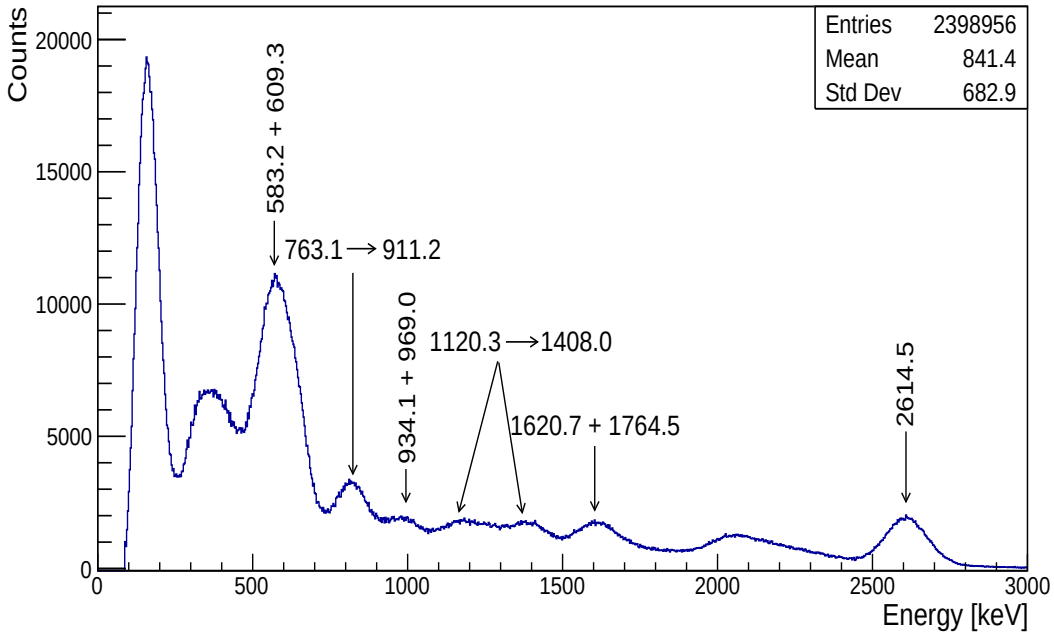

Figure B.33: Gamma-ray spectrum after background subtraction for beach sand measured using NaI:Tl detector inside the water shield.

Appendix C

Publications and Presentations stemming from this study

C.1 Journal paper

Determination of activity concentration of ^{238}U and ^{232}Th series radionuclides in soil using a gamma-ray spectrometer in singles and coincidence modes; M. Bashir, R. T. Newman and P. Jones (2019). Applied Radiation and Isotopes. vol. 154 page 1-11. https://doi.org/10.1016/j.apradiso.2019.108880.

C.2 Peer reviewed conference paper

Measurements of natural radioactivity in soil using an array of cerium doped lanthanum bromide scintillator detectors; M Bashir, R. T. Newman and P. Jones (2017). The proceedings of SAIP2017, the 62nd Annual Conference of South African Institute of Physics, Division B Nuclear, Particle and Radiation Physics, 131-134 ISBN:978-0-620-82077-6.

C.3 Presentations

1. M. Bashir, R. T. Newman, P. Jones; Measurement of activity concentrations of ^{238}U and ^{232}Th series radionuclides in beach sand with a multidetector ($LaBr_3$:Ce) gamma-ray spectrometer, African Nuclear Physics Conference (ANPC), Kruger national park. South Africa, 1-5 June 2019.

2. M. Bashir, R. T. Newman, P. Jones; Measurement of activity concentration of ^{238}U and ^{232}Th series radionuclides in beach sand with a multidetector ($LaBr_3$:Ce) gamma-ray spectrometer, Advanced Nuclear Science and Technology Techniques (ANSTT2) workshop, Cape Town. South Africa, March 18-20 2019.

3. M. Bashir, R. T. Newman, P. Jones; Gamma-gamma coincidence measurements of naturally occurring radioactive materials. 6th International Conference on Collective Motion in Nuclei under Extreme Conditions (COMEX6), Cape Town. South Africa, 29 October 2018 - 2 November 2018.

4. M. Bashir, R. T. Newman, P. Jones; Determination of Buildup Factors associated with ^{60}Co gamma-rays interacting with water. Poster presentation at 1st Biennial African Conference on Fundamental Physics and Applications 28 June - 4 July and 5th African School of Fundamental Physics and Applications, Windhoek, Namibia. 25 June - 14 July 2018.

5. M. Bashir, R. T. Newman, P. Jones; Environmental sample measurement using two cerium doped lanthanum bromide scintillator detectors. Advanced Nuclear Science and Technology Techniques (ANSTT) workshop, Cape Town. South Africa, March 5-9 2018

6. M. Bashir, R. T. Newman, P. Jones; Measurements of natural radioactivity

in soil using an array of 2 in. by 2 in. cerium doped lanthanum bromide scintillator detectors. Presented at the 62nd annual conference of the South African Institute of Physics in Stellenbosch University, South Africa. 3 -7 July, 2017 and South Africa-China Symposium, Kwazulu-Natal, South Africa. 5-7 August 2017.

Bibliography

[1] World Health Organization, Ionizing radiation. `https://www.who.int/ionizing_radiation/en/`.

[2] Valkonic, V.: *Radioactivity in the environment.* Pp. 9, 11, 14, 15, 33 - 35. 1st edn. Elsevier science B. V, 2000.

[3] Lee, C.-J. and Chung, C.: Determination of ^{134}Cs in environmental samples using a coincidence gamma-ray spectrometer. *Applied Radiation Isotopes, Int. J. Radiat. Appl. Instrum. Part A*, vol. 49 (9), pp. 783 – 788, 1991.

[4] Dababneh, S., Al-Nemri, E. and Sharaf, J.: Application of GEANT4 in routine close geometry gamma spectroscopy for environmental samples. *Journ. of Environmental Radioactivity*, vol. 134, pp. 27 – 34, 2014.

[5] Sykora, I., Jeskovsky, M., Janik, R., Holy, K., Chudy, M. and Provinec, P.: Low-level single and coincidence gamma-ray spectrometry. *Journal of Radioanalytical and Nuclear Chemistry*, vol. 276, pp. 779 – 787, 2008.

[6] Wieslander, J.E., Hult, M., Gasparro, J., Marissens, G., Misiaszek, M. and Preusse, W.: The Sandwich spectrometer for ultra low-level γ-ray spectrometry. *Applied Radiation and Isotopes*, vol. 67, pp. 731 – 735, 2009.

[7] Lutter, G., Hult, M., Marissens, G., Andreotti, E., Rosengard, U., Misiaszek, M., Yuksel, A. and Sahin, N.: A new versatile underground gamma-ray spec-

trometry system. *Nuclear Instruments and Methods in Physics Research A*, vol. 610, pp. 522 – 529, 2009.

[8] Kohler, M., Degering, D., Laubenstein, M., Quirin, P., Lampert, M.-O., Hult, M., Arnold, D., Neumaier, S. and Reyss, J.-L.: A new low-level γ-ray spectrometry system for environmental radioactivity at the underground laboratory felsenkeller. *Applied Radiation and Isotopes*, vol. 67, pp. 736 – 740, 2009.

[9] Kozak, K., Mietelski, J.W., Jasifska, M. and Gaca, P.: Decreasing of the natural background counting - passive and active method. *NUKLEONIKA PROCEEDINGS*, vol. 46(4), pp. 165 – 169, 2001.

[10] Povinec, P.P.: Low-level gamma-ray spectrometry for environmental samples. *Journal of Radioanalytical and Nuclear Chemistry*, vol. 276 (3), pp. 771 – 777, 2008.

[11] Joel, G.S.C., Penabei, S., Ndontchueng, M.M., Chene, G., Menkontso, E.J.N., Ebongue, A.N., Ousmanou, M. and David, S.: Precision measurement of radioactivity in gamma-rays spectrometry using two HPGe detectors (BEGe-6530 and GC0818-7600sl models) comparison techniques: Application to the soil measurement. *MethodsX*, vol. 4, pp. 42 – 54, 2017.

[12] Gilmore, G.R.: *Practical Gamma-ray Spectrometry*. Pp. 25 - 37, 40, 108 - 110, 114 - 122, 131 - 134, 151 - 154, 165 - 168, 199, 206 - 212, 237, 315 - 321. 2nd edn. John Wiley and Sons, Ltd., 2008.

[13] L'Annunziata, M.F.: *Handbook of Radioactivity Analysis*. Pp. 71 - 77, 240, 241, 265 - 267, 847 - 854. 2nd edn. Academic Press, 2004.

[14] Keillor, M.E., Aalseth, C., Arnquist, I., Eggemeyer, T., Fuller, E., Glasgow, B., Hoppe, E., Morle, S., Myers, A., Orrell, J., Overman, C., Seifert, A., Shaff, S. and Thommasson, K.: Recent Bremsstrahlung-based assays of ^{210}Pb in lead

and comments on current availability of low-background lead in north america. *Applied Radiation and Isotopes*, vol. 126, pp. 185 – 187, 2017.

[15] Knoll, G.F.: *Radiation Detection and Measurement*. Pp. 50 - 56, 114 - 116, 119, 120 - 125, 227 - 234, 251- 253, 292, 296, 297, 301, 337 - 349. 2nd edn. John Willey and Sons, Inc, 1989.

[16] Metwally, W., Mayo, C., Han, X. and Gardner, R.: Coincidence counting for PGNAA applications: Is it the optimum method? *Journal of Radionalytical and Nuclear Chemistry*, vol. 265, pp. 309 – 314, 2005.

[17] Drescher, A., Yoho, M., Landsberger, S., Durban, M., Biegalski, S., Meier, D. and Schwantes, J.: Gamma-gamma coincidence performance of $LaBr_3$:Ce scintillation detectors vs HPGe in high count-rate scenerios. *Applied Radiation and Isotopes*, vol. 122, pp. 116 – 120, 2017.

[18] Zhang, W., Yi, J., Mekarski, P., Ungar, K., Hauck, B. and Kramer, G.H.: A gamma-gamma coincidence spectrometric method for rapid characterization of uranium isotopic fingerprints. *Journal Radioanalytical Nuclear Chemistry*, vol. 288, pp. 43 – 47, 2011.

[19] Antovic, N. and Svrkota, N.: Development of a method for activity measurements of ^{232}Th daughters with a multidetector gamma-ray coincidence spectrometer. *Applied Radiation and Isotopes*, vol. 67, pp. 1133 – 1138, 2009.

[20] Antovic, N. and Svrkota, N.: Measuring the ^{226}Ra activity using a multidetector γ-ray coincidence spectrometer. *Journal of Environmental Radioactivity*, vol. 100, pp. 823 – 830, 2009.

[21] Britton, R., Burnett, J., Davies, A. and Regan, P.: Coincidence corrections for a multi-detector gamma spectrometer. *Nuclear Instruments and Methods in Physics Research A*, vol. 769, pp. 20 – 25, 2015.

[22] Britton, R., Jackson, M. and Davies, A.: Quantifying radionuclide signatures from a $\gamma - \gamma$ coincidence system. *Journal of Environmental Radioactivity*, vol. 149, pp. 158 – 163, 2015.

[23] Paradis, H., de Vismes Otta, A., Cagnata, X., Piquemal, F. and Gurriaran, R.: Leda: A gamma-gamma coincidence spectrometer for the measurement of environment samples. *Applied Radiation and Isotopes*, vol. 126, pp. 179 – 184, 2017.

[24] Markovic, N., Roos, P. and Nielsen, S.P.: Digital gamma-gamma coincidence HPGe system for environmental analysis. *Applied Radiation and Isotopes*, vol. 126, pp. 194 – 196, 2017.

[25] Tillet, A., Benninger, L., Dermigny, J. and Iliadis, C.: Measurements of thorium and uranium daughters in radioenvironmental samples using $\gamma\gamma$ spectrometry. *Applied Radiation and Isotopes*, vol. 141, pp. 24 – 32, 2018.

[26] Anil, G.K., Mazumdar, I. and Gothe, D.: Experimental measurements and GEANT4 simulations for a comparative study of efficiencies of $LaBr_3$:Ce, NaI(Tl), and BaF_2. *Applied Radiation and Isotopes*, vol. 81, pp. 81 – 86, 2013.

[27] Favalli, A., Mehner, H.-C., Ciriello, V. and Pedersen, B.: Investigation of the PGNAA using the $LaBr_3$:Ce scintillation detector. *Applied Radiation and Isotopes*, vol. 68, pp. 901 – 904, 2010.

[28] Vedia, V., Carmona-Gallardo, M., Fraile, L., Mach, H. and Udias, J.: Performance evaluation of novel $LaBr_3$(Ce) scintillator geometries for fast-timing applications. *Nuclear Instruments and Methods in Physics Research A*, vol. 857, pp. 98 – 105, 2017.

[29] Dorenbos, P. and *et al.*: Gamma ray spectroscopy with a $\phi 19 \times 19$ mm^3 $LaBr_3$: 0.5 % Ce^{3+} scintillator. *IEEE Transactions on Nuclear Science*, vol. 51(3), pp. 1289 – 1296, 2004.

[30] Bashir, M., Newman, R.T. and Jones, P.: Measurements of natural radioactivity in soil using an array of cerium doped lanthanum bromide scintillator detectors. In: *The proceedings of SAIP2017, the 62nd annual conference of South African Institute of Physics. Division B- Nuclear, Particle and Radiation Physics, 131 - 134 ISBN: 978-0-620-82077-6*. 2018.

[31] Ciupek, K., Jednorog, S., Fujak, M. and Szewczak, K.: Evaluation of efficiency for in situ gamma spectrometer based upon cerium-doped lanthanum bromide detector dedicated for environmental radiation monitoring. *Journal of Radioanalalytical Nuclear Chemistry*, vol. 299, pp. 1345 – 1350, 2014.

[32] Rozsa, C.M., Menge, P.R. and Mayhugh, M.R.: Saint-Gobain Crystals Scintillation Products Technical Note: BrillanCe Scintillators Performance Summary Revision. *http://www.crystals.saintgobain.com/sites/imdf.crystals.com/files/documents/brillance_performance_summary.pdf*, 2009.

[33] Regan, P.H., R.Shearman, Daniel, T., Lorusso, G., Collins, S.M., Judge, S.M., Bell, S.J., Pearce, A.K., Gurgi, L.A., Rudigier, M., Podolyak, Z., Marginean, N., Marginean, R. and Kisyov, S.: Applications of $LaBr_3$(Ce) gamma-ray spectrometer arrays for nuclear spectroscopy and radionuclide assay. In: *Journal of Physics: Conference*, no. 012004 in 763. 2016.

[34] Dhibar, M., Mankad, D., Mazumdar, I. and Kumar, G.A.: Efficiency calibration and coincidence summing correction for a large volume (946 cm^3) $LaBr_3$:Ce detector:GEANT4 simulations and experimental measurements. *Applied Radiation and Isotopes*, vol. 118, pp. 32 – 37, 2016.

[35] Nilsson, J.: *Using the LaBr3:Ce scintillation detector for mobile gamma spectrometry*. masters, Lund University, 2010.

[36] Oberstedt, A., Billnert, R. and Oberstedt, S.: Gamma-ray measurements with $LaBr_3$:Ce detectors-thinking outside the box. *Physics Procedia*, vol. 31, pp. 21 – 28, 2012.

[37] Quarati, F., Owens, A., P.Dorenbos, deHaas, J., Benzoni, G., N.Blasi, C.Boiano, Brambilla, S., F.Camera, R.Alba, G.Bellia, C.Maiolino, D.Santonocito, M.Ahmed, N.Brown, Stave, S., Weller, H. and Wug, Y.: High energy gamma-ray spectroscopy with $LaBr_3$ scintillation detectors. *Nuclear Instruments and Methods in Physics Research A*, vol. 629, pp. 157 – 169, 2011.

[38] Weisshaar, D., Wallac, M., Adric, P., Bazin, D., Campbell, C., Cook, J., Ettenauer, S., Gade, A., Glasmacher, T., McDaniel, S., Obertelli, A., Ratkiewicz, A., Siwek, A.R.K. and Tornga, S.: $LaBr_3$:Ce scintillators for in-beam gamma-ray spectroscopy with fast beams of rare isotopes. *Nuclear Instruments and Methods in Physics Research A*, vol. 594, pp. 56 – 60, 2008.

[39] Regan, P.H., R.Shearman, SM.Judge, G.Lorusso, Main, P., S.Bell, Collins, S., P.Ivanov, Jerome, S., Keightley, J., Larijani, C., G.Lotay and AK.Pearce: Development of NANA: A fast-scintillator, coincidence gamma-ray array for radioactive source characterisation and absolute activity measurements at the UK National Physical Laboratory. In: *Journal of Physics: Conference*, no. 012005 in 620. 2015.

[40] Arnold, L., Duval, M., Falgueres, C., Bahain, J.-J. and Demuro, M.: Portable gamma spectrometry with cerium-doped lanthanum bromide scintillators: Suitability assessments for luminescence and electron spin resonance dating applications. *Radiation Measurements*, vol. 47, pp. 6 – 18, 2012.

[41] Galli, L., M.DeGerone, S.Dussoni, D.Nicol, A.Papa, F.Tenchini and G.Signorelli: Timing resolution measurements of a 3 in. lanthanum bromide detector. *Nuclear Instruments and Methods in Physics Research A*, vol. 718, pp. 48 – 51, 2013.

[42] Choong, W.-S.: The timing resolution of scintillation-detector systems: Monte Carlo analysis. *Physics in Medicine and Biology*, vol. 54, pp. 6495 – 6513, 2009.

[43] Regan, P.: Precision measurement of sub-nanosecond lifetimes of excited nuclear states using fast-timing coincidences with $LaBr_3$(Ce) detectors. *Radiation Physics and Chemistry*, vol. 116, pp. 38 – 42, 2015.

[44] Michetti-Wilson, J.: *Characterization of $LaBr_3$:Ce detectors for Picosecond Lifetime Measurements*. masters, University of Guelph, 2013.

[45] Schaart, D.R., Seifert, S., Vinke, R., van Dam, H.T., Dendooven, P., Lohner, H. and Beekman, F.J.: $LaBr_3$:Ce and SiPMs for time-of-flight PET: achieving 100 ps coincidence resolving time. *Physics in Medicine and Biology*, vol. 55, pp. N179 – N189, 2010.

[46] Kuhn, A., Surti, S., Karp, J., Raby, P., Shah, K., Perkins, A. and Muehllehner, G.: Design of a lanthanum bromide detector for TOF PET. In: *2003 IEEE Nuclear Science Symposium. Conference Record (IEEE Cat. No.03CH37515)*, vol. 3, pp. 1953 – 1957. Oct 2003. ISSN 1082-3654.

[47] Oberstedt, A., Billnert, R. and S.Oberstedt: Neutron measurements with lanthanum-bromide scintillation detectors-A first approach. *Nuclear Instruments and Methods in Physics Research A*, vol. 708, pp. 7 – 14, 2013.

[48] Toivonen, H., Vesterbacka, K. and Pelikan, A.: $LaBr_3$ spectrometry for environmental Monitoring. `https://inis.iaea.org/collection/NCLCollectionStore/_Public/43/003/43003958.pdf?r=1&r=1`.

[49] Quarati, F., Bob, A., Brandenburg, S., Dathy, C., P.Dorenbos, Kraft, S., Ostendorf, R., Ouspenski, V. and Owens, A.: X-ray and gamma-ray response of a 2" x 2" $LaBr_3$:Ce scintillation detector. *Nuclear Instruments and Methods in Physics Research A*, vol. 574, pp. 115 – 120, 2007.

[50] Poschl, M. and Nollet, L.M.L. (eds.): *Radionuclide Concentrations in Food and the Environment.* Pp. 8-10, 17, 18. CRC Press.Taylor and Francis Group 6000 Broken Sound Parkway NW, Suite 300 Boca Raton, FL 33487-2742, 2007.

[51] Martin, J.E.: *Physics for Radiation Protection: A Handbook.* Pp. 135 - 137, 259 - 264, 267 - 270, 330 - 340. 2nd edn. WILEY-VCH Verlag GmbH and Co. KGaA, Weinheim, 2006.

[52] Kathren, R.L.: *Radioactivity in the environment: sources, distribution, and surveillance.* Pp. 21, 31, 39 - 41, 45, 54. Harwood academic publishers, 1937.

[53] Eisenbud, M. and Gesell, T.: *Environmental Radioactivity from Natural, Industrial and Military Sources.* Pp. 134 - 139. 4th edn. Academic Press, 1997.

[54] Eisenbud, M.: *Environmental Radioactivity.* Pp 135,136, 144, 155, 160, 165. Mcgraw-hill book Company, Inc., 1963.

[55] Lottermoser, B. (ed.): *Mine wastes characterization, treatment, Environmental impacts.* Pp. 201, 213 - 229. 2nd edn. Springer Berlin Heidelberg New York, 2007.

[56] Decay chains. `http://metadata.berkeley.edu/nuclear-forensics/Decay%20Chains.html`. Modified from Wikipedia's "decay chain" entry.

[57] Cember, H.: *Introduction to Health Physics.* Pp. 75 - 77, 115 -120, 246 - 248, 252, 253. 2nd edn. Pergamon Press, New York, 1988.

[58] Tsoulfanidis, N.: *Measurement and Detection Radiation.* Pp. 67, 68, 141 - 146, 195 - 197, 209, 217 - 226, 279 - 286. Hemisphere Publishing Corporation, Washington New York London, 1983.

[59] Ragheb, M.: Gamma rays interaction with matter. `https://mragheb.com/NPRE%20402%20ME%20405%20Nuclear%20Power%20Engineering/Gamma%20Rays%20Interactions%20with%20Matter.pdf`, 2019.

[60] Siegbahn, K. (ed.): *Alpha-, Beta- and Gamma-ray Spectroscopy*, vol. 1. Pp. 37 - 37, 443, 444, 450. North-Holland Publishing Company Amsterdam, 1965.

[61] Zeb, J., Arshed, W. and Orfi, S.D.: W-shielder, calculates shielding thickness of water for photon emitting radionuclides between 0.5 to 10 MeV. `http://www.nea.fr/abs/html/iaea1417.html`.

[62] Browne, E. and Tuli, J.K.: Nuclear data sheets for A=60. *Nuclear Data Sheets*, vol. 114, p. 1849, 2013.

[63] Jodlowski, P.: Self-absorption correction in gamma-ray spectrometry of environmental samples- an overview of methods and correction values obtained for the selected geometries. *NUKLEONIKA*, vol. 51, pp. S21 – S25, 2006.

[64] Vargasa, M.J., Timon, A.F., Diazb, N.C. and Sanchez, D.P.: Monte carlo simulation of the self-absorption corrections for natural samples in gamma-ray spectrometry. *Applied Radiation and Isotopes*, vol. 57, pp. 893 – 898, 2002.

[65] Landsberger, S. and Peshev, S.: Compton suppresion neutron activation analysis: past, present and future. *Journal of Radionalytical and Nuclear Chemistry*, vol. 202(1-2), pp. 201 – 224, 1996.

[66] Andrukhovich, S., Antovich, N., Berestov, A., Rudak, E. and Hilmanovich, A.: A method for determining the concentration of radon decay products using

coincidence gamma-spectrometer. *Instrum. Exp. Tech.*, vol. 42(1), pp. 111 – 114, 1999.

[67] Ramadhan, R.A. and Abdullah, K.M.-S.: Background reduction by Cu/Pb shielding and efficiency study of NaI:Tl detector. *Nuclear Engineering and Technology*, vol. 50, pp. 462 – 469, 2018.

[68] Hansman, J.: Design and construction of a shield for the 9" × 9" NaI(Tl) well-type detector. *Nuclear Technology and Radiation Protection*, vol. 29, pp. 165 – 169, 2014.

[69] Mrda, D.S., Bikit, I.S., Anicin, I.V., Slivka, J.M., J. J. Hansman, N.M.Z.-T., Varga, E.Z., Curcic, S.M. and Puzovic, J.M.: Background reduction using Fe and Pb shielding. *Journal of Research in Physics*, vol. 1, pp. 49 – 54, 2004.

[70] Roy, T., More, M., Ratheesh, J. and Sinha, A.: Active and passive CT for waste assay using $LaBr_3$:Ce detector. *Radiation Physics and Chemistry*, vol. 130, pp. 29 – 34, 2017.

[71] Berdnikova, A., Dubinin, F., Dmitrenko, V., Zhukov, K., Kantserov, V., Klassen, N., Orlov, A., Pereima, D.Y. and Shmurak, S.: Studying the spectrometric characteristics of an ionizing-radiation detector based on a $LaBr_3$:(Ce) scintillator and a silicon photomultiplier. *Instruments and Experimental Techniques*, vol. 60, pp. 182 – 187, 2017.

[72] Ulyanov, A., Morris, O., Hanlon, L., McBreen, S., Foley, S., Roberts, O.J., Tobin, I., Murphy, D., Wade, C., Nelms, N., Shortt, B., Slavicek, T., Granja, C. and Solar, M.: Performance of a monolithic $LaBr_3$:Ce crystal coupled to an array of silicon photomultipliers. *Nuclear Instruments and Methods in Physics Research A*, vol. 810, pp. 107 – 119, 2016.

[73] Bailey, D.M.: *A comparison of the use of sodium iodide and Lanthanum bromide scintillation crystals for airborne survey.* masters, Colorado State University, 2014.

[74] Mazumdar, I., Gothe, D., Kumar, G.A., Yadav, N., Chavan, P. and Patel, S.: Studying the properties and response of a large vol. (946 cm^3) $LaBr_3$:Ce detector with gamma-rays up to 22.5 MeV. *Nuclear Instruments and Methods in Physics Research A*, vol. 705, pp. 85 – 92, 2013.

[75] Duval, M. and Arnold, L.: Field gamma dose-rate assessment in natural sedimentary contexts using $LaBr_3$:Ce and NaI:Tl probes: A comparison between the threshold and windows techniques. *Applied Radiation and Isotopes*, vol. 74, pp. 36 – 45, 2013.

[76] Saizu, M.A. and Cata-Danil, G.: Lathanum bromide scintillation detector for gamma spectrometry applied in internal radioactive contamination measurements. *U.P.B. Sci. Bull., A*, vol. 73, no. 4, pp. 119 – 126, 2011.

[77] Tatisscheff, V., Kiener, J., Sedes, G., Hamadache, C., Karkour, N., Linget, D., Astorino, A., Gagliuffi, D.B., Blin, S. and Barrillon, P.: "The Restless Gamma-ray Universe". In: *8th INTEGRAL Workshop*. September 27 - 30 2010.

[78] Alzimami, K.: *The potential use of cerium doped lanthanum scintillators and optimization of imaging processing in SPECT*. PhD, University of Surrey, 2010.

[79] Crespi, F., Camera, F., Blasi, N., Bracco, A., Brambilla, S., Million, B., Nicolini, R., Pellegri, L., Riboldi, S., Sassi, M., Wieland, O., Quarati, F. and Owens, A.: Alpha-gamma discrimination by pulse shape in $LaBr_3$:Ce and $LaCl_3$:Ce. *Nuclear Instruments and Methods in Physics Research A*, vol. 602, pp. 520 – 524, 2009.

[80] Introduction to Monte Carlo methods. `http://csep1.phy.ornl.gov/mc/node1.html`.

[81] Briesmeister, J.F. and et al: MCNP: A general Monte Carlo code for neutron and photon transport. Los Alamos National Laboratory, 1986.

[82] Ferrari, A. and et al: FLUKA. `http://fluka.web.cern.ch/fluka`, 2005.

[83] Agostinelli, S. and *et al.,*: GEANT4-a simulation toolkit. *Nuclear Instruments and Methods in Physics Research A*, vol. 506, pp. 250 – 303, 2003.

[84] *GEANT4 User's Guide for Application Developers, version: Geant4 10.3.* 9 December 2016.

[85] Pia, M.: The GEANT4 toolkit: simulation capabilities and application results. *Nuclear Physics B - Proceedings Supplements*, vol. 125, pp. 60 – 68, 2003. Innovative Particle and Radiation Detectors.

[86] Apostolakis, J. and Wright, D.H.: An Overview of the Geant4 Toolkit. In: Albrow, M. and Raja, R. (eds.), *Hadronic Shower Simulation Workshop*, vol. 896 of *American Institute of Physics Conference Series*, pp. 1 – 10. March 2007.

[87] Newman, R.T., Lindsay, R., Maphoto, K.P., Mlwilo, N.A. and Mohanty, A.K.: Determination of soil, sand and ore primordial radionuclide concentrations by full-spectrum analyses of high-purity germanium detector spectra. *Applied Radiation and Isotopes*, vol. 66, pp. 855 – 859, 2008.

[88] Maleka, P.: Private communication on zanzibar sample.

[89] MARINELLI BEAKERS CATALOG. `https://www.ga-maassociates.com/TechArticles/GAMA_PRODUCT_CAT.pdf`, 2018. GA-MA & ASSOCIATES,INC.

[90] Jones, P.: iThemba LABS annual report. `https://tlabs/wp-content/uploads/pdf/Annual_Report_2013_Small.pdf`, 2013.

[91] Pixie-16 manual Version 3.03. Hardware Revisions: B, C, D, F. `http://www.xia.com/`, 2018.

[92] Palmtop MCA User's manual. Institute of Nuclear Research of the Hungarian Academy of Sciences Debrecen, Hungary, 2011.

[93] Brun, R. and Rademakers, F.: Root-an object oriented data analysis framework. *Nuclear Instruments and Methods in Physics Research Section A: Accelerators, Spectrometers, Detectors and Associated Equipment*, vol. 389.1, pp. 81 – 86, 1997.

[94] Bashir, M., Newman, R. and P.Jones: Determination of activity concentration of ^{238}U and ^{232}Th series radionuclides in soil using a gamma-ray spectrometer in singles and coincidence modes. *Applied Radiation and Isotopes*, vol. 154, pp. 1 – 11, 2019.

[95] Wua, S.: Nuclear data sheets for A=214. *Nuclear Data Sheets*, vol. 110, p. 681, 2009.

[96] Martin, M.: Nuclear data sheets for A=208. *Nuclear Data Sheets*, vol. 108, p. 1583, 2007.

[97] DC. Radford, notes on the use of the program gf3. `https://radware.phy.ornl.gov/gf3/`, 2000.

[98] Update of x-ray and gamma ray decay data standards for detector calibration and other applications. volume 1. `http://www.iaea.org/books`, 2007. IAEA.

[99] Gum, evaluation of measurement data - guide to the expression of uncertainty in measurement. `www.bipm.org`, 2008.

[100] Integrated Detector Design. `http://www.crystals.saint-gobain.com`.

[101] Zeng, Z., Pan, X., Ma, H., He, J., Cang, J., Zeng, M., Mi, Y. and Cheng, J.: Optimization of an underwater in-situ $LaBr_3$:Ce spectrometer with energy

self-calibration and efficiency calibration. *Applied Radiation and Isotope*, vol. 121, pp. 101 – 108, 2017.

[102] UNSCEAR: United Nation Scientific Committee on the Effects of Atomic Radiation. *Sources and effects of ionizing radiation, Report to the General Assembly, with Scientific Annexes*, vol. 1, 2000.

[103] X-ray mass attenuation coefficients. `https://physics.nist.gov/PhysRefData/XrayMassCoef/tab4.html`.

[104] Chen, J.: Nuclear data sheets for A=138. *Nuclear Data Sheets*, vol. 146, p. 1, 2017.